



UNIVERSITÀ DEGLI STUDI DI NAPOLI "FEDERICO II"  
Scuola Politecnica e delle Scienze di Base  
Area Didattica di Scienze Matematiche Fisiche e Naturali

&

Université Paris-Saclay (Paris-Sud)  
École doctorale n° 576 Particules, Hadrons, Énergie, Noyau,  
Instrumentation, Imagerie, Cosmos et Simulation (PHENIICS)

Dottorato di Ricerca in Fisica XXX-Ciclo (Tesi in co-tutela)  
Coordinatore: **Prof. Salvatore Capozziello**

Elaborato finale

## Clusters in light nuclear systems: a multi-method approach

Relatori  
**Dr. Ivano Lombardo**  
**Dr. Giuseppe Verde**  
**Prof. Mariano Vigilante**

Candidato  
**Daniele Dell'Aquila**

Anni 2014/2017



# Abstract

Clustering phenomena affect many aspects of nature and social sciences. They consist in the creation of groups of correlated objects which modify the behaviour of a given system introducing symmetries and order. As an example, in the largest scale known to humans, cluster effects determine the formation of conglomerate of galaxies. On human being scales, clustering is widely present in everyday aspects, leading to collective social behaviours as *consensus* in social and technological networks and *synchronization* in biological systems. In nuclear physics, clustering is one of the most fascinating results of the Pauli exclusion principle and characterizes a large variety of nuclear states, especially in light nuclear systems. Nuclear structures resulting from these phenomena are quite unusual and peculiar, and their investigation is extremely important in the understanding of nuclear forces and their related properties. As an example, cluster structures evolve from *self-conjugated* nuclei to neutron-rich ones with the appearance of highly deformed structures. In the latter case, the cluster centers are bounded together by means of extra-neutrons, which act in a glue-like effect increasing the stability of the structure. Clustering plays also a role in nuclear astrophysics, where it is involved in the creation of elements in stars.

In this thesis, we experimentally investigate clustering aspects of light nuclear systems with a *multi-method* approach and by using different and complementary techniques. In Chapter one, we show how the appearance of clustering phenomena is naturally encouraged by independent-particle approaches to nuclear structure and how, for a detailed description of such aspects, further, collective models, are required. After a comprehensive overview of theoretical models attempting to describe clustering phenomena in nuclei, such as the  $\alpha$ -particle model, shell-like model approaches, and microscopic models, and their predictions within physical cases of recent interest, we make a systematic discussion of the experimental techniques which are usually applied to point out such phenomena.

In Chapter 2 we describe the results of our experimental campaign, carried out in different laboratories and facilities, aimed to improve the present knowledge of clusters in light nuclei and their evolution with the neutron excess. These studies have been performed by using nuclear reactions involving light nuclear systems. We started from the  $^{10}\text{Be}$  nucleus. It is associated to a two  $\alpha$ -like structure coupled to two valence neutrons: it presents nice properties of symmetry. The structure

## Abstract

---

of this nucleus is explored by means of direct reactions which involve the population of highly-excited states in  $^{10}\text{Be}$  and their subsequent in-flight decay. The experiment was performed by using a fragmentation cocktail beam at the FRIBs facility of INFN-LNS (Catania) and the CHIMERA  $4\pi$  multi-detector. Invariant mass techniques are used to reconstruct the spectroscopy of  $^{10}\text{Be}$ , giving the hint for the existence of a new state, possibly associated to a new member of the molecular rotational band.

While the effects of clusterization are well visible and quite well understood in beryllium isotopes, they are much less known in carbon isotopes. For this reason, different neutron-poor and neutron-rich carbon isotopes are here investigated, providing interesting information on the carbon isotopic chain  $^{11,12,13,16}\text{C}$ .  $^{11}\text{C}$ , as well as  $^{13}\text{C}$ , are studied by means of low energy compound nucleus reactions; respectively, we measured the  $^{10}\text{B}(p,\alpha)$  reaction ( $E_p = 0.6\text{-}1.0$  MeV) and the  $^9\text{Be}(\alpha,\alpha)$  resonant elastic scattering ( $E_\alpha = 3.3\text{-}10$  MeV) at the Tandem accelerator in Naples. We analyzed the differential cross section with a comprehensive  $R$ -matrix approach, also by including other data published in the literature. We succeeded in refining their spectroscopy above the  $\alpha$ -disintegration thresholds, with interesting speculation on the existence of molecular rotational bands. The structure of the neutron-rich  $^{16}\text{C}$  isotope is studied with the same experimental apparatus of the  $^{10}\text{Be}$  case by using the most intense  $^{16}\text{C}$  beam produced up to date for nuclear physics experiments at intermediate energies. We provide signatures of the possible existence of high-lying excited states of this poorly known nucleus never observed before. To conclude our studies of clustering in carbon isotopes, the Hoyle state in  $^{12}\text{C}$  (7.654 MeV,  $0^+$ ) was investigated via a high-precision dedicated experiment. The cluster properties of this state are quite crucial; as an example, it has been predicted that its three constituent  $\alpha$ -particles may form a *Bose-Einstein* condensate. We proved, with an unprecedented precision, the fully sequential decay width of this state by using the  $^{14}\text{N}(d,\alpha)$  reaction at 10.5 MeV at the Tandem accelerator of INFN-LNS. To achieve a such high precision we developed a new hodoscope detector. Our result is important since it provides stringent constraints on microscopic theoretical calculations which describe clustering in nuclei, as well as to nuclear astrophysics for the production of carbon and heavier elements in the universe.

Clustering phenomena in  $^{19}\text{F}$  and  $^{20}\text{Ne}$  have been studied by means of the  $^{19}\text{F}(p,\alpha)$  reaction at deeply sub-Coulomb energies ( $E_{cm} = 0.18\text{-}0.60$  MeV) at the AN-2000 Van der Graff accelerator of INFN-LNL. An analysis of angular distributions at various energies gives signatures of possible cluster structures in  $^{19}\text{F}$ . The compound nucleus  $^{20}\text{Ne}$  spectroscopy is instead studied by means of a  $R$ -matrix approach; the astrophysical relevance of our work is also discussed.

Chapter 3 is finally dedicated to a different, complementary, point of view in the study of clustering phenomena: the analysis of Heavy Ion Collisions (HICs) at intermediate energies. Cluster states, produced by overlapping zones formed in HICs and characterized by high temperatures and low densities, can be used as a suitable probe for nuclear structure and dynamics. We implemented a thermal model aimed

to reproduce in-flight resonance decay phenomena in HICs. This model has been applied to the case of  $\alpha$ - $\alpha$  correlations in  $^{36}\text{Ar} + ^{58}\text{Ni}$  central collisions data at various bombarding energies (32-95 AMeV); they have been measured with the INDRA  $4\pi$  multi-detector at the GANIL. The comparisons of data with thermal model predictions allows us to make interesting speculations on the processes contributing to the formation of  $^8\text{Be}$  states in such highly excited and diluted environments.

# Contents

<b>Abstract</b>	<b>iii</b>
<b>Contents</b>	<b>vi</b>
<b>List of Figures</b>	<b>viii</b>
<b>List of Tables</b>	<b>xii</b>
<b>1 Introduction: Clusters in Nuclear Physics</b>	<b>1</b>
1.1 Clusters in nature and social sciences . . . . .	1
1.2 Nuclear models and structure . . . . .	4
1.2.1 A first approach to nuclear structure: the liquid drop model . . . . .	6
1.2.2 Towards a mean field approach: the Hartree-Fock method in nuclei . . . . .	9
1.2.3 The simplest independent particle model: the Fermi-gas model	10
1.2.4 The nuclear shell model . . . . .	12
1.3 Cluster models of nuclei . . . . .	15
1.3.1 The $\alpha$ -particle model . . . . .	18
1.3.2 Microscopic cluster models (RGM, GCM, OCM) . . . . .	24
1.3.3 The quartet model . . . . .	26
1.3.4 Molecular Dynamics (MD) models: clustering in unstable nuclei	28
1.3.5 The deformed harmonic oscillator (HO) . . . . .	29
1.4 Applications of cluster models . . . . .	32
1.4.1 Light self-conjugated nuclei: $^{12}\text{C}$ , $^{16}\text{O}$ , $^{20}\text{Ne}$ . . . . .	32
1.4.2 Astrophysical relevance of clustering . . . . .	42
1.4.3 Non-self-conjugated nuclei: nuclear molecules . . . . .	45
1.5 Techniques for the study of clusters in nuclei . . . . .	53
1.5.1 Compound nucleus reactions . . . . .	54
1.5.2 R-matrix theory . . . . .	60
1.5.3 Direct reactions and correlations . . . . .	62
1.5.4 The interplay between structure and dynamics: heavy-ion collisions (HICs) and clusters . . . . .	69
1.6 Summary and organization of the manuscript . . . . .	76

<b>2</b>	<b>Clustering in light systems: an experimental campaign</b>	<b>79</b>
2.1	$^{10}\text{Be}$ cluster states with breakup reactions . . . . .	79
2.1.1	Experimental apparatus and techniques . . . . .	80
2.1.2	Experimental results: $^6\text{He}$ - $^4\text{He}$ correlations . . . . .	82
2.1.3	Impact of our results on successive works . . . . .	88
2.2	The structure of $^{11}\text{C}$ with the $^{10}\text{B}(\text{p},\alpha)^7\text{Be}$ reaction . . . . .	88
2.2.1	Experimental apparatus and techniques . . . . .	90
2.2.2	Angular distributions, integrated cross-sections and S-factor of the $^{10}\text{B}(\text{p},\alpha_0)$ reaction . . . . .	94
2.2.3	$R$ -matrix fit of data and the spectroscopy of $^{11}\text{C}$ . . . . .	97
2.2.4	Impact of our results on successive works . . . . .	101
2.3	Clustering in $^{12}\text{C}$ : the decay path of the Hoyle state . . . . .	103
2.3.1	Experimental technique: the $^{14}\text{N}(\text{d},\alpha)^{12}\text{C}$ reaction . . . . .	104
2.3.2	Analysis of the direct $\alpha$ -decay width of the Hoyle state . . . . .	106
2.3.3	Impact of our results on successive works . . . . .	109
2.4	Clustering in $^{13}\text{C}$ with $\alpha + ^9\text{Be}$ reactions . . . . .	110
2.4.1	Selection of reaction data-set . . . . .	110
2.4.2	Results of $R$ -matrix fit of data . . . . .	112
2.4.3	Impact of our data on molecular bands . . . . .	122
2.5	Clustering in $^{16}\text{C}$ : towards the dripline . . . . .	124
2.5.1	Experimental results . . . . .	124
2.5.2	Consequences of our investigation on successive works . . . . .	126
2.6	Cluster structures in $^{20}\text{Ne}$ and $^{19}\text{F}$ and their role in the $^{19}\text{F}(\text{p},\alpha)^{16}\text{O}$ reaction . . . . .	127
2.6.1	Experimental details . . . . .	129
2.6.2	Angular distribution analysis and $R$ -matrix fit of data . . . . .	133
2.6.3	Impact of our results on successive works . . . . .	137
<b>3</b>	<b>Clustering in HICs as a link between structure and dynamics</b>	<b>139</b>
3.1	Further details on correlations in HICs . . . . .	139
3.1.1	The thermal model for correlations in central HICs at low and intermediate energies . . . . .	141
3.1.2	The In-Flight Decay Simulation Code . . . . .	143
3.1.3	HBT interferometry in Nuclear Physics . . . . .	144
3.1.4	Characterization of the emitting source . . . . .	147
3.2	Application of the thermal model to $\alpha$ - $\alpha$ correlations in $^{36}\text{Ar} + ^{58}\text{Ni}$ with the INDRA $4\pi$ multi-detector . . . . .	148
3.2.1	The INDRA experimental filter . . . . .	148
3.2.2	Analysis of $\alpha$ - $\alpha$ correlations in $^{36}\text{Ar} + ^{58}\text{Ni}$ systematics from 32 AMeV to 95 AMeV . . . . .	155
3.2.3	Discussion on the reaction dynamics . . . . .	162
<b>Conclusions</b>		<b>169</b>

<b>Bibliography</b>	<b>173</b>
<b>Ringraziamenti</b>	<b>189</b>
<b>A A new device for future clustering and correlation studies: OSCAR</b>	<b>191</b>
A.0.4 Detector's layout . . . . .	191
A.0.5 Detector characterization . . . . .	194
A.0.6 Non-uniformity of the $\Delta E$ stage . . . . .	198
A.0.7 Channeling effects in $\Delta E$ detector . . . . .	201
A.0.8 Correlations: the case of $\alpha$ - $\alpha$ correlation and the reconstruction of ${}^8\text{Be}$ . . . . .	203

## List of Figures

1.1 Clustering in biological systems: fish schooling . . . . .	2
1.2 Clustering behaviour in social systems: the bonobo . . . . .	3
1.3 Binding energy per nucleon for self-conjugated nuclei . . . . .	7
1.4 Deviations between experimental nuclear masses and liquid drop model masses . . . . .	8
1.5 Average energy of the first excited state for doubly-even nuclei as a function of the neutron number . . . . .	13
1.6 ${}^{16}\text{O}$ excited states via multi-particles multi-holes shell model excitations .	16
1.7 Spatial correlations as a function of the relative distance between nucleons in the case of non-congruent nucleons and congruent nucleons . . . .	17
1.8 Historical developments of cluster models of nuclei from 1930's. . . . .	19
1.9 Binding energy for the lightest self-conjugated nuclei as a function of the number of bonds between between $\alpha$ -cluster centers . . . . .	20
1.10 Geometrical arrangements of $\alpha$ -clusters in the $\alpha$ -particle model . . . . .	21
1.11 Terms contributing to the compute of the excitation energy of the (210) quartet configuration of ${}^{16}\text{O}$ . . . . .	27
1.12 Energy levels of the deformed harmonic oscillator as a function of the quadrupole deformation $\epsilon_2$ . . . . .	31
1.13 Harmonic oscillator wave-functions and densities for ${}^8\text{Be}$ . . . . .	32
1.14 The Ikeda diagram of self-conjugated nuclei . . . . .	34
1.15 Decomposition of the THSR wave function describing the ${}^{12}\text{C}$ g.s. . . . .	36

1.16	Density distribution $\rho(x, y)$ of the Hoyle state in $^{12}\text{C}$ from microscopic calculations based on the Faddeev three-body formalism and Dalitz plot of its decay . . . . .	37
1.17	$^{12}\text{C}$ energy spectrum from AMD calculations compared to RGM and GCM results . . . . .	38
1.18	$^{12}\text{C}$ experimental bands compared with ACM calculations . . . . .	39
1.19	Rotational bands of $^{16}\text{O}$ calculated with the ACM from [98] . . . . .	41
1.20	Rotational spectra of the heteropolar diatomic molecule compared with theoretical $\alpha + \text{core}$ calculations for $^{16}\text{O}$ and $^{20}\text{Ne}$ from [100] . . . . .	42
1.21	Levels involved in the $3\alpha$ process . . . . .	43
1.22	$3\alpha$ reaction rate calculated with different methods from [111] . . . . .	44
1.23	Modified Ikeda diagram to account cluster structures in the presence of extra neutrons . . . . .	46
1.24	Excitation energy spectrum of $^{10}\text{Be}$ as a result of the variational calculations after spin-parity projection (VAP) in the AMD framework from [120] . . . . .	47
1.25	Schematic representation of molecular orbit $\pi$ and $\sigma$ in the case of two $\alpha$ -centers . . . . .	48
1.26	Comparison between the mirror nuclei $^{11}\text{C}$ and $^{11}\text{B}$ low-lying states . . . . .	50
1.27	Parity-split rotational bands ( $K = 1/2^\pm$ ) based on the $^9\text{Be}(3/2^-, g.s.) + \alpha$ structure from [127] . . . . .	51
1.28	Calculated $^{13}\text{C}$ rotational bands in the GCM framework from [129] . . . . .	52
1.29	Spectroscopic factors of the $^{13}\text{C}$ Hoyle analog state within the OCM framework from [131] . . . . .	53
1.30	Density distributions of $^{16}\text{C}$ valence neutrons and protons as computed by AMD calculations from [132] . . . . .	54
1.31	Calculated positive parity energy levels of $^{16}\text{C}$ , via the AMD, as a function of their angular momentum $J$ , from [132] . . . . .	55
1.32	Energy scheme of a compound nucleus reaction . . . . .	57
1.33	Angular distribution of $^{16}\text{O}(^6\text{Li}, d)^{20}\text{Ne}$ $\alpha$ -transfer reaction from [150] . . . . .	64
1.34	Kinematics of a <i>breakup</i> reaction . . . . .	66
1.35	Angular correlation analysis of breakup fragments, from [153] . . . . .	68
1.36	A schematic view of a symmetric Dalitz plot . . . . .	69
1.37	Symmetry energy with and without cluster-production, from [157] . . . . .	70
1.38	AMD calculations with and without clusters of HICs charge distributions, from [160] . . . . .	71
1.39	An example of $d$ - $\alpha$ correlation function for the structure of $^6\text{Li}$ , from [162] . . . . .	72
1.40	Determination of the spin for the $E_{rel} = 0.774$ MeV resonance in $^8\text{B}$ from $p$ - $^7\text{Be}$ correlations. From [164] . . . . .	74
1.41	Caloric curve with isotopic thermometer and excited state thermometer from [166] . . . . .	75
1.42	Excited state temperatures and isotopic temperatures as a function of the incident energies in central HICs from [171] . . . . .	76

## List of Figures

---

2.1	Identification plot of the FRIBs cocktail beam . . . . .	81
2.2	$\Delta E$ - $E$ spectrum obtained at $\theta_{lab} = 3.1^\circ$ with the CHIMERA multi-detector	82
2.3	$^8\text{Be}$ and $^{12}\text{C}$ relative energy spectrum from the $\alpha$ - $\alpha$ and $3\alpha$ correlations .	83
2.4	$^{10}\text{Be}$ excitation energy spectrum obtained from the $^4\text{He}+^6\text{He}$ decay channel	84
2.5	Angular correlation of $^4\text{He}+^6\text{He}$ break-up channel for the 11.8 MeV . . .	86
2.6	Elastic backscattering spectrum obtained at $\theta_{lab}=140^\circ$ with 0.988 MeV proton beam . . . . .	91
2.7	Kinematic curves of scattering and reaction events on boron and con- taminants in the target obtained at $E_p=0.95$ MeV . . . . .	92
2.8	Schematic drawing of the experimental setup . . . . .	93
2.9	Ejectile spectrum obtained at $\theta_{lab} = 40^\circ$ with 0.988 MeV incident protons	94
2.10	Ejectile spectra obtained at $\theta_{lab} = \pm 160^\circ$ with 0.988 MeV incident protons	95
2.11	Angular distributions of the $^{10}\text{B}(p,\alpha_0)^7\text{Be}$ reaction . . . . .	96
2.12	$^{10}\text{B}(p,\alpha_0)^7\text{Be}$ astrophysical $S$ -factor . . . . .	97
2.13	Global $R$ -matrix fit of $^{10}\text{B}(p,\alpha_0)^7\text{Be}$ $S$ -factor including $^{10}\text{B}(p,p_0)^{10}\text{B}$ DCS at $150^\circ$ and $130^\circ$ and $^{10}\text{B}(p,\alpha_1)^7\text{Be}$ data . . . . .	99
2.14	$^{11}\text{C}$ negative parity rotational band $K^\pi = 3/2^-$ . . . . .	102
2.15	$^{12}\text{C}$ excitation energy spectrum reconstructed by the anti-coincidence telescope . . . . .	105
2.16	Three particle invariant mass spectrum ( $^{12}\text{C } E_x$ ) gated on the Hoyle peak of Figure 2.15 . . . . .	106
2.17	Experimental symmetric Dalitz plots for the decay of the Hoyle state . .	107
2.18	Radial projection distribution $\varepsilon_i$ of the symmetric Dalitz plot for the Hoyle state decay . . . . .	108
2.19	Ejectile energy spectrum observed in $\alpha+^9\text{Be}$ collisions at $E_\alpha = 9.24$ MeV and $\theta_{lab} = 70^\circ$ . . . . .	111
2.20	$R$ -matrix fit of $^9\text{Be}(\alpha,\alpha_0)^9\text{Be}$ DCS at laboratory angles of $160^\circ$ , $150^\circ$ , $135^\circ$ and $110^\circ$ . . . . .	114
2.21	$R$ -matrix fit of low-energy $^9\text{Be}(\alpha,\alpha_0)^9\text{Be}$ DCS at center of mass angles $160^\circ$ and $150^\circ$ . . . . .	116
2.22	$R$ -matrix fit of excitation functions of the $^9\text{Be}(\alpha,n_0)^{12}\text{C}_{GS}$ and $^9\text{Be}(\alpha,n_1)^{12}\text{C}_{4.44}$ angle integrated reaction cross section . . . . .	116
2.23	Zoom of $R$ -matrix fit of the $^9\text{Be}(\alpha,n_0)^{12}\text{C}$ integrated cross section data and the $^9\text{Be}(\alpha,\alpha_0)^9\text{Be}$ DCS at $\theta_{cm} = 160^\circ$ . . . . .	117
2.24	Zoom of $R$ -matrix fit of the $^9\text{Be}(\alpha,\alpha_0)^9\text{Be}$ DCS data at $\theta_{lab} = 160^\circ$ and the $^9\text{Be}(\alpha,\alpha_0)^9\text{Be}$ DCS data at $\theta_{lab} = 160^\circ$ . . . . .	119
2.25	$R$ -matrix fit of the $^9\text{Be}(\alpha,\alpha_1)^9\text{Be}_{1.68}$ DCS data at $\theta_{lab} = 70^\circ$ . . . . .	121
2.26	$^{13}\text{C}$ $K^\pi = 3/2^-$ band and the hypothetical $K^\pi = 3/2^+$ band as obtained from our $R$ -matrix fit . . . . .	123
2.27	$^{16}\text{C}$ excitation energy spectrum obtained from the $^{10}\text{Be}+^6\text{He}$ break-up channel . . . . .	125
2.28	$^{16}\text{C}$ excitation energy spectrum for the three body $^6\text{He}+^6\text{He}+^4\text{He}$ break- up channel . . . . .	127

## List of Figures

---

2.29	Experimental $^{19}\text{F}(\text{p},\alpha_0)^{16}\text{O}$ ejectile spectrum at $\theta_{lab} = 20^\circ, 160^\circ$ and $E_p = 0.347$ MeV with the Al absorber . . . . .	131
2.30	Angular distributions of the $^{19}\text{F}(\text{p},\alpha_0)^{16}\text{O}$ reaction . . . . .	132
2.31	Evolution with the energy of the $A_i$ coefficients of cosine power fit of experimental angular distributions of the $^{19}\text{F}(\text{p},\alpha_0)^{16}\text{O}$ reaction . . . . .	134
2.32	$S$ -factor of the $^{19}\text{F}(\text{p},\alpha_0)^{16}\text{O}$ reaction at low energies . . . . .	135
3.1	Qualitative description of a central HIC at intermediate energies . . . . .	140
3.2	A schematic explanation of the HBT effect in astronomy . . . . .	145
3.3	Geometrical scheme of the INDRA $4\pi$ multi-detector from [334] . . . . .	149
3.4	A photo of the INDRA $4\pi$ multi-detector. . . . .	150
3.5	Maxwellian moving-source fit of Be energy spectra, with the INDRA multi-detector . . . . .	151
3.6	$\eta(E, E')$ matrix used to simulate the effect of the detector for $\alpha$ - $\alpha$ correlations . . . . .	152
3.7	Simulated $\alpha$ - $\alpha$ relative momentum spectrum with the INDRA multi-detector . . . . .	154
3.8	Calibration curve of the $\alpha$ - $\alpha$ excited-state thermometer with the INDRA multi-detector . . . . .	155
3.9	Eperimental two- $\alpha$ coincidence yield, as a function of the relative momentum, for $^{36}\text{Ar} + ^{58}\text{Ni}$ at 74 A MeV . . . . .	157
3.10	Experimental two- $\alpha$ correlation function for $^{36}\text{Ar} + ^{58}\text{Ni}$ at 74 A MeV . . . . .	158
3.11	Coulomb anti-correlation best-fit of IMF-IMF correlations in $^{36}\text{Ar} + ^{58}\text{Ni}$ collisions at 74 A MeV . . . . .	159
3.12	$\alpha$ - $\alpha$ coincidence yield obtained by subtracting the uncorrelated yield and the coulomb anti-correlation effects . . . . .	160
3.13	$\alpha$ - $\alpha$ coincidence yield for all the sistematic here explored . . . . .	161
3.14	Experimental $\alpha$ - $\alpha$ yield ratios compared with the results the pure thermal model . . . . .	163
3.15	Ratio of $\alpha$ - $\alpha$ in-medium reaction rates through the 3.04 MeV state and the ground state of $^8\text{Be}$ . . . . .	165
3.16	IMF-IMF correlation function for the forward and the backward region of emission . . . . .	166
A.1	Atomic Force Microscopy (AFM) profiling the silicon strip detector surface	192
A.2	Frequency histogram of the relative height distribution obtained with the AFM technique . . . . .	192
A.3	A schematic view of the second detection stage of OSCAR . . . . .	194
A.4	A picture of the OSCAR device in the complete configuration . . . . .	194
A.5	A schematic view of the OSCAR telescope . . . . .	195
A.6	Identified particle yield distribution with OSCAR . . . . .	196
A.7	Identified particle yield distribution with OSCAR (simulated) . . . . .	196
A.8	$\Delta E$ - $E$ plot for a pseudo-telescope of the OSCAR device . . . . .	197

A.9	$\Delta E$ - $E_{res}$ plot for nuclei identified as ${}^4\text{He}$ with OSCAR . . . . .	198
A.10	Correlations between expected theoretical and experimental identification thresholds for different identified isotopes in the OSCAR device . . . . .	199
A.11	Bi-dimensional distribution of the SSSSD thickness . . . . .	200
A.12	SSSSD thickness characterization . . . . .	200
A.13	Mass identification resolution as a function of the degree of non-uniformity . . . . .	201
A.14	Channeling effect in the SSSD stage . . . . .	202
A.15	Evolution of the percentage of channeling events as a function of the detector thickness . . . . .	202
A.16	$\alpha$ - $\alpha$ invariant mass spectrum obtained with OSCAR . . . . .	204
A.17	Simulated resolution and efficiency in the reconstruction of the ${}^8\text{Be}$ ground state via $\alpha$ - $\alpha$ correlations with OSCAR . . . . .	204

## List of Tables

1.1	Geometrical configurations proposed by [29–31] for the first self-conjugated nuclei . . . . .	22
1.2	Possible ${}^{16}\text{O}$ configurations predicted by the quartet model . . . . .	28
1.3	Deformed magic numbers in terms of the spherical magic numbers . . . . .	33
2.1	${}^{10}\text{Be}$ level structure from ${}^4\text{He}+{}^6\text{He}$ break-up channel. . . . .	87
2.2	${}^{11}\text{C}$ spectroscopy from the $R$ -matrix fit . . . . .	100
2.3	${}^{13}\text{C}$ level structure derived from our comprehensive the $R$ -matrix best-fit . . . . .	113
3.1	Centrality selection cuts for the ${}^{36}\text{Ar} + {}^{58}\text{Ni}$ here investigated . . . . .	156

# Chapter 1

## Introduction: Clusters in Nuclear Physics

### 1.1 Clusters in nature and social sciences

The dynamical evolution of many body systems in nature is determined by the properties of what physicists define as *potential energy*. In particular, physical systems find more *convenient* reaching stages characterized by lower values of the corresponding potential energy, resulting in a gain in *stability*. A genuine effect of this fact is often the propensity of objects, belonging to a physical system, to congregate in sub-units, named as *clusters*. This collective phenomenon, which is called *clustering*, is present in a large varieties of physical systems and in an extremely broad range of length scales. On the largest one, the universe, it is known for example that the pattern of galaxies in the sky is not random [1]. The study of the survey of 2dF galaxy redshift has indeed pointed out that, as a result of the post Big Bang inhomogeneities, matter congregates into filament-like structures, forming *superclusters* of galaxies [2]. On a smaller scale, our universe shows the interesting appearance of gravitational assemblages of stars into galaxies and planets into solar systems, which represent an analogous example of gravitational clusters but in a more reduced scale. On human beings scales, clustering phenomena may often influence everyday aspects, leading to peculiar collective behaviours such as consensus in social and technological networks [3] and synchronization in biological systems [4]. The first aspect is related to the nascent field of *network science* [5], which involves a quite interdisciplinary mixing of academic fields like *sociology*, *statistics* and *graph theory*. The most complex social networks, the so called *complex networks*, involve indeed features of *social complexity*.

Clustering is a fundamental aspect in the theory of complex networks, since they show non-trivial topologies, where connections between nodes are not entirely random. In such complex systems, the tendency of nodes of a graph to cluster together is observed, resulting in the appearance of knit groups characterized by



Figure 1.1: A group of yellow runner fishes schooling. Staying together in schools helps to protect fish from their enemies. While a predator might easily grab a fish by itself, it is much harder for a predator to single out a victim if a fish is surrounded by hundreds of them.

quite large densities of ties. This trend usually significantly overcomes the average probability of randomly established connections between nodes [6]. An example is the graph structure induced by the friendship links in social networks like Facebook or LinkedIn. Clustering is a fundamental aspect also in social sciences like Economics. Clustering phenomena indeed affect the competition of companies by increasing their productivity, by driving innovation in the field and by stimulating new businesses [7], resulting in the spontaneous creation of interconnected businesses. The study of such agglomerations is very important, for instance, in the so called *strategic management*. A particularly fascinating example is the case of the *Silicon Valley* in California. In the second half of 1990s, it was the gravitational center of a large number of computer-technology related companies and startups. This geographical cluster effect led to a cluster effect in the labour market. In other words, as the number of companies increased in Silicon Valley, an increasing number of highly skilled workers decided to move there, leading to a high density concentration of technically skilled people. So the probability for companies and startups to find good job candidates in the Silicon Valley started to become significantly higher than any other place, giving to high-tech workers a further incentive to move there.

In computer science, clusters of computing nodes, called *computer clusters*, are widely used in order to increase the performances in executing tasks with relatively low costs and better reliability. They consist in a set of connected computers that work together in a system in which each node executes the same task, in a way that they can be seen as a single system.

On aspects related to life, many biological systems exhibit clustering phenomena. Particular species of fishes, for example, are used to stay together for social reasons,

## 1.1 Clusters in nature and social sciences

---



Figure 1.2: The bonobo, formerly called the *pygmy chimpanzee*, is used to clusterize in complex social groups which can amount at 30-80 units. It is a fascinating example of how *clustering* in biological systems can offer evolutionary advantages.

i.e. *shoaling*. Shoaling is a collective behaviour of fish consisting in the formation of a group where fishes swim independently but staying connected. They derive many advantages from shoaling, such as higher probability to survive against predators, enhanced success in providing food or in finding a mate. Another interesting collective behaviour involving fish is the so called *schooling*, where the clustered group starts to swim in the same direction (Figure 1.1). This behaviour allows to improved hydrodynamic efficiency and predator avoidance, and it is mandatory for species like tuns. It represents a nice example of how biological systems recognize the importance of clustering for evolutionary advantages [8]. Clustering behaviours are widely present in other animal species like the *bonobo*, or *pygmy chimpanzee*. They have quite complex social connections, grouping into communities made of 30–80 units and spreading in quite large surfaces. Despite the non-vanishing superpositions of territories belonging to different groups, they behave as social units strongly clustered (Figure 1.2). This attitude offers the advantages of limiting possible aggressions between members of the community and to significantly improve their social communication skills, leading to behaviours which are quite similar to human ones. Finally, microscopic systems also recognize the fundamental importance of collective behaviours and symmetry. In atomic physics, as an example, atoms cluster into molecules and bindings between molecules in chemical compounds also show the propensity to form clusters. An example is the interaction of the Acrylamide compound with water molecules (Arc+W) forming hydrogen bonded clusters, where strong hydrogen bonds between water play a very crucial role [9] allowing to reach

optimized energy states. This acts in a loss of degrees of freedom of the atoms in the compound, imposing more order in the system.

The world of the *extremely small*, such as nuclei or sub-nuclear particles, exhibit peculiar and quite unusual clustering effects [10]. While in sub-nuclear physics the systematic binding of *quarks* in sub-units, made of 3 or 2 constituents, makes it possible the appearance of baryons and mesons, in the nuclear domain clustering phenomena can occur between nucleons. Nuclei are indeed quite far to be static collections of nucleons; they are highly dynamic systems where constituents, i.e. protons and neutrons, move with velocities which amounts to significant fractions of the speed of light. Their dynamics imposes strong correlations, originated by quantum mechanical effects. The Pauli exclusion principle, as an example, forces like-nucleons to couple in *singlet* spin state, i.e. with anti-aligned spins; so they can minimize the repulsion originating from the Pauli principle and increase the *binding energy* of the system. In such a way, the highest correlated system in nuclei is the quartet  $2p + 2n$ , i.e. the so-called  $\alpha$  particle. On a qualitative point of view it does not surprise that the appearance of such highly correlated quartets in nuclei would provide an energetic advantage and that, once formed, these compact sub-units can propagate within the nuclear volume quite unperturbed and for a significant time. This phenomenon is called  $\alpha$ -clustering and it is one of the most fascinating aspects of Nuclear Physics.

In this thesis, clustering phenomena in light nuclei are discussed from a multi-method point of view. Results from our experimental campaigns, providing complementary aspects of nuclear clustering, are described in Chapter 2 and Chapter 3. The present chapter is dedicated to a general description of clustering in nuclei. In Section 1.2, we provide an historical overview of nuclear models attempting to describe static properties of nuclei. The generalities of the cluster model, which will be introduced as a complementary point of view to describe certain aspects of nuclei beyond the mean-field approach, are discussed in detail in Section 1.3, while Section 1.4 is fully dedicated to applications of the cluster model to physical cases of interest in modern nuclear physics. An overview of experimental techniques, which can be used in order to unveil on the presence of clustering phenomena in light nuclear systems, will be described in Section 1.5. Finally, a *résumé* of these contents and a general summary of the entire thesis will be outlined in Section 1.6.

## 1.2 Nuclear models and structure

The most important question of nuclear physics is understanding how nuclei work. They are indeed extremely complex many-body systems where *fundamental* constituents, i.e. protons and neutrons, are not actually fundamental particles. Protons and neutrons are in fact aggregates of *quarks*. Anyway, a comprehensive analytical description of nuclei starting from the Quantum Chromodynamics (QCD) is currently impossible, because of the divergence of the complexity of the problem. At variance,

## 1.2 Nuclear models and structure

---

attempts of describing nuclei as systems of nucleons have been developed starting from the discovery of the atomic nucleus. The force governing such systems can be seen as the residual, at the nucleons scales, of the strong interaction between quarks, and it is therefore an *effective force*. Under this assumption, solving the main problem of nuclear physics is equivalent to the resolution of the Schrödinger equation:

$$H|\Psi\rangle = E|\Psi\rangle \quad (1.1)$$

where the degrees of freedom are the spatial coordinates  $\vec{r}_i$ , spins  $\sigma_i$  and isospins  $\tau_i$  of each nucleon ( $i = 1, \dots, A$ ), i.e.  $\Psi \equiv \Psi(\vec{r}_1, \sigma_1, \tau_1, \dots, \vec{r}_A, \sigma_A, \tau_A)$  and the Hamiltonian  $H$ , consequently, is defined as:

$$H = - \sum_i \frac{\hbar^2}{2m} \nabla_i^2 + \frac{1}{2} \sum_{i \neq j} V(i, j) + \frac{1}{3} \cdot \frac{1}{2} \sum_{i \neq j \neq k} W(i, j, k) \quad (1.2)$$

The particular definition of the Hamiltonian of equation 1.2 involves both a two body term, which is related to nucleon-nucleon interactions, and a three body one, which appear in the presence of three or more bodies. The latter is mandatory in order to describe nuclei and it belongs from the fact that nuclear forces do not present additivity; in other words, extra interactions, not reproducible by adding separately each interaction, occur in the presence of more than two bodies. These strange properties make the problem of equation 1.1 an extremely difficult problem. This kind of approach is called *ab-initio*, since it starts from nucleon-nucleon and multi-nucleon interactions. Recent developments in two-nucleon (like for example the Argonne potential [11]) and three-nucleon potential (see the Urbana potential [12]) have been achieved but, despite the strong effort, only a partial description of the structure of a limited class of light nuclei, can be reasonably obtained.

In the absence of a general and comprehensive theory for the description of nuclei, a number of *nuclear models* have been historically developed in order to reproduce their properties. Each model attempts in reproducing a specific set of properties, under peculiar (and simplifying) assumptions. In this way, different models are able to explain different portions of our experimental knowledge about nuclei. The first *nuclear atom* model was developed by Nagaoka at the very beginning of the XX century [13, 14]. This model, which assumed the existence of *rings* of rotating electrons around a positive charged core, brought however to difficulties in the classical electromagnetic theory. The *charged-cloud* atom model was then developed by J.J. Thomson, in order to circumvent the contradictions introduced by the Nagaoka's model. In the famous Thomson model, electrons were uniformly distributed throughout a sphere of positive charge [15]. The vision given by the Thomson model was contradicted by E. Rutherford [16] by giving the basis of the model which opened the doors to the modern nuclear physics. According to the Rutherford model, the positive charge of the atom had to be concentrated in an extremely small portion of space. Whereas Thomson's atomic cloud has the dimen-

sions of the order of  $10^{-8}$  cm, Rutherford's atomic nucleus has a diameter which doesn't exceed  $10^{-12}$  cm.

### 1.2.1 A first approach to nuclear structure: the liquid drop model

The *liquid drop model* is historically the first model for the description of the properties of nuclei [17]. The basic idea of this model is originated in Bohr's concept of compound nucleus reactions. An incident particle captured by a target nucleus, to form a compound system, shares its energy with all the nucleons quite rapidly. The corresponding mean free path of the particle is significantly shorter than the nuclear radius. To explain this, interactions between nucleons have to be strong and short ranged and particles cannot be considered as independently moving. According to this evidence, nucleons in nuclei should exhibit collective behaviours. Also the nuclear binding energy<sup>1</sup> per nucleon  $B(A, Z)/A$  reflects similar properties of nuclei. The dependence of the binding energy on the number of nucleons clearly exhibits saturation properties typical of short range interactions. Indeed, a non-saturated force would lead to a binding energy given by  $A(A-1)/2$  times the nucleon two-body interaction energy, which is in contradiction with the experimental observation of Figure 1.3. Furthermore, nuclei present low compressibility and well defined surface effects. All these features evidence analogies with liquids. A liquid drop model is therefore useful in order to describe such properties of nuclear systems.

The liquid drop model is particularly suited for quantitative studies of nuclear masses, the nuclear energy surface and the energetic of decays and nuclear reactions. In this model, nuclei are approximated to a charged liquid drop. It is possible to study, under such an approximation, three fundamental terms contributing to the nuclear binding energy. The first one is the so called *volume* contribution and it is responsible of the saturation of  $B(A, Z)/A$ , to values of about  $8\text{MeV} \pm 10\%$ , observed in the experimental data (see Figure 1.3) for  $A \geq 16$ . This term gives:

$$B_V = a_V A \quad (1.3)$$

where the arbitrary constant  $a_V$  is evaluated by empirically fitting the experimental data. The second term reflects also the short range of the force between nucleons. This term can be seen as a correction of the previous one for the nucleons which constitute the nuclear surface, which are only partially surrounded by other nucleons, and, therefore, less bound. A liquid drop treatment of this term lead to:

$$B_S = -a_S A^{\frac{2}{3}} \quad (1.4)$$

---

<sup>1</sup>The *binding energy* of a system is the difference between the mass of the free constituents and the mass of the bound system [14]. In nuclei, the nuclear binding energy of a nucleus with  $A$  nucleons and  $Z$  protons can be calculated as follows:  $B(A, Z) = Z \cdot m(p) + (A - Z) \cdot m(n) - m(Z, A)$ .

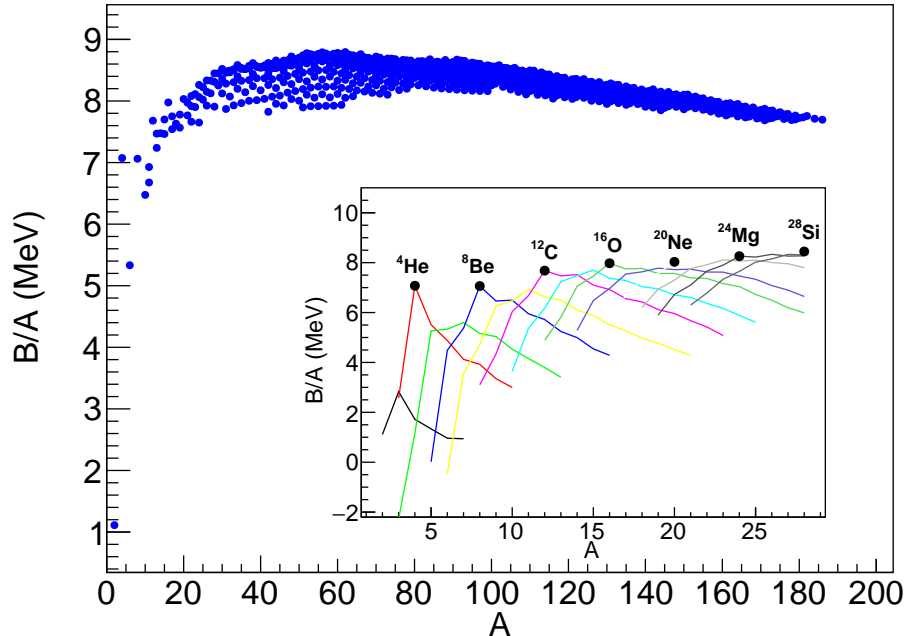


Figure 1.3: The binding energy per nucleon ( $B/A$ ) as a function of the number of nucleons  $A$  for a large variety of nuclei. The systematic of nuclear masses is taken from [18, 19]. The insert shows a zoom of the  $A \leq 28$  mass region, where lines of different colours represent the trend of  $B/A$  for each isotopic chain. They peak on self-conjugated isotopes, which are indicated by labels, as a result of the clustering.

Coulomb effects have to be taken into account since a charge of  $eZ$  is present within the nuclear volume. Considering, according to the model, a sphere of uniform distributed charge, the corresponding correction to the binding energy can be evaluated by means of simple considerations of general physics (see for example [17]):

$$B_C = -a_C Z(Z-1)A^{-\frac{1}{3}} \quad (1.5)$$

The binding energy terms of equations 1.3, 1.4 and 1.5 can be used in order to compute, for a large variety of nuclei, the total binding energy of the system, and, consequently the nuclear mass. In Figure 1.4, deviations of nuclear mass values calculated via a drop model assumption with respect to the experimental values (see [18, 19]) are shown as a function of the proton number  $Z$ . Nuclei have been divided in two classes on the basis of their neutron-proton asymmetry. In particular nuclei obtained with the condition  $|N - Z|/A < 0.22$  (where  $N$  represents the number of neutrons of the nucleus) are plotted in blue colour. Green points represent the complementary set of nuclei, i.e. nuclei characterized by  $|N - Z|/A \geq 0.22$  values, which present a strong neutron or proton excess. From the figure, some conclusions

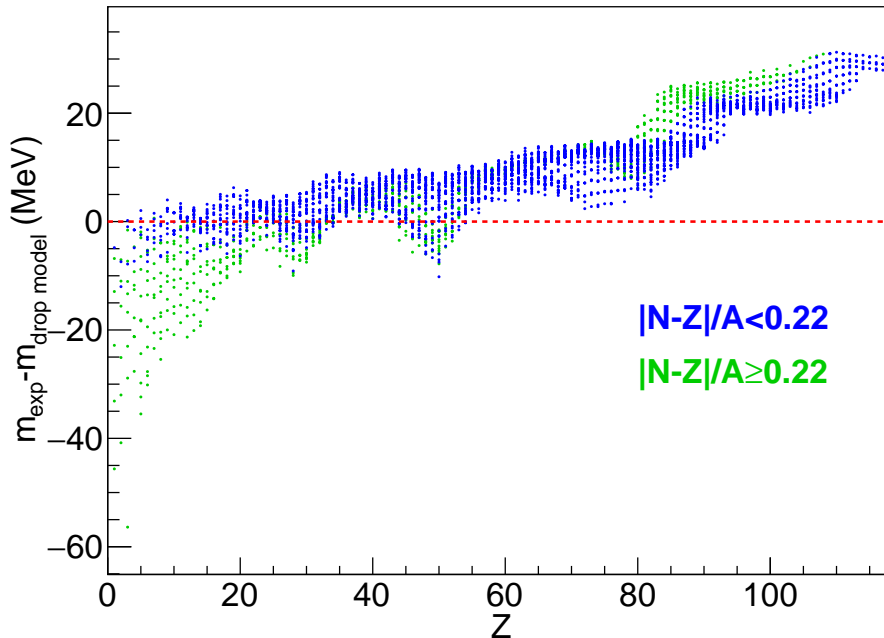


Figure 1.4: Deviations between experimental nuclear masses (taken from [18, 19]) with respect to the ones calculated by means of the nuclear drop model binding energies as a function of the proton number  $Z$ . Green points represent nuclei with a degree of neutron-proton asymmetry ( $|N - Z|/A$ ) larger than 0.22 while blue points are obtained by the condition  $|N - Z|/A < 0.22$ . Periodicity in the shown deviations evidences features that go beyond a liquid drop model treatment of nuclei.

about the validity of nuclear liquid drop model can be drawn. The first is that the description of nuclear masses becomes worst as the neutron-proton asymmetry increases. This is typical of nuclei which are far from the *stability valley*<sup>2</sup>. This fact reflects the appearance of quantum mechanical behaviours in nuclei, which are due to the large asymmetry in these unstable configurations, with significant deviation from a classical liquid drop assumption. Another interesting feature observed in the Figure 1.4 (blue points) consists in the presence of systematic periodicity in the deviations between calculated and experimental masses. These periodicity reflects the so-called *shell closures*, which represent extraordinary conditions of nuclear stability (i.e. nuclei are characterized by extremely low masses) occurring in correspondence of particular number of nucleons. The above mentioned aspects clearly evidence the limitation of the liquid drop model. In the following paragraphs, further de-

---

<sup>2</sup>The so-called *stability valley* is the locus, on the  $(Z, N)$  plane, where the  $m(\frac{A}{Z}X)$  distribution, i.e. the mass of a generic nucleus  $X$  with  $Z$  protons and  $N$  neutrons, reaches an absolute minimum ( $\frac{\partial}{\partial Z}(m(\frac{A}{Z}X))|_A = 0$ ). Nuclei close to the stability valley represent the most stable configurations.

velopments of nuclear models beyond the liquid drop model will be introduced. It will be shown how an independent particle treatment of nuclei can be useful for the description of many of the above aspects, but also the limits of independent particle models will be pointed out. The *cluster model* will be finally introduced, showing his connections with independent particle models.

### 1.2.2 Towards a mean field approach: the Hartree-Fock method in nuclei

Independent-particle approaches to nuclei and nuclear structure are largely used to probe binding energies of nuclei, ground state properties and nuclear levels. Such an independent particle picture assumes the existence of an average nuclear field (the *mean field*) where nucleons can move almost independently from each other and with a large mean-free path. The latter feature can be well understood and qualitatively explained by means of the Pauli principle. Collisions between nucleons are indeed strongly inhibited because of the Pauli principle and, as a consequence, nucleons describe orbits inside the nuclear volume which length is well larger than the average dimensions of the nucleus itself. This is in strong contradiction with a liquid drop behaviour, where instead long mean free paths were excluded.

The fact that nucleons move under an average field is instead much less obvious. An analytical approach to the equation 1.1, consisting in the so called *Hartree Fock* method<sup>3</sup>, can be used in order to approximately solve the equation.

Considering the Hamiltonian of equation 1.2, and reducing, for simplicity, the potential to the two-body term (the approach is more general and can be applied for any choice of the potential), one obtains for each point of the space the following potential energy:

$$U(\vec{r}) = \sum_i \int \varphi_i^*(\vec{r}') V(\vec{r}, \vec{r}') \varphi_i(\vec{r}') d\vec{r}' \quad (1.6)$$

where  $i = 1, \dots, A$  and  $\varphi_i$  is the wavefunction of the  $i$ -th nucleon. This equation shows that, starting from a given two-body interaction, i.e. from a given potential  $V$ , one should know the wavefunctions  $\varphi_i(\vec{r})$  in each point of the space in order to determine the average one-body field  $U(\vec{r})$ , but to evaluate  $\varphi_i$  one should know the average one-body field. This problem is therefore a typical iterative problem, which can be solved either by starting from a set of wavefunctions or a potential  $U(\vec{r})$ . The Schrödinger equation associated to this problem follows from the application of the

---

<sup>3</sup>The Hartree-Fock method is an approximated method for solving Schrödinger equations, largely used and developed in sub-atomic physics, in the presence of many-body interacting objects.

## Chapter 1. Introduction: Clusters in Nuclear Physics

---

variational principle to the equation 1.1:

$$\begin{aligned}
 -\frac{\hbar^2}{2m}\nabla\varphi_\alpha(\vec{r}) + \sum_{i=1}^A \int \varphi_i^*(\vec{r}')V(\vec{r},\vec{r}')\varphi_i(\vec{r})d\vec{r}' \cdot \varphi_h(\vec{r}) \\
 - \sum_{i=1}^A \int \varphi_i^*(\vec{r}')V(\vec{r},\vec{r}')\varphi_i(\vec{r}) \cdot \varphi_\alpha(\vec{r}')d\vec{r}' = \varepsilon_\alpha\varphi_\alpha(\vec{r})
 \end{aligned} \tag{1.7}$$

where the antisymmetrization of the wave functions, written as Slater determinant of single-particle wave functions (needed to satisfy the Pauli principle) results in the appearance of the second additional term to the one-body field. A compact re-write of the equation 1.7 leads to:

$$-\frac{\hbar^2}{2m}\nabla\varphi_\alpha(\vec{r}) + \int U(\vec{r},\vec{r}')\varphi_\alpha(\vec{r}')d\vec{r}' \tag{1.8}$$

where  $U(\vec{r},\vec{r}')$  is the so called self-consistent field, defined by:

$$U(\vec{r},\vec{r}') = \delta(\vec{r}-\vec{r}') \sum_{i=1}^A \int V(\vec{r},\vec{r}'')\varphi_i(\vec{r}'')\varphi_i^*(\vec{r}'')d\vec{r}'' - \sum_{i=1}^A V(\vec{r},\vec{r}')\varphi_i(\vec{r}')\varphi_i^*(\vec{r}') \tag{1.9}$$

This result is extremely important since it demonstrates, starting from a basic nucleon-nucleon interaction, that the collective presence of all the nucleons inside the nuclear volume leads to the appearance of a mean field. The first term of equation 1.9 is the so called *Hartree field* and it is a local term. The second term, a non-local term, is related to the antisymmetrization properties of the wavefunctions and it is called *exchange term* (Fock). A solution to this problem, accordingly to the *Hartree-Fock* method, can be found via an iterative procedure leading, at the convergence, to a set of wavefunctions  $\varphi_\alpha^{HF}(\vec{r})$ , to a potential  $U^{HF}(\vec{r})$  and to the values  $\varepsilon_\alpha^{HF}$ .

### 1.2.3 The simplest independent particle model: the Fermi-gas model

The result obtained with the Hartree-Fock method applied to nuclear systems gives the possibility of describing nuclei as many body systems moving under a common potential, which can be seen as generated by the collective presence of nucleons within the nuclear volume. Under this charming assumption, in antithesis with the liquid drop model description, independent particle models can be developed. The simplest one is the *Fermi-gas model*. In this model, nucleons are described as elements of a fermionic gas which move in a volume of  $4/3\pi r_0^3 A$ , equal to the nuclear volume, and their motion is described by plane waves. Two potential wells, for neutrons and protons, are introduced in this model. The one of protons is less deep because of the Coulomb repulsion, to which it is associated an energy amount

## 1.2 Nuclear models and structure

---

of  $E_C$ , and extends externally the nuclear range with trend  $\propto 1/r$ . Each energy level can be filled with two nucleons in a singlet state, i.e. with different spin orientations. In the limit of zero temperature ( $T = 0$ ), states are fully occupied up to the Fermi level, leading to a density of states which amounts to:

$$n = \frac{VP_F^3}{3\pi^2\hbar^3} \quad (1.10)$$

From this expression it is possible to estimate the highest momentum, i.e. the Fermi momentum  $P_F$ , which a proton or a neutron can have within the nucleus:

$$P_{F,n} = \frac{\hbar}{r_0} \left( \frac{9\pi N}{4A} \right)^{1/3}, \quad P_{F,p} = \frac{\hbar}{r_0} \left( \frac{9\pi Z}{4A} \right)^{1/3} \quad (1.11)$$

In the case of a *self-conjugated*<sup>4</sup> nucleus, as an example, the maximum kinetic energy associated to the less bound nucleons results to be, accordingly to the Fermi-gas model:

$$E_F = \frac{P_F^2}{2m} \approx 33\text{MeV} \quad (1.12)$$

which indicates that nucleons move inside nuclei with velocities which amount to significant fractions of the speed of light, as a reflection of the Pauli principle. This presence of a large amount of *zero-point* energy leads to a strong quantum mechanical *pressure*.

Another very interesting result that can be achieved with the Fermi-gas model is the existence of a further term contributing to the nuclear binding energy, which cannot be predicted by the liquid drop model (see paragraph 1.2.1): the asymmetry term. This term reflects the amount of extra-energy (which contribute to a reduction of the total binding energy) generated by the presence of a non-vanishing neutron-proton asymmetry. According to the above considerations, the average kinetic energy associated to the zero-point motion of nucleons within a nucleus is given by:

$$\langle E(A, Z) \rangle = \langle E(A, Z = A/2) \rangle + \Delta E_{asy} \quad (1.13)$$

where the first term corresponds to the total kinetic energy for a self-conjugated configuration and the second term is the asymmetry energy. This can be expressed in terms of  $(N - Z)/A$  and turns to be:

$$\Delta E_{asy} \approx 11\text{MeV}(N - Z)^2 A^{-1} \quad (1.14)$$

which has to be subtracted to the total binding energy, i.e.  $B_{asy} = -\Delta E_{asy}$ .

---

<sup>4</sup>A self-conjugated nucleus is an even-even nucleus with equal number of protons and neutrons, i.e.  $Z = N = A/2$ . These particular configurations can be decomposed into  $\alpha$  particles.

### 1.2.4 The nuclear shell model

The nuclear shell model was developed in the '50s of the last century. It consists of an independent particle model where nucleons are supposed to move under a central potential. The main differences with the Fermi-gas model are in the use of wave functions of particle moving in a spherically symmetrical potential instead of plane waves. This model offers, especially in the case of light nuclear systems, the possibility of predicting many nuclear spectroscopic properties in addition to binding energies.

One of the principal indications that shell closure should exist in nuclei is obtained by comparing the behaviour of nuclear binding energies with the analogous picture of electrons in atoms. A clear indication of *magic numbers* was indeed obtained while studying the trend of ionization energy of atoms as a function of the number of atomic electrons. This systematic shows conditions of pronounced stability in correspondence of 2, 10, 18, 36, 54, 86 electron numbers, indicating rapid variations of ionization energy while overcoming each shell closure. An interpretation to this fact is that the last electron of the configuration is much less bound, since it starts to fill a new shell and it experiences a screening effect of the Coulomb potential given by the more internal shells. In nuclei, discontinuities are observed, as previously discussed, in the systematics of binding energies and masses (see Figure 1.4) leading to anomalies in total number and relative abundances of isotopes [20] and to higher excitation energy of the first excited state of nuclei characterized by particular  $Z$  and  $N$  numbers. These properties suggest that nuclei containing 2, 8, 20, 28, 50, 82 or 126 protons or neutrons are particularly stable, and they were historically called *magic numbers*. A clear experimental evidence of these numbers can be obtained from the analysis of the first excited states of nuclei. In particular, in Figure 1.5 the trend of the average energy of the first excited state ( $\langle E_{first}^* \rangle$ ) is shown for doubly-even nuclei as a function of the neutron number  $N$ . From this picture the extra-stability achieved in correspondence of magic neutron numbers is very clear. Indeed, under the assumption of the existence of shells, the energy required to populate the first excited state has a discontinuity in correspondence of shell closures. Ideas supporting the shell model have received confirmation by extremely fascinating experiments [21]. Direct observations of shell structures were attained via (p,2p) reactions at protons energy of 50-400 MeV. Measuring the outgoing proton from  $^{12}\text{C} + \text{p} \longrightarrow ^{11}\text{B} + 2\text{p}$  two different contributions to the total strength were identified and associated to a proton in a s-state or p-state of the  $^{12}\text{C}$  nucleus.

The hamiltonian of the shell model can be written in the form:

$$H = \sum_{\alpha=1}^A \left[ T_{\alpha} + V(r_{\alpha}) - f \vec{L}_{\alpha} \cdot \vec{s}_{\alpha} \right] \quad (1.15)$$

where  $V(r_{\alpha})$  is a central field which is normally chosen as a *Wood-Saxon* or an harmonic oscillator potential [20, 22]. The last term is called *spin-orbit coupling*

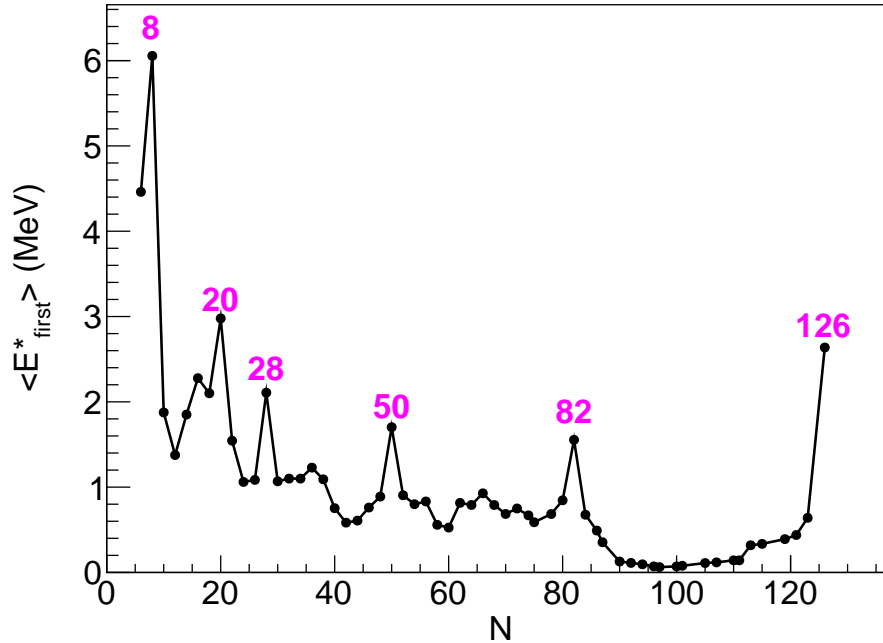


Figure 1.5: Average energy of the first excited state for doubly-even nuclei as a function of the neutron number [17]. Neutron numbers of magic nuclei are labelled in magenta. Peaks evidence shell closures.

and it was independently introduced by Mayer and Haxel, Jensen and Suess in 1949 [23, 24]. They demonstrated that, in order to reproduce the correct sequence of magic numbers in nuclei, a *non-central* component had to be considered in the force acting on a nucleon in the nuclear well. This non-central force depends on the relative orientation of the angular momentum and the spin of the nucleon. In this model they assumed that the spin-orbit force separates the motion of a nucleon with orbital momentum  $l$  into two sub-states with total angular momentum  $j = l \pm \frac{1}{2}$ , where the level having the higher spin is the more stable. The hamiltonian of equation 1.15 does not commute with  $L_z$  and  $s_z$ , while, on the contrary, it commutes with  $j^2 = (\vec{L} + \vec{s})^2$ ,  $j_z = L_z + s_z$ ,  $L^2$  and  $s^2$ . The corresponding eigenstates are therefore of the form  $|n, l, j = l \pm \frac{1}{2}\rangle$ . The corresponding levels for an harmonic oscillator potential split into:

$$1s_{1/2}; 1p_{3/2}1p_{1/2}; 1d_{5/2}2s_{1/2}1d_{3/2}; 2f_{7/2}; 2p_{3/2}1f_{5/2}2p_{1/2}1g_{9/2}; \dots \quad (1.16)$$

where each state of given  $j$  can accommodate  $2j + 1$  neutrons and  $2j + 1$  protons and the shell closures occur at the right  $Z$  and  $N$  magic numbers seen experimentally. The final total wave function of a nucleus depends on the coupling of the individual angular momenta of the nucleons in each state, allowing to predict spectroscopic

## Chapter 1. Introduction: Clusters in Nuclear Physics

---

properties like total spin, parity, magnetic and electric moments of the whole nuclear configuration.

The shell model is able to predict the properties of ground states for an extremely large variety of nuclei in terms of single-particle properties. In attempting to reproduce excited states one can assume that, if the level is sufficiently close to the ground state, it can be described via a single-particle excitation, assuming a well compact core. The situation is anyway much more complicated in the description of higher energy levels, where even nucleons belonging to the core can be excited and the properties of the states cannot be described in terms of single particle excitations. In the presence of multi-particle excitations, a *residual interaction* occurs between nucleons participating in the excitation and a further collective term should be considered in the compute of the excitation energy. These residual interactions can be introduced in the shell model as a small perturbation. If one indicates with  $|\Psi_n\rangle$  the eigenstates of the perturbed hamiltonian  $H = H_0 + V_{ij}$  and with  $|\varphi_i\rangle$  the ones of the unperturbed hamiltonian  $H_0$ , it is possible to re-write the first as a linear combination of the unperturbed solutions:  $|\Psi_n\rangle = \sum_i a_i^{(n)} |\varphi_i\rangle$ . From the property of orthonormality of the  $|\varphi_i\rangle$ , it follows:

$$\begin{cases} (E_n - E_j^0) a_j^{(0)} - \sum_i a_i^{(n)} \langle \varphi_j | V_{ij} | \varphi_j \rangle = 0 \\ \sum_i [(E_n - E_j^0) \delta_{ij} - \langle \varphi_j | V_{ij} | \varphi_j \rangle] = 0 \end{cases} \quad (1.17)$$

which is a system of two coupled homogeneous equations. Under the assumption that the majority of the contributions to the  $|\Psi_n\rangle$  are given by the first terms of the linear combinations, it is possible to use the system of equation 1.17 to determine the set of coefficients  $a_i^n$  which gives the most realistic energies  $E_n$  and wave-functions  $\langle r | \Psi_n \rangle$ . This method was used by Zuker [25] to determine the excited states of  $^{16}\text{O}$  starting from a core of  $^{12}\text{C}$  and 4 further nucleons. The picture considered by Zuker and collaborators in their calculations is the one proposed in Figure 1.6 (left), where the nucleons of the core occupy the  $1s_{1/2}$  and  $1p_{3/2}$  shells and the 4 nucleons, two protons and two neutrons, can be placed in the  $1p_{1/2}$ ,  $2s_{1/2}$  and  $1d_{5/2}$  shells. By choosing different combinations of 4 nucleons arrangement in these orbitals it is possible to well reproduce the  $^{16}\text{O}$  levels as in Figure 1.6 (right). As an example, for the first excited state of  $^{16}\text{O}$  (6.05 MeV,  $0^+$ ) the result of the perturbation calculation gives (omitting amplitudes smaller than 0.28):

$$|\Psi_1\rangle = -0.34p^4 - 0.62s^4 + 0.39d^2(01)s^2(01) - 0.40d^2(10)s^2 \quad (1.18)$$

where the configurations  $x^n$  indicate a state produced by a  $n$ -particles  $n$ -holes excitation ( $np$ - $nh$ ) in the  $l$ -shell and number in parenthesis indicate the  $JT$  spin-isospin coupling (see [25]). In other words, the wave function  $|\Psi_1\rangle$ , relative to the first excited state of  $^{16}\text{O}$ , calculated starting from the residual interaction of the 4 further neutrons, and considering a  $^{12}\text{C}$  core as prescribed by the shell model, exhibits a predominant ( $4p, 4h$ ) nature. The corresponding amplitude  $\langle \alpha \otimes ^{12}\text{C} | \Psi_1 \rangle$  for which

the calculation is not easy and requires the use of four angular momentum coupling coefficients, turns out to be  $\approx 1$ , revealing a pronounced  $\alpha$ -cluster nature of the state.

Residual interactions leading to clustering phenomena can be also used to understand apparently anomalous low-lying levels of light nuclei [26]. For instance, in  $^{19}\text{F}$  there are two possible cluster decompositions involving *closed-shell* nuclei. The  $\alpha$ - $^{15}\text{N}$  substructure has an inter-cluster binding energy of only 4 MeV. If one assumes that the clusters are in a relative  $s$ -state, the corresponding spin and parity are  $\frac{1}{2}^-$ . The only cluster decomposition that one could expect from the shell model is instead the  $^{16}\text{O}$ - $^3\text{H}$  substructure. It has an inter-cluster binding energy of 12 MeV and, according to the Nilsson model<sup>5</sup>, its spin and parity are  $\frac{1}{2}^+$ . The first excited state of  $^{19}\text{F}$  lies at only 0.11 MeV excitation energy and it has spin-parity  $\frac{1}{2}^-$ . Its simple shell model interpretation is the excitation of a proton coming from the  $^{16}\text{O}$ -like core to the Nilsson  $1/2^+$  orbital, leaving a hole in the  $1p_{1/2}$  state. This would result in several MeV of excitation energy. Evidently, the couples of two protons and two neutrons holding the  $(1/2^+)$  Nilsson orbitals tend to form a very compact  $\alpha$ -like cluster, and the energy gain in forming such a  $\alpha$ - $^{15}\text{N}$  sub-structure is responsible of a large reduction of the excitation energy to a few hundreds of keV. Therefore, the appearance of such a low lying excited state in  $^{19}\text{F}$  can be associated to a *cluster model joke*.

These intriguing results demonstrate that cluster structures emerge naturally while modifying the shell model including residual interaction of nucleons participating in the collective excitation. These long range correlations between nucleons are a signature of cluster structure. Anyway, the spatial localization of clusters, which is considered one of the most important aspects of clustering in nuclei, is not easily describable with shell model. In the following section, an overview of theoretical models trying to explain the appearance of clusters in nuclei will be presented.

### 1.3 Cluster models of nuclei

The main aim of nuclear models attempting to describe clustering phenomena consists in the study of the spatial distribution of clusters within the nuclear volume. To do this job it is useful to define the so-called *correlation operator*, which represents the probability of finding two nucleons respectively with momentum  $Q^{(1)}$  and  $Q^{(2)}$

---

<sup>5</sup>The  $A \approx 20$  region is characterized by strong deformations, and the ordinary shell model based on spherical potential is no longer valid. An extension of the single-particle shell model to deformed potentials was theoretically developed by S.G. Nilsson [26]. The main effect of (quadrupolar) deformation results in the removal of degeneracy of spherical shell states, leading to energy-split of sub-shells. For example, the  $1d_{5/2}$  spherical shell orbital is split into three different sub-shells (Nilsson orbitals)  $(1/2^+)$ ,  $(3/2^+)$  and  $(5/2^+)$ , characterized by increasingly larger energies. The valence proton in  $^{19}\text{F}_{gs}$  holds the  $(1/2^+)$  Nilsson orbital, and this explains the experimental value of  $J^\pi = 1/2^+$ .

## Chapter 1. Introduction: Clusters in Nuclear Physics

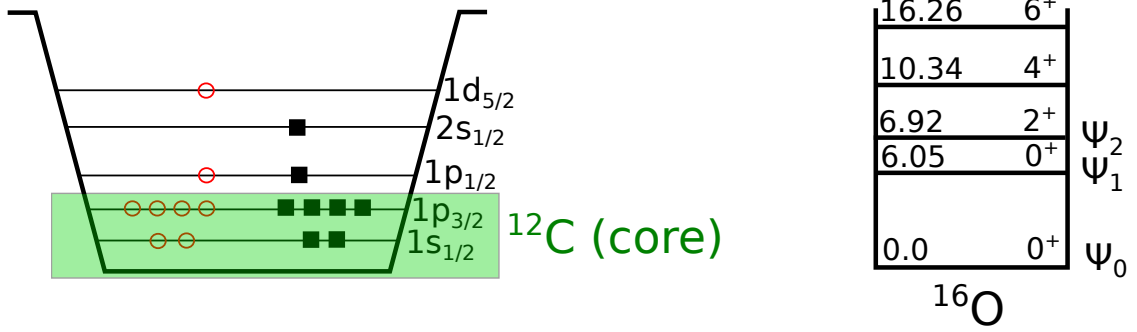


Figure 1.6: (left) Schematic view of the picture used by Zuker and collaborators [25]. The shells  $1s_{1/2}$  and  $1p_{3/2}$  are the  $^{12}\text{C}$ , used as a core in the calculations. States of  $^{16}\text{O}$  (indicated in the right panel) can be predicted by changing the configurations of the 4 extra nucleons in the shells  $1p_{1/2}$ ,  $2s_{1/2}$  and  $1d_{5/2}$ .

when the nucleus is in the ground state  $\Psi$  [28]:

$$\langle i|g(\vec{x}^{(1)}, \vec{x}^{(2)})|f\rangle \equiv \int_{Q^{(3)}} \dots \int_{Q^{(A)}} \Psi^*(\vec{x}^{(1)}, \vec{x}^{(2)}; i; Q^{(3)}, \dots, Q^{(A)}) \Psi(\vec{x}^{(1)}, \vec{x}^{(2)}; f; Q^{(3)}, \dots, Q^{(A)}) \quad (1.19)$$

where each integral is extended to the whole momentum space and the compact notations  $i$  and  $f$  represent two different sets of values of spin and isospin coordinates. The diagonal terms of this operator give the probability for two nucleons to be at a distance  $r = |\vec{x}| = |\vec{x}^{(1)} - \vec{x}^{(2)}|$ . The spatial correlation of a pair of nucleons will be then:

$$g(r) = \sum_i \langle i|g|i\rangle \quad (1.20)$$

The sum is here extended to couples of nucleons with same charge and spin (that will be indicated in the following as *congruent nucleons*, and identified by the suffix =) and to couples of nucleons which differ either for the charge or the spin or both (*non-congruent*,  $\neq$ ). Congruent nucleons can be in any of the four states  ${}^3(\tau)_{\pm 1} {}^3(\sigma)_{\pm 1}$ , while non-congruent nucleons can be in any of the other 12 possible states. The correlation operator of eq. 1.19 can be re-written in terms of the ordinary and mixed densities, as a first approximation, neglecting any two-body interaction between nucleons and by assuming that each nucleon wave-function is a plane wave:

$$\langle i|g|f\rangle^{(0)} = \frac{1}{A(A-1)} \cdot \frac{1}{16} [\langle i|1|f\rangle \rho(\vec{x}^{(1)}) \rho(\vec{x}^{(2)}) - \langle i|P_\sigma P_\tau|f\rangle |\rho(\vec{x}^{(1)}, \vec{x}^{(2)})|^2] \quad (1.21)$$

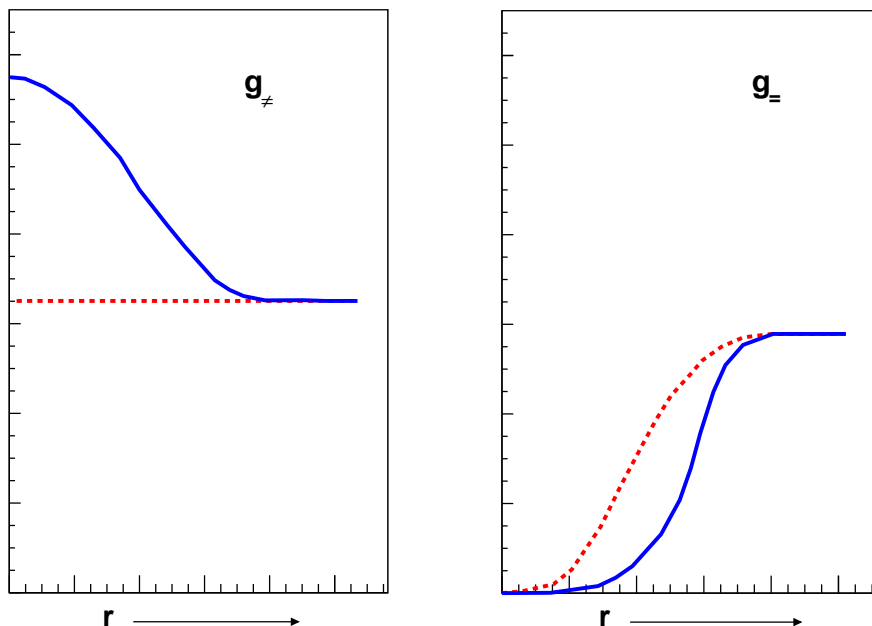


Figure 1.7: Spatial correlations as a function of the relative distance between nucleons in the case of non-congruent nucleons (left) and congruent nucleons (right). The dashed line is the result of the calculations in which no account is taken of nuclear interactions. The solid line is the result of the calculations via the procedure shown in [27].

Here,  $P_\sigma$  and  $P_\tau$  are spin and isospin projectors, while

$$\rho(\vec{x}) = \frac{A}{V} \quad (1.22)$$

$$\rho(\vec{x}^{(1)}, \vec{x}^{(2)}) = \frac{A}{V} G(r) \quad (1.23)$$

are the ordinary and mixed densities. The mixed density  $\rho(\vec{x}^{(1)}, \vec{x}^{(2)})$  is connected to the superposition of nucleon wave-functions respectively in the positions  $\vec{x}^{(1)}$  and  $\vec{x}^{(2)}$ . The function  $G(r) = \frac{3}{(\gamma \aleph r)^3} (\sin(\gamma \aleph r) - (\gamma \aleph r) \cos(\gamma \aleph r))$  derives from the solution of the integral 1.19, being  $\aleph^{-1}$  the range of nuclear forces ( $\approx 2$  fm) and  $\gamma \equiv \frac{(9\pi)^{1/3} \cdot (\aleph r_0)^{-1}}{2}$ , with  $r_0$  the radius of a nucleon. The eq. 1.21 then becomes, for large  $A$  values:

$$\langle i|g|f \rangle^{(0)} = \frac{1}{16V^2} [\langle i|1|f \rangle - \langle i|P_\sigma P_\tau|f \rangle G^2(r)] \quad (1.24)$$

One can obtain, under this approximation:

$$g_{=}^{(0)}(r) = \frac{1}{16V^2}[4 - 4G^2(r)] = \frac{1}{4V^2}[1 - G^2(r)] \quad (1.25)$$

$$g_{\neq}^{(0)}(r) = \frac{1}{16V^2}[12 - 0G^2(r)] = \frac{3}{4V^2} \quad (1.26)$$

These indicate that, even in the absence of two-body nuclear interactions, correlations appear between congruent nucleons. The corresponding spatial correlation has the trend of Figure 1.7 (right panel, dashed line). The decreasing at small values of relative distance is the effect of the Pauli exclusion principle. In the case of non-congruent nucleons, instead, no correlations appear and the corresponding spatial correlation is flat, as indicated by the dashed line of Figure 1.7 (left). A simplified nuclear interaction can be taken into account by following the method described in [27]. This method brings to a next approximation of the spatial correlations:

$$g_{=}^{(1)}(r) = -\frac{1}{4V^2} \cdot \frac{br_0}{4\pi^2} \cdot \frac{1}{3}(G_{ord}^{(1)} - G_{exch}^{(1)}) \quad (1.27)$$

$$g_{\neq}^{(1)}(r) = \frac{1}{4V^2} \cdot \frac{br_0}{4\pi^2} \cdot \left[ \frac{2}{3}(G_{ord}^{(1)} - G_{exch}^{(1)}) + \frac{3}{2}(1 + q)G_{exch}^{(1)} \right] \quad (1.28)$$

where  $G_{ord}$  and  $G_{exch}$  derive from the integral 1.19 once that a reliable nucleon-nucleon force constituted by a ordinary and an exchange term is included. The constant  $q$  represents the ratio between strengths of singlet and triplet components of the force, while  $b$  is a constant related to the strength of the nucleon-nucleon interaction [28]. The trends of  $g_{=}^{(1)}(r)$  and  $g_{\neq}^{(1)}(r)$  are shown in Figure 1.7 with solid lines. The effect of nuclear interaction is to widen the *hole* in the spatial correlation of congruent nucleons while, in the case of non-congruent nucleons, correlations start to manifest. These result in an accumulation of nucleons close to  $r = 0$ . The density fluctuations due to nuclear interaction thus favour the appearance of clusters. The simplest, and most correlated, is made by four nucleons in different spin and isospin states, which are called  $\alpha$ -clusters.

A second order approximation gives a correction to the nuclear energy. This contribution (see [28]) is always negative and can be interpreted as a gain in binding energy of the nucleus as a result of the clusterization, as observed in the systematic of binding energies of self-conjugated nuclei of Figure 1.3 (insert). Anyway, the gain in binding energy of a given nucleus is dependent on the particular interaction used to create  $\alpha$ -clusters as well as the properties of the cluster themselves. Theoretical models in which  $\alpha$ -clusters are recognized from the outset lead to more refined results in the description of energetics of cluster states. In the Figure 1.8, a summary of the historical development of such cluster models is presented.

### 1.3.1 The $\alpha$ -particle model

The first and simplest model aimed at the description of cluster states in nuclei is the so-called  *$\alpha$ -particle model*. This model was developed in 1930's, starting from

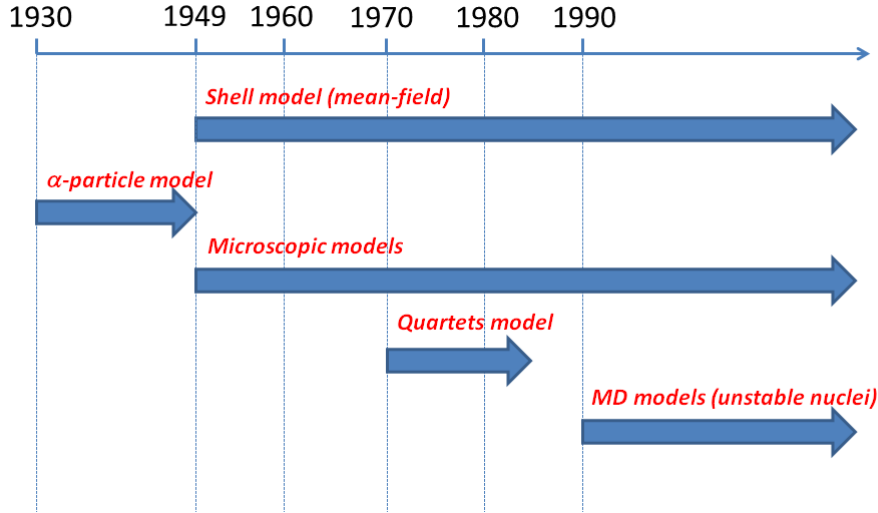


Figure 1.8: Historical developments of cluster models of nuclei from 1930's.

the experimental observations of Wefelmeier [30, 31] and of Hafstad and Teller [29]. They brought out the fact that the binding energies of self-conjugated nuclei showed local maxima, as a result of the appearance of clustering. This fact is evident in the insert of Figure 1.3, where self-conjugated configurations clearly exhibit peaks on the corresponding isotopic lines. Another important fact pointed out by Hafstad and Teller was that, if one assumes an  $\alpha$ -particle structure of self-conjugated systems, their binding energies are linearly correlated with the possible number of connections between  $\alpha$  centers. This evidence supported the assumption of a geometrical model describing these nuclei as consisting of close packing of rigid spheres ( $\alpha$ -particles), with a certain number of *bonds* (pairs of adjacent particles). In such a way, one can describe their binding energies as the sum of the binding energy of each constituent  $\alpha$ -cluster and the  $\alpha$ -binding energy, i.e. the binding energy associated to each bond between  $\alpha$ -particles. Figure 1.9 shows the correlation between the total binding energy of the lightest self-conjugated nuclei and the corresponding number of bonds, following the scheme of Hafstad and Teller, compared with the result of a linear fit. These structures, as supposed by [29] and reported in [10], are shown in Figure 1.10 for self-conjugated nuclei up to  $^{28}\text{Si}$ . They are summarized in the table 1.1 together with the empirical values of binding energies associated to  $\alpha$ -particle bonds; the geometrical arrangements of  $\alpha$ -particles in the first self-conjugated systems, up to  $^{32}\text{S}$ , are also indicated. Empirical  $\alpha$ -binding energies show clearly a proportionality with the number of bonds and, as a consequence, the  $\alpha$ -binding energy per number of bonds is surprisingly almost constant for each system<sup>6</sup>, indicating an apparently

<sup>6</sup>The value of  $\alpha$ -binding energy per bond of 2.130 MeV in the case of  $^{20}\text{Ne}$  is slightly lower than the neighbouring nuclei ones; Ref.[32] suggests that also a *squared pyramid*  $\alpha$ -configuration might

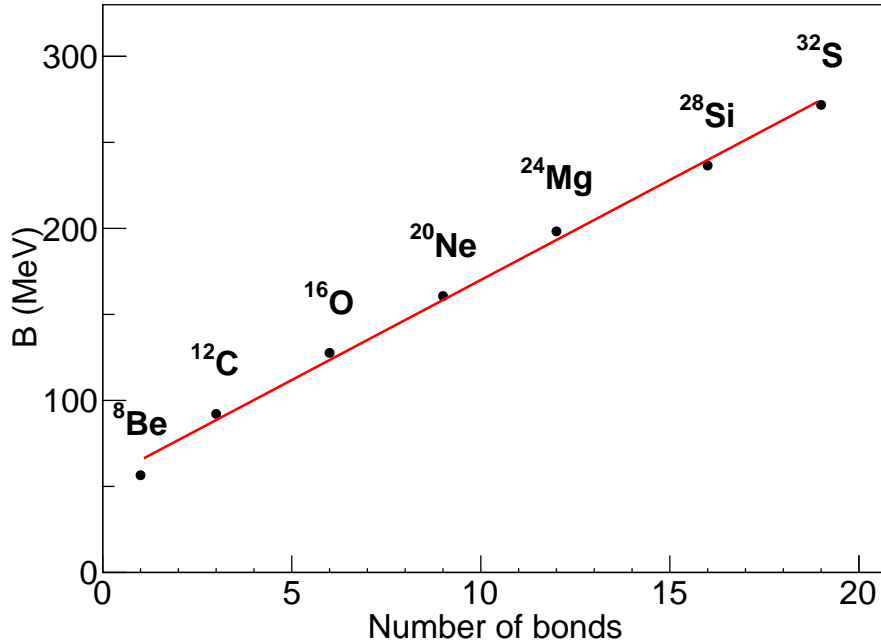


Figure 1.9: Binding energy for the lightest self conjugated-nuclei as a function of the number of bonds between between  $\alpha$ -cluster centers, see [29]. The red line is the result of a linear fit of data. Experimental binding energies are extracted from [18, 19].

constant  $\alpha$ - $\alpha$  interaction and the resilience of the  $\alpha$ -particle constituents in the ground states of light self-conjugated systems.

All the above mentioned experimental evidences supported the development of the  $\alpha$ -particle model of nuclei. This model describes self-conjugated nuclei as systems of interacting  $\alpha$ -particles and, therefore, the development of the model historically followed the theoretical study of the  $\alpha$ - $\alpha$  interaction. The basic ideas of the interaction between  $\alpha$  particles were proposed by Wheeler [33] and were used as a starting point in the building of the  $\alpha$ -particle model. The theory is based on the application of the Hartree-Fock variational method (see paragraph 1.2.2) to the system of eight nucleons, which constituted two interacting  $\alpha$ -particles. The vector

---

be used to describe the structure of  $^{20}\text{Ne}$  with just 8 bonds instead of the 9 bonds correspondent to the *trigonal bipyramid*. In such a case, a  $\alpha$ -binding energy per bond of 2.396 MeV would result in better agreement with the other self-conjugated nuclei. In any case, the arbitrariness of the choice of the particular configuration represents a limit of the model. Another qualitative interpretation of the low value of binding energy per bond of  $^{20}\text{Ne}$  is given by [30, 31], and suggests that the two extremal  $\alpha$ -particles of the (more symmetric) trigonal bipyramid configuration are shielded from each other by the presence of a quite compact triangular basis; hence, one should count  $^{20}\text{Ne}$  as having only 8 effective bonds.

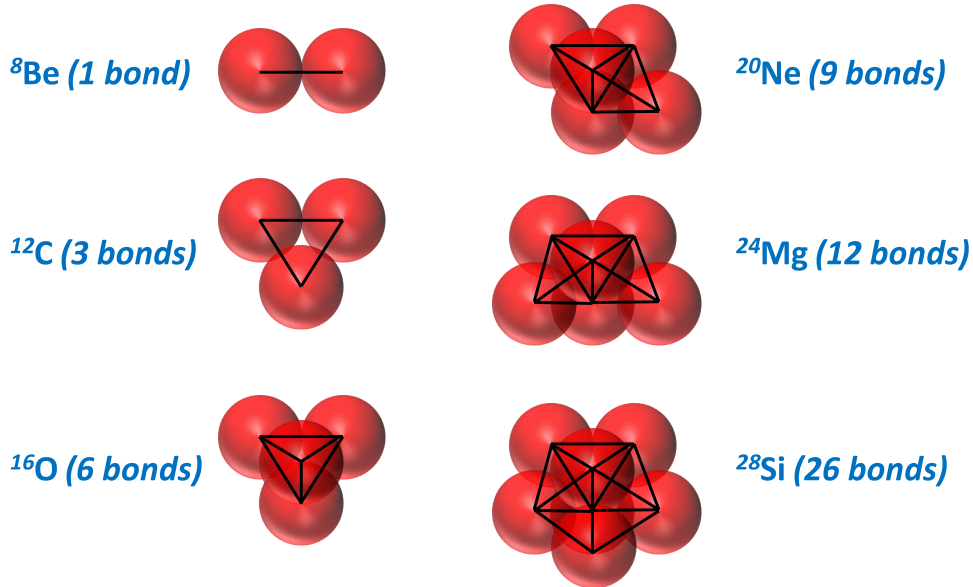


Figure 1.10: Arrangements of  $\alpha$ -particle constituents in self-conjugated nuclei, following the scheme of [29], for the lightest self-conjugated systems. The number of bonds is indicated for each geometrical configuration [10].

$\vec{R}$  joining the centers of mass of the two  $\alpha$ -particles is treated as a parameter. The difference between the total energy of the system and the one of the two  $\alpha$ -particles at an infinite distance, i.e. not interacting, gives the interaction energy. Indicating with  $\vec{x}^{(i)}$  ( $i = 1, 2, 3, 4$ ) the vectors from the center of mass of the first  $\alpha$ -cluster to its constituents, one can write the Slater determinant of such a system, considered as an aggregate of two  $\alpha$ -clusters by using only two distinct spatial eigenfunctions of individual nucleons:  $\varphi(\vec{x}^{(i)})$  and  $\varphi(\vec{R} - \vec{x}^{(i)})$  ( $i = 1, 2, 3, 4$ ). They have to be multiplied by the appropriate spin and isospin eigenfunctions. The result of the first approximation of calculations is strongly dependent on the *exchange* properties and on the distance dependence of the interaction between two nucleons. The interaction energy of the two  $\alpha$ -particles represents an attractive potential for every value of  $R$ , and the resulting range is of the same order of the nucleon-nucleon potential; repulsive contributions will clearly dominate both at small distances, because of the increase of kinetic energy of the  ${}^8\text{Be}$  system, and at large distances, where the Coulomb repulsion is the only interaction. If the nucleon-nucleon interaction has a sufficiently strong *tail*, or residual intensity, the attractive part of the  $\alpha$ - $\alpha$  potential may become strong enough to overcome the Coulomb repulsion at intermediate distance; moreover, if the tail of the nucleon potential is of the ordinary type, the attraction between  $\alpha$ -centers will exhibit additivity properties typical of intermolecular van der Waals forces. A simplified assumption on the nucleon inter-

## Chapter 1. Introduction: Clusters in Nuclear Physics

---

Nucleus	N. of $\alpha$ -s	Configuration	N. bonds	$\alpha$ -binding energy (MeV)	$\alpha$ -binding energy per bond (MeV)
$^8\text{Be}$	2	straight line	1	-0.092	-0.092
$^{12}\text{C}$	3	triangle	3	7.275	2.425
$^{16}\text{O}$	4	tetrahedron	6	14.437	2.406
$^{20}\text{Ne}$	5	trigonal bipyramid	9	19.167	2.130
$^{24}\text{Mg}$	6	tetragonal bipyramid (octahedron)	12	28.483	2.374
$^{28}\text{Si}$	7	pentagonal bipyramid	16	38.467	2.404
$^{32}\text{S}$	8	sphenoidal bipyramid	19	45.415	2.390

Table 1.1: Geometrical configurations proposed by [29–31] for the first self-conjugated nuclei. The number of bonds is indicated together with the  $\alpha$ -binding energy and the  $\alpha$ -binding energy per bond.

action represented by a Gauss potential was introduced by Margenau [34]. As trial wavefunctions  $\varphi(\vec{x})$  for the variational approach, he used simple harmonic oscillator eigenfunctions involving a variational parameter. However, at a first order of approximation, a repulsive force results in the  $\alpha$ - $\alpha$  interaction at all distances, and higher approximations are required to account for the binding energy of  $\alpha$ -particles. This fact reflects the closed structure of  $\alpha$ -particle (analogous to the rare gas configuration in atomic systems) and it has a more general scope [35]: mutual attractions can only manifest themselves through virtual *polarization* of such structures. These features appear in the second approximation of the model. In the Margenau calculations it has been shown that attractive forces result in the second order but with a range shorter than the first order repulsion. This feature is reversed in the case of intermolecular forces, where the analogous term has the longer range, representing the van der Waals attraction. The result of this fact is that, at the second order approximation of the  $\alpha$ -particle model, there can be no additivity of the interaction between more than two  $\alpha$ -particles. Any simple explanation of the regularities showed in the empirical values of the table 1.1 cannot be therefore given from the results of  $\alpha$ - $\alpha$  interaction of the Margenau's model. These features can be explained in terms of complicated compensations between energy terms of different orders of approximations, involving essentially non-additive many body features of  $\alpha$ -particle interactions [28].

Anyway, it is important to underline that the assumption of a rigid  $\alpha$ -structure of the nucleus has been questioned by many authors. In fact, in finite nuclei one can

### 1.3 Cluster models of nuclei

expect to find a considerable amount of local correlations of particles that can give rise to *instantaneous*  $\alpha$ -groupings, but, because of the interaction, they continually merge one to another without preserving their identity for any appreciable length of time [36].

The  $\alpha$ -particle model, as seen from the previous discussion, is not able to explain, on a quantitative and theoretically exhaustive basis, the energies of self-conjugated nuclei as reported in table 1.1. Anyway, more quantitative predictions can be attained in describing rotations and vibrations of  $\alpha$ -nuclei. Let us consider, as an example, the  $n$ -th surface vibration mode of a nucleus, and be  $\lambda \approx 2\pi R/n$  (where  $R$  is the nuclear radius) the corresponding wave-length. If  $n$  is sufficiently small, i.e.  $n \leq A^{\frac{1}{3}}$ ,  $\lambda/2$  is larger than the dimension of an  $\alpha$ -cluster. Under this assumption, the angular frequency  $\omega$  can be obtained via the Rayleigh formula [28]:

$$\omega^2 = n(n-1)(n+2)\gamma_s \cdot \frac{4\pi}{3} \cdot \frac{1}{mA} \quad (1.29)$$

being  $\gamma_s = \frac{a_s}{4\pi R^2}$  the surface tension of the nucleus, with  $a_s$  the surface coefficient of the semi-empirical mass formula,  $R$  the radius of the nucleus and  $m$  the average mass of a nucleon. For the period one can derive the approximate formula [28]:

$$\tau \approx n^{-\frac{3}{2}} A^{\frac{1}{2}} \cdot 0.4 \cdot 10^{-21} \text{s} \quad (1.30)$$

The *frailty* of an  $\alpha$ -cluster in this state can then be defined as the time  $t$  required by such a cluster to exchange a nucleon with a part of its surroundings moving in opposite phase. The latter is of the same order of magnitude of the time required for a nucleon to *diffuse* through a distance  $\lambda/2$ , which can be classically determined as [28]:

$$t \approx n^{-2} A^{\frac{2}{3}} \cdot 0.6 \cdot 10^{-21} \text{s} \quad (1.31)$$

The conditions for treating the nucleus as a system of  $\alpha$ -particles are fulfilled in the case of rotational or vibrational states at low excitation energy. For increasing excitation energies,  $\alpha$ -clusters tend gradually to dissolve and the behaviour of nuclei as liquid droplets without cluster structures dominates. The vibrational quanta expected for an  $\alpha$ -nucleus according to the  $\alpha$ -particle model can be obtained by considering the potential energy of the quasi-elastic forces responsible for the vibration mode, taken for an amplitude corresponding to the dissociation of an  $\alpha$ -particle, and the value of the binding energy of this particle to the residual nucleus. For the lightest  $\alpha$ -nuclei, vibration quanta turn to be of the order of few MeV, which correspond to the lowest ( $n = 2$ ) mode of surface vibration of the classical liquid drop of the equation 1.29.

Regarding the order of magnitude of rotational quanta, they can be estimated starting from the moment of inertia  $I_S$  of a spherical homogeneous distribution of the nuclear mass:

$$I_S = \frac{2}{5} mAR^2 = \frac{2}{5} mr_0^2 A^{\frac{5}{3}} \quad (1.32)$$

## Chapter 1. Introduction: Clusters in Nuclear Physics

---

The corresponding rotational quanta  $\hbar^2/I_S$  are of the order of:

$$\hbar^2/I_S \approx 54A^{-\frac{5}{3}}\text{MeV} \quad (1.33)$$

which gives hundred keV in the case of light  $\alpha$ -nuclei and only a few keV for heavy nuclei. The latter estimate is at least one order of magnitude lower than experimental observation on fine structures in  $\alpha$  spectra coming from the decay of actinide nuclei [37]. More reliable estimates can be obtained by explicitly taking into account the appearance of  $\alpha$  clustering in heavy nuclei [28]. Such a model assumes (in a very simplified way) the nucleus as constituted by an ensemble of  $N_\alpha$   $\alpha$  particles. The rotation of such a structure of identical particles of a given angle  $\varphi$  can be always replaced by a suitable displacement (translation) of the  $\alpha$  particles [38]. This symmetry forbids the appearance of groups of rotational levels at too low excitation energies, leading to predictions (of the order of 0.2 MeV for  $A \approx 200$  nuclei) much closer to the experimental values [28].

The appearance of symmetries triggered by the  $\alpha$  cluster structure of nuclei plays an important role also in the case of light nuclei, where it causes a considerable reduction in the number of low-lying levels. As an example, in the case of the two  $\alpha$ -particle system  ${}^8\text{Be}$ , only wave-functions corresponding to even values of the angular momentum satisfy the requirement of the Bose statistics. A number of states results indeed to be shifted to levels of excitation higher than in the spectrum of analogous systems of nucleons without  $\alpha$ -particle structure. At higher excitation energies, the spectrum assumes a purely classical behaviour, merging into that of a vibrating fluid continuum.

### 1.3.2 Microscopic cluster models (RGM, GCM, OCM)

Microscopic cluster models [39, 40] are based on a detailed treatment of the Pauli principle among clusters and on a detailed description of the inter-cluster motion. Developments of microscopic cluster models have been remarkably done in the early 1960s (see Figure 1.8) with the realization of the Resonating Group Method (RGM) [41]. The RGM strongly influenced the evolution of cluster models in the subsequent decades as well as the development of the Generator Coordinate Method (GCM) [42] and the Orthogonality Condition Method (OCM) [43]. The RGM and GCM are fully-microscopic models while the OCM is considered a semi-microscopic model, since the treatment of *Pauli blocking* effects does not reflect a completely microscopic treatment.

The basic ideas of the RGM have been given by Wheeler [41]. The description of nuclei given in this model is that of a superposition of all possible type of nucleon clusters, i.e. attributing to the nucleus a *resonating group structure*. Nucleons are treated as spending part of their time in different configurations called *groups*; for example, they can be arranged into  $\alpha$ -particles or into other groupings. The method of resonating group structure is therefore in contrast with the concept of

### 1.3 Cluster models of nuclei

mean field which emerges from the Hartree-Fock procedure. The wave function built with this method is made of a properly antisymmetrized combination of partial wave functions, which correspond to any possible type of grouping. This wave function for the whole nucleus, out of partial wave functions which describe the close interaction within the individual group, clearly takes advantage from the saturation of nuclear binding, being the largest part of the binding energy accounted by the internal binding of each separate group. Considering a system of  $m$  protons and  $n$  neutrons, the total wave function  $\Psi$  can be written, according to this model, as the sum of parts, of which each term represents a particular grouping (configuration) of the  $N = m+n$  particles. Such a term is the product of wave functions  $\Phi$ , which represent the motion of particles within each group. They are also multiplied by particular functions of the positions and spin variables (the total angular momentum  $m_S$  of a group)  $F(X, m_S)$ . The  $F^i$  functions are unknown and they belong to different configurations. For instance, for the  ${}^6\text{Li}$  nucleus,  $F^1$  might represent the relative motion of a  $\alpha$ -particle and a deuteron, while  $F^2$  could represent a configuration of  ${}^5\text{Li}$  plus neutron, etc. The general expression of the anti-symmetrized wave function assumes therefore the form:

$$\Psi \propto \sum_i F^i[\vec{X}_i(I), m_{S_i}(I); \vec{X}_i(II) m_{S_i}(II)] \Phi_i(I) \Phi_i(II) \quad (1.34)$$

the sum extends over all configurations of possible groupings of, for simplicity, two clusters, indexed by  $i$ .  $\Phi_i$  represents the wave-functions of each of the two clusters  $I$  and  $II$ . The coefficients  $F^i$  depend only on the inter-cluster coordinates  $\vec{X}_i(I) - \vec{X}_i(II)$ , resulting in a reduction of the corresponding degrees of freedom. They should be determined as solutions of a certain set of integral-differential equations involving these coordinates as variables; the expression of these equations is rather heavy and not systematic and the reliability of the model is for this reason limited to systems involving a small number of nucleons. The RGM has been recently fruitfully applied to describe nuclear reactions and scattering processes involving light nuclei; in particular, for example, it is able to reproduce nicely the trend of experimental  $S$ -factor<sup>7</sup> of the astrophysically important  ${}^3\text{He}(\alpha, \gamma){}^7\text{Be}$  reaction at very low energies [44].

The restrictions imposed by the RGM can be overcome via the GCM. In this model, the  $F^i$  functions, describing the relative motion of clusters, are expanded over a set of projected gaussian functions, centered at different *generator coordinates*  $R_n$ .

---

<sup>7</sup>The  $S$ -factor is an alternative way to display a reaction cross section at very low energies, free from effects due to entrance channel penetrability. It is commonly adopted in Nuclear Astrophysics, where reactions are measured at low incident energies. Indeed, because of Coulomb barriers in the entrance channel, reaction cross sections usually exhibit exponential falls for decreasing energies, leading to difficulties in representing the data. The  $S$ -factor is defined by the equation:  $S(E) = \frac{1}{E} e^{2\pi\eta(E)} \sigma(E)$ , where  $\sigma(E)$  is the reaction cross section and  $e^{2\pi\eta(E)}$  is the inverse of the  $s$ -wave penetrability factor.

The wave-function of eq. 1.34 can be rewritten as:

$$\Psi^{JM\pi} \propto \sum_{lS} \sum_n f_{lS}^{J\pi}(R_n) \Phi_{lS}^{JM\pi}(R_n) \quad (1.35)$$

where  $J\pi$  represent spin and parity of the system and  $M$  the projection of the total spin. The first sum is extended over all values of channel spins  $S$  and angular momenta  $l$ , while the second one runs over all generator coordinates. The  $f_{lS}^{J\pi}(R_n)$  functions are called *generator functions*. Their calculation is quite systematic when changing system, and can therefore be applied with large versatility to systems much more complicated than in the RGM.

### 1.3.3 The quartet model

The *quartet model* aims at the description of excited states of self-conjugated nuclei that cannot be easily described via the independent particle shell model. The picture given in the quartet model is the existence of quartets. A quartet is a strong interacting structure made of 2 protons and 2 neutrons occupying a fourfold degenerate single particle state [45]. The separation energy of a nucleon in a self-conjugated nucleus is much larger than the one of an  $\alpha$ -particle. For example, while the neutron emission threshold in  $^{16}\text{O}$  is 15.7 MeV, the  $\alpha$  emission threshold is only 7.2 MeV. This empirical evidence means that the less bound nucleon interacts strongly with the other three which make up the emitted  $\alpha$ -particle and much more weakly with the rest. More in detail, in  $^{16}\text{O}$ , a proton of the  $p_{1/2}$  orbit has about 5 MeV of interaction energy with the  $^{12}\text{C}$  core and about 10 MeV interaction with the remaining nucleons of the  $p_{1/2}$  orbit. In the quartet model, excited states of self-conjugated nuclei are obtained by means of particle-hole excitations of quartet structures, characterized by strong internal binding energies and weak interaction between each others. For self-conjugated systems from  $^{12}\text{C}$  to  $^{52}\text{Fe}$ , quartets are restricted to the  $(0p)$ ,  $(0d,1s)$  and  $(0f,1p)$  shells of a spherical harmonic oscillator. The interaction energy between two quartets across the  $0p$  and  $(0d,1s)$  and across the  $(0d,1s)$  and  $(0f,1p)$  shells can be determined by the position of the first  $0^+$  excited state of  $^{16}\text{O}$  and  $^{40}\text{Ca}$ <sup>8</sup>, respectively, while the interaction between the  $(0p)$  and  $(0f,1p)$  shell is supposed to be small due to the extremely small radial overlap of the relative wave-functions. Independently on the mass number and the number of excited quartets, quartet-hole interactions are supposed constant in this model. Assuming  $^4\text{He}$  as the core, one can indicate as  $[xyz]$  a generic configuration of quartets arranged in the above mentioned shells in the following way:  $x$  quartets are in the  $N = 1$  major shell,  $y$  quartets are in the  $N = 2$  major shell and  $z$  quartets are in the  $N = 3$  major shell. One can designate with  $Q_p^x$ ,  $Q_{(sd)}^y$  and  $Q_{(pf)}^z$  these configurations. Restricting

---

<sup>8</sup>It is known from the literature that such states have a large  $\alpha$ -structure [45].

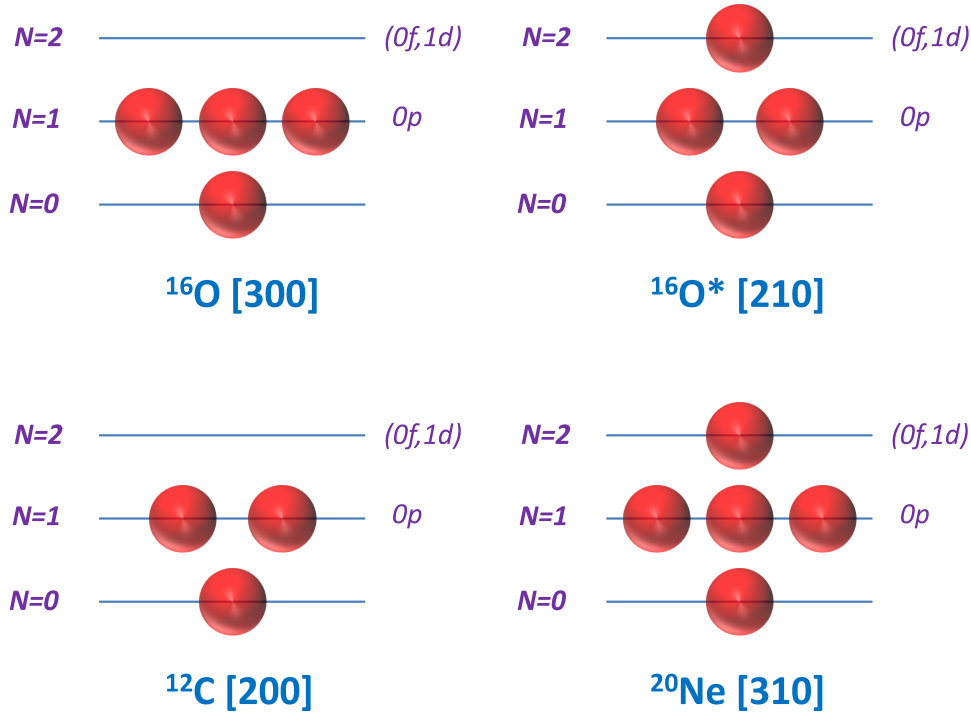


Figure 1.11: Terms contributing to the compute of the excitation energy of the [210] configuration of  $^{16}\text{O}$ , i.e. the first excited state (6.05 MeV,  $0^+$ ). The difference of the interaction energy of the  $^{12}\text{C}$  [200] and the  $^{16}\text{O}$  [300] configurations corresponds to the interaction energy of a hole in the  $N = 1$  shell.

the calculation, for simplicity, to the first two orbits,  $N = 1, 2$ , one finds:

$$\begin{aligned}
 E^*(Q_p^x Q_{(sd)}^y) = & E_0(4x + 4, 2x + 2) + E_0(4y + 16, 2y + 8) \\
 & - E_0(4(x + y) + 4, 2(x + y) + 2) - E_0(16, 8) + (3 - x)yV_{p,(sd)}
 \end{aligned} \tag{1.36}$$

In the formula of eq. 1.36,  $E_0(A, Z)$  represents the interaction energy of a nucleus with  $A$  nucleons and  $Z$  protons, while  $V_{p,(sd)}$  is the interaction between  $y$   $N = 2$  quartets and  $(3 - x)$   $N = 1$  holes. The latter is fixed by setting the one-quartet one-hole excitation energy equal to the excitation energy of the first excited  $J^\pi = 0^+$  state in  $^{16}\text{O}$ . To better clarify the above discussed method, Figure 1.11 shows the configurations which contribute to the compute of the excitation energy, as an example, of the first excited state (6.05 MeV,  $0^+$ ) of  $^{16}\text{O}$ , assumed to be in the [210] configuration. In detail eq. 1.36 becomes:  $E^*(Q_p^2 Q_{(sd)}^1) = (E_0(12, 6) - E_0(16, 8)) + (E_0(20, 10) - E_0(16, 8)) + V_{p,(sd)}$ , where the first term in round brackets represents the interaction energy of a hole in the  $N = 1$  shell, the second term in round brackets corresponds to the interaction energy of a quartet in the  $N = 2$  shell, and the last

$^{16}\text{O}$ [xyz]	$E^*(\text{MeV})$
[300]	0.0
[210]	6.06
[201]	11.1 + $V$
[120]	15.0
[111]	19.5 + $2V$
[102]	20.0 + $4V$
[030]	23.1
[021]	23.1 + $3V$
[012]	23.1 + $6V$
[003]	23.1 + $9V$

Table 1.2: Possible  $^{16}\text{O}$  configurations predicted by the quartet model. Both two shells and three shells [xyz] configurations are shown.  $V$  represents the interaction between the  $(0p)$  and  $(0f,1p)$  shell, here left unspecified [45].

term is the quartet-hole interaction. Table 1.2 finally reports the  $^{16}\text{O}$  states which can be predicted by using the above mentioned procedure.

Much more accurate predictions concerning the spectroscopy of light nuclei as  $^{20}\text{Ne}$ ,  $^{24}\text{Mg}$  and  $^{28}\text{Si}$  have been recently obtained by using a fully microscopical quartet model [46], that has been extended to include quartets with arbitrary values of isospin and angular momentum [47]. Excellent description of the low energy part of level schemes of self-conjugated and non self-conjugated nuclei have been reported, pointing out the importance of four-body correlations in light and medium-light nuclei [47].

### 1.3.4 Molecular Dynamics (MD) models: clustering in unstable nuclei

Molecular Dynamics (MD) many-body models are extensively used to provide direct connections to the observable physical states [48]. These models are based on the resolution of the Schrödinger equation by using single-particle wave functions as Gaussian wave packets of the form:

$$\varphi_i = \phi_{\vec{X}_i} \chi_i \tau_i \quad (1.37)$$

where  $\phi_{\vec{X}_i}$  represents the spatial part of the wave-function of the  $i$ -th nucleon:

$$\phi_{\vec{X}_i}(\vec{r}_j) \propto e^{-v\left(\vec{r}_j - \frac{\vec{X}_i}{\sqrt{v}}\right)^2} \quad (1.38)$$

$\chi_i$  and  $\tau_i$  are, respectively, the intrinsic spin function and the isospin function.

Particularly interesting for the description of clustering phenomena in nuclei is the *Antisymmetrized Molecular Dynamics* (AMD) model. The AMD model was developed by Kanada-En'yo, Horiuchi and co-workers [48–50], and it has been used quite extensively in the description of nuclear systems beyond the  $N = Z$  line and to investigate structures which are not easily obtained with shell model calculations. This model is able to reproduce a big variety of nuclear properties, such as excitation energy, radii, magnetic moments and electromagnetic transition probabilities. The AMD wave functions are given by an antisymmetrized product (Slater-determinant) of single particle MD functions of the type in eq. 1.37:

$$\Phi_{AMD}(\mathbf{Z}) = \frac{1}{\sqrt{A!}} \mathcal{A} \{ \varphi_1, \varphi_2, \dots, \varphi_A \} \quad (1.39)$$

The AMD wave function is parametrized by a set of complex parameters  $\mathbf{Z} \equiv \{X_{ni}, \xi_i\}$  with  $n = 1, 2, 3$  indexing the spatial coordinates  $X$  and  $i = 1, \dots, A$ . The Gaussian center positions  $X_i$  and the intrinsic-spin orientations  $\xi_i$  are treated independently as variational parameters. The optimum wave function is determined from the set of parameters which minimize the expectation value of the energy  $\mathcal{E} \equiv \langle \Phi | H | \Phi \rangle / \langle \Phi | \Phi \rangle$ . The AMD model contains mean-field states as well as cluster states, which represents one of the most powerful features of this model, allowing to describe, in a consistent way, the coexistence of shell and cluster states [51].

Another interesting approach for the study of the structure of light nuclei is the *Fermionic Molecular Dynamics* (FMD) model. The FMD wave function is of the same type of the AMD, with the major difference regarding the *width* parameter, which is chosen as common for all nucleons in the case of AMD and which can be independently chosen for each nucleon in the case of FMD. In structure studies, the flexibility in the treatment of the width parameters of the FMD is particularly powerful, for example, to unveil the neutron-halo structure of neutron-rich nuclei [52].

#### 1.3.5 The deformed harmonic oscillator (HO)

Apart from the clear connection between clustering phenomena and energetics, a further key ingredient, *symmetries*, strongly affects the appearance of clusters in nuclei. They have impact in the collective excitation of nuclei, driving the formation of clusters themselves via their influence on the mean-field of light nuclei [10]. These connections between mean-field and the cluster degree of freedom can be understood via the so called *deformed harmonic oscillator* model of nuclei.

The harmonic oscillator (HO) is one of the possible central potentials which can be used in the nuclear shell model (see Section 1.2.4). In this picture, nucleons are supposed to move in a parabolic potential, which leads to energy levels in the form:

$$E = \hbar\omega(n + 3/2) \quad (1.40)$$

## Chapter 1. Introduction: Clusters in Nuclear Physics

---

where  $n$  is the number of oscillator quanta. Introducing a deformation of the potential, for example along the  $z$ -axis, the oscillation frequency becomes lower along the direction of the deformation while it is increased in the perpendicular directions. The *degeneracy* of equation 1.40 is therefore removed and the new values of energy are:

$$E = \hbar\omega_{\perp}n_{\perp} + \hbar\omega_z n_z + \frac{3}{2}\hbar\omega_0 \quad (1.41)$$

being  $\omega_z$  the oscillation frequency along the deformation axis,  $\omega_{\perp}$  the one for oscillations perpendicular to the  $z$ -axis and  $\omega_0 = (2\omega_{\perp} + \omega_z)$ . The so-called *quadrupole deformation*  $\epsilon_2$  can be expressed as:

$$\epsilon_2 = (\omega_{\perp} - \omega_z)/\omega_0 \quad (1.42)$$

with a total number of oscillator quanta which is the sum of those on the parallel and perpendicular axes ( $n_z + n_{\perp}$ ). Energy levels of the deformed HO are shown in Figure 1.12 [53]. Crossings of levels in the picture represent energy values having high degeneracy. Shell structures appear in this model in correspondence of those energy values for which the degeneracy is maximized. As clearly visible from the picture, shell structures which appear at  $\epsilon_2 = 0$  (spherical nucleus) disappear as the potential is deformed, but reappear for deformations ( $\omega_{\perp} : \omega_z$ ) of 2 : 1 or 3 : 1. This occurs when the ratio of the parameters describing three-dimensional deformed potential,  $(\omega_x, \omega_y, \omega_z)$ , are integers. By examining the sequence of degeneracies, one observes that the values (2, 6, 12, 20, ...) are repeated twice at a deformation 2 : 1 and three times for a deformation of 3 : 1, etc. An application of this model to the case of  ${}^8\text{Be}$  is rather simple. Being 2 : 1 the corresponding deformation, the levels which are labelled with degeneracy 2 are given by the quantum numbers  $[n_{\perp}, n_z] = [0, 0]$  and  $[0, 1]$ . These levels can be occupied by pairs of protons and neutrons coupled to a zero-spin state. The corresponding density distributions are given by the square of the wave-functions  $\varphi_{0,0}$  and  $\varphi_{0,1}$ , which correspond to the two distinct levels. The overall  ${}^8\text{Be}$  density is given by the sum  $|\varphi_{0,0}|^2 + |\varphi_{0,1}|^2$ . This is plotted in the Figure 1.13 b) as a function of the  $z$  coordinate [53]. The feature which emerges is that the density is double humped corresponding to the arrangement of protons and neutrons into two  $\alpha$ -particles. The HO wave-functions can be expressed in terms of the above basis of linearly independent states  $\varphi_i$ :

$$\phi_{\alpha(\pm)} = \frac{1}{\sqrt{2}}(\varphi_{(0,0)} \pm \varphi_{(0,1)}) \quad (1.43)$$

which corresponds to project out the point symmetry of the two clusters. The overlap of an isolated  $\alpha$ -particle,  $\phi_{\alpha} = \frac{1}{\pi}e^{(-\omega^2 r^2/2)}$  is found to be  $> 90\%$  [53]. The square of the two wave-functions is shown in the Figure 1.13 a) (dashed lines) together with the overall  ${}^8\text{Be}$  density. What is evident is that the symmetries found in degeneracies of deformed HO approach are present even in the density, and they give rise to new magic numbers which are called *deformed magic numbers*. They have

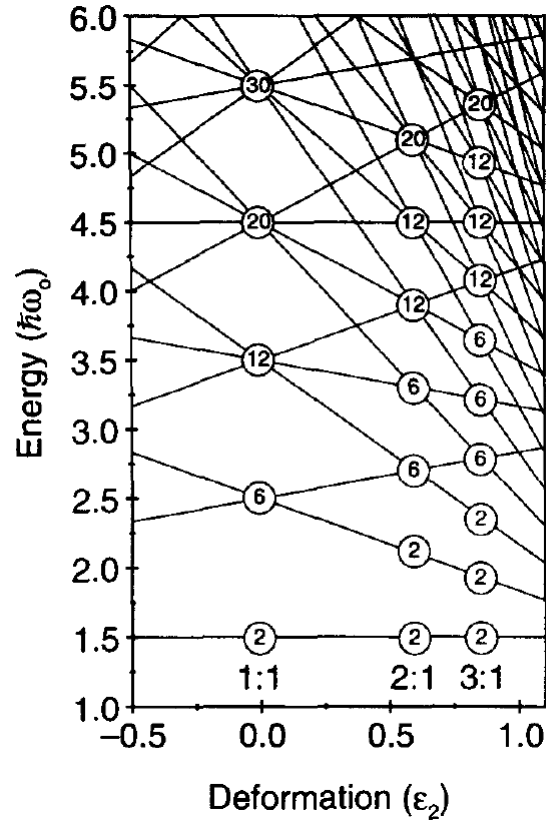


Figure 1.12: Energy levels of the deformed harmonic oscillator as a function of the quadrupole deformation  $\epsilon_2$ . The numbers inside circles indicate the degeneracy of the levels in correspondence of each crossing point. Shell structure appears for spherical configurations and 2 : 1 and 3 : 1 deformed configurations. From [53].

been largely explored in the literature in order to identify some particular cluster partitions [10]. Rae [54] focused on details about deformed magic numbers in order to explicitly probe the cluster decompositions. He demonstrates that these numbers could be expressed as the sums of spherical magic numbers. The results of his work are shown in table 1.3. This description locates at each deformation the associated cluster structure. In correspondence of a 2 : 1 deformation, for example, *superdeformed* structures should be found in  ${}^8\text{Be}$  ( $\alpha + \alpha$ ),  ${}^{20}\text{Ne}$  ( ${}^{16}\text{O} + \alpha$ ),  ${}^{32}\text{S}$  ( ${}^{16}\text{O} + {}^{16}\text{O}$ ), etc., while, in correspondence of a 3 : 1 structure, hyperdeformations are predicted in  ${}^{12}\text{C}$  ( $\alpha + \alpha + \alpha$ ),  ${}^{24}\text{Mg}$  ( $\alpha + {}^{16}\text{O} + \alpha$ ), etc.

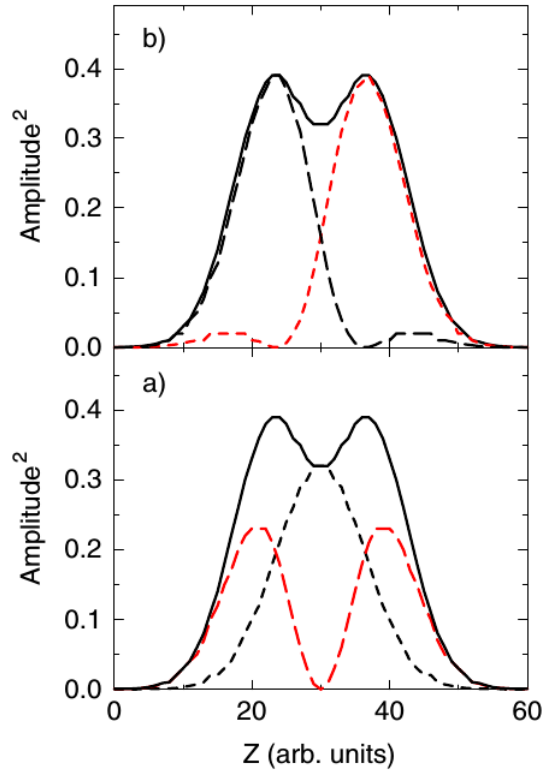


Figure 1.13: a) HO wave-functions of the form given in 1.43 shown as dashed lines. The solid line represents the overall  ${}^8\text{Be}$  density  $|\varphi_{0,0}|^2 + |\varphi_{0,1}|^2$ . b) The density corresponding to the HO configurations for  ${}^8\text{Be}$  (solid line). Dashed lines show the two separate contributions  $|\varphi_{0,0}|^2$  and  $|\varphi_{0,1}|^2$ . From [10].

## 1.4 Applications of cluster models

In the previous section we gave a brief summary of the ideas on which cluster models of nuclei are based. This section is dedicated to a discussion on applications of cluster models to physical cases of interest in nuclear physics. It is important to stress that, even if the content of this section offers a quite comprehensive overview of the nuclei of interest for the present thesis, and also of other particularly remarkable cases, we are certainly far from a complete overview of the state of the art of nuclear cluster physics, for which more details can be found, for example, in Refs. [10, 55–58].

### 1.4.1 Light self-conjugated nuclei: ${}^{12}\text{C}$ , ${}^{16}\text{O}$ , ${}^{20}\text{Ne}$

Since the beginning of nuclear clustering physics, self-conjugated nuclei were object of several theoretical investigations. It became clear in the early 1960s, from the work of Ikeda and collaborators [59], that clustering phenomena should not mani-

## 1.4 Applications of cluster models

Deformed magic numbers	Spherical magic numbers	Cluster configuration
$\omega_{\perp} : \omega_z = 2 : 1$		
4	2 + 2	$\alpha + \alpha$
10	8 + 2	$^{16}\text{O} + \alpha$
16	8 + 8	$^{16}\text{O} + ^{16}\text{O}$
28	20 + 8	$^{40}\text{Ca} + ^{16}\text{O}$
40	20 + 20	$^{40}\text{Ca} + ^{40}\text{Ca}$
$\omega_{\perp} : \omega_z = 3 : 1$		
6	2 + 2 + 2	$\alpha + \alpha + \alpha$
12	2 + 8 + 2	$\alpha + ^{16}\text{O} + \alpha$
18	8 + 2 + 8	$^{16}\text{O} + \alpha + ^{16}\text{O}$
24	8 + 8 + 8	$^{16}\text{O} + ^{16}\text{O} + ^{16}\text{O}$
36	8 + 20 + 8	$^{16}\text{O} + ^{40}\text{Ca} + ^{16}\text{O}$

Table 1.3: Decomposition of deformed magic numbers in terms of spherical magic numbers, at a deformation of 2 : 1 and 3 : 1, from [54]. The associated cluster structure is indicated for each deformed magic number.

fest in the ground states of  $\alpha$ -nuclei but, on the contrary, they should emerge for increasing internal energies of the nucleus. At the point where the nucleus is separated into its clusters, an energy which corresponds to the mass difference between the host and the clusters is required. This semi-quantitative evidence led Ikeda in formulating his hypothesis regarding the formations of clusters. In order to form a cluster structure, with large probability, an excitation energy close to the nucleus separation energy into clusters should be required. This result is summarized in the so-called *Ikeda diagram*, which is shown in Figure 1.14. This diagram shows the possible  $\alpha$ -cluster decompositions of light self-conjugated nuclei in correspondence of each decay threshold. In this way, there is a gradual transition from the compact ground state to the fully  $N$ - $\alpha$  clustered structure. The  $\alpha$ -particle configurations are here shown schematically as linearly arranged, even if that is not the most stable configuration [60]. The picture proposed in the diagram suggests that the cluster degree of freedom is only liberated while the excitation energy of the system approaches the one of the cluster emission threshold. As an example, while  $^8\text{Be}$  has a strongly clustered structure in its ground state, which is located at about 0.0918 MeV from the 2- $\alpha$  threshold, an excitation energy of about 7.27 MeV is suggested to search for the 3- $\alpha$  structures in  $^{12}\text{C}$ .

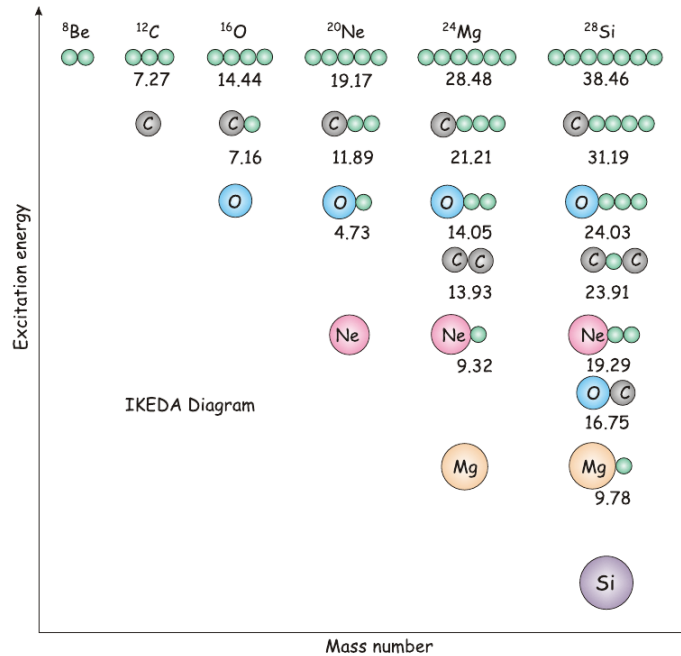


Figure 1.14: The Ikeda diagram [59] of self-conjugated nuclei. Possible  $\alpha$ -cluster arrangements, and their evolution with the excitation energy, are shown. As the energy increases, fully  $N$ - $\alpha$  structures appear. The basic idea held by this diagram is that clustering phenomena are expected to manifest, with larger probability, around the corresponding decay threshold. From [55].

#### 1.4.1.1 The $^{12}\text{C}$ and the Hoyle state

Following the scheme of Ikeda, it does not surprise that the excitation energy region of the  $^{12}\text{C}$  nucleus close to the  $3\alpha$  decay threshold (7.274 MeV) is particularly interesting in the comprehension of clustering phenomena in nuclei [61–63]. Carbon, as well as beryllium isotopes, are indeed intriguing examples of clustering, because of their 3-centers and 2-centers behaviour [10, 61]. A number of models have been deployed to understand the structure of  $^{12}\text{C}$  in this complicated energy region. Single-particle approaches are for example able to describe rather well the energy of the first  $2^+$  excited state ( $2_1^+$ , 4.44 MeV [26]), while a void in such calculations is present in the region of the second  $0^+$  state ( $0_2^+$ , 7.654 MeV) [64]. This state, named *Hoyle state*, is crucial since it presents a well developed and quite unusual cluster configuration [65] and also for its astrophysical relevance in the *nucleosynthesis* of elements [66] (see paragraph 1.4.2).

The states of  $^{12}\text{C}$  close to the  $3\alpha$  threshold were object of several theoretical calculations. The  $\alpha$ -cluster model is able, for example, to suggest the geometrical arrangement of  $\alpha$ -particles by varying their location and size to minimize the energy of the system. Within this framework, Brink [67] suggested two possible  $\alpha$ -structures

## 1.4 Applications of cluster models

---

of  $^{12}\text{C}$ , an *equilateral triangular* arrangement and a *linear chain* configuration. The first was associated to the ground state while the second, where  $\alpha$ -clusters assume a linear shape was directly linked to the 7.654 MeV state. This idea supported the Morinaga [68] scheme, where, based on the 3- $\alpha$  linear structure of the Hoyle state, he predicted the  $2^+$  member of the rotational band to be located at around 9.70 MeV. The subsequent rotational excitation of such a deformed structure were instead predicted at 14.18 MeV. These two states were linked, respectively, to the experimental 9.61 MeV and the 14.16 MeV, whose spectroscopic properties were unknown at the time. With the increasingly precise information on  $^{12}\text{C}$  spectroscopy obtained during five decades of experimental investigations, the idea of a linear chain in  $^{12}\text{C}$  lost its relevance, being in striking contrast with experimental data.

Microscopic models have well reproduced the spectrum of the low-lying excited states of  $^{12}\text{C}$  observed below 15 MeV. By using a fully-microscopic  $\alpha$ -particle model, where the Pauli principle is treated exactly, Uegaki and collaborators [62] successfully described such a spectrum in the GCM framework. Together with the compact configurations usually expected in low energy nuclear states, they found a new *phase* of aggregation. In a number of the states characterized by the new *phase*,  $^{12}\text{C}$  is described as constituted by a fully dissociated 3- $\alpha$  weakly interacting system, where the clusters move freely over a wide spatial region. The energy of the  $0_2^+$  state is well reproduced within this model, and it appears not as a chain-like state but as a finite  $\alpha$ -boson gas. The ground state of  $^{12}\text{C}$  is predicted to have a stable deformation with a compact 3- $\alpha$  triangular configuration, as well as the entire rotational band  $K^\pi = 0^+$  build on it. Similar results, concerning the description of the Hoyle state as an  $\alpha$ -particle gas state, were attained by Kamimura [63] in his RGM microscopic calculations.

Given the bosonic nature of the 3- $\alpha$  system, it is possible to assume, if the inter-cluster separation is sufficiently large, that the internal structure of  $\alpha$ -particles becomes no longer so important. The condition needed to achieve this is that the nuclear radius is large enough that an  $\alpha$ -particle may explore (by tunnelling) the classically prohibited region, increasing the nuclear volume. In such a circumstance, the antisymmetrization properties of the fermionic system play a negligible role and the system can be treated as made of 3 bosons, which may form a *condensate*. This hypothesis was supported, for the  $^{12}\text{C}$   $0_2^+$  state, by electron scattering experiments [71], which pointed out that the Hoyle state has a radius well larger (of a factor  $\approx 1.5$ ) than the one of the ground state. Microscopic calculations were developed to describe the Hoyle state as a *Bose-Einstein condensate* under the framework of the THSR (Tohsaki, Horiuchi, Schuck and Röpke) wave function [72–75]. They succeeded in the reproduction of the charge form factor derived from electron scattering experiments [72] without any arbitrary normalization. The Figure 1.15 shows the decomposition of the THSR wave function, as a result of the calculations of Refs. [69, 70], into its orbital components, for the ground state and the Hoyle state in  $^{12}\text{C}$ . This reveals that, for the Hoyle state, the THSR wave function has a strong ( $\approx 70\%$ ) overlap with one of 3  $\alpha$ -particles in the  $S_1$ -orbital, while other contributions

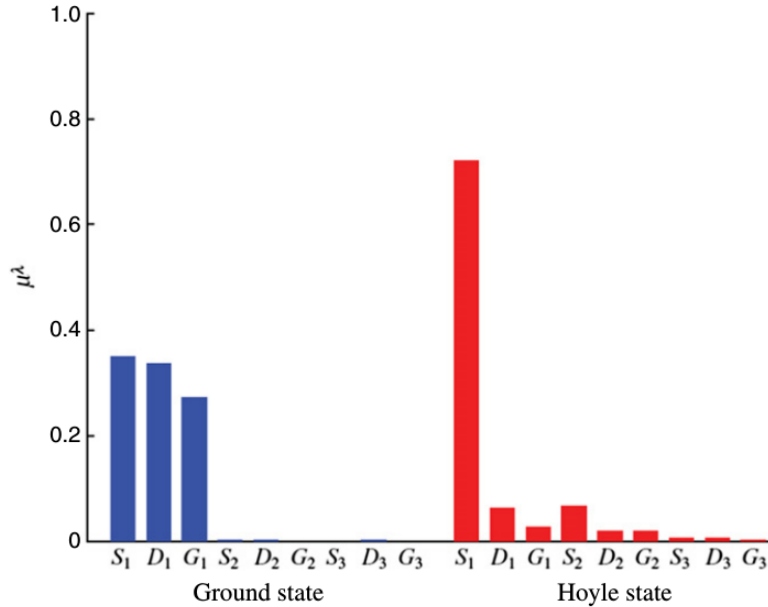


Figure 1.15: Decomposition of the THSR wave function describing the  $^{12}\text{C}$  g.s. (left) and the  $^{12}\text{C}$  Hoyle state ( $0_2^+$ , right) into its components. The 70% of superposition with the S orbital for the Hoyle state wave function indicates a possible BEC nature. This behaviour is not present in the g.s., where S, D and G orbitals contribute with almost the same amplitude. From [69, 70].

are small, a clear evidence that BEC phenomena are predicted to occur in this description. The 30% of overlap with orbitals different from the  $S_1$  indicates that the Pauli principle plays a small role in the interior region of the Hoyle state. The same picture for the ground state (Figure 1.15) clearly indicates that BEC phenomena do not occur in such a state, where, on the contrary, there is an almost equal contribution of S, D and G orbitals, reflecting the strong influence of the Pauli principle. FMD calculations also succeed in the reproduction of the electron scattering form factors of [71]. They predict the Hoyle state as constituted by a dominant weakly bounded  $\alpha$ -particles structure, with relative positions of  $\alpha$ -clusters which reflect a  $\alpha+^8\text{Be}$  configuration. In such a model, antisymmetrization properties are not negligible and this is in contradiction with an hypothesis of the BEC nature of this state.

Very recent microscopic 3- $\alpha$  calculations, based on the Faddeev three-body formalism [26], were published by Ishikawa [76]. They show the presence of three distinct local peaks in the calculated density  $\rho(x, y)$  in correspondence of the resonance energy of the Hoyle state, denoted with A, B and C in Figure 1.16 (left) and corresponding to three distinct  $\alpha$ -clusters. This picture is the one of a strongly clustered structure, where the inter-cluster A-B distance is reduced compared to the

## 1.4 Applications of cluster models

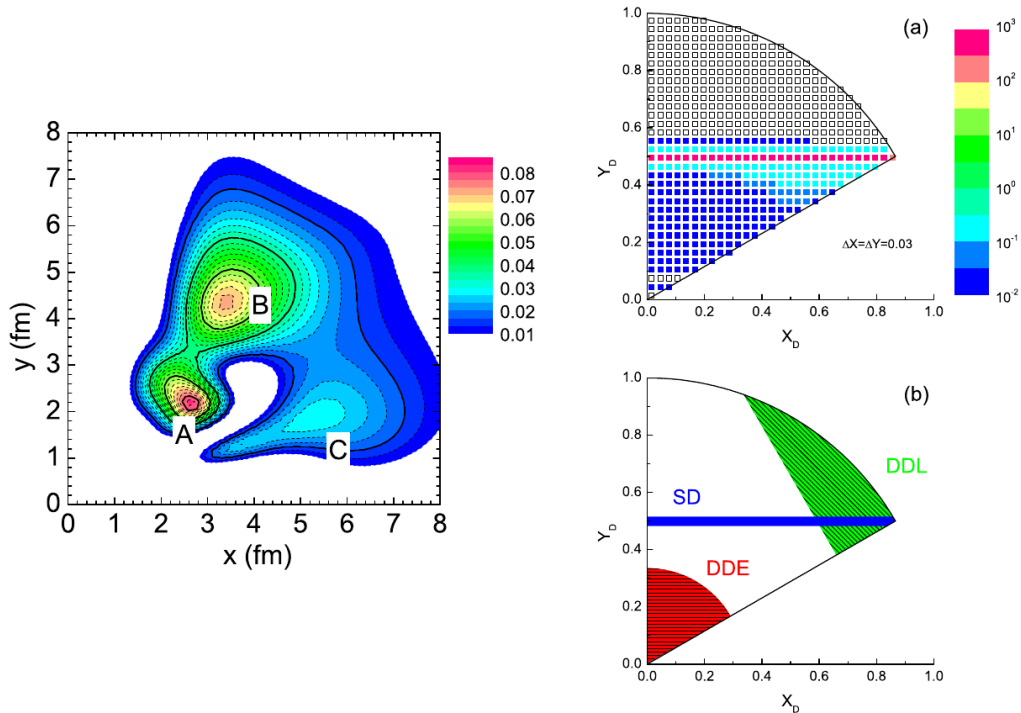


Figure 1.16: (left) Density distribution  $\rho(x, y)$  of the Hoyle state in  $^{12}\text{C}$  from microscopic calculations based on the Faddeev three-body formalism. (right) Symmetric Dalitz plot of Hoyle state  $3\text{-}\alpha$  decay (a) obtained from the calculations of the left panel. (b) schematic explanation of the region of the plot occupied by *sequential decays* (SD), *Direct Decays from a Linear chain* (DDL) and *Direct Decay with Equal energy* (DDE). The figures are extracted from [76].

A-C and B-C distances, indicating the presence of a  $^8\text{Be}$  together with an  $\alpha$ -particle. The structure of the Hoyle state is found to be a weak mixture of configurations including a possible *bent-arm* arrangement. This model allows to describe the decay path of the Hoyle state. An analysis with the symmetric Dalitz plot technique (see Paragraph 2.3 of Chapter 2), as shown in Figure 1.16 (right), points out a dominant *sequential decay* (SD) mode, i.e. the decay in the  $\alpha+^8\text{Be}$  final state, contribution, which is associated, in the plot, to an horizontal band (as shown by the Figure 1.16 (b), right panel). Other contributions, i.e. *Direct Decays from a Linear chain* (DDL) and *Direct Decay with Equal energy* (DDE) are found to be well below 1% of the total decay width. A possible bent-arm configuration for the Hoyle state is also found in Ref. [77] by means of an *ab-initio* lattice calculation. In the framework of the lattice calculations, they found a compact triangular configuration of  $\alpha$ -clusters for the ground state and the first  $2^+$  state of  $^{12}\text{C}$ , while, an obtuse triangular configuration (bent-arm) is found to describe the structure of the Hoyle state and to provide

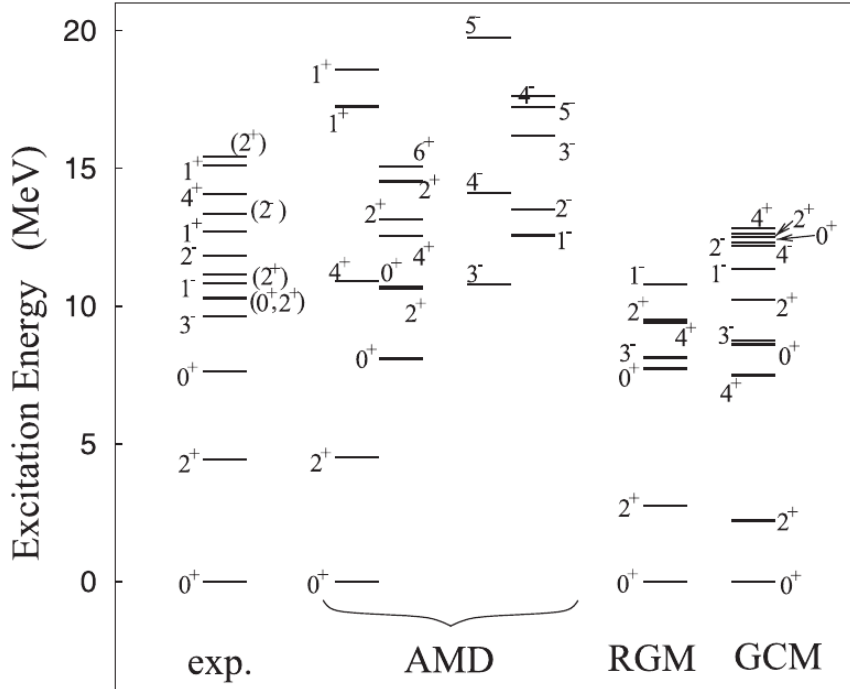


Figure 1.17: Energy levels of  $^{12}\text{C}$  obtained from the AMD calculations of Ref. [79] compared to the experimental one and to RGM [63] and GCM [62] results. From [79].

evidence of the second  $2^+$  state. The latter is linked to the rotational excitation of the Hoyle state, which is currently one of the hot topics in nuclear physics [78].

AMD calculations of  $^{12}\text{C}$  structure have been performed in Ref. [79]. This model, employed by Kanada-En'yo and von Oertzen, provides a good description of  $^{12}\text{C}$  excited states for both shell model and cluster states. The corresponding energy spectrum of  $^{12}\text{C}$  states is reported in Figure 1.17 (from [79]), in comparison with the experimental one and with those obtained from, respectively, RGM [63] and GCM [62] calculations. The latter are able to reproduce some states above threshold, but fail in reproducing the energy of the  $2_1^+$  state. For the Hoyle state it is found that it is dominated by a  $[^8\text{Be}(0^+) \otimes l = 0]_{J=0}$  ( $\alpha + ^8\text{Be}$ ) configuration and that it exhibits cluster-gas features. The  $2_2^+$  state, which is considered to be the first rotational excitation of the Hoyle state, is found at an excitation energy of about 9.9 MeV. The authors linked this state to the one experimentally observed in Ref. [80].

Finally, calculations made using the Algebraic Cluster Model (ACM, see for example [83]) have been recently applied to  $^{12}\text{C}$  structure in [81]. In this model,  $\alpha$ -clusters are assumed to be the corners of an equilateral triangle. In analogy with molecular physics, the wave-function of a symmetric object has to obey to particular

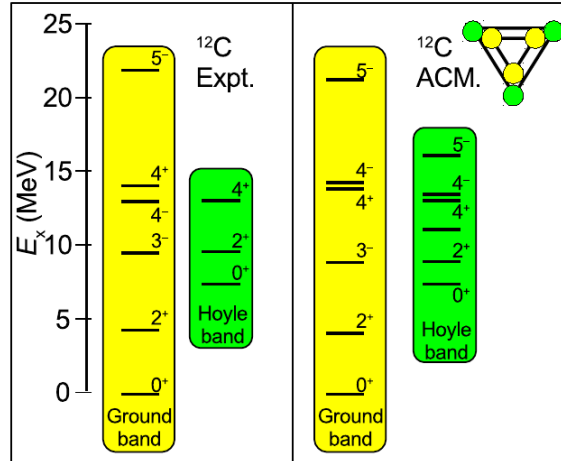


Figure 1.18: (left) Comparisons between experimental observed states currently assigned to the ground state and Hoyle band in  $^{12}\text{C}$  and (right) the calculated ones via the ACM [81]. From [82].

symmetries that are well described in the group theory [84]. For example, for an equilateral triangle, the  $\mathcal{D}_{3h}$  symmetry has to be used. Excited states of such a structure can be constructed both through rotation of the whole triangle or through expansions and contractions of its corners. Starting from the  $\mathcal{D}_{3h}$  symmetry, the authors of Ref. [81] predicted a peculiar sequence of states, at increasing excitation energy, having  $J^\pi = 0^+$ ,  $2^+$ ,  $3^-$ ,  $4^\pm$  and  $5^-$ . The energies predicted by the ACM are shown in Figure 1.18 (right) compared with the ones obtained in experimental works (left). Two types of structures are identified: the first, with a smaller moment of inertia, is associated to the ground state and gives rise to a rotational band (ground band,  $K^\pi = 0_1^+$ ), the second is instead much more deformed and gives rise to the Hoyle band, i.e. the rotational band having the Hoyle state as band-head ( $K^\pi = 0_2^+$ ). The  $0^+$  and  $2^+$  excitations correspond to the rotation of the triangle around an axis lying in the plane of the triangle, while states of higher order of spin are relative to rotations around an axis perpendicular to the plane itself. The ACM not only reproduces the ground state properties of  $^{12}\text{C}$  and the ground band<sup>9</sup>, but also describes the Hoyle state and its excitations as a symmetric stretching vibration

<sup>9</sup>Hints for the presence of a triangular  $\alpha$ -cluster configuration even in the ground state of  $^{12}\text{C}$  were obtained from high precision experiments performed by the Naples and Milan groups in the '70 [85, 86]; unfortunately, these works were largely overlooked. They measured angular distributions of  $p+^{12}\text{C}$  elastic scattering data at energies going from 3 to 64 MeV. At these energies, the projectile wavelength is of the same order (some fm) of the inter-cluster separation distances, and peculiar diffraction patterns would appear. From very accurate measurements and analysis of angular distributions, the authors of Refs. [85, 86] quoted a 20% probability that  $\alpha$  triangular structure can appear even in  $^{12}\text{C}$  ground state and estimated an average inter- $\alpha$ -cluster distance of about 4 fm.

of the equilateral triangle coupled to a rotation.

In general, the properties of the Hoyle state which are described by means of cluster models could be better understood by means of high precision experiments. As an example, the identification of the missing Hoyle band members is of crucial importance, since it makes possible to experimentally extract quantities like the moment of inertia of the rotating structure and therefore its deformation<sup>10</sup>. The  $2^+$  member of the Hoyle band was initially identified by Itoh and co-workers [80] and recently confirmed by Freer and collaborators [87] using inelastic proton scattering experiments and by Zimmermann et al [88] by carbon photo-disintegration. In 2011, the authors of [89] found evidence of a  $4^+$  state at about 13.3 MeV and having a width of 1.7 MeV. This state can be attributed to the  $4^+$  member of the Hoyle band, seen in the ACM calculations of Figure 1.18 and further confirmed in [90]. These results, together with the theoretical studies, allow to rule out possible conjectures about a linear chain structure of the Hoyle state.

### 1.4.1.2 Theoretical calculations for $^{16}\text{O}$ and $^{20}\text{Ne}$

The  $\alpha$ -particle model has been successfully applied to the case of  $^{16}\text{O}$ . In Ref. [91], it is proposed a tetrahedral symmetry of  $4\alpha$  particles, where the  $\alpha$ -clusters lie in the corners of a tetrahedron,  $T_d$  symmetry. Two kinds of rotating structures, respectively associated with  $^{12}\text{C} + \alpha$  and  $4\alpha$  configurations, are proposed. They should be observed, following the Ikeda scheme, around an energy of, respectively, 7.16 MeV and 14.44 MeV. The head of the  $K^\pi = 0_2^+$  band (lying at 6.05 MeV excitation energy) is linked with a quasi-planar structure. ACM calculations have been also employed for describing the spectrum of  $^{16}\text{O}$ . An attempt to describe the rotation-vibration spectrum of  $4\alpha$  configuration with tetrahedral symmetry is made in Ref. [92] by means of ACM calculations. These theoretical predictions, which are capable of describing the full dynamics of four-body clusters, show evidence for the occurrence of this symmetry in the low-lying spectrum of  $^{16}\text{O}$ . Within this model, the authors were also able to make a detailed description of energies, electromagnetic transition rates, form factors, and  $B(EL)$  values. The  $^{16}\text{O}$  spectrum obtained from these calculations is shown in Figure 1.19, where four rotational bands are identified with different symmetries. They reproduce in a quite satisfactory way the observed  $^{16}\text{O}$  spectrum [93]. Other theoretical calculations involving the  $^{16}\text{O}$  nucleus include the Hartree-Fock (HF) approximation [94, 95], the Nilsson-Strutinsky (NS) model [96] and the core +  $\alpha$  potential model [97].

The cluster structure of  $^{20}\text{Ne}$  is particularly remarkable, since two closed shell nuclei are involved in its cluster decomposition (see table 1.3): the  $\alpha$ -cluster resides outside the  $^{16}\text{O}$  magic core. The simple core +  $\alpha$  potential model of Buck and

---

<sup>10</sup>In a simple rigid body model, energy of rotational members belonging to a band is connected to their total angular momentum  $J$  through the moment of inertia of the rotating structure:  $E_J = \frac{\hbar^2}{2I} J(J+1)$ . The latter can be extracted if one knows the values of excitation energies of rotating states for different  $J$  values.

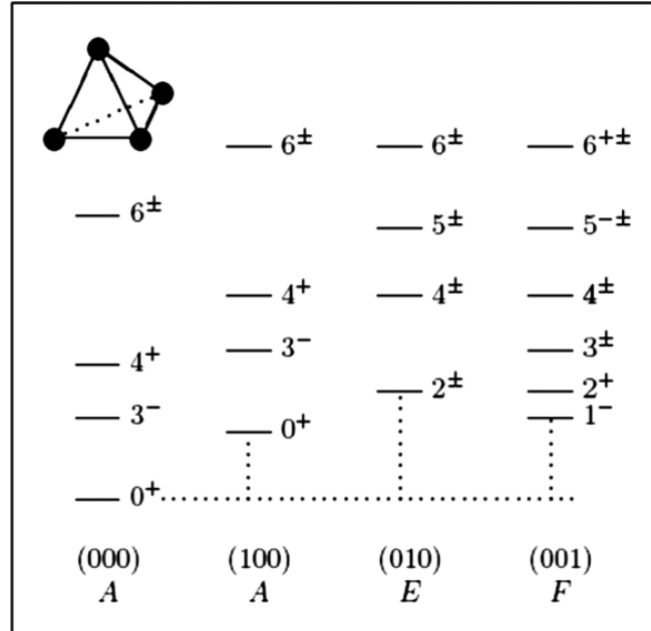


Figure 1.19: Schematic spectrum of  $^{16}\text{O}$  calculated by assuming spherical top with  $4-\alpha$  tetrahedral symmetry. Four rotational-vibrational bands are identified, having  $A$ -  $E$ - and  $F$ -like  $S_4$  symmetries. From [98].

collaborators provides a rather good description of a number of low-lying states belonging to positive and negative parity bands [99]. A further improved theoretical interpretation of these rotational bands has been given in [100], where they pointed out the molecular nature of  $^{20}\text{Ne}$  in studying self-conjugated nuclei rotational bands. They showed that the first rotational bands  $K^\pi = 0^\pm$  of  $^{16}\text{O}$  and  $^{20}\text{Ne}$  could be unified as the twins of the same molecule-like structure of an  $\alpha$ -particle with a residual nucleus. In the case of  $^{16}\text{O}$ , the positive parity band built on the  $0_2^+$  state was attributed to configurations in which a  $^{12}\text{C}$  core is coupled with a  $\alpha$ -particle in the  $sd$  shell [101]. The second  $^{16}\text{O}$  band built on the  $1^-$  state (9.58 MeV excitation energy) was instead explained as a result of the *grazing* motion of the  $\alpha$ -particle around the  $^{12}\text{C}$  core. The same picture was extended by Horiuchi and Ikeda [100] to the detailed description of the ground state band in  $^{20}\text{Ne}$  ( $K^\pi = 0^+$ ) and the  $K^\pi = 0^-$  (built on the  $E_x = 5.80$  MeV state). A summary of their results is shown in the Figure 1.20, where the energy spectra of the  $K^\pi = 0^\pm$  rotational bands of  $^{16}\text{O}$  and  $^{20}\text{Ne}$ , calculated via a molecule-like  $\alpha +$  residual structure, are displayed. This asymmetric cluster molecule-like structure is also rather well described in the framework of the AMD [102] model, from which it emerges quite naturally and without any a-priori constraint on the arrangement of the 20 nucleons. The quartet model has been, finally, used to probe  $\alpha$ -like structures of  $^{20}\text{Ne}$  under and above the  $\alpha$ -decay threshold (4.73 MeV) [45–47].

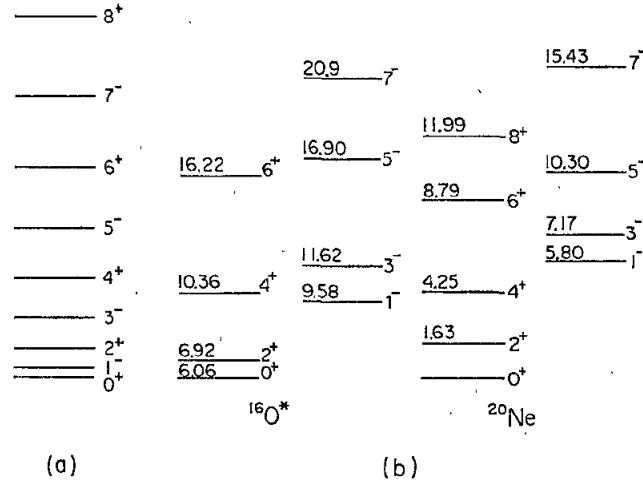


Figure 1.20: (a) Rotational spectra of a heteropolar diatomic molecule used for comparison. (b) Energy spectra of  $K = 0^+$  and  $K = 0^-$  rotational bands for:  $^{16}\text{O}$  (left),  $^{20}\text{Ne}$  (right). They are calculated assuming a  $\alpha + \text{core}$  molecule-like structure. In the case of  $^{20}\text{Ne}$ , the  $K = 0^+$  band is built on the ground state, while the  $K = 0^-$  band has the  $1^-$  5.8 MeV state as band-head. From [100].

## 1.4.2 Astrophysical relevance of clustering

Clustering phenomena assume a key role also in nuclear astrophysics, where different scenarios of stellar nucleosynthesis can be affected by the properties of nuclear states involved in the reactions [103]. A very interesting example is the case of  $^{12}\text{C}$ . It is useful to clarify the importance of clustering in astrophysics and it is of particular relevance for this work since it is object of one of the investigations we will discuss in Chapter 2.  $^{12}\text{C}$  is one of the major constituents of living beings, and, therefore, understanding its origins represents a challenging problem. Our knowledge traces the origin of  $^{12}\text{C}$  to the so-called  $3\alpha$  process of stellar nucleosynthesis [104, 105]. This process occurs in stars during the helium burning stages of their evolution and proceeds essentially via the initial fusion of two  $\alpha$ -particles followed by the subsequent radiative capture of a third  $\alpha$  to the ground state of  $^{12}\text{C}$ . Anyway, the reaction rate of this process is strongly suppressed by its intermediate stage, where a  $^8\text{Be}$  is formed. The extremely short life-time of the unbound  $^8\text{Be}$  (of the order of  $10^{-16}\text{s}$ ) acts indeed as a sort of bottleneck for the whole process. A non-resonant two-step process, therefore, cannot explain the observed abundances of carbon, and consequently of the heavier elements, in the universe. This fact led Fred Hoyle, in 1953, formulate the hypothesis that the  $3\alpha$  process should be a resonant process, proceeding through a resonant state of  $^{12}\text{C}$  located close to the corresponding  $^8\text{Be} + \alpha$  decay threshold [106, 107], as schematically shown in Figure 1.21. This state, according to

## 1.4 Applications of cluster models

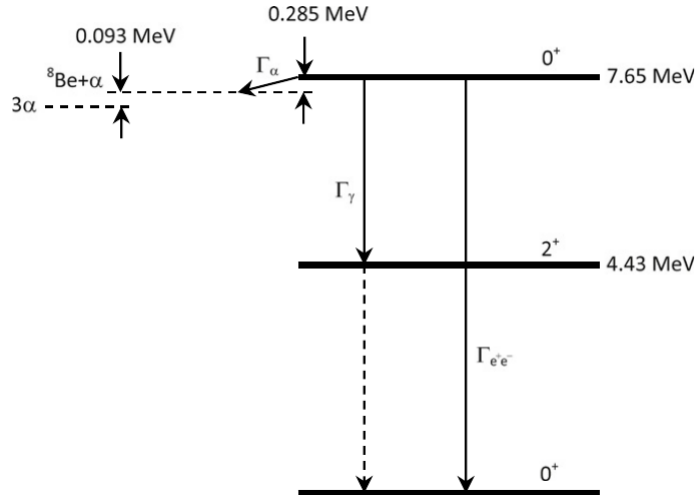


Figure 1.21: Scheme of low-lying states of  $^{12}\text{C}$ . The Hoyle state ( $7.654\text{ MeV}$ ,  $0^+$ ) is shown together with the corresponding  $3\alpha$  and  $\alpha+^8\text{Be}$  decay thresholds. The  $^{12}\text{C}(7.654) \rightarrow \alpha+^8\text{Be}$  decay and the possible electromagnetic transitions to the ground state are shown. From [10].

the Hoyle hypothesis, should be characterized by  $J^\pi = 0^+$ , in such a way that the centrifugal barrier of the  $\alpha$ -capture vanishes ( $s$ -wave capture) and the second step of the process maximizes the probability of producing  $^{12}\text{C}$ . The fusion probability is further increased if one assumes a strongly clustered  $^8\text{Be} + \alpha$  structure for the Hoyle state. This state was then confirmed a few years later by Cook and collaborators [108], and it was found to lie at  $7.654\text{ MeV}$ , only  $285\text{ keV}$  above the  $\alpha$  decay threshold, as shown in Figure 1.21.

Since three body collisions are strongly inhibited in the temperature range where the helium burning occurs, one can conclude that the  $3\alpha$  process is essentially a two-step process made of:



where the second step is maximized by the fact that the  $92\text{ keV}$  of energy required to make such a fusion is remarkably close to the energy of the so-called *Gamow window*<sup>11</sup> [103], which is located, as an example, at around  $85\text{ keV}$  ( $60\text{ keV}$  width) for a temperature of  $10^8\text{ K}$ . The amount of  $^{12}\text{C}$  that is so formed can be calculated

<sup>11</sup>The Gamow window, see the Section 2.6 of Chapter 2, corresponds to the range of energies which mainly contribute in the compute of the *reaction rate* within a star. In other words, only nuclear resonances which are approximately inside the Gamow window give a sizeable contribution to the reaction rate.

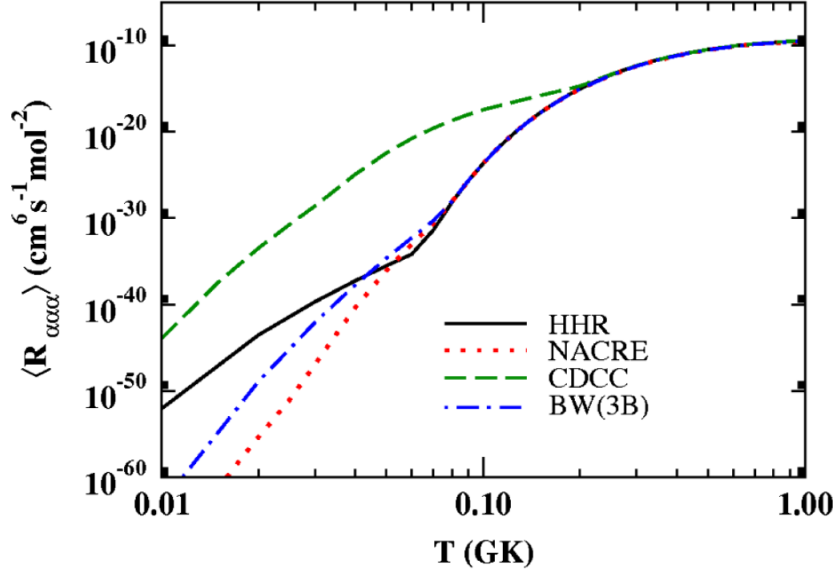


Figure 1.22: Evaluation of the  $3\alpha$  reaction rate with different methods: hyperscalar harmonic R-matrix method (solid), the NACRE evaluation [109] (red dotted), the Continuum Discretized Coupled Channel (CDCC) [66, 110] and the more recent three-body Breit Wigner method BW(3B) [111]. From [111].

from the competition between  $\alpha$ -decays of the Hoyle state (which are regulated by the  $\Gamma_\alpha$  partial width [103]) and radiative ones ( $\Gamma_{rad} = \Gamma_\gamma + \Gamma_{e^+e^-}$ ) for the two possible radiative transitions, e.g. gamma emission through the  $2_1^+$  state and pair production, which lead to the ground state of  $^{12}\text{C}$  (see Figure 1.21). The corresponding reaction rate is so fully determined by the properties of the Hoyle state:

$$\langle \sigma v \rangle \propto \frac{\Gamma_\alpha \Gamma_{rad}}{\Gamma} e^{-\frac{E_R}{k_B T}} \quad (1.46)$$

being  $E_R$  the energy of the Hoyle resonance,  $k_B$  the Boltzmann constant and  $\Gamma$  the total level width. The latter is known to be fully dominated by the  $\alpha$  decay width, i.e.  $\Gamma = \Gamma_\alpha + \Gamma_{rad} \approx \Gamma_\alpha$ , and so it results in a dynamical equilibrium  $^4\text{He} + ^8\text{Be} \rightleftharpoons ^{12}\text{C}^*$  only broken by the small leakage to the  $^{12}\text{C}$  ground state given by the radiative decays. At stellar temperatures of  $T \approx 10^8 - 10^9 \text{K}$  this process is thus dominated by the fusion through the  $^8\text{Be}$  ground state, which is therefore regulated by the so-called *sequential decay* (SD) width of the Hoyle state, which corresponds to  $\alpha$ -decays leading the residual  $2\alpha$  system under the 92 keV  $^8\text{Be}$  level. However, in astrophysical scenarios that burn helium at lower temperatures, like for instance helium-accreting white dwarfs or neutron stars with small accretion rate, the reaction rate of the  $3\alpha$  process is completely dominated by another decay mode of the Hoyle state: the non-resonant, or *direct*,  $\alpha$  decay (DD) [110, 112, 113], where the two  $\alpha$  particles bypass the formation of  $^8\text{Be}$  via the 92 keV resonance. Recent theoretical calculations

show that, at temperatures below 0.07GK, the reaction rate of the direct process is largely enhanced with respect to the one calculated by assuming only the sequential scenario [109]; as an example, for temperatures around 0.02GK such enhancement is predicted to be 7-20 orders of magnitude [66, 111, 112, 114, 115]. This can be seen in Figure 1.22, where the authors of [111] show the reaction rate of the  $3\alpha$  process computed with different models in comparison with their three-body Breit-Wigner method BW(3B), which represents the state of art of reaction rate calculations for such a process.

A precise knowledge of the above mentioned decay widths of the Hoyle state is therefore required to understand its astrophysical relevance, especially for low temperature stars, where even a small contribution of *direct decays* would result in strong enhancements of the  $3\alpha$  reaction rate. In Section 2.3 (Chapter 2) we will discuss the results of our experiment aimed to improve the present knowledge of such a *branching ratio*.

### 1.4.3 Non-self-conjugated nuclei: nuclear molecules

Clustering phenomena beyond pure  $\alpha$ -clustering appear also in the case of non-self-conjugated nuclei. For example, in the case of neutron-rich nuclei, clustering features are strongly influenced by the presence of extra neutrons. The first attempt to theoretically describe clustering phenomena in non- $\alpha$ -conjugated systems was made by Hafstad and Teller [29] considering a series of neutron-rich isotopes with only one extra-neutron respect to the corresponding self-conjugated configuration:  ${}^5\text{He}$ ,  ${}^9\text{Be}$ ,  ${}^{13}\text{C}$  and  ${}^{17}\text{O}$ . They observed how the binding energies of these  $4n + 1$  nuclei depend not only on the  $\alpha$ - $\alpha$  interaction, but also on the role of the extra neutron, which reflects the additional degrees of freedom brought by the extra-neutrons to systems. In this way, while the binding energy of  ${}^5\text{He}$  was reflecting the  $\alpha$ - $n$  interaction, the  ${}^9\text{Be}$  ( $\alpha + n + \alpha$ ) was recognized having a contribution to the Hamiltonian from an *exchange* interaction. The basic description of neutron-rich nuclei given by Hafstad and Teller was that of clustered systems in which *covalent exchange neutrons* are shared between  $\alpha$ -cores in order to increase the stability of the structure. This behaviour presents a quite clear analogy with the case of *covalent bonding* in molecules and, therefore, the extra neutrons are often called *covalent particles*, while the corresponding nuclear configuration is named *nuclear molecule*. They gave the basis of the treatment of clustering phenomena in non-self-conjugated nuclei, even if significant progress has been achieved only 50 years later. As in the case of self-conjugated nuclei, we will focus here on a limited class of examples, which will be useful for the analysis that will be presented in Chapter 2. For a more detailed and comprehensive review, see Refs. [10, 55] and references therein.

Nuclear molecules<sup>12</sup> are a special class of systems which can be described in terms of the exchange of valence particles between stable clusters. The variety

---

<sup>12</sup>It is important to stress that in the case of nuclei with an extra-neutron outside of the  $\alpha$ -centers, the analogy to molecules is a bit delicate. Indeed, the Born-Oppenheimer approximation

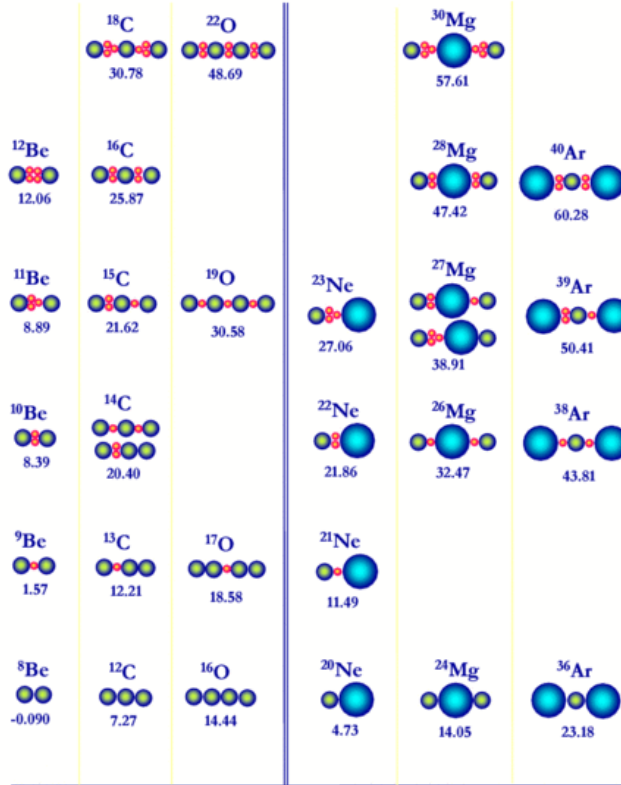


Figure 1.23: Modified Ikeda diagram to account cluster structures in the presence of extra neutrons. In analogy to the analogous diagram for self-conjugated nuclei (Figure 1.14) cluster configurations of neutron rich nuclei are shown in correspondence of the emission thresholds.

of cluster structures which can be in such a way obtained for light neutron-rich nuclei is shown in Figure 1.23. This diagram is called *modified Ikeda diagram*, since it provides a scheme analogous to the one proposed by Ikeda for self-conjugated nuclei (Figure 1.14) but extended to the case of systems with extra-neutrons. The evolution of clustering phenomena is here described as a function of the *neutron-richness* and the corresponding decay thresholds at which these structures should appear are also shown. Carbon and beryllium isotopes are remarkable examples, since they represent the simplest nuclear molecules constituted, respectively, by a two-center (*dimeric*) and a three-center (*trimeric*) configuration.

[84] treats the extra-electron as a rapidly moving particle with a negligible weight. This approximation is reasonably valid for molecules, where the mass ratio of the electron to nucleus is of the order of  $10^{-4}$ , but less valid in nuclear molecules, where the mass of the valence particle is of the same order of the ones of the  $\alpha$ -centers [36].

## 1.4 Applications of cluster models

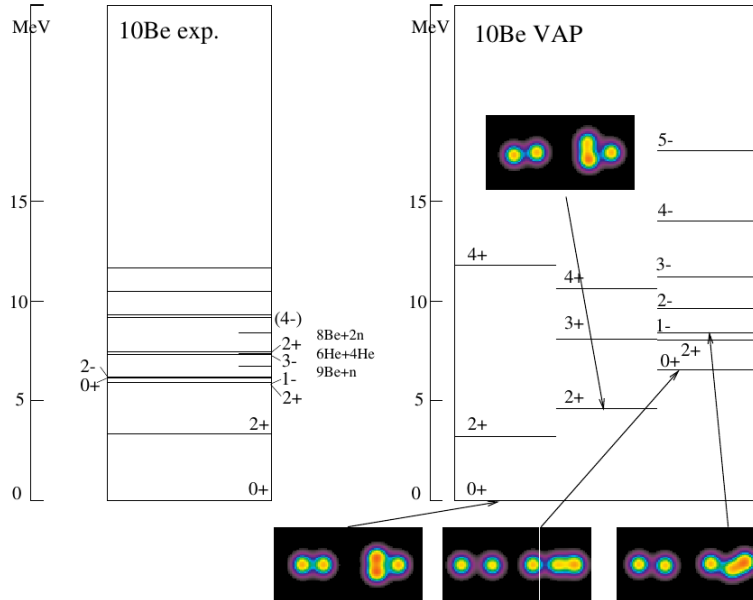


Figure 1.24: Excitation energy spectrum of  $^{10}\text{Be}$  as a result of the variational calculations after spin-parity projection (VAP) in the AMD framework (right) compared to the experimental one from [119] (left). Density distributions for protons (left) and neutrons (right) are shown for each state considered as band head of a rotational band, i.e.  $0_1^+$ ,  $2_2^+$ ,  $0_2^+$  and  $1_1^-$ . From [120].

The exchange of neutrons between  $\alpha$ -particle cores is an extremely important concept which gives the basis to the treatment of the beryllium isotopic chain [61, 116]. The glue-like effect played by extra neutrons can be quite well understood by looking at the case of  $^9\text{Be}$ . While  $^8\text{Be}$  is unbound against  $\alpha$ -decay,  $^9\text{Be}$  is stable. Giving the highly clustered nature of  $^8\text{Be}$ , one can assume a  $\alpha+n+\alpha$  structure for an appropriate description of  $^9\text{Be}$ . The presence of a further neutron makes it possible for the structure to be bound, and, furthermore,  $^9\text{Be}$  is the only stable beryllium isotope. Moreover, electron scattering on  $^9\text{Be}$  has suggested a high deformation of this nucleus, in possible agreement with a dimeric structure [117, 118].  $^{10}\text{Be}$  is a further interesting case since it can be described in terms of a symmetric nuclear *dimer* with a couple of valence neutrons [61]. The AMD model provides a good description of both shell model and molecular-like aspects, which often coexist within the domain of light neutron-rich nuclei. In order to theoretically study low-lying excited state of the  $^{10}\text{Be}$  isotope, Kanada-En'yo, Horiuchi and Doté [120] developed variational calculations after parity and total angular momentum projection in the framework of AMD. Results are shown in Figure 1.24 (right panel). Excited levels are grouped into rotational bands such as  $K = 0_1^+$ ,  $2_2^+$ ,  $0_2^+$  and  $1_1^-$ . For each state, here considered as band-head of rotational bands, proton (left) and neutron (right)

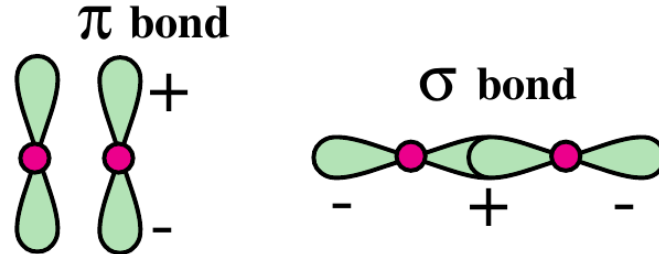


Figure 1.25: Schematic representation of molecular orbit  $\pi$  (left) and  $\sigma$  (right) in the case of two  $\alpha$ -centers. In the case of a  $\pi$  bond, the valence neutrons lie orthogonally to the axis of the two  $\alpha$ -cores, while in the  $\sigma$  bond they lie between the  $\alpha$ -cores. The inter-cluster separation is much more pronounced in the  $\sigma$  orbital. From [120].

density distributions are shown. They indicate quite deformed shapes, as a reflection of the  $2\alpha + 2n$  clustering structure. From an analysis of the single-particle wavefunctions of valence neutrons, the  $0_1^+$  as well as the  $2^+$  and  $4^+$  members of the ground band are found to be in the negative parity orbits, characterized to be  $\pi$  bonds (Figure 1.25 left). In this configuration, valence neutrons lie orthogonally to the  $\alpha$ -centers axis which, consequently, have a less pronounced separation. On the other hand, clustering phenomena are more evident in the  $1^-$  band and, especially, in the  $0_2^+$  band (built, respectively, on the 5.96 MeV  $1^-$  and the 6.18 MeV  $0^+$  states). The latter is characterized by significant components of positive parity orbits, which are analogous to the  $\sigma$  orbit (Figure 1.25 right). In this case valence neutrons are localized in the region in between the clusters, leading to a larger separation of clusters and a much more developed cluster nature. These findings are in agreement with the ones of von Oertzen [61], obtained with his dimer model of beryllium isotopes. More recent calculations have been performed by using a microscopic  $\alpha + \alpha + n + n$  model based on the molecular orbit (MO) model. Low-lying states of  $^{10}\text{Be}$  were predicted by using several configurations of valence neutrons built as combinations of three basic orbitals whose positions are determined variationally. These orbits originate from the low-lying  $3/2^-$ ,  $1/2^+$  and  $1/2^-$  states in  $^9\text{Be}$ . The  $^{10}\text{Be}$  ground state together with the  $0_3^+$  state appear to be characterized by the  $\pi$  orbit of the valence neutrons. The first is therefore, in analogy with Refs. [61, 120], rather strongly bound and it does not exhibit a particularly pronounced cluster separation. The second  $0^+$  state exhibits instead a large inter-cluster distance (as in the case of the AMD calculations [120]), being characterized by a  $\sigma$  orbit. The present experimental knowledge of  $^{10}\text{Be}$  cluster states and rotational bands is quite controversial [121], and it will be one of the subjects of the experimental investigation we will present in Section 2.1 of Chapter 2.

The above discussion concerning two-center nuclear molecules can be naturally extended to the case of multi-center molecules: the so-called nuclear polymers [61].

## 1.4 Applications of cluster models

---

Carbon isotopes represent the simplest cases of nuclear polymers, since they are constituted by 3  $\alpha$ -cores, and, therefore, they are a particularly significant example of nuclear molecules with more than 2 centers [10, 55]. Along the carbon isotopic chain, particularly remarkable examples are present among both *proton-rich* and *neutron-rich* isotopes. In the first case,  $^{11}\text{C}$  is considered an interesting isotope, being it constituted by a missing neutron with respect to the self-conjugated  $^{12}\text{C}$  configuration. Kanada and collaborators proposed a systematic study of its negative parity states within the AMD framework [122]. In this work, they succeeded for the first time in reproducing the  $3/2_3^-$  state of  $^{11}\text{C}$  at an excitation energy of 8.10 MeV. It has been linked to a structure quite similar to the one of the Hoyle state in  $^{12}\text{C}$ , and, therefore, considered as a gas-like state with a pronounced  $2\alpha + ^3\text{He}$  configuration, where the two  $\alpha$ -clusters and the  $^3\text{He}$  are weakly interacting and spatially extended. On the other hand, a  $5/2_2^-$  state, which is considered a non-cluster state, is found quite at the same excitation energy. An analysis of the *mirror nucleus*  $^{11}\text{B}$ , i.e. the nucleus obtained from  $^{11}\text{C}$  by exchanging of role protons with neutrons, has revealed a correspondence between states of these two nuclei with same properties. As an example, the above discussed  $3/2_3^-$  state of  $^{11}\text{C}$  is linked to the 8.56 MeV mirror state in  $^{11}\text{B}$ , which presents a diluted-gas structure [123, 124]. These states are summarized and compared to the ones of  $^{11}\text{B}$  in Figure 1.26, taken from [123]. Cluster states of  $^{11}\text{C}$  have been organized into rotational bands, and these results are discussed in [125, 126].

The first neutron-rich carbon isotope is the  $^{13}\text{C}$ . As in the case of  $^{11}\text{C}$ , its cluster-configurations are strongly linked to the ones of  $^{12}\text{C}$ , since it has only a further neutron outside of the  $^{12}\text{C}$  configuration [61]. In the case of  $^{13}\text{C}$ , a quite large number of theoretical papers have been published regarding its cluster structure. Milin and von Oertzen [127] focused on *parity doublets*, i.e. couples of rotational bands with opposite parity and the same structure. These bands reflect the intrinsic asymmetry of the underlying structure ( $^9\text{Be} + \alpha$  or  $\alpha + \alpha + \alpha + n$ ). They proposed two opposite parity bands, the  $K^\pi = 3/2^-$  built on the 9.897 MeV state and the the  $K^\pi = 3/2^+$ , which has the 11.080 MeV as band-head, based on the  $^9\text{Be}(3/2^-, g.s.) + \alpha$  structure. All the states belonging to these bands, i.e. the  $5/2^\pm$ ,  $7/2^\pm$ ,  $9/2^\pm$  and  $11/2^\pm$  members<sup>13</sup> (see Figure 1.27), are found to be populated in reactions involving  $\alpha$ -transfer. This evidence allowed the authors to conclude that they are strongly characterized by a pronounced  $\alpha$ -cluster nature. The properties of these states have also been characterized on the basis of a molecular orbital model. The band heads are found to coincide with the two lowest states based on the three-center molecular orbital approach. From an analysis of the moment of inertia they suggest a linear chain arrangement of the three  $\alpha$ -particles bound by a covalent neutron. States corresponding to the  $^9\text{Be}(1/2^+, 1.68 \text{ MeV}) + \alpha$  structure are predicted as

---

<sup>13</sup>Many of the  $J^\pi$  assignments, especially those for high- $J$  values, are very tentative and often subject of debate. In Section 2.4 we will report new results on  $^{13}\text{C}$  spectroscopy at energies above the  $\alpha$  threshold.

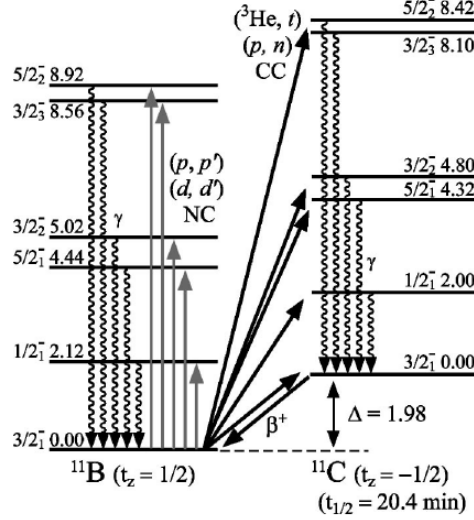


Figure 1.26: Comparison between the mirror nuclei  $^{11}\text{C}$  (right) and  $^{11}\text{B}$  (left) low-lying states from [123]. An almost perfect correspondence is reported between couples of states. As an example, the  $3/2_3^-$  state of  $^{11}\text{C}$ , lying at 8.10 MeV, has the 8.56 MeV  $3/2_3^-$  as a correspondent in  $^{11}\text{B}$ . They are both characterized by a diluted-gas cluster three-center configuration, respectively  $2\alpha + {}^3\text{He}$  and  $2\alpha + t$ .

well and they have been linked by the authors to possible triangular configurations. A doublet of  $J^\pi = 1/2^\pm$  experimentally observed states lying, respectively, at 10.996 MeV and 8.86 MeV are considered as candidates for this structure. Finally, they suggested that the distinction between linear and triangular fashions in the  $^{13}\text{C}$  cluster arrangement should be linked to considerations of  $\sigma$  and  $\pi$ -orbitals for the ground and first excited states of  $^9\text{Be}$ , in which the valence neutron occupies two different and orthogonal configurations.  $^{13}\text{C}$  low-lying states have been also object of microscopic  $3\alpha$ - $n$  calculations [128–131].

High energy  $^{13}\text{C}$  rotational bands, based on its  $3\alpha$  cluster structure, were predicted by Furutachi and co-workers [129] via a  $3\alpha + n$  cluster model based on the GCM wave-function. Their model is able to reproduce the energy of the ground state of  $^{13}\text{C}$  but not the energies of the  $5/2_1^-$  and  $7/2_1^-$ , which belong as well to the ground state rotational band and which are probably not consistent with the model assumption of  $3\alpha$ -clusters. Two excited rotational bands are predicted to be built on  $3/2_2^-$  (11.4 MeV) and  $3/2_3^-$  (14.5 MeV) states around the threshold energy, called, respectively  $K^\pi = 3/2_2^-$  and  $3/2_3^-$  (see Figure 1.28). Both bands appear as characterized by large moment of inertia and a pronounced cluster configuration. The  $K^\pi = 3/2_2^-$  band, which is linked by the authors to the  $3/2^-$  band of [127] (blue open squares in figure) corresponds to a *bent*  $3\alpha$  linear chain configuration, more compact than the gas-like configurations predicted by the same model in the case

## 1.4 Applications of cluster models

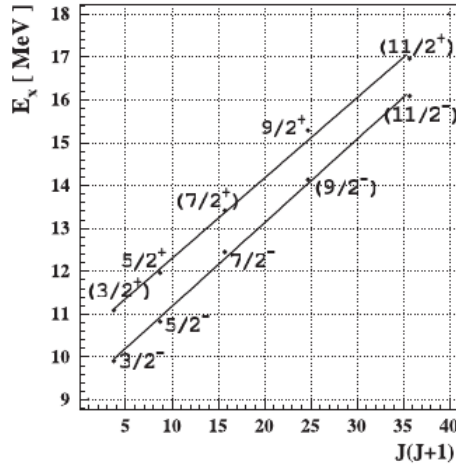


Figure 1.27: Parity split rotational bands ( $K = 1/2^\pm$ ) based on the  ${}^9\text{Be}(3/2^-, g.s.) + \alpha$  structure, as suggested in [127] on the basis of a three-center molecular orbital model. Energy of their rotational members is plotted as a function of  $J(J + 1)$ . They correspond to linear chain arrangements of 3  $\alpha$ -cores with a valence neutron. From [127].

of  ${}^{12}\text{C}$ . A  $1/2_2^-$  state (yellow circle in Figure 1.28) is finally found around the  $3\alpha + n$  threshold (12.221 MeV), but it is not linked to the previously discussed rotational bands since it is not described by a  $3\alpha + n$  structure.

The possible existence of  $1/2$  states in  ${}^{13}\text{C}$  based on a  $3\alpha$  nature is extremely important, since they can be possibly related to the coupling of a valence neutron to the Hoyle state in  ${}^{12}\text{C}$ . AMD calculations with the constraint of the harmonic oscillator quanta (HON) pointed out that, differently from the  $1/2_2^-$  state predicted in [129], the  $1/2_3^-$  ( $E_x \approx 18.0$  MeV) has a strong  $3\alpha + n$  structure, giving rise to a linear chain band ( $K^\pi = 1/2^-$ ) with a large deformation [130]. The  $1/2_1^+$  state identified at 14.9 MeV is associated to the  $K^\pi = 1/2^+$  rotational band. The  $K = 1/2^\pm$  bands form a parity doublet which reflects the asymmetric intrinsic structure of  ${}^{13}\text{C}^*$  seen as a nuclear molecule. A  $1/2_2^+$  state, lying at about 15.7 MeV excitation energy, is associated to a large  ${}^{12}\text{C}(0_2^+) \otimes n(s_{1/2})$  spectroscopic factor. This state can be interpreted as the *Hoyle analog* state in  ${}^{13}\text{C}$ , i.e. as the  $0_2^+$  state of  ${}^{12}\text{C}$  accompanied by a valence neutron in s-wave. This state has a larger radius (2.78 fm) than the one of the ground state of  ${}^{13}\text{C}$  (2.52 fm), further confirming its analogous nature to the Hoyle state. However, it should be noted that such a gas-like structure is distorted by the presence of the valence neutron, which makes the radius smaller than the one observed for the Hoyle state (2.90 fm). Another possible Hoyle analog state is found, by means of  $3\alpha + n$  OCM calculations [131], at an excitation energy of about 14.9 MeV. This state, named as  $1/2_5^+$  by the authors of [131], is described by a gas-like configuration with an extremely large radius (4.3fm).

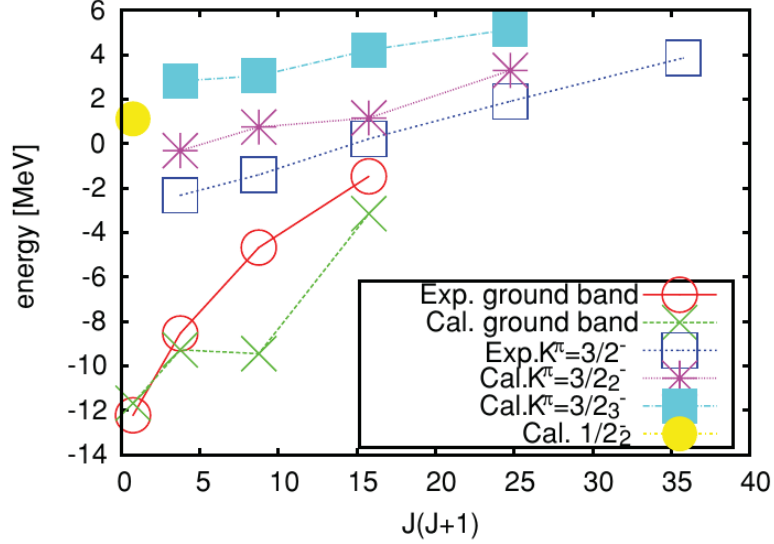


Figure 1.28: Energy of the calculated  $^{13}\text{C}$  rotational bands, computed from the  $3\alpha + n$  decay threshold (12.221 MeV) as a function of the  $J(J+1)$ . The one labeled as  $\text{Exp. } K^\pi = 3/2^-$  corresponds to the one suggested by the Ref. [127] and shown in Figure 1.27. From [129].

It is characterized by a dominant ( $\approx 0.6$ )  $^{12}\text{C}(0^+_{2}) \otimes n(s_{1/2})$  spectroscopic factor, as observed in the Figure 1.29.

The last example here discussed is the case of  $^{16}\text{C}$ . Its possible cluster molecular-like configurations are constituted by a symmetric three-center structure of the type  $3\alpha + 4n$ . This structure is the most promising candidate for a stable linear-chain configuration because its stability against the bending motion was pointed out by molecular-orbital model calculations [133]. Despite its importance, our present experimental knowledge of  $^{16}\text{C}$  is extremely poor [134], and only a few experiments concerning its cluster configurations are reported in the literature and with extremely low statistics [135, 136]. Very recently, a theoretical calculation, performed with the AMD code, has been published [132]. Two kind of  $3\alpha$  structures are suggested, the one with the  $\alpha$ -clusters forming an isosceles triangular configuration and the other where they are arranged in a linear-chain, see Figure 1.30. The latter is particularly stable thanks to the role of the valence neutrons. In the case of the triangular configuration, the surrounding valence neutrons are found to occupy the  $sd$  shell, while the linear-chain configurations are qualitatively understood in terms of  $3/2^-_{\pi}$  and  $1/2^-_{\sigma}$  molecular orbits, as predicted by the molecular-orbital model [133]. Such states have been organized by the authors of Ref. [132] in rotational bands as in Figure 1.31. Triangular and linear rotational bands are here found to be built, respectively, on the 8.0 MeV and 15.5 MeV states. The latter is characterized by hyper-deformation. Only few of these states (mainly at low energies, represented by the open boxes in

## 1.5 Techniques for the study of clusters in nuclei

---

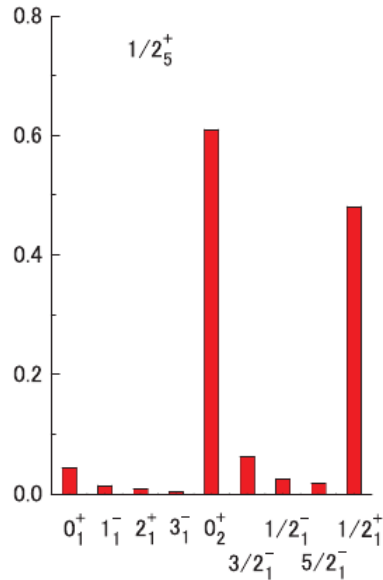


Figure 1.29: Spectroscopic factors of the  $^{12}\text{C}(J_C^\pi) + n$  ( $J_C^\pi = 0_1^+, 1_1^-, 2_1^+, 3_1^-, 0_2^+$ ) and  $^9\text{Be}(J_9^\pi) + \alpha$  ( $J_9^\pi = 3/2_1^-, 1/2_2^-, 5/2_1^-, 1/2_1^+$ ) channels for the  $1/2_5^+$  state in  $^{13}\text{C}$ ,  $E_x = 14.9$  MeV. The strong ( $\approx 0.6$ )  $0_2^+$  configuration indicates that this state is a candidate to be the  $^{13}\text{C}$  Hoyle analog state. From [131].

the figure) have been experimentally observed and therefore new investigations are needed to understand the clustering nature of this isotope, especially close to the  $^4\text{He} + ^{12}\text{Be}$  (13.808 MeV) and  $^6\text{He} + ^{10}\text{Be}$  (16.505 MeV) thresholds.

## 1.5 Techniques for the study of clusters in nuclei

Clustering phenomena in light nuclei can be experimentally probed by investigating their *spectroscopy*. The spectroscopy of a nucleus consists in the knowledge of the characteristics of its excited states, i.e.  $E_x$ ,  $J$ ,  $T$ ,  $\pi$ ,  $C^2S$ , where  $E_x$  represents the excitation energy of the state,  $J$  is the total angular momentum,  $T$  is the isospin,  $\pi$  is the parity of the corresponding wave-function, connected to its spatial symmetry, and  $C^2S$  are the so-called *spectroscopic factors*. The latter are the square modules of the *spectroscopic amplitudes*, which are formally connected, as better explained below, to the decompositions of the nuclear wave-function in each possible nuclear configuration.

These information can be obtained by means of different types of experiments which involve nucleus-nucleus collisions at low and intermediate energies. Basically, they can be divided into two principal categories: *compound nucleus reactions*, i.e. reactions which involve the *formation* of a resonant state as a intermediate stage,

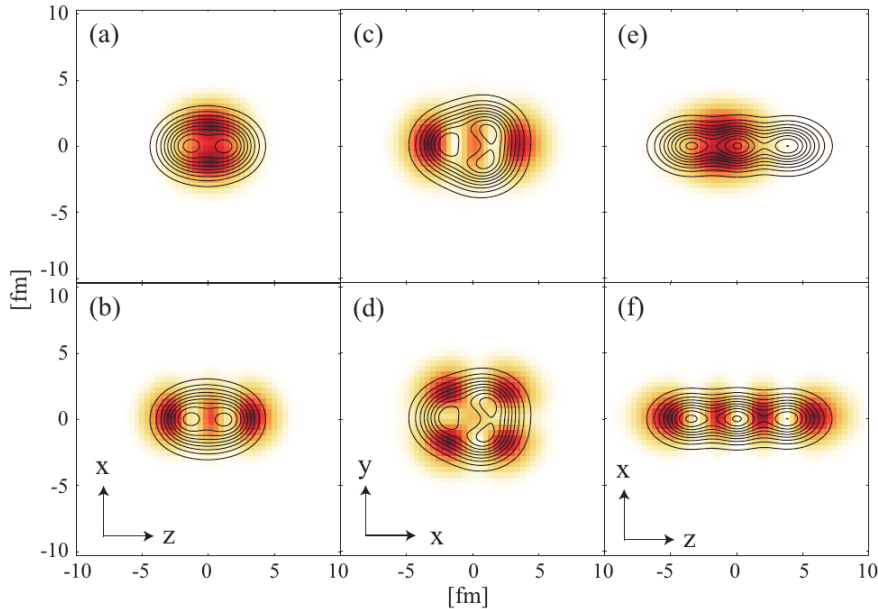


Figure 1.30: Density distributions of  $^{16}\text{C}$  valence neutrons and protons as computed by AMD calculations [132] for the ground state (a,b), the triangular configuration (c,d) and the linear chain states (e,f). The contour lines represent the proton density, while neutron densities are represented by the color plots. The lower panels show the most weakly bound two valence neutrons, while the other two are shown in the upper ones. From [132].

and reactions involving the *production* of a resonance as a final product of the collision, whose properties can be investigated by detecting the corresponding decay products (particle-particle and multi-particle *correlations*). The first case is discussed in paragraph 1.5.1, where we will give the basic ideas of the treatment of resonances in compound nucleus reactions. A powerful method for the interpretation of such experimental data, and their link to the formal quantities given by the theory of resonances, is discussed in paragraph 1.5.2. Finally, particle-particle and multi-particle correlation techniques, and their link to clustering aspects, are discussed in paragraph 1.5.3.

### 1.5.1 Compound nucleus reactions

High-precision experiments involving the formation of a compound nucleus represent a powerful way to probe clustering in nuclei<sup>14</sup>. When a projectile nucleus  $a$

<sup>14</sup>The concept of compound nucleus reaction was firstly introduced by Niels Bohr. According to the Bohr idea, when the bombarding particle has sufficiently low energy, it can be absorbed by the target nucleus, and it shares its momentum with the other nucleons of the target. The kinetic

## 1.5 Techniques for the study of clusters in nuclei

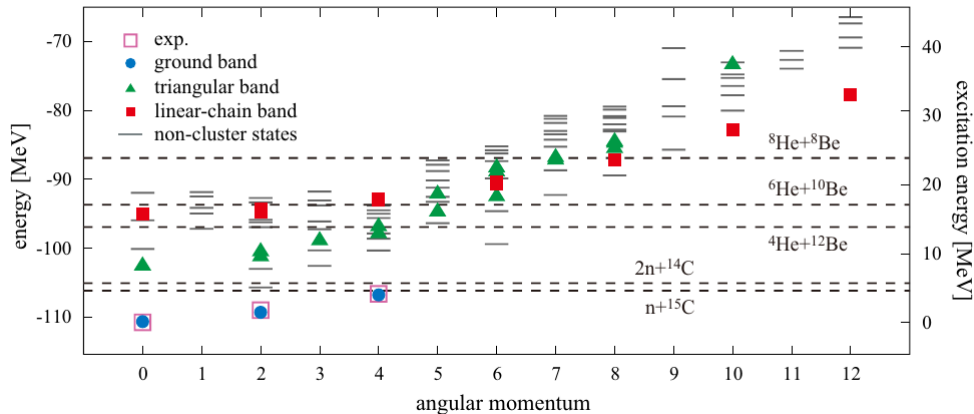


Figure 1.31: Calculated positive parity energy levels of  $^{16}\text{C}$  as a function of their angular momentum  $J$ , up to  $J^\pi = 12^+$ , as obtained in [132] with the AMD model. Open boxes indicate experimentally observed states. Ground, triangular and linear-chain bands are represented, respectively, by circles, triangles and filled squares.

impinges on a target nucleus  $A$  at low energy, the formation of a resonant state of the compound system  $C$  can occur. It can subsequently decay in any of the *open*<sup>15</sup> channels. Assuming that the formation of the compound nucleus  $C$  occurs via an isolated resonance, and that there are only two open channels,  $a$  and  $b$  (the latter corresponds to the emission of the *ejectile*  $b$  and the *residual*  $B$ , see the Figure 1.32), the expression of the *cross section*  $\sigma$  contains the properties of the excited state of the compound nucleus through the logarithmic derivative  $f_l$  of the radial wave-function  $u_l(r)$  at the nuclear boundary  $r = R$ . The expression of the radial wave-function, solution of the Schrödinger equation outside of the nuclear surface, has the general form (see Refs.[36, 138] for a complete derivation):

$$\begin{aligned} u_l(r) &= Au_l^+(r) + Bu_l^-(r) \\ &= Ae^{-i\delta_l}[G_l(r) + iF_l(r)] + Be^{-i\delta_l}[G_l(r) - iF_l(r)], \quad r > R \end{aligned} \quad (1.47)$$

where  $u_l^+$  and  $u_l^-$  correspond, for large distances, respectively to the incoming and outgoing spherical wave representing the asymptotic behaviour of the nuclear reaction. The quantity  $\delta_l$  is the Coulomb *phase shift*. In the case of  $l = 0$  neutrons,  $F_l = krj_l(kr)$  and  $G_l = kr\eta_l(kr)$  represents spherical Bessel and Neumann functions. For a charged particle with a generic orbital angular momentum  $l$ , they correspond, respectively, to the *regular* and *irregular* Coulomb wave-functions. Particularly important in this frame are the real quantities  $S_l$  and  $P_l$ , which are called

energy, as well as the binding energy, of the incoming particle will be converted into an excitation energy of the system formed by the fusion of target + projectile, the so-called *compound nucleus* [137].

<sup>15</sup>*Open* means that this channel fulfils all the conservation laws characterizing the strong interaction: energy, momentum, angular momentum, parity, charge, isospin, barionic number.

## Chapter 1. Introduction: Clusters in Nuclear Physics

---

respectively *shift factor* and *penetration factor*. They are completely determined by the boundary conditions of  $f_l$  outside the nucleus:

$$\begin{aligned} f_l &= R \left( \frac{1}{u_l^+(r)} \frac{du_l^+(r)}{dr} \right)_{r=R} \\ &= R [G_l(dG_l/dr) + F_l(dF_l/dr) + iG_l(dF_l/dr) - iF_l(dG_l/dr)] \\ &\equiv S_l + iP_l \end{aligned} \quad (1.48)$$

where

$$\begin{aligned} S_l &= R \left[ \frac{F_l(dF_l/dr) + G_l(dG_l/dr)}{F_l^2 + G_l^2} \right]_{r=R} \\ P_l &= R \left( \frac{k}{F_l^2 + G_l^2} \right)_{r=R} \end{aligned} \quad (1.49)$$

These quantities depend on the wave-number  $k$  in the center of mass system, the channel radius  $R$  and the orbital angular momentum  $l$ . For  $l = 0$  neutrons, for example, being  $F_0 = \sin(kr)$  and  $G_0 = \cos(kr)$  [139], they give  $P_0 = kr$  and  $S_0 = 0$ , which means that the shift factor vanishes in absence of a barrier. The reaction cross section close to an isolated resonance can be derived in terms of  $P_l$  and  $S_l$  by means of the *Breit-Wigner* formula:

$$\sigma = (2l + 1) \frac{\pi}{k^2} \frac{\Gamma_a \Gamma_b}{(E - E_r)^2 + \Gamma_r^2/4} \quad (1.50)$$

where  $\Gamma_a$  and  $\Gamma_b$  are the so-called *partial widths* for, respectively, the entrance channel and the exit channel of the reaction and they are equal to

$$\begin{aligned} \Gamma_a &\equiv - \frac{2(P_l(E))_a}{(\partial f_l / \partial E)_{E_r, q=0}} = 2P_l^a(E) \gamma_a^2 \\ \Gamma_b &= 2P_l^b(E) \gamma_b^2 \end{aligned} \quad (1.51)$$

In the equations 1.51,  $P_l^a(E)$  and  $P_l^b(E)$  represent, respectively, the penetrability factors for the entrance and the exit channel. The penetrability factor appears in the definition of the partial widths since a particle has to penetrate the barrier in order for a reaction to occur.  $\gamma_a^2$  and  $\gamma_b^2$  are the so-called *reduced widths*, and they are easily obtained via Eqs. 1.51 once the contributions due to the penetrability factor are removed from the partial width value. The cross section depends on the properties of nuclear interior through these numbers. Furthermore, they are connected to the above mentioned spectroscopic factors  $C^2S$ , whose meaning will be discussed below.

The total width of the resonance, which corresponds in first approximation to the width of the observed resonance in the measured cross section (see the sketch of Figure 1.32) and which is linked to the inverse of the resonance lifetime, is given by the sum of each partial width:

$$\Gamma_r = \Gamma_a + \Gamma_b \quad (1.52)$$

## 1.5 Techniques for the study of clusters in nuclei

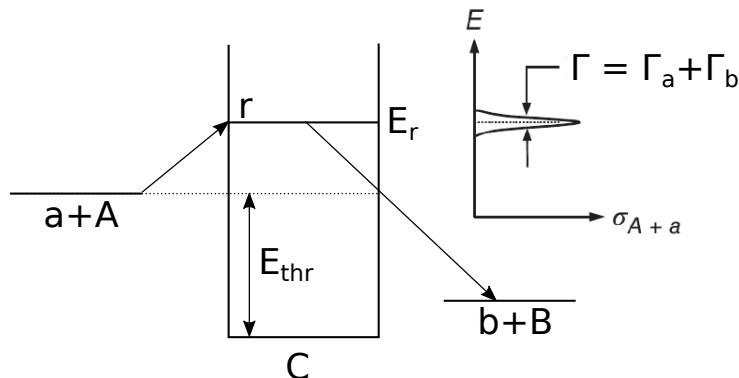


Figure 1.32: Level scheme of a compound nucleus reaction of the type  $a + A \longrightarrow C^* \longrightarrow b + B$ . The resonance  $r$  is populated at an excitation energy  $E_r$ . The behaviour of the cross section for the isolated resonance is qualitatively shown in the right part. The width  $\Gamma$  of the level is the Full Width at Half Maximum (FWHM) of the resonance in the cross section as a function of the energy and it corresponds to the sum of all the partial widths which contribute to the decay of the state  $\Gamma = \Gamma_a + \Gamma_b$ .

Finally, a special attention must be given to the resonance energy  $E_r$ . It is defined as:

$$E_r = E_r^0 + \frac{S_l(E)}{(\partial f_l / \partial E)_{E_r^0, q=0}} = E_r^0 - S_l(E) \gamma_a^2 \quad (1.53)$$

which means that the observed resonance energy, appearing in the formulation of the cross section in the proximity of an isolated resonance, is shifted respect to the formal energy (or *level energy*)  $E_r^0$  of a quantity  $-S_l(E) \gamma_a^2$ . This fact reflects the presence of a barrier in the entrance channel.

To understand how the above discussed quantities are linked to the nuclear structure and, specifically, to clustering phenomena, a few details on the treatment of particle emission from a nuclear state have to be given. Let us consider, as an example, a possible state of  $^{57}\text{Fe}$ , whose wave function  $\Psi_1$  corresponds to the ground state of  $^{56}\text{Fe}$  with a further neutron in the  $3s_{1/2}$  orbit, i.e.

$$\Psi_1(^{57}\text{Fe}) = \Psi(^{56}\text{Fe}_{\text{gs}}) \Psi(3s_{1/2}) \quad (1.54)$$

Being the  $^{56}\text{Fe}$  an even-even nucleus its ground state is  $0^+$  and thus the state of equation 1.54 would have  $J^\pi = 1/2^+$ . This represents a highly excited state of  $^{57}\text{Fe}$  with an unbound neutron, which can be released in a nucleon-emitting process like:

$$^{57}\text{Fe} \longrightarrow ^{56}\text{Fe}_{\text{gs}} + n(3s_{1/2}) \quad (1.55)$$

Calling  $v_i$  its velocity within the nucleus and  $R$  the radius of the nucleus, the extra-neutron will reach the nuclear surface in a time of the order of  $R/v_i$ . In correspon-

## Chapter 1. Introduction: Clusters in Nuclear Physics

---

dence of the surface, it will experience a change in the potential which can reflect it again inside the nucleus. It is possible to demonstrate (see [140]) that on average it will be reflected a number of times equal to  $v_i/4v_e$ , where  $v_e$  is the velocity of the emitted outgoing neutron. The average time required for a neutron to be emitted is thus:

$$\tau_0 \approx \frac{R}{v_i} \frac{v_i}{4v_e} = \frac{R}{4v_e} \quad (1.56)$$

which is usually called *Wigner limit* and which results in a decay rate of  $\lambda_0 = \frac{1}{\tau_0}$ . If one now considers all the possible configurations of the type of equation 1.54 leading to a  $J^\pi = 1/2^+$  state, we have to write:

$$\begin{aligned} \Psi_i(^{57}\text{Fe}) = & c_{i1} \Psi(^{56}\text{Fe}_{\text{gs}}) \Psi(3s_{1/2}) + c_{i2} \Psi(^{56}\text{Fe}_{1-}) \Psi(2p_{3/2}) + c_{i3} \Psi(^{56}\text{Fe}_{2-}) \Psi(2p_{3/2}) + \\ & c_{i4} \Psi(^{56}\text{Fe}_{0-}) \Psi(2p_{1/2}) + c_{i5} \Psi(^{56}\text{Fe}_{1-}) \Psi(2p_{1/2}) + \dots \end{aligned} \quad (1.57)$$

This represents a wave-function expansion of a generic  $1/2^+$  state  $i$  of  $^{57}\text{Fe}$  in the  $^{56}\text{Fe} + n$  configurations. All these configurations dynamically mix in such a way that the nucleus will spend some time in each of them. The decay partial width of the state  $i$  via neutron emission will be:

$$\Gamma_i = \hbar \sum_k \lambda_{0k} c_{ik}^2 \quad (1.58)$$

where  $\Gamma_i = \hbar \lambda_i$ ,  $\lambda_{0k}$  is the decay rate of the  $k$ -th configuration (see equation 1.56) and the factors  $c_{ik}^2$ , the square of the amplitudes  $c_{ik}$ , are equivalent to the fraction of the time the nucleus spends in the  $k$ -th configuration. The sum of all these amplitudes gives:

$$\theta_i^2 = \sum_k |c_{ik}|^2 \quad (1.59)$$

which corresponds to the *dimensionless* reduced partial widths, i.e. the ratio of the above discussed decay partial widths to the ones at the Wigner limit  $\theta_i^2 = \frac{\gamma_i^2}{\gamma_{W_i}^2}$ . From the nature of the factors  $c_{ik}$  defined in equation 1.57, it follows the *sum rule*:

$$\sum_i \theta_i^2 \leq 1 \quad (1.60)$$

The consequence of equation 1.60 is that, for a generic state  $i$  decaying via neutron emission,  $\theta_i^2 \leq 1$ . If the structure of the state  $i$  is fully dominated by a particular single-particle configuration, like, in our example,  $^{56}\text{Fe} + n$ , it will have  $\theta_i^2 = 1$  and one says that the corresponding decay partial width of equation 1.58 is at the *Wigner limit*. The investigation of the particle emission rate of a nuclear state, and thus of the corresponding partial width, is therefore useful to probe if a particular configuration is dominant in the corresponding structure. This is the case of clustering phenomena. So it is possible to claim a particular cluster configuration if one

## 1.5 Techniques for the study of clusters in nuclei

---

observes, when the resonance is populated by a compound nucleus reaction, a decay partial width in the cluster channel characterized by having a significant fraction of the Wigner limit.

The above subject not only applies to the case of  $l = 0$   $X + n$  configurations (which is a simplified case because of the absence of any barrier), but also to any other possible configuration. Its extension to the case of charged particle emission with arbitrary  $l$  values (see Ref. [138, 140] for more details) can be obtained in the following way. Let us assume that the compound nucleus is configured in the resonance  $r$  and that there is only one open channel  $c$ . The corresponding wave-function, which contributes to the emission in the channel  $c$  will be, for the above discussion, a linear combination of radial single-particle wave-functions  $u_{rk}^c$ , each of them contributing to a particular configuration of the compound system in the decomposition  $c$ <sup>16</sup>:

$$\Psi_r(\vec{R}) = \left[ \sum_k c_{rk} u_{rk}^c(R) \right] \frac{Y_{lm}(\theta, \varphi)}{R} \quad (1.61)$$

The partial width  $\Gamma_c$  of the level  $r$  can be determined as the probability flux of the particle through the only open channel  $c$ . This number can be calculated by integrating the quantum-mechanical current [141], through a sphere of radius  $R$ , in the whole solid angle:

$$\Gamma_r^c = \hbar \int_{d\Omega} R^2 j d\Omega = \hbar \int_{d\Omega} R^2 \frac{\hbar}{2im} \left( \Psi_r^* \frac{\partial \Psi_r}{\partial r} - \frac{\partial \Psi_r^*}{\partial r} \Psi_r \right) d\Omega \quad (1.62)$$

With some algebra (see Ref.[138]) one obtains:

$$\Gamma_r^c = \sum_k 2 \frac{\hbar^2}{mR^2} P_l^c(E) C^2 S \varphi_{ck}^2 \quad (1.63)$$

with:

$$C^2 S = c_{rk}^2 \quad (1.64)$$

$$\varphi_{ck}^2 = \frac{R}{2} |u_{rk}^c(R)|^2 \quad (1.65)$$

The first are called *spectroscopic factors*<sup>17</sup>, which are the square of the *spectroscopic amplitudes* used in the linear combination of equation 1.61, while the second represent the decay rate in the channel  $c$  from each configuration  $k$ . The spectroscopic

---

<sup>16</sup>A channel (decomposition  $c$ ) is typically formed by two particles:  $b + Y$ . The *particular configuration of a given decomposition* corresponds to solve the Schrödinger equation for the single-particle Hamiltonian describing the motion of particle  $b$  within the well generated by  $b + Y$ . This equation admits several (discrete) solutions that will represent a *particular configuration* of the decomposition  $c$  ( $\equiv b + Y$ ).

<sup>17</sup> $C^2$  represents the square of an isospin Clebsch-Gordan coefficient, while  $S$  is the actual spectroscopic factor. In the literature anyway it is usual to indicate with *spectroscopic factor* the whole product  $C^2 S$ .

factor, which gives the structure configuration of a state, depends on the many-nucleon structure of the level  $r$  and it is a measure of the probability that a compound state  $r$ , with a cluster configuration  $c$ , can be described by the single-particle configuration  $k$ . From the equation 1.63 it turns out that the partial width of the decay of a state in a particular channel is a product of three factors: (i) the probability that the nucleons will arrange themselves in the configuration corresponding to the final state ( $C^2S$ ), the probability of the particle to be emitted ( $\propto |u_{rk}^c(R)|^2$ )<sup>18</sup>, and the probability of the particle to penetrate centrifugal and Coulomb barrier ( $R/2P_l^c(E)$ ).

### 1.5.2 R-matrix theory

In a compound nucleus reaction, the *R-matrix* theory can be used in order to extract, from the experimental data of cross sections, spectroscopic properties of nuclear states like  $E_x$ ,  $J$ ,  $\pi$ ,  $\gamma_c^2$ . The last, in particular, can be used to access the spectroscopic factors  $C^2S$  and, consequently, to prove clustering phenomena in such systems. While a detailed treatment of *R-matrix* theory can be found in Ref. [143, 144], a simplified description is given in this paragraph.

This method was firstly introduced by Wigner and developed by Wigner and Eisenbud [145, 146]. It aims to describe the observed reactions in terms of parameters such as the radius  $a$  of a *nuclear sphere*, the energy levels and the reduced widths, without describing the microscopic structure inside the compound nucleus. These are normally considered as free parameters for best-fit procedures. No assumptions are indeed made concerning the form of the wave-functions inside the nuclear *sphere*, and only their properties at the surface  $r = a$  are employed. These properties are expressed in terms of the logarithmic derivatives of the wave-functions at the boundaries, which form the matrix element of the *R-matrix*. The theory is therefore very general, since it is free of any physical model, except the assumption regarding the formation of a compound nucleus. The *R-matrix* theory allows to extend the previously discussed Breit-Wigner formula of the cross section to a more general formulation which includes an arbitrary number of channels and an arbitrary number of resonances, taking into account the interference effects between resonances. The *R-matrix* relates the value of the wave-function in the internal region to its derivative at each channel entrance. It is defined, for an arbitrary number of channels  $c, c'$ , as:

$$\mathfrak{R}_{c,c'} \equiv \sum_r \frac{\gamma_{rc'} \gamma_{rc}}{E_r - E} \quad (1.66)$$

the definition 1.66 connects the elements of the *R-matrix* explicitly to the energy, since  $\gamma_{rc}$  and  $E_r$  are energy-independent parameters. The poles of the *R-matrix* occur at each value  $E_r$  of energy and each of the elements  $\mathfrak{R}_{c,c'}$  represents a real

---

<sup>18</sup>This quantity, usually set to unity in simplified calculations [142], can be more precisely evaluated by solving the Schrödinger equation for a Wood-Saxon potential. See [138] for details.

## 1.5 Techniques for the study of clusters in nuclei

---

number. The position of the poles is furthermore independent on the channels  $c$  and  $c'$ . In the framework of  $R$ -matrix, a channel is identified by the quantum numbers  $\{\alpha(I_1 I_2) s l, J M\}$ , where  $\alpha(I_1 I_2)$  represent a specific state of excitation  $\alpha$  of a specific pair of nuclei 1 and 2, having spins  $I_1$  and  $I_2$ ,  $\vec{s} = \vec{I}_1 + \vec{I}_2$  is the channel spin,  $l$  is the orbital angular momentum of their relative motion and  $\vec{J}$  and  $M$  are the total spin and its component along a quantization axis. For the entrance channel consisting of a projectile and a target nucleus, one can set  $\vec{I}_1 = \vec{j}_p$  and  $\vec{I}_2 = \vec{j}_t$ , consequently:

$$\vec{J} = \vec{l} + \vec{j}_p + \vec{j}_t \quad (1.67)$$

Because of the degeneracy of these values, there are  $(2l+1)(2j_p+1)(2j_t+1)$  different sets of spin orientations with the same probability. The cross section has therefore to be multiplied by the relative probability that projectile and target will be found to have a total spin  $J$ :

$$g(J) = \frac{2J+1}{(2l+1)(2j_p+1)(2j_t+1)} \quad (1.68)$$

The cross section, as well as the phase shifts, can be derived from the  $R$ -matrix by using the boundary conditions and the energy independent parameters  $\gamma_{rc}$ . As an example, in the case of an isolated resonance and an arbitrary number of channels, one can derive the so-called *generalized one-level Breit-Wigner formula* for a generic reaction leading from the  $\alpha$  channel to the  $\alpha'$ :

$$\sigma(\alpha, \alpha') = \frac{\pi}{k^2} \frac{2J+1}{(2j_p+1)(2j_t+1)} \frac{(\sum_{ts} \Gamma_{rc})(\sum_{t's'} \Gamma_{rc'})}{(E - E_r - \Delta_r)^2 + \Gamma_r^2/4} \quad (1.69)$$

where  $\Gamma_{rc} = 2P_c(E)\gamma_{rc}^2$  are the partial widths,  $\Gamma_r(E) = \sum_c \Gamma_{rc}(E)$  is the total width of the resonance  $r$  and  $\Delta_r(E) = \sum_c \Delta_{rc}(E)$  is the total level shift. The latter is the superposition of partial level shifts, which appeared in the formulation of the single channel Breit-Wigner of paragraph 1.5.1:  $\Delta_{rc}(E) = -[S_c(E) - S_c(E_r)]\gamma_{rc}^2$ . Both penetration and shift factors are referred to the *interaction radius*. Normally it is chosen to be as small as possible so that the quantities of the resonance theory contain primarily information on the nuclear interaction. For this reason, it is commonly taken equal to the smallest separation distance of the nuclear pair for the reaction to occur, i.e. the *channel radius*  $R = r_0(A_t^{1/3} + A_p^{1/3})$ , with a radius parameter lying in the range  $r_0 = 1.0$ -1.5 fm. A simplification of equation 1.69 was introduced by Thomas in 1951, observing that since the shift factor  $S_c(E)$  depends only weakly on the energy, it could have been expanded in the following way:

$$E - E_r - \Delta_r \approx (E - E_r) \left[ 1 - \left( \frac{d\Delta_r}{dE} \right)_{E_r} \right] \quad (1.70)$$

By using the result of equation 1.70, the commonly used formulation of equation 1.69, which reproduces the cross section of the  $\alpha \longrightarrow \alpha'$  cross section for an isolated

resonance  $r$ , becomes:

$$\sigma(\alpha, \alpha') = \frac{\pi}{k^2} \frac{2J+1}{(2j_p+1)(2j_t+1)} \frac{(\sum_{ls} \Gamma_{rc}^o)(\sum_{l's'} \Gamma_{rc'l}^o)}{(E - E_r)^2 + \Gamma_r^2/4} \quad (1.71)$$

where the *formal widths*  $\Gamma_{rc}$  have been replaced by the *observed widths*  $\Gamma_{rc}^o$ :

$$\Gamma_{rc}^o \equiv \frac{\Gamma_{rc}}{1 - (d\Delta_r/dE)_{E_r}} = \frac{\Gamma_{rc}}{1 - \left( \sum_{c''} \gamma_{rc''}^2 \frac{dS_{c''}}{dE} \right)_{E_r}} \quad (1.72)$$

which applies also to the reduced widths. The difference between formal and observed width is much more important as the reduced width of the state becomes large.

Operatively, one uses multi-channel multi-level  $R$ -matrix formulations like [147] to find the set of parameters  $E_x$ ,  $J$ ,  $\pi$ ,  $\gamma_c^2$  which reproduces the experimental trend of the cross section for each channel and each process considered. Since clustering phenomena are related to states having pronounced (i.e. close to the Wigner limit) partial widths for  $\alpha$ -emission ( $\Gamma_\alpha$ ), the study of compound nucleus reaction channels which involve the emission of an  $\alpha$ -particle, like *resonant elastic scattering* (RES) ( $\alpha, \alpha$ ), *resonant inelastic scattering* ( $\alpha, \alpha'$ ), ( $p, \alpha$ ) and ( $d, \alpha$ ) reactions, is of great help to determine the  $\Gamma_\alpha$  partial width of a given excited state from best-fit procedures.

### 1.5.3 Direct reactions and correlations

In addition to compound nucleus reactions, which occur when the incident energy is low, there is another class of nuclear reactions of particular interest for clustering: the so-called *direct reactions*. This type of reactions becomes increasingly important as the bombarding energies increase<sup>19</sup> and they have a crucial role in revealing the structure of nuclei both below and above the cluster decay thresholds. Particularly relevant for this aim are *transfer reactions* and *breakup reactions*. All these reactions have in common that the time of interaction is of the order of the time spent by the incident particle to traverse the nuclear diameter of the target, which is typically of the order of  $10^{-22}$  s. This time is much shorter than the time required for a system to form a compound nucleus, and this is the main difference between the two mechanisms. Another important feature of direct reactions is that there is no mechanism for significantly altering the direction of the momentum carried by the incident particle. In other words, while in a compound nucleus reaction the direction of the incident particle is changed by repeated collisions with consequently isotropic angular distributions of the emitted particles, in direct reactions there are few (or just one) collisions and a resulting strong asymmetry of angular distributions. The

---

<sup>19</sup>Evidences for direct reaction mechanisms at very sub-barrier energies have been reported in the literature, especially in presence of a pronounced cluster structure of the reaction partners [148, 149].

## 1.5 Techniques for the study of clusters in nuclei

---

consequence is that the direction of the emitted particles is highly correlated with the direction of the incident momentum. The direction of the emitted particles is for this reason peaked at the forward direction.

Transfer reactions are classified in *pick-up* and *stripping* reactions. In them, as an incident particle passes through the nucleus, nucleons are transferred from one to the other. Pick-up reactions are characterized by the transfer of nucleons from the target to the projectile, while in stripping reactions nucleons are *stripped off* the incident particle by the target nucleus. The disturbance of the nucleus is minimal in these types of phenomena and, for this reason, there is a strong tendency for the residual nucleus to be left in a state of low excitation. One important feature of all direct reactions is the relationship between the angular momentum transferred in the reaction and the angular distribution of the emitted particle. Normally, an angular distribution of a transfer reaction results from a superposition of waves emanating from all parts of the nuclear surface. This generates an interference effect which leads to diffraction-like pattern of intensity variations. These effects are taken into account by means of the Distorted Wave Born Approximation (DWBA) by treating the incident and emitted particles as moving under the influence of an optical-model potential. DWBA calculations are able to predict the dependence of the cross section of transfer reaction processes as a function of the emission angle. Particular types of one-nucleon transfer reaction, i.e. a stripping process that involves the exchange of only one nucleon, are represented by the  $(d, p)$  or  $(d, n)$  reactions. The first case involves the transfer of a neutron from the projectile to the target nucleus. Under the assumption that the transferred neutron enters one of the orbits without otherwise disturbing the nucleus, the angular distribution of the cross section  $\sigma(\theta)$  can be written as follows:

$$\sigma(\theta) = C^2 S \cdot \sigma_{DWBA}(\theta) \quad (1.73)$$

where  $C^2 S$  is the spectroscopic factor describing the degree to which the model used in the DWBA calculation correctly describes the nuclear structure changes. An interesting example is the  $^{58}\text{Ni}(d, p)^{59}\text{Ni}$  one-neutron transfer reaction. If one indicates with  $l_t$  and  $j_t$ , respectively, the orbital angular momentum of the transferred neutron and its total angular momentum, the configuration of the nucleus upon its entry is:

$$^{58}\text{Ni}_{\text{gs}} + n(l_t, j_t) \quad (1.74)$$

Being the ground state of  $^{58}\text{Ni}$  a  $0^+$  state if, for example,  $l_t = 1$  and  $j_t = 3/2$ , the state formed in  $^{59}\text{Ni}$  would be  $3/2^-$ . In general, the state is the mixing of all the possible configurations like equation 1.74 weighted by the corresponding spectroscopic amplitude. The probability for any particular  $3/2^-$  state of  $^{59}\text{Ni}$  to be formed will be therefore proportional to the fraction of its time it spends in each of the configurations. In other words, the wave-function for some  $3/2^-$  state  $i$  will be:

$$\Psi_{3/2}(i) = \theta_1 \Psi[^{58}\text{Ni}_{\text{gs}}] \Psi(p_{3/2}) + \dots \quad (1.75)$$

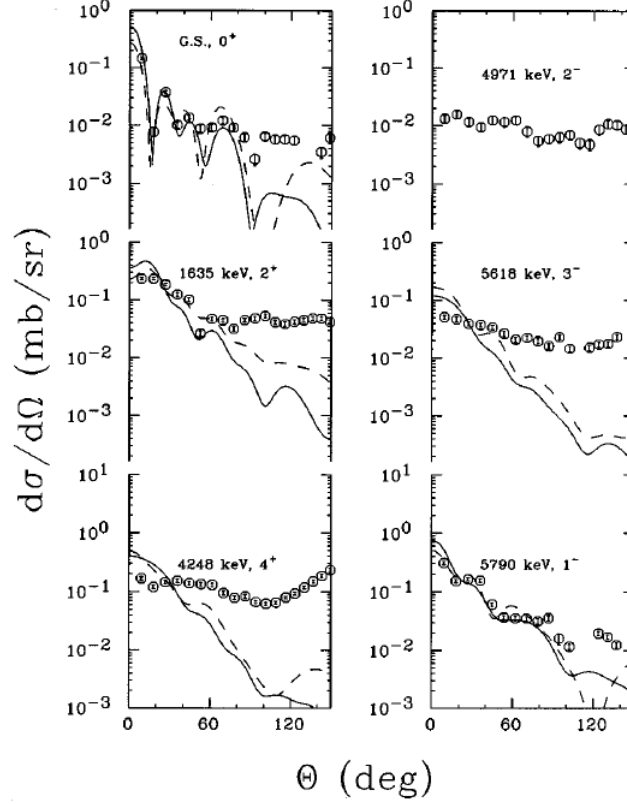


Figure 1.33: Angular distribution of  $^{16}\text{O}(^6\text{Li},d)^{20}\text{Ne}$   $\alpha$ -transfer reaction for low-lying states of  $^{20}\text{Ne}$ . The curves are theoretical results from DWBA calculations. From [150].

If a particular  $\theta_j^2 = 1$ , only one of the above terms contributes to the state  $i$ . So we have just the model used in calculating  $\sigma_{DWBA}$  and, from equation 1.73,  $C^2S = 1$ . In general, each  $C^2S$  referred to a particular configuration used in calculating the angular distribution via the DWBA is equal to the square of the corresponding amplitude  $\theta_j^2$ . So  $C^2S$  are the spectroscopic factors related to each configuration. Differently from the use of compound nucleus reactions, where the structure configurations are extracted from the reduced widths of states above threshold, here it is possible to directly obtain the spectroscopic factors under a precise model assumption. This is possible even for states which are below threshold and for which it is not possible to define decay partial widths.

The above argument applies also to multi-nucleon transfer reactions. In particular,  $\alpha$ -particle transfers are useful to prove clustering features of nuclear states [150]. In Figure 1.33, as an example, angular distributions of  $^{16}\text{O}(^6\text{Li},d)^{20}\text{Ne}$   $\alpha$ -transfer reaction are shown for the first low-lying states of  $^{20}\text{Ne}$ . Each state is identified by a different value of transferred momentum  $L$ . The trend of the data exhibits the

## 1.5 Techniques for the study of clusters in nuclei

---

typical diffraction-like peaks which are reproduced by a DWBA fit following the formulation:

$$\sigma(\theta) = N \cdot C^2 S_\alpha \cdot \sigma_{DWBA,L}(\theta) \quad (1.76)$$

Here,  $N$  is a constant factor that takes into account the degree of clustering in the specific projectile nucleus used to induce the  $\alpha$  transfer reaction; it can be determined by comparing the DWBA cross section to the experimental cross section populating a state for which the  $\alpha$  spectroscopic factor is already known. The equation 1.76 allows to extract the  $\alpha$  spectroscopic factor  $C^2 S_\alpha$  for each state and, as a consequence, to investigate their cluster nature.

*Breakup* reactions are another class of direct reactions which allow to investigate the possible presence of states characterized by  $\alpha$  clustering above the emission threshold. They consist in the excitation of a nucleus by means of the interaction with another nucleus (via inelastic scattering or transfer primary mechanisms) above the particle decay threshold, and the subsequent de-excitation of the excited nucleus via particle emission. One distinguishes between *projectile* and *target* breakup, if the nucleus that finally disintegrates is, respectively, the projectile or the target of the collision. Normally, depending on the experimental setup used to detect the emitted fragments, one can evidence one type of breakup or the other. As an example, in a target breakup reaction breakup products are emitted in a large cone, almost isotropic, and they have low energies, since the boost given by the target is reduced, being the target almost at rest after the reaction. In a projectile breakup reaction, on the contrary, breakup fragments are normally forward focused, because of the boost given by the projectile, and they have higher energies. Furthermore, one distinguishes between *sequential* and *direct* breakup. In the latter, the nucleus suddenly disintegrates by means of the forces given by the gradient of density which occurs during its interaction with the target [151]. In this case, breakup fragments do not bring any significant information on the spectroscopy of the emitting nucleus. On the contrary, sequential breakup reactions are often used to probe the structure of nuclei. They occur via a two-step process in which the nucleus is initially excited by means of the interaction with the target and then it asymptotically (sequentially) breaks-up as a de-excitation process.

The spectroscopy of the nucleus prior to decay can be inspected by measuring masses and momenta of the outgoing particles. Let us assume a sequential breakup reaction of the type  $X + Y \rightarrow X^* + Y \rightarrow \sum_i x_{i=1}^N + Y$ , where the  $N$  breakup fragments  $x_i$  of masses  $m_i$  are emitted by the intermediate resonance  $X^*$ . The quadri-momentum of the  $i$ -th fragment will be

$$q_i \equiv (x_i^0; x_i^1, x_i^2, x_i^3) = (E_i, p_i^x, p_i^y, p_i^z) \quad (1.77)$$

where we used its covariant components and we assumed  $c = 1$ . The usual vector  $(p_i^x, p_i^y, p_i^z)$  is the momentum of the  $i$ -th fragment, while the first component of the quadri-vector represents its total energy  $E_i = \sqrt{p_i^2 + m_i^2}$ . The total quadri-momentum then will be  $q = \sum_{i=1}^N q_i$ . The calculation of its invariant square is

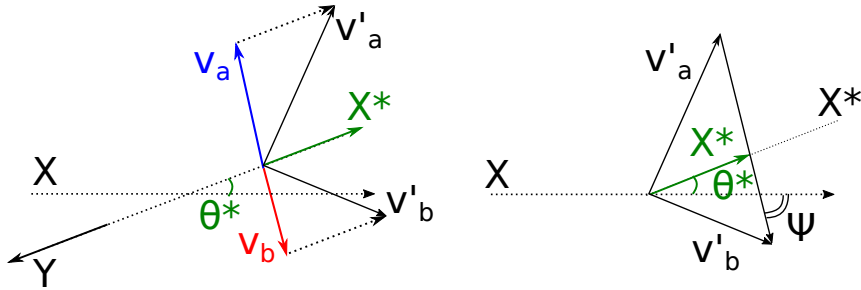


Figure 1.34: Kinematics of a sequential projectile breakup reaction of the type  $X + Y \rightarrow X^* + Y \rightarrow a + b + Y$ . The primed quantities are referred to the laboratory frame while the non-primed are in the center of mass frame. In the right panel, vectors are only shifted to the origin for clarity reasons.  $\theta^*$  is here defined as the angle formed by the scattered projectile  $X^*$  with the beam axis in the reaction center of mass.  $\Psi$  is the angle formed by the relative velocity vector of the two emitted fragments with the beam axis.

trivial and it leads to the following quantity:

$$\sqrt{s} = q^\mu q_\mu = q^0 q^0 - q^1 q^1 - q^2 q^2 - q^3 q^3 \quad (1.78)$$

which is called *invariant mass* and which is a relativistic invariant quantity, i.e. a quantity which is independent on the reference frame. It represents the mass of the particle which emitted the  $N$  fragments leading to the quadri-momentum  $q$ . The excitation energy of  $X^*$  prior to decay then is just the difference between its invariant mass and the mass of the ground state  $X$ :

$$E_x = \sqrt{s} - m(X) \quad (1.79)$$

The equation 1.79 allows to obtain information on the energy position of excited states populated in a breakup reaction. This technique is called *multi-particle correlation* and is particularly sensitive to cluster configuration, since they have pronounced decay widths for the emission of constituent clusters. Similar techniques allow also to obtain further information regarding the nuclear structure of the emitting nucleus, like the spin  $J$ . For simplicity, let us consider the case of a binary process occurring via the emission of a couple of spinless particles from the emitting source  $X^*$ . In such a case the reaction can be schematically indicated with the notation  $X + Y \rightarrow X^* + Y \rightarrow a + b + Y$ , where  $a$  and  $b$  are the correlated breakup fragments. The process is sketched in the left panel of Figure 1.34, where the velocity vectors of all the particles emitted in the final states are drawn. In the center of mass of the reaction,  $X^*$  and  $Y$  are emitted in opposite directions and the same occurs in their emission center of mass frame for the fragments  $a$  and  $b$ , i.e. in the reference frame where  $X^*$  is at rest. The figure allows to define some important quantities. The first is the angle formed by the direction of  $X^*$  in the reaction center

## 1.5 Techniques for the study of clusters in nuclei

---

of mass and the incoming beam direction, which is normally called  $\theta^*$ . Another important quantity is the one defined by the right panel of Figure 1.34. It is the angle formed by the relative velocity vector  $v_{rel}^{\vec{}} = \vec{v}_b' - \vec{v}_a'$  of the two fragments in the laboratory frame with the beam axis,  $\Psi$ . Under the assumption that the emission of  $a$  and  $b$  proceeds via an intermediate resonant state  $X^*$ , in a semi-classical approach the double differential cross section  $\frac{d^2\sigma}{d\Omega d\Omega_\Psi}$  has the following dependence on  $\theta^*$  and  $\Psi$  [152, 153]:

$$\frac{d^2\sigma}{d\Omega d\Omega_\Psi} \propto |P_l(\cos(\Psi + \alpha\theta^*))|^2 \quad (1.80)$$

where  $P_l$  is the  $l$ -order Legendre polynomial,  $l$  is the relative angular momentum of the two emitted particles and the phase shift  $\alpha$  corresponds to the quantity  $l_f/J$ , i.e. the ratio of the final state *grazing* angular momentum to the spin of the resonance  $J$ . The equation 1.80 gives rise to *ridges* in the double differential cross section like the ones of the Figure 1.35 (right panel) [153]. If one projects the data in a direction orthogonal to the ridges, the obtained picture is the one shown in the same figure (left panel), where the periodicity reflects the  $l$ -order Legendre polynomial. In such a way, one obtains an indirect measurement of  $l$  and, in the case of a couple of spinless particles, directly the  $J$  of the resonance  $J = l$ . Another commonly used strategy to obtain the  $l$  of the emission is to restrict the data to small values of  $\theta^*$ , so that the corresponding phase shift term  $\alpha\theta^*$  does not significantly contribute to the angular distribution of  $\Psi$ , which can be directly fitted in terms of squared Legendre polynomial, see for example [154].

When the decay of a resonant state occurs via the emission of more than 2 fragments, one can use multi-particle correlation techniques to inspect the decay path of the state, i.e. the individual<sup>20</sup> partial widths which contribute to the global partial width of the particular decay channel. A simple example is the decay of a resonance in three equal-mass particles. In such a case, as for the Hoyle state in  $^{12}\text{C}$  (see paragraph 1.4.2) one can expect direct resonance decays of the type  $X^* \rightarrow y_1 + y_2 + y_3$  or sequential decays, where a two-step process occurs:  $X^* \rightarrow y_1 + Y^* \rightarrow y_1 + y_2 + y_3$ . If they are the only two ways for the resonance decay, the partial width of the decay will be the sum of the direct and the sequential ones:  $\Gamma_{y_1+y_2+y_3} = \Gamma_{direct} + \Gamma_{sequential}$ . The symmetric Dalitz plot can be used in order to geometrically visualize both decays and to extract their amplitudes. These plots were introduced in particle physics by Dalitz [155] but they are widely used in in-flight resonance decay studies of nuclei [156]. A symmetric Dalitz plot can be built by using the kinetic energy of the three particles in the reference frame where the parent nucleus  $X^*$  is at rest. Calling  $E_{i,j,k}$  these values, one can define the Dalitz plot coordinates as follows:

$$\varepsilon_{i,j,k} = E_{i,j,k}/(E_i + E_j + E_k) \quad (1.81)$$

---

<sup>20</sup>*Individual* in the sense of the partial width associated to a peculiar decay pattern of a given channel.

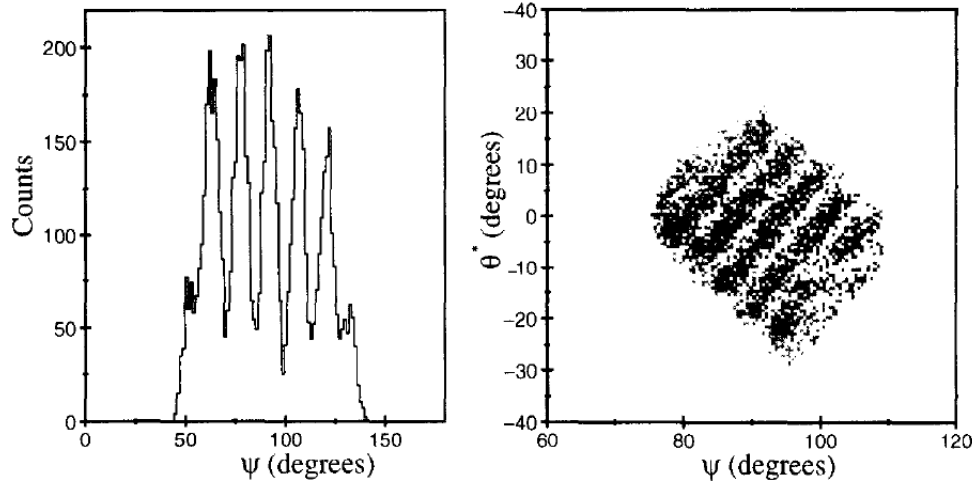


Figure 1.35: (right) Double differential cross section  $\frac{d^2\sigma}{d\Omega d\Omega_\Psi}$  of the  $^{12}\text{C}(^{16}\text{O}, ^{12}\text{C}^{12}\text{C})\alpha$  reaction. The typical *ridges* are well visible. (left) Projection of the differential cross section data in a direction perpendicular to the ridges. Periodicity in such a distribution reflects the  $l$  of the two-particle relative motion. From [153].

which are called *normalized decay energies*. They can be used as coordinates of a system of axis like the one in Figure 1.36. Since the sum of each of the coordinates is a constant, experimental points, corresponding to  $(\varepsilon_i, \varepsilon_j, \varepsilon_k)$  energy coordinates, are therefore localized inside the triangle<sup>21</sup> in figure. Furthermore, from the energy conservation in the decay we must have  $\varepsilon_i + \varepsilon_j + \varepsilon_k = 1$ , which results in a constraint that confines the data into the green circle of Figure 1.36. In the case of direct decays, according to the *phase space* available, the energy can be shared with any of the possible combinations  $\varepsilon_{i,j,k}$ , and the circle is almost uniformly filled. For the case of sequential decays, instead, the energies of the decay have to obey to more restrictive constraints. If one calls  $Q_I$  the kinetic energy shared between the particles after the first emission  $X^* \rightarrow y_1 + Y^*$ , from the conservation of energy and momentum in the decay it follows  $\varepsilon_1 = Q_I \frac{M_{Y^*}}{M_{Y^*} + m_1} = \varepsilon$ , where  $m_1$  and  $M_{Y^*}$  are the masses of  $y_1$  and  $Y^*$ . In other words, three straight bands of equations  $\varepsilon_{i,j,k} = \varepsilon$  are populated within the circle in presence of a sequential decay of energy  $Q_I$ . This locus is represented in Figure 1.36, as an example, by the red bands. A similar plot can be generated in cartesian coordinates by using the following equations:

$$\begin{aligned} x &= \sqrt{3}(\varepsilon_j - \varepsilon_k) \\ y &= 2\varepsilon_i - \varepsilon_j - \varepsilon_k \end{aligned} \quad (1.82)$$

<sup>21</sup>The possibility of representing such coordinates into an equilateral triangle follows from the *Viviani's theorem*. For a generic point  $P$  inside the triangle (see the Figure 1.36), the sum of its distances from each side of the triangle is a constant, i.e.  $\overline{PA} + \overline{PB} + \overline{PC} = \text{const.}$

## 1.5 Techniques for the study of clusters in nuclei

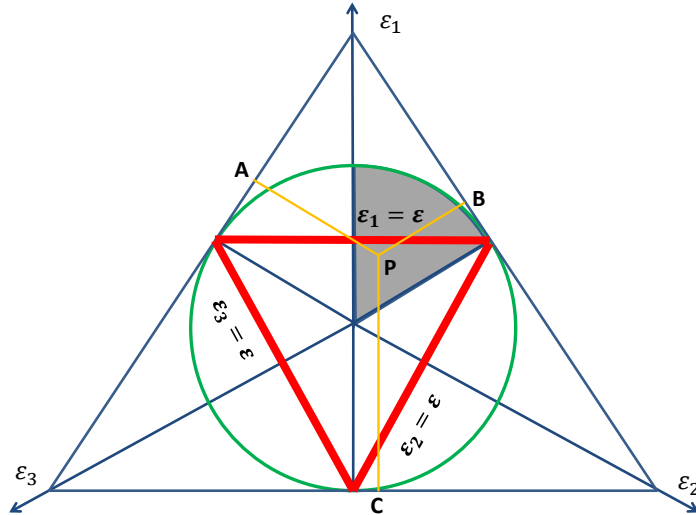


Figure 1.36: A schematic view of a symmetric Dalitz plot. The three axis correspond to the normalized energies of the three particles in their decay center of mass  $\epsilon_{1,2,3}$ . The conservation of energy  $\epsilon_1 + \epsilon_2 + \epsilon_3 = 1$  results in the data to collapse inside the green circle. The red straight lines correspond to the three loci occupied by the data if, for example, the decay occurs in a two-steps process (sequential).

By selecting  $\epsilon_i > \epsilon_j > \epsilon_k$  the data collapse into the shaded region of Figure 1.36, where the red horizontal band is associated to sequential decay processes, while the remaining part of the sector will be populated by direct events.

### 1.5.4 The interplay between structure and dynamics: heavy-ion collisions (HICs) and clusters

In the previous sections we discussed the importance of studying nuclear structure and clustering phenomena in light nuclei. Among the various experimental techniques for studying clusters, we have discussed compound nucleus reactions and direct reactions. In particular, particle-particle and multi-particle correlation techniques have been introduced as a tool to explore the properties of resonances produced in nuclear collisions. Such techniques are largely used to explore the phenomenology associated to nuclear clusters and resonance decays also in more dissipative processes such as *heavy-ion collisions* (HICs). At low ( $E/A < 10$  MeV), intermediate ( $10 \text{ MeV} < E/A < 100$  MeV), relativistic ( $100 \text{ MeV} < E/A < 2$  GeV) and ultrarelativistic energies ( $E/A > 2$  GeV), including the regime where *LHC* and *RHIC* facilities operate, the observation of resonance properties associated to the decay of short- and long-lived unbound states is important to study the properties of the medium composed of portions of *dilute/dense* and *hot* nuclear matter. At

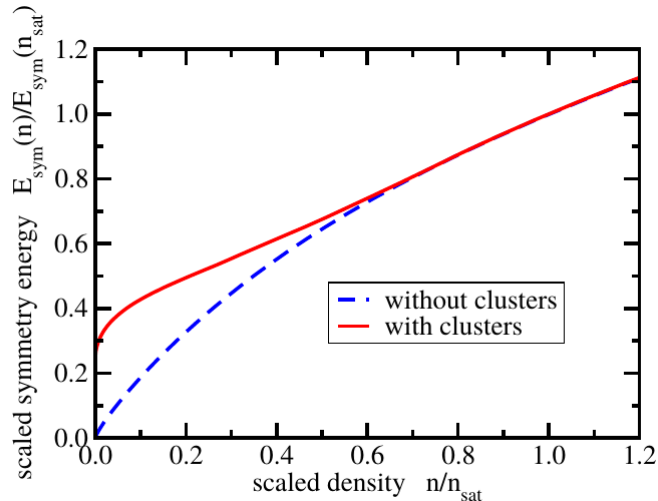


Figure 1.37: Behaviour of the nuclear symmetry energy  $E_{sym}$ , normalized to the saturation one  $E_{sym}(n_{sat})$  as a function of the density  $n/n_{sat}$  for zero-temperature nuclear medium. The blue dashed line is the calculation performed neglecting clustering-phenomena, while the red line is the one calculated including the production of clusters. The two predictions dramatically differ at low densities. From [157].

intermediate energies ( $10 \text{ MeV} < E/A < 100 \text{ MeV}$ ), the interplay of nucleon-nucleon collision and mean field dynamics drives the time evolution of the many-body system consisting of the colliding projectile and target nuclei. Such a system can lead to a dilute region probing the *sub-saturation* density<sup>22</sup> region of the nuclear *equation of state* (EoS), around  $\rho/\rho_0 \approx 0.01 - 0.6$ . Such system is also hot, with temperatures of the order of a few MeVs. Under such conditions the system explores instability regions where complex fragments, including  $\alpha$ -clusters, are produced. The structure properties of these fragments and clusters and their interplays with the EoS is presently matter of investigations. In particular, it may affect predictions on the density dependence of the *symmetry energy*<sup>23</sup> [158, 159]. A recent investigation performed with a Generalized Relativistic Density Functional approach [157] has shown that, when nuclear matter is brought at low densities and finite temperatures, corresponding to conditions typically achieved during heavy-ion collisions at intermediate energies,  $\alpha$ -clusters appear and can significantly modify the density dependence of the symmetry energy, see Figure 1.37. The dashed line in Figure 1.37 shows that

<sup>22</sup>The adopted value of the saturation density is  $\rho_0 = 0.17 \text{ fm}^3$ . This is the value of barionic density, almost constant in the nuclear interior, which is observed in ordinary nuclei.

<sup>23</sup>The symmetry energy is defined as the second derivative of the energy per nucleon  $E(n, \beta)/A$  in nuclear matter with respect to the neutron-proton asymmetry  $\beta$ , thus representing the curvature of the energy per nucleon in the direction of *isospin asymmetry*.

## 1.5 Techniques for the study of clusters in nuclei

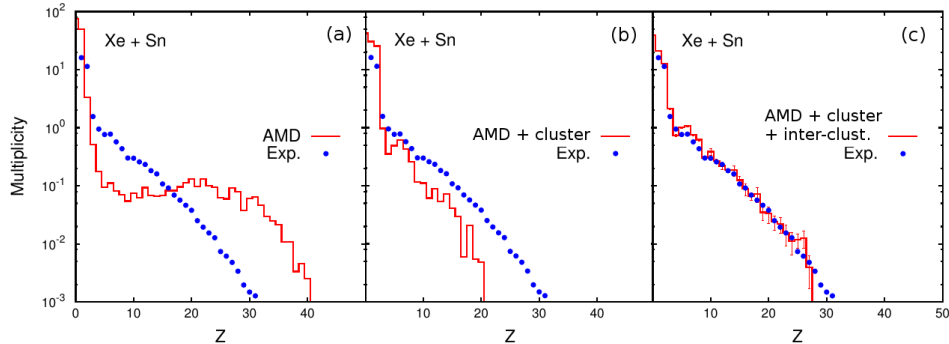


Figure 1.38: Charge distributions measured in central Xe + Sn collisions with the INDRA  $4\pi$  multi-detector [161] compared to the prediction of a dynamical version of the AMD model without cluster production (a), and with cluster production (b) and (c). In panel (c), which shows the best fit of the data, the inter-cluster correlations are taken into account. From [160].

the prediction of the trend of the symmetry energy in the absence of clustering phenomena strongly deviates from the one calculated assuming the formation of clusters (red line). The importance of  $\alpha$ -cluster production in low density matter is also shown by the recent work performed with the AMD transport model (a dynamical version of the AMD structure model already described in paragraph 1.3.4) that explicitly introduces  $\alpha$ -particle production as well as  $\alpha$ - $\alpha$  interactions during the dynamical evolution of the system. Figure 1.38 shows a comparison of charge distributions measured in central Xe + Sn collisions and AMD simulations with and without the inclusion of  $\alpha$ -clusters and their mutual interactions and correlations. Such comparison clearly indicates that only an explicit introduction of these cluster aspects in the dynamical evolution of the system, panel (c) in the figure, allows one to reproduce the experimental data [160].

By performing multi-particle correlation measurements, it is possible to observe a large variety of resonance peaks corresponding to the decay of unbound states produced in the dilute and hot medium. Figure 1.39 shows an example of deuteron- $\alpha$  correlations measured in  $^{40}\text{Ar} + ^{197}\text{Au}$  central collisions at  $E/A = 60$  MeV, and represented as a function of their relative momentum <sup>24</sup>. They are associated to the decay of excited states in  $^6\text{Li}$ . The prominent peak at low relative momentum, for instance, is due to  $d$ - $\alpha$  couples emitted by the  $T = 0$  state of  $^6\text{Li}$  at 2.186 MeV excitation energy ( $J^\pi = 3^+$ ,  $\Gamma = 24$  keV). On the one hand, these resonances are expected to display features that are strongly affected by thermal and dynamical properties (temperature, density, time evolution and lifetimes) of the medium where they are

<sup>24</sup>In particle-particle correlation studies, correlation functions are often shown in terms of the relative momentum of the two particles, i.e. the momentum associated to their relative motion.

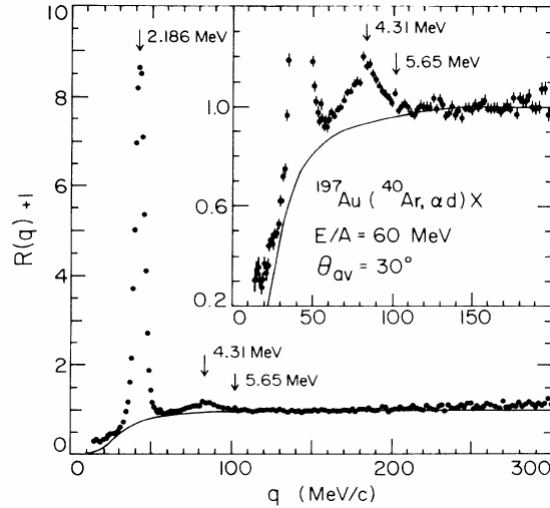


Figure 1.39:  $d$ - $\alpha$  correlation function, obtained in  $^{40}\text{Ar} + ^{197}\text{Au}$  central collisions at  $E/A = 60$  MeV, shown in terms of their relative momentum. The solid curve represents the background. Peaks are relative to excited states in  $^6\text{Li}$ . The top right panel is a magnified view. From [162].

produced. On the other hand, the phenomenology associated to these multi-particle correlations and their abundance has suggested that heavy-ion collision experiments may be used as a tool for exploring the spectroscopic properties of unbound states in light nuclei and clusters, similarly to what is done in less dissipative reactions. Such an approach has been used in a number of investigations with the Miniball detector [163], the LASSA array [164] and the INDRA  $4\pi$  detector [165]. Heavy-ion collisions, in this respect, offer advantages and disadvantages with respect to investigations performed with other techniques. Among the advantages we mention the very large number of unbound states that can be produced, with high statistics, in just one single experiment. By studying the collective and thermal properties of the colliding system, one can produce a *global bath* (portion of nuclear matter medium) where these resonances are produced and decay. By means of large solid angle coverages provided by  $4\pi$  detectors one can well characterize the collective properties of the overall system (impact parameter, reaction plane, temperature, excitation energy, etc.) and use correlation measurements to probe important aspects of the observed decaying states, such as their energy, widths, branching ratios and spins. In Refs. [163] and [165], the branching ratios are probed for a number of important  $\alpha$ -cluster states. In [165], the  $3\alpha$  decay of  $^{12}\text{C}$  and other  $\alpha$ -conjugate nuclei have been investigated, and the same experiment has provided the possibility of studying an important *proton-rich* isotope of C, namely  $^{10}\text{C}$ . This nucleus is considered a *Brunnian* or *Doubly-Borromean* nucleus due to the fact that it has a  $2\alpha + 2p$  cluster structure where any combination of three or two of its components (for ex-

## 1.5 Techniques for the study of clusters in nuclei

---

ample,  ${}^9\text{B}$ ,  ${}^6\text{Be}$ ,  ${}^5\text{Li}$ ,  ${}^8\text{Be}$ ) are all unbound and only the presence of the 4 clusters (two  $\alpha$ s and two protons) ensure the binding of the overall system. The experiment has allowed to discriminate between different decay modes of  ${}^{10}\text{C}$ . In particular, it has been shown that the sequential decay mode  ${}^{10}\text{C} \longrightarrow \text{p} + {}^9\text{Be} \longrightarrow \text{p} + \text{p} + 2\alpha$  dominates over the others.

An interesting method to estimate the spin of in-medium produced resonances is shown in Ref. [164]. A central heavy-ion collision between Xe and Au nuclei is used to produce a thermalized system and p- ${}^7\text{Be}$  correlation functions are measured to determine the spin of the astrophysical important state at  $E_{rel} = 0.774$  MeV in  ${}^8\text{B}$ . The authors show that, in such an equilibrated system, one can relate the nuclear correlation function to the properties of the medium and to the properties of specific resonances under study, such as spin and widths. By properly taking into account the properties of the medium, it is therefore possible to extract spectroscopic information about unbound states in light nuclei, thus offering an efficient technique, complementary to light-ion reactions, to study nuclear structure. Similarly, when the structure properties of the observed resonances are well known, one can use correlation studies to probe the collective and thermal properties of the system. On Chapter 3 of the present dissertation, a thermal model is introduced to show how the observation of resonances corresponding to the decay of internal states in the clusterized nucleus  ${}^8\text{Be}$  can be used to determine the temperature of the system. Such investigation raises an important question about the interplays of structure and dynamics in nuclear collisions.

The use of nuclear structure properties in nuclear dynamics has played an important role in the studies concerning the nuclear caloric curve [167, 168] and, more in general, in nuclear thermometry [166]. The caloric curve of hot nuclei was measured for the first time in an experiment conducted at GSI by the ALADiN collaboration aiming at studying the decay of projectile spectator systems produced in Au+Au collisions at relativistic energies,  $E/A = 600$  MeV [169]. Such reactions produce spectator systems with excitation energies that range between 2 and 15 MeV per nucleon, depending on the impact parameter. This excitation energy range spans the region where a finite nucleus is expected to disassemble into its constituents undergoing the so-called *liquid-gas phase transition*. As the excitation energy deposited in such hot system increases, a change in its decay mechanism is observed. At low excitation energies ( $E/A < 3$  MeV) the system behaves like a hot liquid drop evaporating light particles ( $Z = 1$  and  $2$ ) or undergoing fission. At high excitation energy ( $E/A > 10$  MeV) the system is very hot and explodes into isolated light particles and clusters in what is commonly assumed to be a vaporization phenomenon. In between these two regimes ( $3 < E/A < 10$  MeV) one crosses an average excitation energy region around 8 MeV per nucleon, namely the average binding energy per nucleon of finite nuclei: the observed phenomenon of multifragmentation, consisting of the breakup of the system into a conspicuous number ( $N > 2$ ) of fragments with charge  $Z = 3-30$  (commonly named Intermediate Mass Fragments, IMF), has been historically associated to the occurrence of a liquid-gas phase transition in nuclear matter

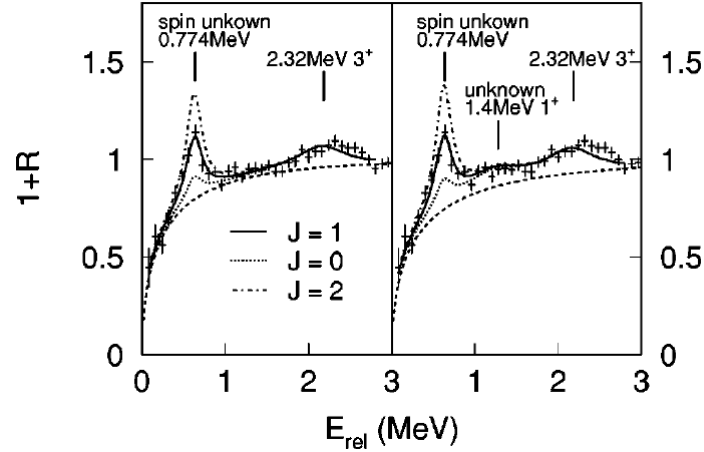


Figure 1.40:  $p$ - ${}^7\text{Be}$  correlation function in  ${}^{129}\text{Xe} + {}^{197}\text{Au}$  central collisions at 50A MeV fitted by assuming (left) that there are only two states at 0.774 MeV and 2.32 MeV and by considering (right) an additional 1.4 MeV state. The result of the best fit is represented by the solid line (obtained by assuming  $J = 0$  for the unknown 0.774 MeV  ${}^8\text{B}$  resonance) while the fitted background is shown as a dashed line. From [164].

[169]. In order to confirm this phenomenon, temperatures of the decaying projectile spectators were extracted by means of different techniques. Figure 1.41 shows the caloric curve of the already mentioned ALADiN experiment with a correlation between excitation energy per nucleon and the temperature of the reconstructed projectile-spectator systems. The solid symbols refer to temperatures deduced with a method that consists of measuring the double ratios between yields of pairs of isotopes differing by the same number of nucleons. This technique is typically referred to as *isotopic thermometer* [170]. The *plateau* at temperatures  $T \approx 5$  MeV and at intermediate excitation energies of  $E/A = 3$ -10 MeV has been associated to a signal of liquid-gas phase transition similar to the one occurring in ordinary matter. An alternative technique to extract the *temperature* in HICs is obtained by using the so-called *excited state thermometer*, which will be described in detail in Chapter 3, and which is based on two-particle correlation measurements. These correlation measurements, as it will be discussed in Chapter 3, allow one to determine the population of internal unbound states of light fragments profiting from their internal structure properties [162]. The open symbols on Figure 1.41 show the results obtained by using this excited state thermometer technique. The deduced temperatures were not in agreement with the ones obtained with the isotopic thermometer. They seem to remain constant over the excitation energy region where, in contrast, isotopic temperatures increase. Such an effect may be related to the fact that each thermometer depends on a specific measured observable. Therefore,

## 1.5 Techniques for the study of clusters in nuclei

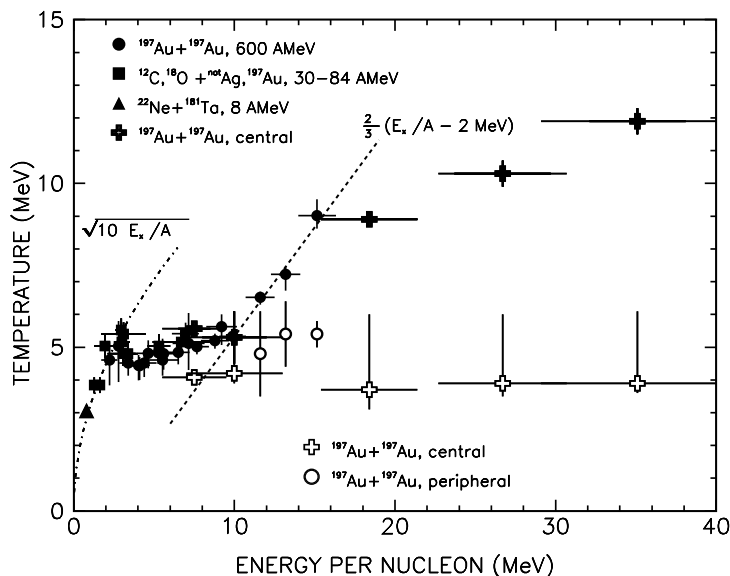


Figure 1.41: The caloric curve of hot nuclei shown with a correlation between excitation energy per nucleon and the temperature of the reconstructed projectile spectator systems. The latter is obtained by means of isotopic thermometers (full symbols) or excited state thermometers (open symbols). The differences in the observed temperature trend in between the two different methods is attributed to the sensitivity of the thermometers to different stages of the collisions. From [166].

it reflects the temperatures at which that observable achieves its *freeze-out* stage. The chemical freeze-out at which light isotopes are formed and contribute to the measured yields may occur earlier than the freeze-out of the degree of freedom associated to the internal populations of states. Therefore, different thermometers may reflect the temperature at different stages of the evolution of the system.

Similar results were found at MSU, where isotopic temperatures were compared to excited state temperatures in central Kr + Nb collisions at  $E/A = 35-120$  MeV [171]. Figure 1.42 shows excited state temperatures (full symbols), constructed with the decay of  $^4\text{He}$ ,  $^5\text{Li}$  and  $^8\text{Be}$  unbound states, compared to isotopic temperature obtained from the C-Li and the He-Li isotopic thermometers (open symbols), as a function of the beam energy. It is interesting to observe that, while the He-Li isotopic temperature follows a similar behaviour as compared to the one described in Ref. 1.41, the C-Li isotopic thermometer gives results in a good agreement with the ones obtained by using excited state thermometers. These differences confirm the possible presence of an evolutionary fragmentation mechanism where a certain hierarchy in particle species production occurs. Studying more accurately the pop-

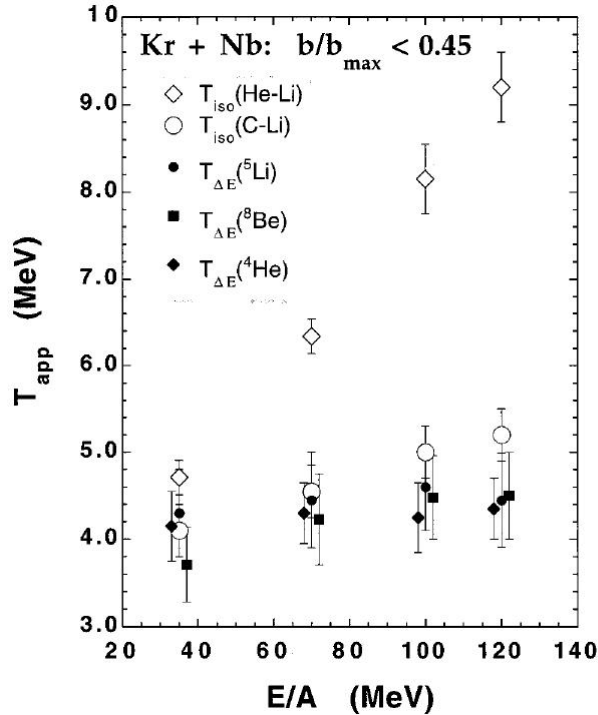


Figure 1.42: Excited state temperatures and isotopic temperatures as a function of the incident energy in central Kr + Nb collisions at  $E/A = 35$ -100 MeV. The results of the isotopic thermometer are compatible with the ones of the excited state thermometer if one uses heavier isotopes. From [171].

ulation of internal states of isotopes, rather than simply measuring their yields, enriches investigations on nuclear dynamics and thermodynamics. Inclusions of structure details into transport models or as an additional secondary decay step in so-called *hybrid* approaches represents an interesting perspective to improve EoS investigations.

## 1.6 Summary and organization of the manuscript

In the next chapters (2 and 3) we will discuss results of new analysis on clustering phenomena in light nuclei and in HICs at the light of the phenomenology described in this chapter. The present thesis is not based on a single experiment but clustering aspects in nuclei are here examined by means of a *series* of different experiments, which allow to explore such fascinating phenomena by means of a multi-method and quite comprehensive approach. We organized the manuscript as follows: in Chapter 2 we discuss the experimental campaigns aimed to the investigation of cluster configuration in light systems by means of compound nucleus and direct reactions,

## 1.6 Summary and organization of the manuscript

---

in Chapter 3 we explore clustering aspects in HICs and their interplay with the collision dynamics. In Chapter 2, molecular two-center configurations have been investigated by means of projectile breakup reactions in the case of  $^{10}\text{Be}$  (Section 2.1). Particular attention has been given to the case of carbon isotopes, which represent a key example of clustering in nuclei. Different isotopes of carbon have been here studied, providing a view of how clustering phenomena evolve as a function of the neutron excess and moving from a dimeric to a three-center configuration.  $R$ -matrix approaches of compound nucleus reactions are used to explore the structure of the proton rich  $^{11}\text{C}$  (Section 2.2) and the neutron rich  $^{13}\text{C}$  (Section 2.4) isotopes. The self-conjugated  $^{12}\text{C}$  nucleus is studied by means of multi-particle correlation techniques in direct reactions populating the Hoyle state and involving its disintegration in  $3\alpha$  particles. The Daliz plot technique has been used to examine the decay path of the Hoyle state (Section 2.3). The neutron-rich  $^{16}\text{C}$  isotope is studied via projectile sequential breakup reactions (Section 2.5). Moving to heavier self-conjugated systems, another example here discussed is the  $^{20}\text{Ne}$  nucleus, which is studied via an  $R$ -matrix analysis of low energy compound nucleus reactions data (Section 2.6). Its astrophysical relevance is also discussed. Finally, in the Chapter 3, which concludes the thesis, clustering phenomena in HICs are discussed as a complementary approach. The interplay between structure and dynamics is inferred by developing and using a thermal model based on  $\alpha$ - $\alpha$  correlations. These aspects are investigated at various incident energies in reactions involving heavy ions and compared with results of nuclear dynamics studies.



# Chapter 2

## Clustering in light systems: an experimental campaign

The subjects of the previous chapter suggest that nuclear reactions involving light-systems are an extremely powerful tool to explore, with high-precision, the spectroscopy of light nuclei and, in particular, cluster states. In this chapter we describe the results of our experimental campaign made of a series of experiments that with different, but complementary, approaches explore the possible existence of clustering phenomena in a number of light isotopes of general interest in the current research in Nuclear Physics.

### 2.1 $^{10}\text{Be}$ cluster states with breakup reactions

Sequential breakup reactions are well suited to explore the structure of unstable nuclei, as discussed in detail in paragraph 1.5.3. In this section, we report on a new investigation of  $^{10}\text{Be}$  structure by means of projectile breakup reactions induced on  $\text{CH}_2$  target, with the aim of studying the spectroscopy of this nucleus above the  $\alpha$ -threshold. On an experimental point of view, spectroscopic information regarding  $^{10}\text{Be}$  states are not free from ambiguities. Many theoretical results have been published about the possible existence of rotational bands based on *super-deformed* structures (see paragraph 1.4.3), but the experimental situation is much less clear and not yet fully understood [172].  $0^+$  and  $2^+$  members of the ground state rotational band are known, while the identification of the  $4^+$  state, predicted at excitation energy of about 11–12 MeV, is still uncertain [172–174]. The existence of a negative parity rotational band, with the 5.96 MeV ( $1^-$ ) state as band-head, is known [55]. Near the energy threshold of  $^4\text{He}+^6\text{He}$  cluster decay, the existence of a  $0^+$  state is reported. This state can be well described in terms of molecular  $\alpha : 2n : \alpha$  structure. A rotational excitation of this super-deformed molecular structure is indicated by the existence of a  $2^+$  state at 7.54 MeV. The subsequent  $4^+$  member of this molecular band is predicted to be located at about 10.5 MeV excitation energy. The presence

## Chapter 2. Clustering in light systems: an experimental campaign

---

of an excited state at about 10.2 MeV has been observed in the  ${}^7\text{Li}({}^7\text{Li}, {}^4\text{He}+{}^6\text{He}){}^4\text{He}$  reaction [175]. This state was considered by Curtis et al to have  $J^\pi=3^-$  by an analysis of angular correlations [176]. This assignment was subsequently contradicted in Ref. [177] and in recent  ${}^6\text{He}+{}^4\text{He}$  inverse kinematic resonant elastic scattering experiments [121, 178], where a  $4^+$  assignment is done. This state could therefore be the  $4^+$  member of the molecular rotational band. Very recently, preliminary results obtained in a new resonant elastic scattering experiment at the ANASEN facility [178] tentatively suggest the existence of a  $6^+$  excited state in  ${}^{10}\text{Be}$  at about 13.6 MeV. This state could represent a new further member of the cluster band in  ${}^{10}\text{Be}$  [179].

### 2.1.1 Experimental apparatus and techniques

Our experiment was performed at the FRIBs facility of INFN-Laboratori Nazionali del Sud (Catania, Italy). Starting from a 55 MeV/nucleon  ${}^{18}\text{O}$  primary beam accelerated by the LNS K-800 Superconducting Cyclotron, a fragmentation beam was produced and delivered to the experimental hall. A 1.5 mm thick  ${}^9\text{Be}$  target was used for fragment production. They were subsequently selected in magnetic rigidity ( $B\rho \approx 2.8\text{ Tm}$ ) via the LNS-Fragment Separator, with a momentum acceptance of  $\Delta p/p \approx 0.01$ . A cocktail beam with high intensity of  ${}^{16}\text{C}$  at 49.5 MeV/u ( $\approx 10^5$  particles per second),  ${}^{13}\text{B}$  ( $\approx 5 \times 10^4$  particles per second) and  ${}^{10}\text{Be}$  at 56 MeV/u ( $\approx 4 \times 10^4$  particles per second), is obtained in such a way and delivered on various targets for physics experiments. A tagging system [180], made by a MicroChannel Plate (MCP) detector and a Double Sided Silicon Strip Detector (DSSSD, 140  $\mu\text{m}$  thick), installed along the beam line, was used to identify each incoming isotope produced by projectile fragmentation. The identification of fragmentation products is obtained by correlating the energy loss in the DSSSD and the time of flight (ToF) needed to cover the flight path from the MCP to the DSSSD detector ( $\approx 13$  meters). Figure 2.1 shows an example of the capabilities of the tagging system. It allows to obtain a good isotopic separation of beam particles one by one. A tracking system based two position sensitive DSSSD was then used to determine the impinging position on the target. The beam spot size on the target was of the order of  $1.5 \times 1.5\text{ cm}^2$  with a maximum angular spread of  $1^\circ$ .

To induce projectile break-up reactions we used a 50  $\mu\text{m}$  polyethylene  $(\text{CH}_2)_n$  target. The break-up products from the  ${}^1\text{H}({}^{10}\text{Be}, {}^4\text{He}{}^6\text{He}), {}^{12}\text{C}({}^{10}\text{Be}, {}^4\text{He}{}^6\text{He})$  reactions were detected by using the  $4\pi$  multi-detector CHIMERA [181, 182]. This multi-detector consists of 1192 Si-CsI(Tl) telescopes, covering  $\simeq 94\%$  of the whole solid angle. The first stage of the telescope is constituted by a 300  $\mu\text{m}$  thick silicon detector and it is followed by a CsI(Tl) crystal, with thicknesses ranging from 6 to 12 cm, depending on the angular position in the detector, and read-out by a photodiode. Further details about the array and its detection and identification capabilities are described, for example, in Ref. [182]. In our experiment we used the first three forward rings of the CHIMERA array, covering the polar angle range

## 2.1 $^{10}\text{Be}$ cluster states with breakup reactions

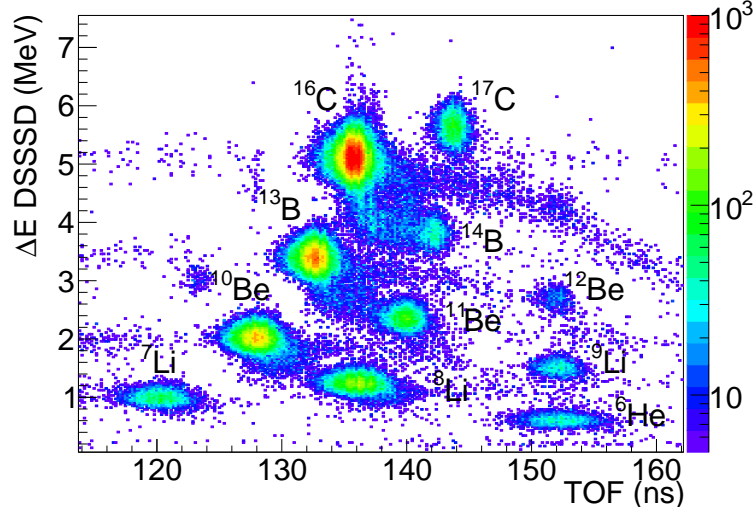


Figure 2.1: Identification plot of the FRIBs cocktail beam. Each ion of the cocktail beam (indicated by label) is located in a well defined region in  $(TOF, \Delta E \text{ DSSSD})$  plane. The finite resolution is due to the combination of detector resolution and LNS-FRS momentum acceptance.

$2.2^\circ \leq \theta \leq 6.4^\circ$ , with a reasonable granularity for this experiment (solid angles covered by a single module vary from 0.133 to 0.458 msr at increasing polar angles). As it is reported in [183], the projectile break-up cross section is forward peaked; therefore we expect to detect a large amount of fragments coming from projectile break-up in the present angular domain.

Si and CsI(Tl) detectors of the CHIMERA array were calibrated by using elastic scattering of various light ion beams impinging on a polyethylene target. Large care was dedicated to the CsI(Tl) calibration. The dependence of CsI(Tl) response on the mass and charge of incident particles [184] has been taken into account by using the parametrization given in [185], as discussed in detail in Ref. [186]. The identification in mass and charge of the detected fragments was based on the  $\Delta E$ -E technique. A typical particle identification matrix is shown in Fig. 2.2, which is obtained by correlating the energy loss of the particle in the first detection stage ( $\Delta E$ ) with the residual energy of the particles  $E_{res}$ <sup>1</sup>. The lines corresponding to different nuclear species, from helium to carbon, are clearly identified. As seen in the insert of Fig. 2.2,  $^4\text{He}$  and  $^6\text{He}$  can be unambiguously identified. Reasonable isotopic identifications can be also obtained up to beryllium isotopes. In particular, in the case of beryllium, the dominant contribution to the scatter plot comes from

<sup>1</sup>In the  $\Delta E$ -E technique it is commonly used to correlate the energy loss inside a thin stage of material to the residual energy  $E_{res}$  instead of the total incident energy  $E = \Delta E + E_{res}$ . In such a way one can use the energy signal as measured by the ADC without calibrating, thus avoiding any further indetermination due to the calibration procedures.

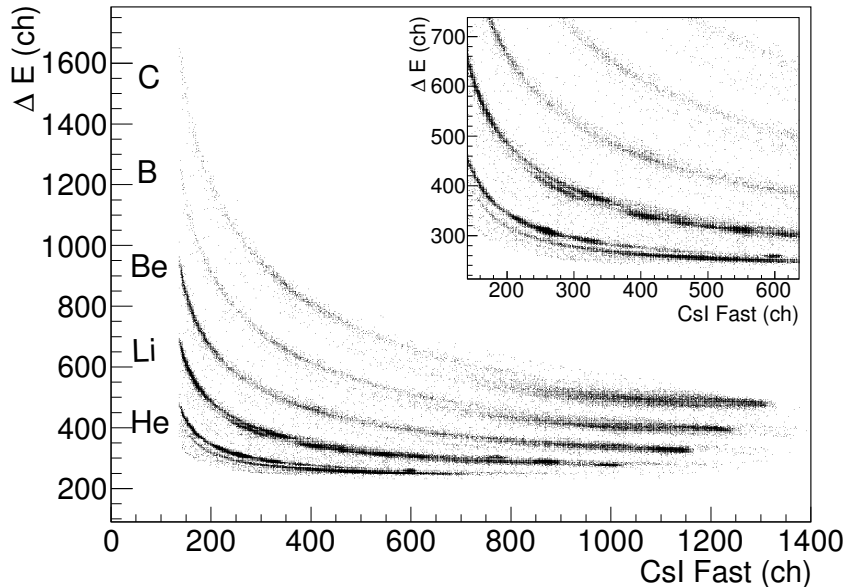


Figure 2.2:  $\Delta E$ - $E$  spectrum obtained at  $\theta_{lab} = 3.1^\circ$ . x-axis values are proportional to the residual energy released in the second detection stage (CsI(Tl) scintillator) while y-axis values represent the energy loss in Si first stage  $\Delta E$  detector (in channels). The insert shows a magnified view of the same identification plot.

the  $^{10}\text{Be}$  line, ending with the  $^{10}\text{Be}$  elastic scattering peak.

In our experiment, because of the presence of various different nuclides in the cocktail beam, we simultaneously studied different cases. In the following, we will report on the results obtained by analysing reaction products induced by the  $^{10}\text{Be}$  beam. Results obtained by selecting the  $^{16}\text{C}$  beam are instead discussed in Section 2.5.

### 2.1.2 Experimental results: $^6\text{He}$ - $^4\text{He}$ correlations

The excitation energy of the decaying nuclear states was obtained by analysing correlations between couples of breakup fragments coming from the *in-flight resonance decay* of the  $^{10}\text{Be}$  projectiles. The corresponding excitation energy is obtained via the invariant mass technique by adding to the energy threshold ( $E_{th}$ ) the measured total kinetic energy in the emitting nucleus frame (relative energy,  $E_{rel}$ ). Details about this technique can be found, for example, in Refs. [176, 187–190] and in paragraph 1.5.3.

As a preliminary step, we experimentally checked the capabilities of the CHIMERA device to perform this type of studies. For this purpose, we analysed the case of  $\alpha$ - $\alpha$  and  $3\alpha$  correlations. In the first case, the obtained invariant mass spectrum,

## 2.1 $^{10}\text{Be}$ cluster states with breakup reactions

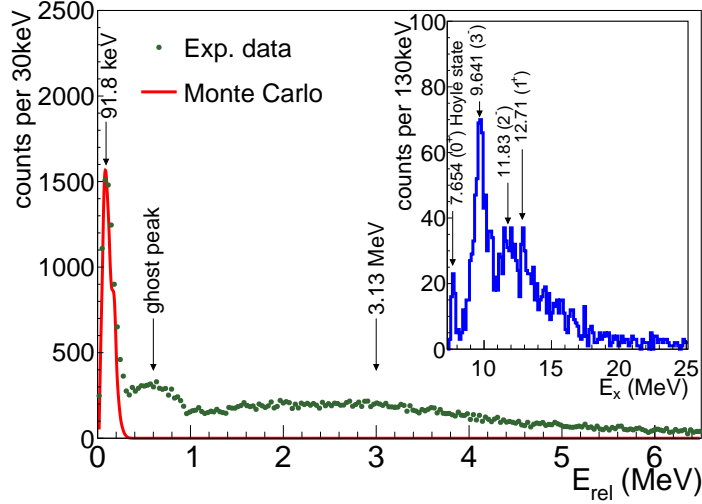


Figure 2.3:  $^8\text{Be}$  relative energy spectrum from the  $\alpha$ - $\alpha$  correlations (green points). The red line is the result of a Monte Carlo simulation considering  $^8\text{Be}$  disintegration from the ground state. Insert shows the  $^{12}\text{C}$  excitation energy spectrum obtained from the  $3\alpha$  correlations. Arrows indicate the energy position of  $^{12}\text{C}$  known states reported in literature. The low energy narrow peak is associated to the Hoyle state.

reported in Figure 2.3, shows a narrow peak at about 0.09 MeV, clearly compatible with the emission from the  $^8\text{Be}$  ground state. This evidence is supported by the result of a Monte Carlo simulation (red line), obtained with the assumptions described below. A wide bump also appears centered at about 3 MeV: it is due to the 3.04 MeV  $2^+$  state of  $^8\text{Be}$ . A further peak is present in the spectrum at about 0.6 MeV: it is reasonably associated to the so-called *ghost peak* due to the decay by neutron emission of the  $^9\text{Be}$  2.43 MeV  $5/2^-$  state. This peak is also present, as an example, in [191], confirming the consistency of the procedure. Interesting results have been obtained also from the triple coincidences. In this case we can investigate the disintegration of  $^{12}\text{C}$  via  $3\alpha$  emission. The corresponding excitation energy spectrum is shown in the insert of Figure 2.3. Arrows indicate the position of known states in  $^{12}\text{C}$ . In particular, the narrow peak at low energies, well separated from the large peak at 9.64 MeV due to the  $3_1^-$  state, evidences the  $3\alpha$  disintegration of  $^{12}\text{C}$  from the Hoyle state<sup>2</sup>.

The excitation energy of  $^{10}\text{Be}$  nucleus has been reconstructed via the  $^4\text{He}+^6\text{He}$  cluster break-up channel, by using two-particle correlation techniques. In Figure 2.4 we show the invariant mass ( $E_x$ ) spectrum obtained from our data. The vertical arrows in Figure 2.4 indicate the energies of  $^{10}\text{Be}$  excited states known in the lit-

<sup>2</sup>An inspection of the decay mode of the Hoyle state from such data shows that almost all the decay events pass through the  $^8\text{Be}_{gs}$  formation (sequential decay). Results of a dedicated experiment with much larger statistics and much lower background will be discussed in Section 2.3.

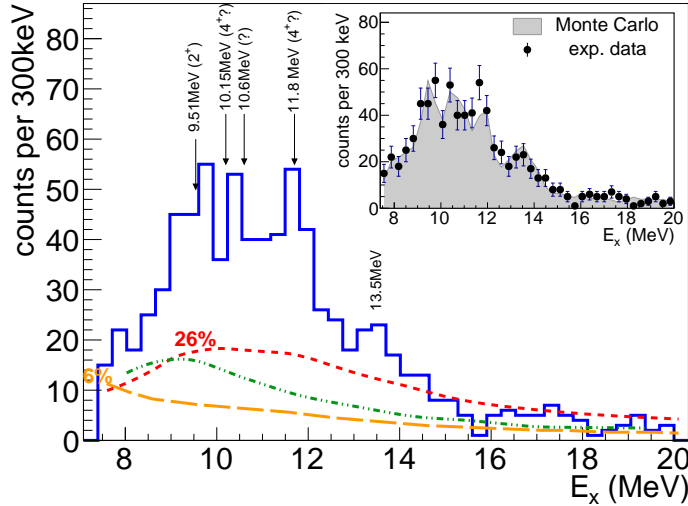


Figure 2.4:  $^{10}\text{Be}$  excitation energy spectrum obtained from the  $^4\text{He}+^6\text{He}$  decay channel. Vertical arrows indicate the energies of known states of this nucleus. In round brackets we plot the  $J^\pi$  assignment taken from the literature. The dashed lines represent the simulated detection efficiencies obtained by assuming hydrogen recoil (red dotted line) or carbon recoil (orange dashed line). The green dashed-dotted line is the uncorrelated background estimated by an event mixing procedure. The insert shows the results of a Monte Carlo simulation obtained by considering the contributions of the excited states listed in Table 2.1, compared to the experimental data (black points with error bars).

erature (and reported in Table 2.1). Despite of the low statistics and the limited relative energy resolution, they are in agreement with the present data. Particularly interesting is the appearance of a bump at  $E_x \simeq 13.5$  MeV. This suggests the possible fingerprint of a new, unreported, state. To check if the observed peak can be really ascribed to the existence of an excited state in  $^{10}\text{Be}$  or is due to different effects, we evaluated the expected background (due to spurious coincidences or to a non-resonant component) and the detection efficiency.

As a first approximation, the background can be described by considering the contribution of uncorrelated couples of particles (*event-mixing*<sup>3</sup>). The background due to event-mixing, shown in Fig. 2.4 with the green dashed-dotted line, was calculated by selecting couples of  $^4\text{He}$  and  $^6\text{He}$  coming from different events of reaction induced by all the isotopes of the cocktail beam.

The detection efficiency (dashed lines in different colours) was estimated by

<sup>3</sup>The event-mixing technique is widely used in correlation techniques [192]. In this paragraph, we describe an extremely simple example of the use of such a technique for background estimation. A more complex example of event-mixing analysis is instead described in Chapter 3 for the case of HICs.

## 2.1 $^{10}\text{Be}$ cluster states with breakup reactions

performing a Monte Carlo simulation of the CHIMERA multi-detector apparatus. We simulated the sequential emission of a couple of  $^4\text{He}$  and  $^6\text{He}$  by inelastically scattered  $^{10}\text{Be}$  nuclei. Their angular distribution in the reaction center of mass frame was described, as suggested in the literature [183, 188, 193], by the formula:  $\frac{d\sigma}{d\Omega_{cm}} \propto e^{-\frac{\theta_{cm}}{\alpha}}$ , where  $\alpha$  is a fall-off factor of the order of 12-16 degrees. This results in forward peaked emission of breakup fragments. Two different efficiency curves have been obtained, by taking into account the interaction of projectiles with hydrogen (red dotted curve in Figure 2.4) and carbon (orange dashed curve in Figure 2.4). The trends of the two estimated efficiency curves are different because of the different scattering kinematics: at  $E_x = 10$  MeV in  $^{10}\text{Be}$ , the limiting angle for scattering on hydrogen is about  $5.2^\circ$ , while for scattering on carbon there is no limiting angle. Therefore, the geometrical coverage of the first three rings of the CHIMERA array leads to higher detection efficiency in the case of hydrogen target because of the more forward-focused kinematics. In the case of hydrogen target, in fact, the emission angles are almost coincident with the beam axis and this results in the formation of an almost flat region in the corresponding estimated efficiency. Outside from this region, the efficiency is much lower. This region coincides with the region of excitation energies, i.e. opening angle of the two-particles emission cone, for which the two emitted fragments fall into the first three rings, maximizing the detection efficiency. In all cases, the shapes of the event mixing background and of the efficiency curves are very smooth and should not lead to the appearance of spurious peaks in the relative energy spectrum. All these analyses give us the possibility to suggest that the 13.5 MeV bump can be attributed to the decay from an excited state in  $^{10}\text{Be}$ .

Another interesting point that we explored is the possible membership of this state to the  $^{10}\text{Be}$  molecular rotational band. It would be indeed energetically compatible with the missing  $6^+$  member of the  $^{10}\text{Be}$  molecular rotational band, studied in [177], and made of the 6.179 MeV state as a  $0^+$  member, the 7.542 MeV as a  $2^+$  member and the 10.2 MeV state (observed also in this experiment) as a possible  $4^+$  member. Spin and parity of the suggested 13.5 MeV state can be tentatively estimated by angular correlation analysis in terms of Legendre polynomials, with a procedure analogous to the one described in Refs. [152–154] and in paragraph 1.5.3 of the present thesis. Fig. 2.5 shows the  $|\cos(\Psi')|$  distribution for the 13.5 MeV peak, where  $\Psi' = \Psi + \Delta\Psi$ , being  $\Psi$  the angle formed by the relative velocity vector of the two detected fragments with the beam axis and  $\Delta\Psi$  the phase shift correction, as discussed in Section 1.5.3. The last term can be calculated via the relation  $\Delta\Psi = \frac{\ell_i - J}{J} \theta_{cm}$ , where  $\ell_i$  is the angular momentum of the dominant partial wave in the entrance channel,  $J$  is the spin of the resonance and  $\theta_{cm}$  is the inelastic scattering angle in the center of mass frame. The  $\theta_{cm}$  angle can be estimated by means of kinematics calculations; the nature of the recoiling target can be discriminated with selections on the  $Q$ -value spectrum. Considering that, at intermediate energies, inelastic scattering processes have essentially a direct and peripheral nature, only

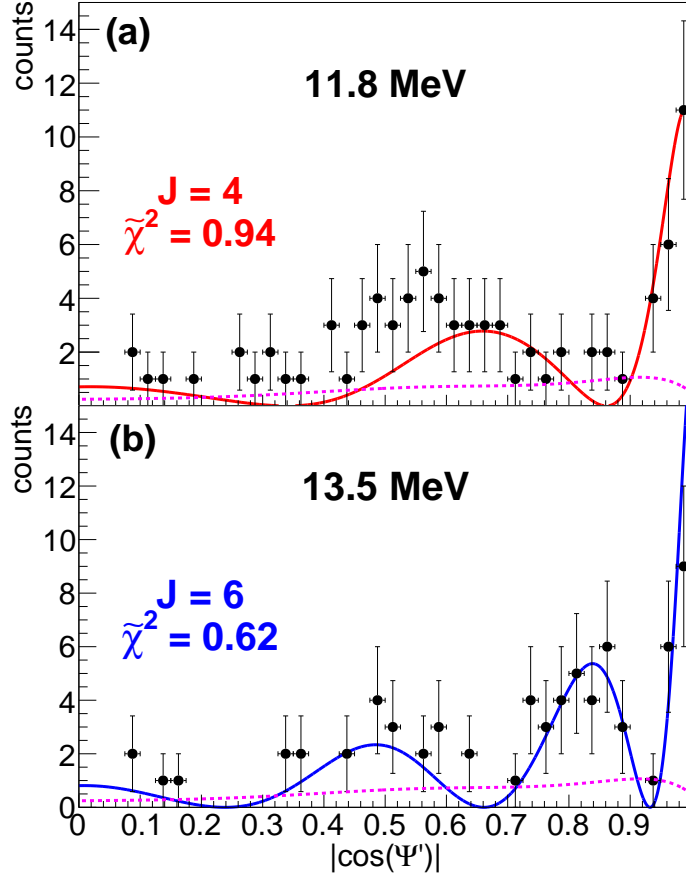


Figure 2.5: Angular correlation of  ${}^4\text{He}+{}^6\text{He}$  breakup channel for the 11.8 MeV (a) and for the 13.5 MeV (b) structures seen in the  ${}^{10}\text{Be}$  excitation energy spectrum, compared with the expected angular distribution assuming (a)  $J = 4$  (red line) and (b)  $J = 6$  (blue line). Theoretical angular distributions are corrected for the detection efficiency, presented with the magenta dashed line. The corresponding reduced  $\chi^2$  are also indicated for each case.

a narrow window of angular momenta centred around the grazing value  $l_g$  would contribute to the scattering amplitude because of the short range of the nuclear part of the interaction [194]. This allows us to assume  $l_i \approx l_g$  as a first approximation. The  $l_g$  has been calculated with the Wilcke model [195]. For example, in the present case we estimate  $l_g \approx 10\hbar$  for proton target.

The behaviour of the experimental data, shown for the 11.8 MeV bump in the case of  $J = 4$  assignment (Figure 2.5(a)) and for the 13.5 MeV bump in the case  $J = 6$  (Figure 2.5(b)) assignment, is compared with the theoretical prediction  $W(\theta^*, \Psi) \propto |P_J(\cos(\Psi'))|^2$ , where  $P_J$  are the Legendre polynomials of  $J$ -order; this theory is valid for spinless particles in the exit channel. Because all the known excited states of  ${}^6\text{He}$  decay by particle emission with  $t_{1/2} \geq 5.8 \times 10^{-21}$  s (a factor

## 2.1 $^{10}\text{Be}$ cluster states with breakup reactions

$E_x$ (MeV)	$J^\pi$	$\Gamma_{tot}$ (MeV)
9.51	$2^+$ [183, 191, 197]	0.14 [176, 196]
10.6[196]		0.20 [175, 176]
11.8	$(4^+)$ [93, 196]	0.12 [93, 196]
$\simeq 13.5$	$(6^+)$ [178], this work	$(< 0.35)$ this work

Table 2.1:  $^{10}\text{Be}$  level structure from  $^4\text{He}+^6\text{He}$  break-up channel.

$\approx 10^{12}$  times smaller than the typical time of flight of detected particles), the direct detection of  $^6\text{He}$  breakup fragments entails that we are observing  $^6\text{He}$  produced in their  $0^+$  ground state. The theoretical curves (solid lines) have been corrected for the calculated detection efficiency, estimated via a Monte Carlo simulation (shown by the magenta dashed lines). Moreover, being the Legendre polynomials squared even functions, i.e.  $|P_J(\cos(\Psi'))|^2 = |P_J(|\cos(\Psi')|)|^2$ , we have presented the  $|\cos(\Psi')|$  distribution, instead that  $\cos(\Psi')$ , in order to increase the statistics. An application of this procedure to the 11.8 MeV state, well visible in Figure 2.4, and for which the literature suggests a possible  $J^\pi = 4^+$  assignment [93, 196], is shown in the top panel. This reasonably agrees, within the error bars, with the theoretical curve for a  $4^+$  assignment. The discrepancies can be attributed to the presence of a not negligible background or to contributions of close lying states with different  $J^\pi$  values.

A similar analysis has been carried out for the 13.5 MeV state; in detail, experimental angular correlation has been compared with theoretical predictions for various  $J$  values from 0 to 8. Based on  $\chi^2$  analysis, the best fit of data is obtained assuming  $J^\pi = 6^+$  ( $\tilde{\chi}^2 = 0.62$ ). Despite of the low statistics and the presence of background, the agreement is reasonably good as visible on Figure 2.5(b).

A complete Monte Carlo simulation of the experiment, considering all the states listed in Table 2.1 and assuming that, as a first approximation, the reaction mechanism leads to equal state population, has been finally performed to test the above findings. In the simulation we have carefully taken into account the  $J^\pi$  of each state, by considering the corresponding angular correlation, as well as the expected background due to non-resonant contributions as previously discussed. To allow a much easier comparison, the simulated spectrum has been normalized to the area of the experimental one. Figure 2.4 (insert) shows the result of such an analysis. The simulated spectrum (shadowed histogram) is in nice agreement with the experimental data (black dots), confirming the good consistency of the spectroscopic data reported in Table 2.1. These calculations point out also that, at  $\approx 13.5$  MeV excitation energy, the relative energy resolution of the experimental device is  $\approx 0.45$  MeV. In this way we can give an upper limit of  $\approx 0.35$  MeV for the 13.5 MeV state width<sup>4</sup>.

---

<sup>4</sup>The Wigner limit for such a  $\ell$  value in correspondence of this relative energy amounts at  $\Gamma \approx 150$  keV for a channel radius  $R = 1.4({}^3\sqrt{4} + {}^3\sqrt{6})$  fm = 4.77 fm. Our finding appears to be compatible with this limit.

## Chapter 2. Clustering in light systems: an experimental campaign

---

It is interesting to observe that the possible existence of a 13.5 MeV  $6^+$  state in  $^{10}\text{Be}$  has been suggested by the recent observations on resonant elastic scattering reported in Ref. [178], where the  $J^\pi$  of the 13.5 MeV peak is estimated by means of  $R$ -matrix fit of experimental data. On the contrary, no evidence of such a state has been found in a recent ( $^{18}\text{O},^{17}\text{O}$ ) neutron transfer investigation [198]. This finding could indicate the  $\alpha$  cluster nature of the 13.5 MeV state in  $^{10}\text{Be}$ , being the  $\alpha$  resonant elastic scattering and the cluster break-up techniques particularly sensitive to evidence  $\alpha$  cluster states (especially of molecular nature, thanks to the pronounced  $\alpha + 2n$  structure of  $^6\text{He}$ ), while neutron transfer reactions are usually more sensitive towards single particle excitations.

All the above mentioned results have been recently published in Ref. [199].

### 2.1.3 Impact of our results on successive works

Some investigations, related to our work, have been reported in the literature after the publishing of our results [199]. Amos and co-authors [200] used a multi-channel algebraic scattering (MCAS) method to find a representation of the spectrum of  $^{10}\text{Be}$  up to more than 10 MeV excitation energy. They performed a detailed calculation to attempt in reproducing the  $6^+$  13.5 MeV state suggested in our work. However, with their model such a state appears at higher energies, close to 20 MeV. The existence of such a state was instead confirmed by experimental observations of Jiang et al. [201]. They used the transfer  $^9\text{Be}(^9\text{Be},^{10}\text{Be})^8\text{Be}$  reaction at 45 MeV to inspect excited states in  $^{10}\text{Be}$  up to an excitation energy of 18.80 MeV via missing mass and invariant mass methods. They found a high-precision indication of the existence of a state in  $^{10}\text{Be}$  lying at  $E_x = 13.5 \pm 0.10$  MeV by analyzing the  $^6\text{He} + ^4\text{He}$  correlations from the cluster decay of  $^{10}\text{Be}$ . This finding is in good agreement with our observation and gives support to the existence of such a new state in  $^{10}\text{Be}$ .

## 2.2 The structure of $^{11}\text{C}$ with the $^{10}\text{B}(p,\alpha)^7\text{Be}$ reaction

While the effects of clusterization are well visible and quite well understood in beryllium isotopes ( $^8\text{Be}$ ,  $^9\text{Be}$ ,  $^{10}\text{Be}$ , etc), they are much less known in carbon isotopes (see Section 1.4). Very often the uncertainties on the structure of such nuclei do not belong to a lack of theoretical predictions, but rather to a poor experimental knowledge of the spectroscopy of excited states above their  $\alpha$  disintegration threshold. In the next sections, we will describe the results of four experiments aimed to improve our knowledge of the spectroscopy of carbon  $^{11,12,13,16}\text{C}$ .

In the present section, experimental results on the  $^{11}\text{C}$  nucleus are discussed. As stated in paragraph 1.4.3, this nucleus and its mirror  $^{11}\text{B}$  could be characterized by structures  $2\alpha + t$  and  $2\alpha + ^3\text{He}$  at high excitation energies. Similar configurations could give rise to molecular bands [202]. Unfortunately, the spectroscopy of  $^{11}\text{C}$  at

## 2.2 The structure of $^{11}\text{C}$ with the $^{10}\text{B}(\text{p},\alpha)^7\text{Be}$ reaction

excitation energies above the  $\alpha$ -threshold ( $Q_\alpha = -7.544$  MeV) is still uncertain, and the possible existence of clustering phenomena in this nucleus is not fully clarified. A particularly suited method to study the spectroscopy of  $^{11}\text{C}$  is to analyze nuclear reactions which lead to the formation of a compound nucleus of  $^{11}\text{C}$  ( $S_p = 8.690$  MeV) at high excitation energies. Among them, to investigate this nucleus we selected the  $^{10}\text{B}(\text{p},\alpha_0)$  ( $Q = 1.145$  MeV) together with the elastic scattering  $^{10}\text{B}(\text{p},\text{p})$ .

The  $^{10}\text{B}(\text{p},\alpha)$  reaction [203–206] has a multi-disciplinary interest<sup>5</sup>. Together with the  $^7\text{Be}(\alpha,\alpha)$ ,  $^7\text{Be}(\alpha,\gamma)$ ,  $^{10}\text{B}(\text{p},\gamma)$ ,  $^{10}\text{B}(\text{p},\text{p})$  and transfer reactions, it allows to study the spectroscopy of the  $^{11}\text{C}$  compound nucleus (see, e.g. [202, 212, 213]). It has been shown that the analysis of  $\Gamma_\alpha$ ,  $\Gamma_p$  and  $\Gamma_\gamma$  partial widths of  $^{11}\text{C}$  near and above the  $\alpha$ -threshold could be useful to unveil the existence of molecular states [202, 213] in this interesting proton-rich isotope, see also paragraph 1.4.3 of the present thesis. Partial widths can be extracted by studying excitation functions and angular distributions by means of  $R$ -matrix theory. On the other hand, the accurate knowledge of the  $^{10}\text{B}(\text{p},\alpha_0)$  reaction  $S$ -factor at low energies ( $\leq 10$  keV) is fundamental to correctly describe the destruction of the  $^{10}\text{B}$  isotope in stars<sup>6</sup> [215]. Recent indirect investigations with the Trojan Horse method explored the trend of the  $S$ -factor down to zero energy [215–217]. To minimize systematic errors, these indirect data need to be normalized to good quality direct data at high energies, e.g. in the 1.0 – 1.5 MeV region.

The  $^{10}\text{B}(\text{p},\alpha)$  reaction at low energy exhibits two different exit channels, i.e.  $^{10}\text{B}(\text{p},\alpha_0)^7\text{Be}_{gs}$  and  $^{10}\text{B}(\text{p},\alpha_1)^7\text{Be}_{0.43}$ . Typically, a given excited state in the  $^{11}\text{C}$  compound nucleus could decay to both channels  $\alpha_0$  and  $\alpha_1$ . However, because of the Coulomb penetrability in the outgoing channel and the phase space, at low bombarding energies ( $E_p < 1$  MeV) the  $\alpha_1$  channel is strongly suppressed respect to the  $\alpha_0$  one [218]. For this reason, in this analysis we will focus our attention mainly to the  $^{10}\text{B}(\text{p},\alpha_0)^7\text{Be}_{gs}$  reaction. The data reported in the literature concerning the  $^{10}\text{B}(\text{p},\alpha)$  reaction are quite poor, and often affected by large uncertainties. Recently, a strong effort has been done by using indirect methods of analysis, such as the Trojan Horse one [219–221]; the results of these analyses are discussed in Ref. [215], where the  $S$ -factor of the  $^{10}\text{B}(\text{p},\alpha_0)$  has been extracted down to zero energy. At higher bombarding energies, the integrated cross section for summed  $\alpha_0$  and  $\alpha_1$  channels has been measured by Jenkin et al ( $E_p \approx 3$ -5.5 MeV) [222] and, more

<sup>5</sup>The  $^{10}\text{B}(\text{p},\alpha)$  reaction is important in Nuclear Fusion technology [207] for the development of new generation laser-induced *aneutronic fusion* reactors, based on the  $^{11}\text{B}(\text{p},\alpha)$  reaction [208–210]. This could avoid serious radio-protection problems due to neutron flux emitted by the more conventional  $d + d$  or  $d + t$  fusion reaction. Being natural boron composed by  $^{11}\text{B}$  at 80.1% level, while the remaining 19.9% is  $^{10}\text{B}$ , the  $^{10}\text{B}(\text{p},\alpha)^7\text{Be}$  reaction can occur on  $^{10}\text{B}$  contaminants leading to the emission of long-living  $^7\text{Be}$  radioactive nuclei ( $\tau \simeq 52.7$  days). They can hit the reactor vessel, causing important radiation safety issues. A correct estimate of the  $^{11}\text{B}$  enrichment level needed to avoid radioactive hazard requires an accurate knowledge of the  $^{10}\text{B}(\text{p},\alpha)$  integrated cross section at low energies ( $< 0.3$  MeV) [211].

<sup>6</sup>The destruction of Li, Be, B isotopes in stars occurs at different depths, and the analysis of the resulting atmospheric abundances can be used as a fingerprint of mixing processes [214].

## Chapter 2. Clustering in light systems: an experimental campaign

---

recently, by Kafkarkou et al ( $E_p \approx 2 - 5.5$  MeV) [211]. Apart from different absolute normalizations (at 16% level), these two data sets are in good agreement. The situation is more problematic for the intermediate bombarding energy range ( $E_p \approx 0.5 - 2.0$  MeV). In this domain, the only angle-integrated measurement reported in the literature is described in Ref. [223]. It is obtained with the activation technique of boron samples, which does not discriminate the  $\alpha_0$  and  $\alpha_1$  channels; the thick target yields reported in Ref. [223] have been subsequently transformed into  $S$ -factor by the NACRE collaboration [109, 224]; the resulting data-set is affected by very large error bars (of the order of 20-30%). In this energy region, other two (very old) data sets have been reported in the literature: the data by Brown et al ( $E_p \approx 0.5$ -1.6 MeV, in  $\approx 25$  keV step [225]) and by Cronin ( $E_p \approx 0.8$ -1.7 MeV, in  $\approx 70$  keV step [218]). They have been obtained with very refined detection devices (a magnetic spectrometer and an electrostatic analyser, respectively). Unfortunately, the first data set [225] reports the differential cross section (DCS) for  $\alpha_0$  and  $\alpha_1$  channels obtained only at one angle ( $\theta_{cm} \approx 140^\circ$ ), while in the second data set [218] angular distributions are reported only for five bombarding energies, down to 1 MeV.

If we want to improve our knowledge of  $^{11}\text{C}$  spectroscopy, we need more accurate data. For this reason, we performed a new measurement of the  $^{10}\text{B}(p,\alpha_0)$  reaction in the bombarding energy range 0.6 - 1.0 MeV by means of the TTT3 tandem accelerator in Naples [226–229].

### 2.2.1 Experimental apparatus and techniques

The experiment has been performed at the TTT3 tandem accelerator of Laboratorio dell'Acceleratore (LdA) of Federico II University of Naples [226–229]. Proton beams were obtained by using a TiH compound introduced in the sputtering source. In order to reduce pile-up effects, typical intensities of the proton beam used in this experiment did not exceed 1 nA. The accelerator was energy calibrated by analysing the  $\gamma$  yield of the  $^{19}\text{F}(p,\alpha\gamma)$  reaction near the 0.872 MeV resonance and by inspecting several resonances in the elastic scattering of proton and  $\alpha$  beams on  $^{12}\text{C}$  and  $^{16}\text{O}$  targets [230]. The maximum estimated beam energy spread was about 0.2%, and the diameter of beam spot on the target did not exceed 2 mm. The proton energy was varied in the range 0.63-1.028 MeV, in  $\approx 40$  keV steps. Beam intensity was monitored by means of a Faraday-cup and the collected charge was estimated by a digital current integrator. The typical dead time was  $\approx 1$ -2% maximum. The vacuum in the scattering chamber was of the order of  $10^{-6}$  mbar.

Particular attention was devoted to the choice of the target. We used a boron layer ( $38 \mu\text{g}/\text{cm}^2$  nominal thickness, isotopically enriched in  $^{10}\text{B}$  at 99.9% level), obtained by  $e$ -beam evaporation. Because of the extreme fragility of the boron layer, a small quantity of polyvinyl formal ( $\text{C}_3\text{H}_6\text{O}_2$ , of the order some  $\mu\text{g}/\text{cm}^2$ ) was used to reinforce it. It was mounted orthogonally respect to the beam axis. The stability of target was checked all along the experiment by monitoring elastic scattering peaks. Even if our target was specifically manufactured to reduce the amount of

## 2.2 The structure of $^{11}\text{C}$ with the $^{10}\text{B}(p,\alpha)^7\text{Be}$ reaction

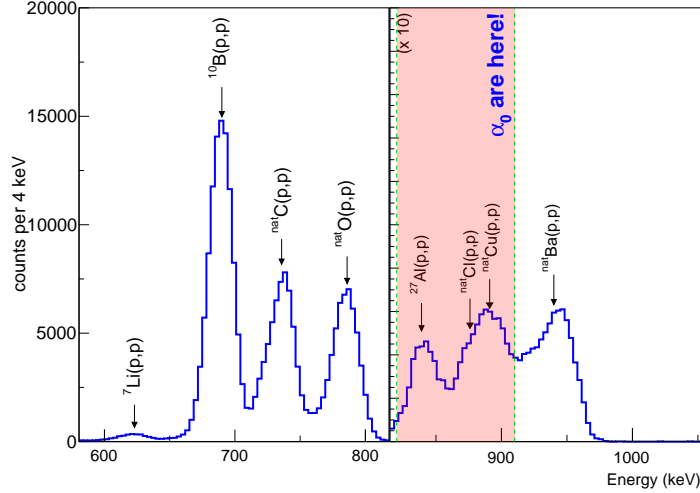


Figure 2.6: Elastic backscattering spectrum obtained at  $\theta_{lab}=140^\circ$  by bombarding the target with 0.988 MeV proton beam. Note the change of the vertical scale at 0.82 MeV. The energy positions of the various scattering and reaction products due to  $^{10}\text{B}$  and contaminants are shown by arrows. The energy region where  $\alpha_0$  contributions lie is indicated by a light red band.

contaminants, a not negligible presence of reaction products coming from residual contaminants in the target is present in the spectrum of the reaction products. We performed a dedicated characterization of the target by means of elastic backscattering ( $\theta_{lab}=140^\circ$ ) of 0.988 MeV protons. The resulting backscattering spectrum is shown in Figure 2.6. The presence of Li and Al is due to contaminants in the boron powder used to manufacture the target; carbon and oxygen are due to the polyvinyl formal layer; Cu is due to the use of a copper mortar for the boron  $e$ -beam evaporation; and finally Cl and Ba are due to the use of  $\text{BaCl}_2$  release agent in the target manufacturing procedure. Peaks due to these contaminants (especially the heavier ones) largely overlap with the  $\alpha_0$  signal, leading to strong difficulties in the extraction of  $\alpha_0$  yields at backward angles by ejectile energy analysis.

The discussed analysis allows to obtain a precise indication of the nature of the contaminants present in the target. In this way we can perform a systematic study of the possibility to distinguish the reaction products of interest from contaminant signals at various emission angles. In Figure 2.7, we plot the result of such an analysis in terms of kinematic curves of scattering and reaction events that can occur on the boron target and its contaminants, when the bombarding energy is  $E_p=0.95$  MeV.  $E_i$  is the ejectile energy, while  $\theta_{lab}$  is the detection angle. The  $^{10}\text{B}$  layer was assumed to be  $40 \mu\text{g}/\text{cm}^2$  thick. For simplicity, contaminants are supposed to be only at the entrance surface of the target, but this assumption does not affect significantly our deductions. The blue filled area indicates the angular region largely shadowed

## Chapter 2. Clustering in light systems: an experimental campaign

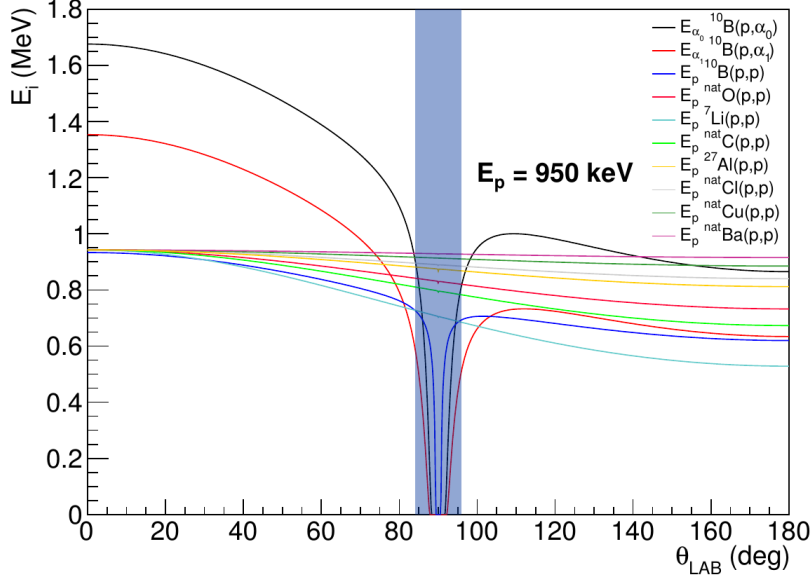


Figure 2.7: Kinematic curves of scattering and reaction events on boron and contaminants in the target obtained at  $E_p=0.95$  MeV.  $E_i$  is the ejectile energy, while  $\theta_{lab}$  is the detection angle. The  $^{10}\text{B}$  layer was supposed to be  $40 \mu\text{g}/\text{cm}^2$  thick. For simplicity, contaminants are assumed to be at the entrance face of the target. The blue filled area indicates the angular region shadowed by the target frame.

by the target frame. Kinematic curves of different scattering and reaction events are shown in various colours. At forward angles, the ejectiles are well separated, and they can be safely identified by their energy. At variance, we can expect a strong overlap between the  $^{10}\text{B}(p,\alpha_0)$  reaction and the  $^{nat}\text{Ba,Cu,Cl}(p,p_0)$  scattering products at backward angles; this effect is further amplified if we considered the kinematical spread introduced by the finite angular opening of the detectors.

The arrangement of detectors used in the present experiment, sketched in Figure 2.8, was designed to take into account all these peculiar aspects of reaction kinematics. The detection system consisted of 10 silicon detectors ( $1 \times 1 \text{ cm}^2$  collimated area), placed at 10 cm from the target. Their energy resolution is of the order of 0.3% for 5.48 MeV  $\alpha$  particles. The first four silicon detectors were placed at  $30^\circ$ ,  $40^\circ$ ,  $50^\circ$  and  $60^\circ$  angles. At these forward angles, the identification of the  $\alpha_0$  peak can be easily done, provided that the pile-up is safely reduced. An example of spectrum obtained at  $40^\circ$  when  $E_p = 0.988$  MeV is shown in Figure 2.9. The  $^{10}\text{B}(p,\alpha_0)$  peak is clearly seen at  $\simeq 1.57$  MeV while a less intense  $^{10}\text{B}(p,\alpha_1)$  peak can be identified at  $\simeq 1.26$  MeV. The yield ratio here observed at  $E_p = 0.988$  MeV and  $\theta_{lab} = 40^\circ$  ( $\frac{Y_{\alpha_1}}{Y_{\alpha_0}} = 6.7 \pm 1.0\%$ ) is in reasonable agreement with the value  $\approx 5.5\%$  based on data reported in Ref. [218] at  $E_p = 1.1$  MeV and  $\theta_{cm} = 100^\circ$ . Besides the forward ones, six silicon detectors have been further mounted at  $\theta_{lab} = \pm 120^\circ$ ,  $140^\circ$ ,

## 2.2 The structure of $^{11}\text{C}$ with the $^{10}\text{B}(p,\alpha)^7\text{Be}$ reaction

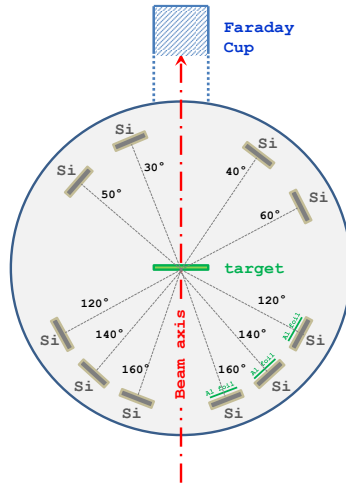


Figure 2.8: Schematic drawing of the experimental setup.

$160^\circ$  in a symmetric displacement with respect to the beam axis. The symmetric displacement has been obtained with mechanical and optical procedures and tested via Rutherford scattering of a 1 MeV proton beam on barium ( $BaF_2$  thin target). The observed left-right asymmetry is of the order of 0.6% maximum in yield and it has been taken into account in the data analysis phase. A  $3\ \mu\text{m}$  thick aluminium foil has been placed in front of three out of the six detectors (on the same side), while the remaining have been left unshielded. The use of aluminium foils allows to extract the yield of the  $\alpha_0$  channel at backward angles, otherwise hidden by the presence of other scattering products, as shown in Figures 2.6 and 2.7. More in detail, the aluminum foil strongly slows down (or even stops)  $\alpha_0$  particles; at variance, protons are able to punch through the foil and be detected. In such a way, to estimate the  $\alpha_0$  yield, one can make the difference between the left-side (unshielded detector) energy spectrum and the right-side (shielded) one in the region of interest where the  $\alpha_0$  particles are expected. We indicate this method as *inverse absorber technique*. To compare the shielded and unshielded detector spectra, we need firstly to simulate the effect of aluminium absorber in the unshielded detector. To do this, the unshielded detector spectrum has been processed with a Monte Carlo code that simulated the effect of energy loss and straggling in the aluminium absorber, supposing that all the particles hitting the detector are protons. The average energy loss curve is taken from Ziegler [231] and straggling values are taken from the Chu theory, as discussed in Ref. [230]. In Figure 2.10 we show, as blue solid line, the right-side spectrum obtained at  $-160^\circ$  (shielded detector) compared to the left-side  $+160^\circ$  (unshielded detector) spectrum processed with the Monte Carlo code to take into account the absorber effect (red solid line). Figure 2.10 refers to  $E_p = 0.988$  MeV and  $\theta_{lab} = 160^\circ$ , but similar results are seen also at different bombarding ener-

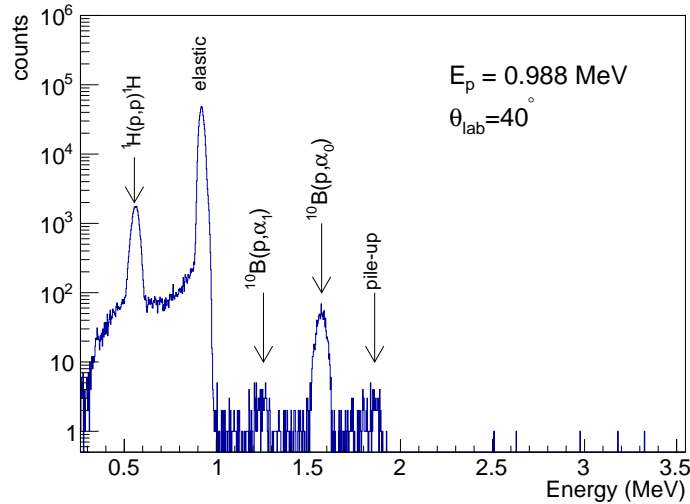


Figure 2.9: Ejectile spectrum obtained at  $\theta_{lab} = 40^\circ$  when the target is bombarded by 0.988 MeV protons. The contributions due to the various ejectiles are indicated by arrows.

gies and detection angles. The two spectra are in very good agreement, except for the 0.62 - 0.76 MeV proton-equivalent energy region, where the  $\alpha_0$  contribution is expected from kinematics (the broadening being due to the angular opening of the detector) and energy loss considerations. Subtracting the two spectra in this region of interest we are able to obtain the yield of  $\alpha_0$  particles at backward angles, shown as blue filled area in Figure 2.10. The uncertainty introduced by this procedure is  $\approx 4\%$  maximum. In this way, angular distributions can be obtained, for the first time, in a quite wide angular domain.

### 2.2.2 Angular distributions, integrated cross-sections and S-factor of the $^{10}\text{B}(p,\alpha_0)$ reaction

The differential cross section (DCS) of the  $^{10}\text{B}(p,\alpha_0)^7\text{Be}$  was estimated by using the measured experimental  $\alpha_0$  yields at various incident energies. We used an internal normalization procedure, based on the simultaneously measured  $^{10}\text{B}(p,p_0)$  yield, to obtain DCS in absolute units. The  $^{10}\text{B}(p,p_0)^{10}\text{B}$  yields have been estimated by fitting our spectra at  $140^\circ$  and  $160^\circ$  with three Gaussian curves plus a polynomial background. The DCS of the elastic scattering  $^{10}\text{B}(p,p_0)$  at backward angles ( $140^\circ$ ,  $160^\circ$ ) have been already measured and reported in Ref. [233]; more recently, these DCS have been carefully benchmarked and corrected in Ref. [234]. In Figure 2.11, we report the resulting angular distributions of the  $^{10}\text{B}(p,\alpha_0)^7\text{Be}$  reaction. At  $E_p \leq 0.785$  MeV, some points at forward angles are missing, because of the overlap with the pile-up peak. At  $E_p = 1.010$  MeV, our angular distribution is compared with

## 2.2 The structure of $^{11}\text{C}$ with the $^{10}\text{B}(p,\alpha)^7\text{Be}$ reaction

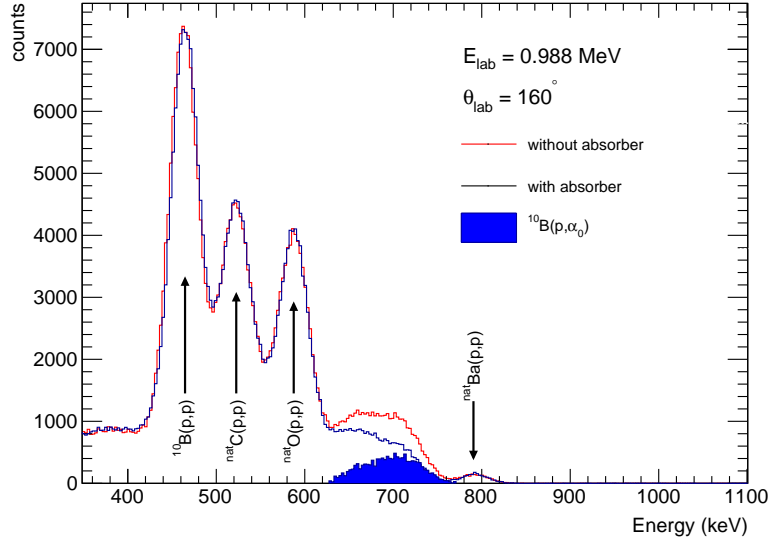


Figure 2.10: Ejectile spectra obtained at  $\theta_{lab} = \pm 160^\circ$  when the target is bombarded by 0.988 MeV protons. Blue line: detector preceded by aluminium absorber. Red line: unshielded detector. In this case the original spectrum has been processed with a Monte Carlo technique to simulate the effect of the aluminium absorber. Blue filled area: subtraction of the two spectra in the energy region where the  $^{10}\text{B}(p,\alpha_0)$  contribution is expected.

the one reported by Cronin [218] at 1 MeV. In their overlap region a reasonable agreement between the two data sets can be observed; this finding gives consistency to the experimental methodology applied in the present analysis. To our knowledge, before this work, the 1 MeV angular distribution of Ref. [218] was the only one available in the literature in the  $E_p \approx 0.5\text{-}1.0$  MeV domain. At lower energies ( $E_p \approx 0.15\text{-}0.45$  MeV), angular distributions have been reported by Youn et al [235]. Interestingly, angular distribution shapes of our lowermost energy data ( $E_p < 0.7$  MeV) and of the higher-most energy data by Youn et al ( $E_p > 0.37$  MeV) are similar, pointing out the presence of non-negligible  $2^{nd}$ -order terms in the Legendre Polynomial fit of data. The peculiar shape of these angular distributions could be due to the excitation of a state in  $^{11}\text{C}$  by a proton reaction with  $\ell \neq 0$ , as discussed in more details in the following.

To derive angle-integrated cross sections from the experimental data, we fitted the above discussed angular distributions with Legendre polynomials. The  $\ell$ -order of these polynomials reflects the partial waves of the reaction. In the bombarding energy domain explored in the present measurement, we can assume that only low- $\ell$  partial waves are contributing ( $\ell \leq 2$ ). This allows us to limit the maximum order of the polynomials used in the fit. In detail, we used Legendre polynomial up to the  $4^{th}$  order in the  $E_p = 0.827\text{-}1.028$  MeV range, and up to the  $2^{nd}$  order in the

## Chapter 2. Clustering in light systems: an experimental campaign

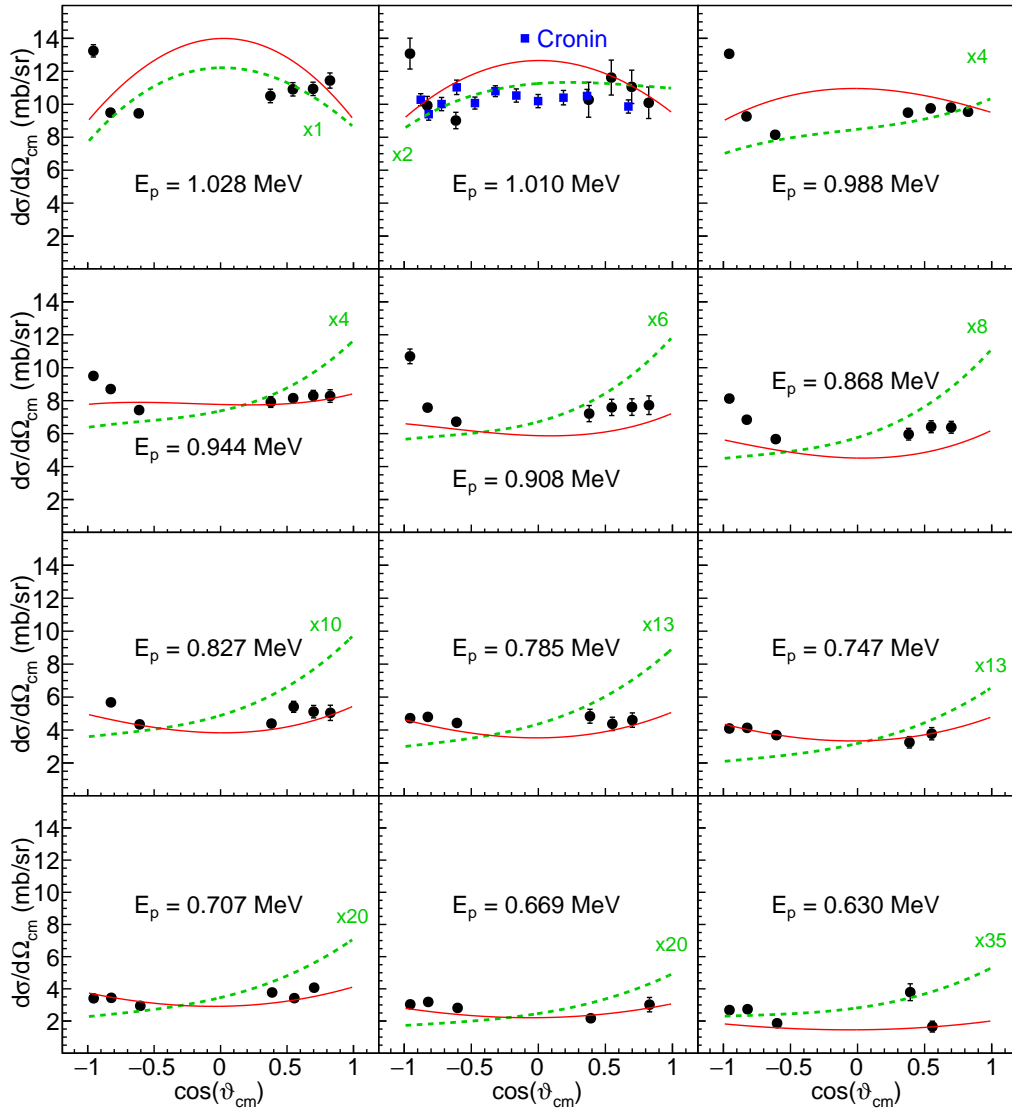


Figure 2.11: Angular distributions of the  $^{10}\text{B}(p, \alpha_0)^7\text{Be}$  reaction, as a function of the proton energy. Vertical bars represent statistical errors. Blue squares report angular distribution data obtained by Cronin [218] at 1 MeV. Green dashed lines:  $R$ -matrix calculations of angular distributions obtained by using the resonance parameters reported in the literature [202, 212, 213, 215, 232]. The absolute cross section scales have been multiplied by the scaling factors indicated in the figure for ease of display. Red solid lines:  $R$ -matrix calculations of angular distributions (mb/sr) obtained by using parameters reported in Table 2.2, columns 3-10, that have been derived from the data fit procedure described in paragraph 2.2.3.

## 2.2 The structure of $^{11}\text{C}$ with the $^{10}\text{B}(p,\alpha)^7\text{Be}$ reaction

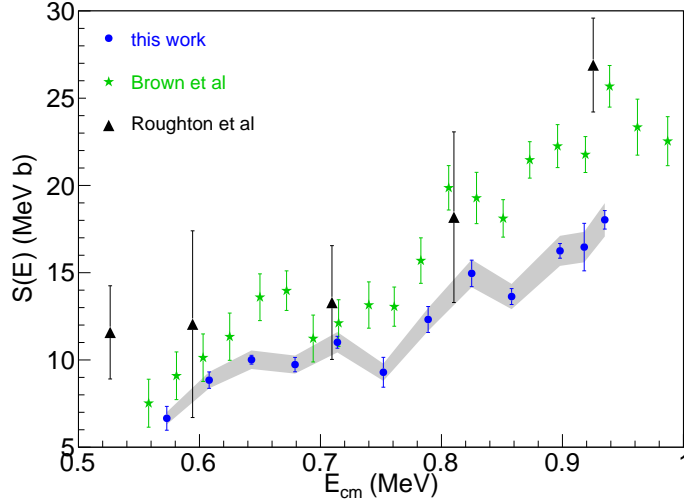


Figure 2.12:  $^{10}\text{B}(p,\alpha_0)^7\text{Be}$  astrophysical  $S$ -factor. Blue dots: present data (vertical bars: statistical errors; grey band: non-statistical errors). Green stars: data by Brown et al [225] as reported in [109, 224]. Black triangles: data by Roughton et al [223] as reported in NACRE [109] and NACRE2 [224].

$E_p = 0.630\text{-}0.785$  MeV range. The resulting  $S$ -factor is shown in Figure 2.12 (blue full dots), as a function of the center of mass energy  $E_{cm}$ . Vertical bars indicate statistical uncertainties, while the grey band indicates non-statistical ones (coming from the internal normalization procedure). We reported also, for comparison, data taken from the literature and reported in the compilations NACRE [109] and NACRE2 [224]. They are derived from Brown et al data (green stars) [225] and from Roughton et al [223] data (obtained using the thick target activation method; black triangles). Our data are  $\approx 30\%$  lower than Roughton et al ones [109, 223, 224]. Interestingly, the data sets point out the presence of a broad bump at  $E_{cm} \approx 0.65$  MeV. The presence of such a bump could reflect the excitation of some resonant state in  $^{11}\text{C}$  at  $E_x \approx 9.36$  MeV not reported up to date. The list of  $^{11}\text{C}$  excited states at  $E_x \approx 9\text{-}11$  MeV is reported in Table 2.2;  $E_x$  and  $J^\pi$  values reported in the first two columns are taken from the literature [202, 212, 213, 232].

### 2.2.3 $R$ -matrix fit of data and the spectroscopy of $^{11}\text{C}$

We tried to improve the spectroscopy of  $^{11}\text{C}$  excited states at  $E_x \approx 9\text{-}11$  MeV by performing a  $R$ -matrix fit of the present experimental data and also of other data reported in the literature. In particular,  $S$ -factor data of the  $^{10}\text{B}(p,\alpha_0)^7\text{Be}$  reaction derived from the present measurement and those of Refs. [218, 225, 236] (Figure 2.13a), the DCS data of the  $^{10}\text{B}(p,\alpha_1)^7\text{Be}_{0.429}$  reaction at  $90^\circ$  (Figure 2.13d) and the elastic scattering  $^{10}\text{B}(p,p_0)^{10}\text{B}$  DCS at  $130^\circ$  and  $150^\circ$  from Refs. [233, 234] (Figure

## Chapter 2. Clustering in light systems: an experimental campaign

---

2.13b-c) have been simultaneously used to perform a comprehensive  $R$ -matrix fit. In details, the  $^{10}\text{B}(p,\alpha_0)^7\text{Be}$   $S$ -factor in the bombarding region between 0.5 and 2.5 MeV has been obtained by complementing our data with the ones derived from the literature. Unfortunately, as discussed above, in this energy domain very few data have been reported up to date. The thick target yield data obtained by Roughton et al [223] and used by the NACRE collaboration [109] supply the sum of  $\alpha_0$  and  $\alpha_1$  channels; for this reason we did not include these data in the systematic of the  $^{10}\text{B}(p,\alpha_0)^7\text{Be}$  reaction. Apart from this measurement, the other data reported in the literature are DCS taken at various angles (mainly at about  $90^\circ$  in the laboratory frame) [218, 222, 225, 236]. Angular distributions reported by Cronin [218] in the 1.0-1.63 MeV domain point out the presence of small anisotropic effects, of the order of  $\pm 10\%$  or lower. Therefore, in absence of more comprehensive data and *as a first approximation*, we calculated the  $^{10}\text{B}(p,\alpha_0)^7\text{Be}$  angle-integrated cross section by using the DCS at  $\theta_{lab} \approx 90^\circ$  of Cronin [218] and Overley and Whaling [236] and assuming isotropy. It is interesting to note that these two data sets agree in their overlap region (at about  $E_p \approx 1.5$ -1.6 MeV). We used also the data by Brown et al [225] (DCS at  $\theta_{lab} \approx 137.8^\circ$ ) in the  $E_p \approx 0.5$ -1.2 MeV domain; we discarded the  $E_p > 1.2$  MeV data because of the possible presence of systematic errors in this energy region, as pointed out by Brown et al themselves [225] and Cronin [218]. The data by Brown et al have been subsequently normalized to our cross section scale; with a common scaling factor of  $\approx 0.76$ , our data and Brown et al ones are in agreement. An overall  $\pm 10\%$  uncertainty, taking into account for possible anisotropies in angular distributions, has been assigned to the  $\sigma(E)$  data obtained from Cronin [218], Overley and Whaling [236] and Brown et al [225] data. They are reported, as  $S$ -factor, in the panel (a) of Figure 2.13 as green stars (Overley and Whaling), black triangles (Cronin) and white diamonds (Brown et al). Our data are reported as blue dots (with statistical errors). A reasonable consistency between all data sets is observed. The list of  $^{11}\text{C}$  excited states at  $E_x \approx 9$ -11 MeV is reported in Table 2.2;  $E_x$  and  $J^\pi$  values reported in the first two columns are taken from the literature [202, 212, 213, 232]. Finally,  $^{10}\text{B}(\alpha,\alpha_0)$  elastic scattering data, published by Refs. [202, 237], have not been considered in the global fit because of strong differences between them.

To perform the  $R$ -matrix fit of all these data sets we used the  $R$ -matrix code AZURE2 [147, 238]. The channel radii have been estimated with the formula  $R = 1.4 \times (A_1^{1/3} + A_2^{1/3})$  fm [213]. In the fit procedure, we allow the overall normalization of the elastic scattering data by Refs. [233, 234] to be slightly varied within 15%.

We started to calculate the scattering and reaction cross sections by including excited states of  $^{11}\text{C}$  at 8.699, 9.20, 9.65, 9.78, 9.97, 10.083, 10.67 MeV [202, 212, 213, 232]. The used resonance parameters ( $E_x$ ,  $J^\pi$  and partial widths) were taken from the literature, namely from [202, 212, 213, 215, 232]. A grey dashed line in Figure 2.13(a) shows the results of such a calculation for the  $^{10}\text{B}(p,\alpha_0)^7\text{Be}$  reaction channel. The overall agreement is not satisfactory ( $\tilde{\chi}^2 \approx 24$ ) especially at low ener-

## 2.2 The structure of $^{11}\text{C}$ with the $^{10}\text{B}(p,\alpha)^7\text{Be}$ reaction

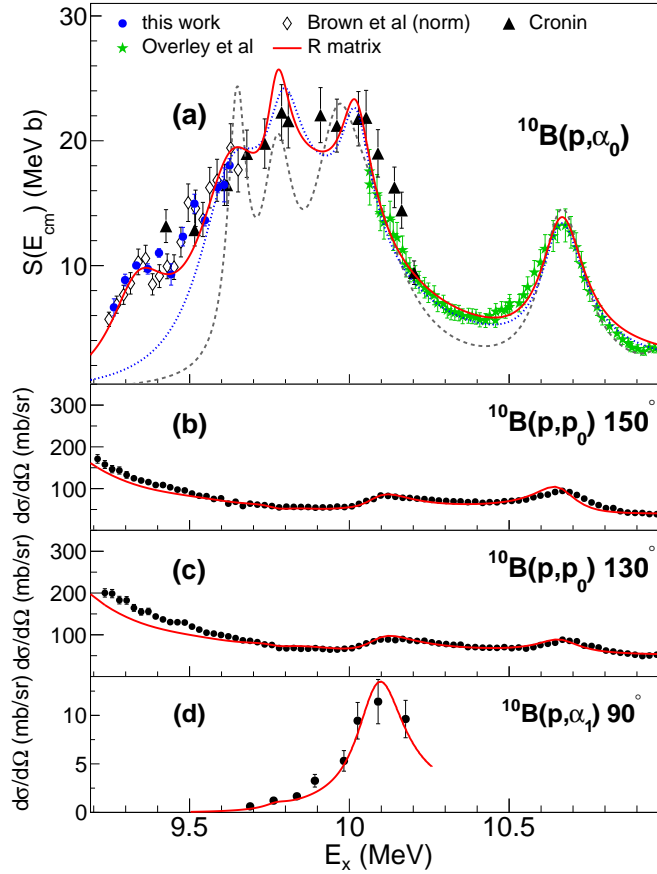


Figure 2.13: (a)  $S$ -factor of the  $^{10}\text{B}(p,\alpha_0)^7\text{Be}$  reaction derived from the present experimental data and from the DCS data taken from Refs. [218, 225, 236], as discussed in the text. (b,c)  $^{10}\text{B}(p,p_0)^{10}\text{B}$  DCS at  $150^\circ$  and  $130^\circ$  respectively, taken from [233, 234]. (d)  $^{10}\text{B}(p,\alpha_1)^7\text{Be}$  DCS at  $90^\circ$  from [218]. In all panels, red lines indicate the result of the global  $R$ -matrix fit.

gies ( $E_x < 9.7$  MeV); strong disagreements are also observed for the other channels here investigated (not reported in Figure 2.13(b-d) for clarity reasons). We verified that a change of the sign of interference between the two  $5/2^+$  states at low energy does not lead to an improvement of the data fit. We performed also angular distribution calculations at the various energies here studied. The results (in absolute units) are shown as green dashed lines in Figure 2.11. They have been multiplied by the factors given by labels in the Figure 2.11 for clarity reasons. A strong disagreement, both in shape and in absolute values, is observed especially at the lowest energies ( $E_p < 0.7$  MeV). With the level scheme given in the literature, this region is dominated by the tails of the very broad 9.20 MeV  $5/2^+$  state ( $E_p = 0.56$  MeV,  $\Gamma_{lab} = 0.55$  MeV) and of the 9.64 MeV ( $3/2^-$ ) state ( $E_p = 1.05$  MeV,  $\Gamma_{lab} = 0.23$  MeV). The observed disagreement puts in question these assignments. Indeed, the

## Chapter 2. Clustering in light systems: an experimental campaign

$E_x$ (MeV)	$J_{lit}^\pi$	$\Gamma_{tot}^{lit}$	$E_x$ (MeV)	$J^\pi$	$\ell_{\alpha_0}$	$\Gamma_{p_0}$	$\Gamma_{\alpha_0}$	$\Gamma_{\alpha_1}$	$\Gamma_{tot}$	Ref.
9.20	$5/2^+$	$500 \pm 90$								[202, 212, 213, 232]
			9.36	$(5/2^-)$	2	4	235		239	this work
9.65	$(3/2^-)$	$210 \pm 40$	9.65	$(3/2^-)$	0	45	223		268	[202, 212, 213, 218, 232]
9.78	$(5/2^-)$	$240 \pm 50$	9.80	$5/2^-$	2	12	116	4	132	[202, 212, 213, 232]
9.97	$(7/2^-)$	$120 \pm 20$	9.98	$7/2^-$	2	498	66	4	568	[202, 212, 232]
10.08	$7/2^+$	$\approx 230$	10.02	$7/2^+$	3	13	105	1	119	[202, 212, 213, 218, 232]
			10.10	$(5/2^+)$				36	183	this work
10.68	$9/2^+$	$200 \pm 30$	10.67	$9/2^+$	3	126	37		163	[202, 212, 213, 232, 236]

Table 2.2: (first 3 columns)  $^{11}\text{C}$  states reported in the literature ([232] database) in the  $9\text{MeV} < E_x < 11\text{MeV}$  excitation energy domain. (columns 4-10)  $^{11}\text{C}$  spectroscopy obtained from the  $R$ -matrix fit of the angle-integrated cross section data set of this work and shown in Figure 2.13. Round brackets indicate tentative  $J^\pi$  assignments.

difficulties to describe DCS of the  $^7\text{Be}(\alpha, \alpha_0)^7\text{Be}$  and  $^{10}\text{B}(\text{p}, \alpha_0)^7\text{Be}$  reactions with a very broad  $5/2^+$  state placed at 9.20 MeV have been pointed out by other works [202, 213]. These findings underline the need of a revision of  $^{11}\text{C}$  spectroscopy in this excitation energy region.

In our fit procedure, the resonance energy  $E_x$  and the partial width of states were allowed to vary within reasonable values (i.e. the resonance energy  $E_x$  should not overcome some tens of keV with respect to the value reported in the literature [232] and the partial widths should not overcome the corresponding single particle (Wigner) limit, defined as  $\Gamma_W = 2P_\ell \gamma_W^2$ , where  $\gamma_W^2 = \frac{3\hbar^2}{2\mu R^2}$  [142]). The contribution of the 8.699 MeV state is found to be negligible in the presently explored energy domain, while the 9.20 MeV state falls outside the region here investigated. The  $J^\pi$  assignments of the 9.65, 9.78, 9.97, 10.083, 10.67 MeV states were fixed to the values reported in the literature [202, 212, 213, 232]. Because of the already discussed problems in the description of low energy experimental angular distributions, we included in the fit the presence of a state in the  $E_x = 9.3\text{-}9.4$  MeV region, and we tried different  $J^\pi$  assignments. Further, to simultaneously describe the resonant peak at about 10.1 MeV in the  $^{10}\text{B}(\text{p}, \alpha_1)^7\text{Be}_{0.429}$  DCS and the broad bump at about 10.1 MeV in the elastic scattering DCS, we suggest to introduce a  $5/2^+$  state at 10.1 MeV, having only  $\Gamma_{p_0}$  and  $\Gamma_{\alpha_1}$  partial widths. This assumption is supported by the systematic energy shift (about 0.1 MeV) observed between the peaks in DCS of reaction or scattering experiments involving  $^{11}\text{C}$  compound nucleus and having  $\alpha_0$  or  $\alpha_1$  exit channels. As an example, both Brown et al and Cronin [218, 225] pointed out an energy shift of about 0.1 MeV in the  $^{10}\text{B}(\text{p}, \alpha_0)$  and  $^{10}\text{B}(\text{p}, \alpha_1)$  DCS; Cronin [218] observed that these two peaks could in principle be due to different states of  $^{11}\text{C}$ . In more recent times Yamaguchi et al [202] reported  $^7\text{Be}(\alpha, \alpha_0)$  and  $^7\text{Be}(\alpha, \alpha_1)$  scattering data and, despite the low statistics, a similar shift appears possible. The

## 2.2 The structure of $^{11}\text{C}$ with the $^{10}\text{B}(p,\alpha)^7\text{Be}$ reaction

result of such a fit gives a reasonably good description of all channels here studied: it is represented by solid red lines in Figure 2.13(a-d). In particular, a  $\tilde{\chi}^2 \approx 1.2$  is obtained for the  $^{10}\text{B}(p,\alpha_0)$  reaction. The good overall description, in terms of shapes and absolute cross sections, of the angular distributions at  $E_p < 0.827$  MeV (Figure 2.11, red solid lines) suggests a tentative ( $5/2^-$ ) assignment for the 9.36 MeV state. The parameters obtained by the fit procedure are reported in Table 2.2, columns 3-10. The exclusion of the 9.36 MeV state from the fit leads to a much poorer description of the experimental data in the  $E_{cm} < 1$  MeV region, as shown in Figure 2.13a by the blue dotted line for the  $(p,\alpha_0)$  channel ( $\tilde{\chi}^2 \approx 8$ ). In general,  $\Gamma_{\alpha_0}$  values are of the order of 10 – 30% of the corresponding Wigner limits, except for the 9.36 MeV ( $5/2^-$ ) state ( $\frac{\Gamma_{\alpha_0}}{\Gamma_W} \approx 0.7$ ); this large  $\alpha$ -width suggests a pronounced  $\alpha$ -cluster nature of this state. For simplicity, in the present analysis we have not considered the possible presence of a direct contribution in the  $(p,\alpha_0)$  cross section at low energies [239]; its presence could modify the  $\Gamma_p$  and  $\Gamma_{\alpha_0}$  values here quoted.

Finally, it is interesting to observe that the experimental angular distributions at higher energies ( $E_p > 0.9$  MeV) are poorly reproduced by  $R$ -matrix calculations performed with the parameters reported in Table 2.2. These discrepancies could be explained by considering different  $J^\pi$  assignments for the 9.64 and 9.78 MeV states, that have been tentatively reported in the literature as ( $3/2^-$ ) and ( $5/2^-$ ), respectively [232]. Unfortunately, the present data on angular distributions explore only very partially the bombarding energy region between the resonance peaks, and therefore no definite conclusions can be drawn. New measurements of the  $^{10}\text{B}(p,\alpha_0)^7\text{Be}$  reaction with finer energy steps and with broader bombarding energy and angular ranges, together with extended measurements of  $\alpha+^7\text{Be}$  elastic scattering cross sections, would allow to obtain finer conclusions on the spectroscopy of  $^{11}\text{C}$ . Finally, the results discussed in this Section have been recently published in Ref. [240].

### 2.2.4 Impact of our results on successive works

The  $^{10}\text{B}(p,\alpha_0)$  cross section here measured is in very good agreement with the results of a subsequent experiment of Caciolli and collaborators [241]. They measured the total cross section of the  $^{10}\text{B}(p,\alpha_0)^7\text{Be}$  reaction in the energy range  $E_{cm} = 250\text{-}1182$  keV by using the activation method at INFN-LNL. Furthermore, the existence of the 9.36 MeV ( $5/2^-$ ) and 10.15 MeV ( $5/2^+$ ) states in  $^{11}\text{C}$  has been very recently confirmed in a new global  $R$ -matrix fit performed by Wiescher et al. in Ref. [242]. The authors of [242] selected our work as the most comprehensive  $R$ -matrix analysis of the  $^{11}\text{C}$  nucleus published in the literature up to date and used our fit parameters as a starting point for their fitting procedures. They reported a level scheme quite similar to the present one (Table 2.2). Another extremely recent  $R$ -matrix calculation is reported in Ref. [243]. In this work, indirect data obtained with the *Trojan Horse Method* (THM) allowed to complement the existing data sets down to energies of astrophysical interest, e.g. in the range  $5 \text{ keV} \leq E_{cm} \leq 1.5 \text{ MeV}$ . The result of the complete  $R$ -matrix analysis in the low energy range gives further

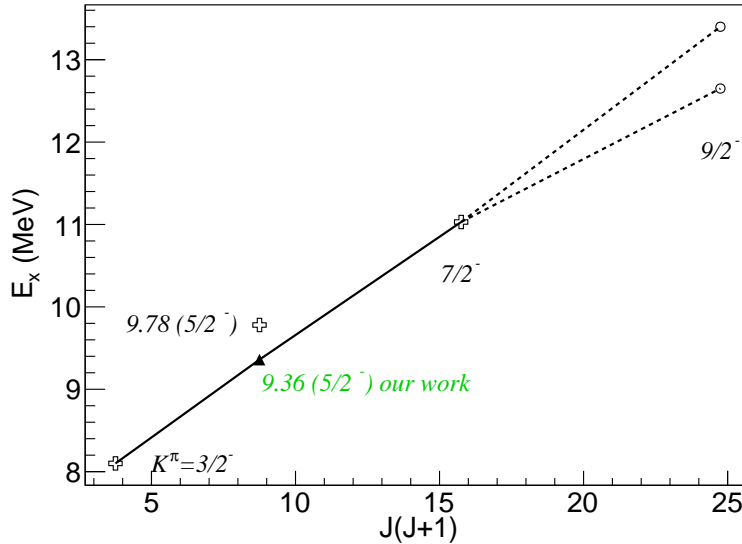


Figure 2.14:  $^{11}\text{C}$  negative parity ( $K^\pi = 3/2^-$ ) rotational band proposed in Ref. [202]. The  $3/2^-$ ,  $5/2^-$ ,  $7/2^-$  and hypothetical  $9/2^-$  members (open symbols) are indicated in [202], while the black filled triangle represents the 9.63 MeV  $5/2^-$  state proposed in our work [240].

hints on the consistency of the existence of the 9.36 MeV ( $5/2^-$ ) state. Furthermore, an improved normalization of indirect data was obtained by using our values of astrophysical  $S$ -factor in the energy range explored in the present work [240].

Finally, a naive speculation coming from the present analysis. A new negative-parity rotational band ( $K^\pi = 3/2^-$ ) in  $^{11}\text{C}$  was proposed in Ref. [202]. The band-head of such a band is the 8.10 MeV state ( $3/2^-$ ). The second member is considered by the authors to be the 9.78 MeV  $5/2^-$  state. The subsequent member is indicated to lie at 11.03 MeV, as shown by their  $R$ -matrix fit, that reports a state with a possible  $7/2^-$   $J^\pi$  value. Their systematic predicts even a further  $9/2^-$  member which could be located at around 13 MeV. The authors of [202] proposed two possible states as candidates for this high-spin member, either the 12.65 MeV or the 13.4 MeV state. The members of this band were associated to a cluster  $2\alpha$ - $^3\text{He}$  configuration. Interestingly, if one includes the 9.36 MeV  $5/2^-$  state, as observed in our analysis, in the rotational band described in Ref. [202] (black filled triangle in Figure 2.14), one observes a linear correlation better than the one obtained by including the 9.78 MeV state as  $5/2^-$  member, as suggested in [202]. Giving the pronounced  $\alpha$ -nature of the 9.36 MeV state, one can naively speculate that this state could be the  $5/2^-$  member of such a molecular rotational band. A linear extrapolation of this band would result in the presence of a 13.4 MeV state as the  $9/2^-$  member. Experimental investigations near this excitation energy are therefore required to confirm such a speculation.

## 2.3 Clustering in $^{12}\text{C}$ : the decay path of the Hoyle state

Exploring the structure of  $^{12}\text{C}$  is extremely fascinating, since it is strongly linked to the existence of  $\alpha$ -clusters in atomic nuclei and to the interplay between nuclear structure and astrophysics. As discussed in paragraph 1.4.2 of Chapter 1, an interesting state of the  $^{12}\text{C}$  nucleus, the so-called Hoyle state, lies at an excitation energy of 7.654 MeV. The structure properties of the Hoyle state are quite unusual and their investigation represents one of the most important open problems in modern nuclear physics. In particular, it is known that its decay mode is dominated by the  $\alpha$  *sequential decay* (SD), but a precise measurement of its *direct decay* (DD) width is required to constraint theoretical models attempting to describe its cluster structure (a detailed description of these models and their recent results is given in paragraph 1.4.1 of the present thesis). From the astrophysical point of view, the SD of the Hoyle state is important in stars which burn helium at low temperature ( $T < 0.08$  GK, see paragraph 1.4.2 for details).

Despite of the importance of a precise knowledge of its decay modes, no definitive conclusions can be at present drawn from an experimental point of view regarding the Hoyle state in  $^{12}\text{C}$ . Recently, a quite large number of experiments have been carried out to explore how the Hoyle state decays via  $3\alpha$  emission, i.e. what is the *direct* decay rate relative to the *sequential* one. An upper limit to the direct decay branch was first given by Freer et al. in 1994 [244]. In their work they reported that the branching ratio (BR) of the Hoyle state decay bypassing the  $^8\text{Be}$  ground state was lower than 4%, i.e.  $(\Gamma_\alpha - \Gamma_{\alpha_0})/\Gamma_\alpha < 0.04$ . Here  $\Gamma_\alpha$  indicates the global  $\alpha$  decay width and  $\Gamma_{\alpha_0}$  is the partial width of the  $\alpha$  emission leading to the ground state of  $^8\text{Be}$ . More recently, Raduta et al. [245] reported a result in strong contradiction with the previous one, finding a rather high value ( $17 \pm 5\%$ ) of direct BR. Such contrasting results stimulated a series of new experiments aimed at determining the actual value of the direct decay BR of the Hoyle state. New upper limits of 0.5% (95% C.L.) and 3.9% (99.75% C.L.) were obtained by Kirsebom et al. [156] and by Manfredi et al. [246] respectively. Two more recent experiments by Rana et al. [247] and Morelli et al. [248] suggested non-zero values of direct decay BR, respectively of  $(\Gamma_\alpha - \Gamma_{\alpha_0})/\Gamma_\alpha = 0.91 \pm 0.14\%$  and  $1.1 \pm 0.4\%$ . Finally, thanks to a high statistics experiment, Itoh et al. [249] determined an improved upper limit of the direct BR of 0.2% (95% C.L.). It is important to underline that, as discussed in [244, 249], the use of strip detectors introduces the presence of a non-vanishing background, that reduces the sensitivity in measuring the small signal of the direct decay BR. Taking into account the importance of fully understanding  $\alpha$  clustering effects in the nuclear structure of  $^{12}\text{C}$ , it is mandatory to improve our knowledge of the direct-to-sequential decay BR of the Hoyle state, since theoretical estimations of this quantity are given at the 0.1% level, i.e. well below the most recent upper limit reported in the literature [51, 249].

### 2.3.1 Experimental technique: the $^{14}\text{N}(\text{d}, \alpha)^{12}\text{C}$ reaction

To account all the above discussed issues, and to shed light on the direct to sequential BR of the Hoyle state, we performed a new high-precision and high statistics experiment. The basic idea of our investigation was to populate  $^{12}\text{C}$  nuclei in their Hoyle state and then to detect, with a high resolution apparatus, their decay through  $3\alpha$  emission. The decay path of the Hoyle state can be in such a way studied via invariant mass techniques and the use of the Dalitz plot, as discussed in paragraph 1.5.3 of the present thesis. In this work, we used the  $^{14}\text{N}(\text{d}, \alpha)^{12}\text{C}$  nuclear reaction. A 10.5 MeV deuteron beam was provided by the 15 MV tandem accelerator of the INFN-LNS (Catania, Italy). As a detection apparatus we used the combination of a  $\Delta\text{E-E}$  telescope and a high granularity hodoscope detector. We completely reconstructed the kinematics of the reaction by simultaneously detecting the four  $\alpha$  particles emitted in the final state, namely the  $\alpha$  ejectile, used to tag the excitation of the  $^{12}\text{C}$  residue at its Hoyle state ( $E^* = 7.654$  MeV), and the three  $\alpha$  particles from by the Hoyle state decay.

The hodoscope detector, named *superOSCAR*, is a modified version, specifically built for this experiment, of the *OSCAR* hodoscope [250]. While the *OSCAR* device is based on two-detection stage modules (see Appendix A.0.4), the *superOSCAR* hodoscope consists in only one detection stage, which corresponds to 4 *OSCAR* modules without the first detection stage and arranged as a square of  $2 \times 2$  modules. It was designed to ensure the detection of the three  $\alpha$  particles coming from the Hoyle state decay with the highest possible efficiency and to avoid the artificial introduction of background. This is achieved by using a system of independent silicon detectors. The independency of detection cells allow to obtain an unambiguous particle tracking, free from track misassignment previously seen in similar experiments performed with DSSSDs [249]. Globally our hodoscope is constituted by  $8 \times 8$  independent silicon pads ( $1 \text{ cm}^2$ ,  $300 \mu\text{m}$  thick). It is placed in such a way that its center is aligned with the axis of the  $^{12}\text{C}(7.654)$  three  $\alpha$  emission cone, when the corresponding  $\alpha$  tagging ejectile is detected by the  $\Delta\text{E-E}$  telescope.

The  $^{12}\text{C}$  excitation energy spectrum, reconstructed from the measurement of kinetic energy and emission direction of the particles detected in the  $\Delta\text{E-E}$  telescope, is shown on Figure 2.15 by the blue line. Only particles stopping in the first detection stage are selected, allowing to strongly reduce contaminations from (d,d) and (d,p) reactions on the target constituents. This technique, named *anti-coincidence* telescope technique, was previously used, in the same reaction, in Ref. [251]. In the present work, a  $100 \mu\text{m}$  silicon stage, followed by a thick  $1500 \mu\text{m}$  silicon is used as  $\Delta\text{E-E}$  anti-coincidence telescope. We made a systematic study of the reaction contaminants which are expected when deuterons impinge on any of the possible elements present in the target. The anti-coincidence telescope allows to exclude largest part of events due to the contaminants simply by imposing the anti-coincidence of the first and the second detection stage of the telescope. The excitation energy spectrum reduces to the filled one if we select events with 4-particles in coincidence, i.e.

### 2.3 Clustering in $^{12}\text{C}$ : the decay path of the Hoyle state

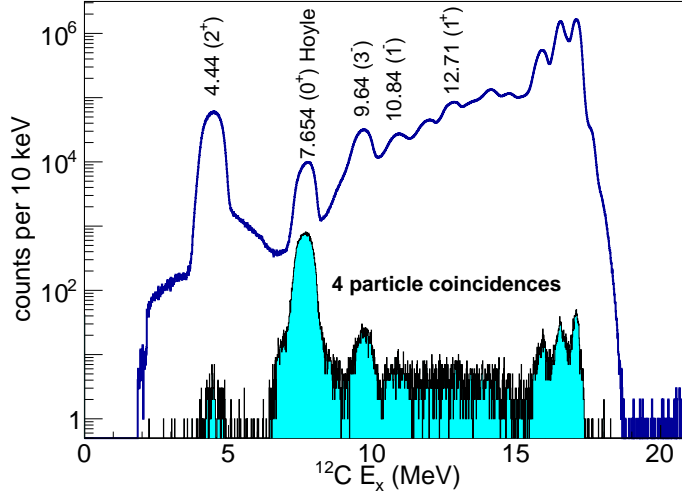


Figure 2.15:  $^{12}\text{C}$  excitation energy spectrum reconstructed from the measured momentum of particles detected by the  $\Delta E$ - $E$  anti-coincidence telescope (blue line). Labels are used to indicate the energy and spins of well-known states of  $^{12}\text{C}$ . (filled histogram) Same spectrum obtained by selecting 4-particles coincidences.

by selecting events where 3 particles are detected in coincidence by the hodoscope. This spectrum exhibits a pronounced peak at  $E_x = 7.654$  MeV, corresponding to the energy position of the Hoyle state, while background as well as other peaks are strongly suppressed. For the subsequent analysis, events are selected by gating on the Hoyle peak and on the corresponding four-particle total energy spectrum, which unambiguously identifies the reaction channel of interest.

In Figure 2.16 we report (full dots) the  $^{12}\text{C}$  excitation energy spectrum obtained by an invariant mass analysis of ternary coincidences inside the hodoscope, assuming that they are  $\alpha$  particles<sup>7</sup>. The red dashed line is the result of a complete Monte Carlo simulation of the effect of the detection system on the reconstruction of the three  $\alpha$  particles resulting from the in-flight decay of the Hoyle state. To produce this result we consider four  $\alpha$  particles fully reconstructed events from  $^{14}\text{N}(d, \alpha_2)^{12}\text{C}(7.654)$  reaction simulated data. In our simulation we have taken into account both the profile of the beam on the target and the angular distribution of the emitted  $\alpha$  ejectile, as reported in [252] at the same incident energy. The geometry of the detectors and their energy resolution are also taken into account in the simulation. The result of the simulation is in excellent agreement with the experimental data, confirming the unambiguous reconstruction of this physical process. The invariant mass of the Hoyle state is determined with a resolution of about 47

<sup>7</sup>The possible amount of events different from the  $^{14}\text{N}(d, \alpha_2)^{12}\text{C}(7.654)$  reaction ( $4\alpha$ ) is strongly suppressed thanks to the great sensitivity of the apparatus to this specific reaction channel, even without identifying in charge and in mass the three particles in the hodoscope.

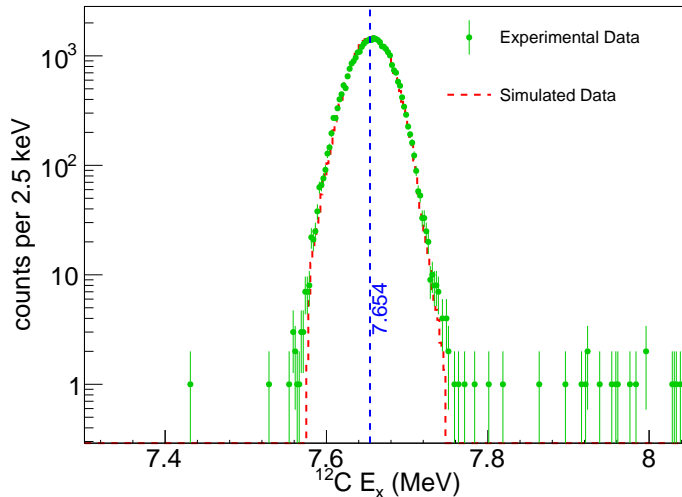


Figure 2.16: Three particle invariant mass spectrum ( $^{12}\text{C } E_x$ ) gated on the Hoyle peak of Figure 2.15. Experimental points are compared with the result of a Monte Carlo simulation of the  $^{14}\text{N}(d, \alpha_2)^{12}\text{C}(7.654)$ , which details are explained in the text. Events under the peak centered at 7.654 MeV are due to the decay of the Hoyle state. The evaluated background level is about 0.036%.

keV (FWHM), while the center of the distribution is in agreement with the position of the Hoyle state within an indetermination smaller than 1 keV. Four- $\alpha$  fully detected events are thus selected by means of a further bi-dimensional cut on the  $Q$ -value and on the invariant mass of the three  $\alpha$ -particles. In such a way we obtain a number of about 28000 decay events of Hoyle state, an amount well higher than any other previous investigation. This plot is particularly useful since it allows to estimate the amount of background events, i.e. spurious events which are topologically compatible with the events of interest. The background level is extremely low thanks to the stringent constraints on the data, the sensitivity of the apparatus to the physical process and the unambiguous particle track identification achieved by the use of the hodoscope. It can be evaluated by inspecting the right and left sides of the spectrum; it amounts to about 0.036% of the total number of selected events.

### 2.3.2 Analysis of the direct $\alpha$ -decay width of the Hoyle state

Details about the three- $\alpha$  decay mechanisms of the Hoyle state can be studied by using the symmetric Dalitz plot, as explained in paragraph 1.5.3 of Chapter 1. This technique is particularly suited to geometrically visualize the decay pattern into three equal-mass particles by using the cartesian coordinates of equation 1.82, where  $\varepsilon_{i,j,k}$  (the normalized energies of the three particles in their decay frame) are selected so that  $\varepsilon_i \geq \varepsilon_j \geq \varepsilon_k$ . In Figure 2.17 we show the Dalitz plot obtained from

### 2.3 Clustering in $^{12}\text{C}$ : the decay path of the Hoyle state

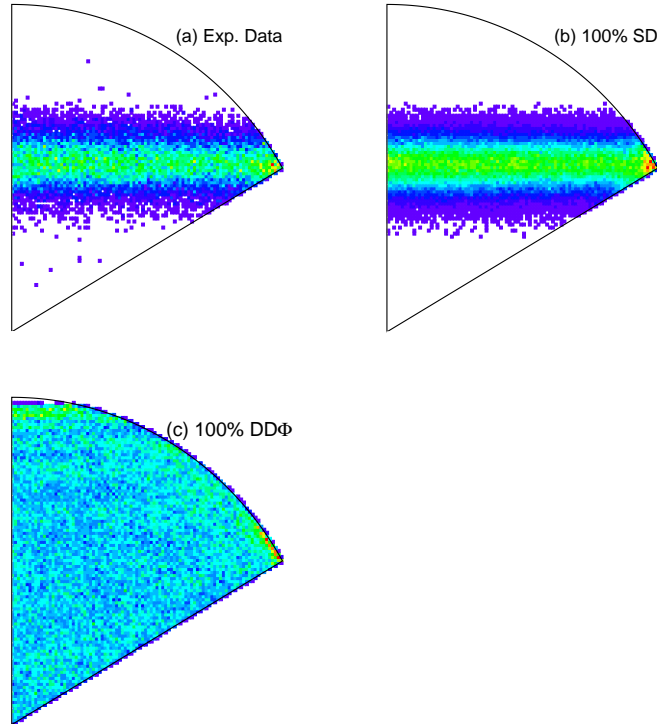


Figure 2.17: Experimental symmetric Dalitz plot (a) compared with Monte Carlo simulations of (b) 100% SD and (c) 100% DD $\Phi$  decays. Further details on the simulation procedure are explained in the text. Simulated SD events result in an horizontal band and the effect of our experimental apparatus is expected to not introduce any significant contamination outside this band, as instead observed in previous works [244, 249].

the experimental data selected with the above discussed procedure (a) compared with the analogous plot constructed with simulated 100% sequential decay (SD) data (b) and the 100% DD $\Phi$  data (c). Simulated data have been obtained with the same prescription used to construct Figure 2.16. In this Dalitz plot representation, a sequential decay (SD) mechanism would populate a uniform horizontal narrow band, while a spread of events along the whole plot region would be observed in the case of DD $\Phi$  (the direct decay into the available phase space). The plots of Figure 2.17(b) and (c) are particularly useful to characterize the expected distortion introduced by the experimental apparatus on the analysis to discriminate the decay mechanism. In particular, two significant conclusions can be extracted from these plots. First, the effect of the detection device on the three  $\alpha$  reconstruction results only in a broadening of the SD band, without introducing a significant background

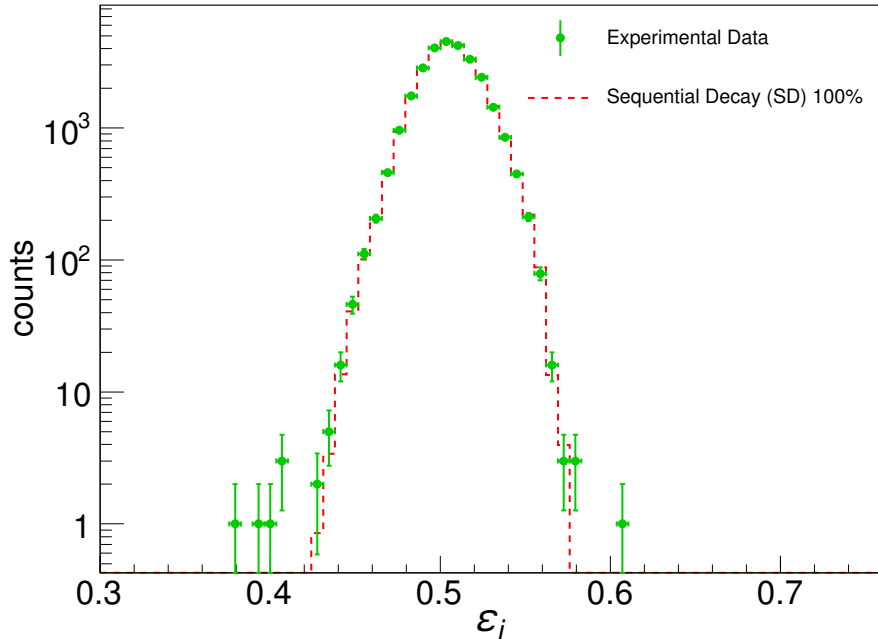


Figure 2.18:  $\varepsilon_i$  distribution, i.e. the largest energy among the normalized decay energy of the three  $\alpha$  particles in their emitting reference frame. Experimental data (green circles) are compared with the result of a Monte Carlo simulation (red dashed line) where we assumed 100% sequential decay (SD).

contamination in the region outside the band. This result demonstrates that we are able to distinguish between the two mechanisms, for the first time, with an exceptionally low background level. In previous investigations [249], the Dalitz plot constructed with simulated sequential decays shows the presence of data points outside the above mentioned horizontal band, thus containing ambiguities and leading to a reduced sensitivity on direct decay contributions. These difficulties arise from the misassignment of particle tracks inside the strip detectors used in their experiment, as the authors of Ref. [249] state. Our experiment is free from such problems thanks to the use of an hodoscope of independent detectors free of pixel assignment ambiguities, which helps to unambiguously disentangle sequential and direct decays. A second, very important conclusion can be deduced by comparing the behaviour of the experimental Dalitz plot of Figure 2.17(a) with the simulated ones. An excellent agreement with the simulated SD horizontal band is clearly seen, while only few counts populate the region outside the SD band.

A more quantitative analysis can be achieved by inspecting the  $\varepsilon_i$  distribution, i.e. the distribution of the largest energy among the  $\varepsilon_{i,j,k}$  normalized energies [249].

## 2.3 Clustering in $^{12}\text{C}$ : the decay path of the Hoyle state

---

The  $\varepsilon_i$  distribution is shown by the green points of Figure 2.18. These values are expected to lie, in the case of a DD $\Phi$  decay, between 0.33 (when particles share an equal amount of the decay energy) and 0.67 (when one  $\alpha$  is emitted in the opposite direction of the other two). In contrast, a value of about 0.506 is expected for a SD mechanism. In order to estimate the BR of direct decays contributing to the width of the Hoyle state, we have compared the experimental data with the result of a Monte Carlo simulation assuming 100% of SD (red dashed line on Figure 2.18). From an analysis of this spectrum, it is possible to identify an extremely small amount of counts not reproduced by the SD simulation. They correspond to background events falling into the selection of Figure 2.16 and, eventually, to a *signal* of DD.

Starting from the observed experimental data, we can determine the *lower* and *upper* limits of the DD BR, by assuming that both the DD and background counts are regulated by the Poisson statistics [253]. In doing this evaluation, we follow the Feldman and Cousin’s approach to the analysis of small signals described in Ref. [254], and we carefully take into account the different expected detection efficiencies for DD and SD decay, as determined with Monte Carlo simulations. The lower limit is found to be compatible with *zero*. Therefore we quote an upper limit on the BR of the direct three  $\alpha$  decay of 0.043% (95% C.L.). This value is about a factor 5 lower than the state of the art experiment [249] and it is in agreement with the previous results by Freer et al. [244], Manfredi et al. [246], Kirsebom et al. [156] and Itoh et al. [249], introducing an improvement of about a factor 5 with respect to the previous most statistically significant work [249]. These results provide important information about the  $\alpha$  cluster structure of  $^{12}\text{C}$  Hoyle state and can be useful for theoretical models attempting to reproduce its structure. They have also a significant astrophysical impact. Indeed, the further reduction of the upper limit of direct decay implies that calculations of the triple- $\alpha$  stellar reaction rate at temperatures lower than  $10^8$  K should to be correspondingly revised [66, 110].

### 2.3.3 Impact of our results on successive works

The results on the direct decay width of the Hoyle state here discussed have been recently published in Ref. [255]. An independent and almost simultaneous work was performed by the Birmingham group, and published in Ref. [256]. They used inelastic scattering of  $\alpha$ -particles on  $^{12}\text{C}$  to populate the Hoyle state, and then they used an array of four DSSSDs detectors to study their corresponding disintegrations. They place an upper limit of 0.047% of the total events to the direct decay width of the Hoyle state. This result is in excellent agreement with ours, being achieved with a completely different experimental technique. Both results of Refs. [255, 256] have been the object of a recent *Viewpoint in Physics* [257].

## 2.4 Clustering in $^{13}\text{C}$ with $\alpha + {}^9\text{Be}$ reactions

Despite strong theoretical efforts made to clarify the structure of  $^{13}\text{C}$ , as largely discussed in paragraph 1.4.3, experimental data on the spectroscopy of this nucleus at excitation energies above the  $\alpha$  emission threshold are quite fragmentary and often characterized by contrasting  $J^\pi$  assignments that prevent any firm conclusions on the structure of this nucleus. There is a class of nuclear reactions which could help to clarify the present situation<sup>8</sup>, like, for example, the  $\alpha + {}^9\text{Be}$  elastic and inelastic resonant scattering [259–265], the  ${}^9\text{Be}(\alpha, n){}^{12}\text{C}$  reactions [266–268], the  $n + {}^{12}\text{C}$  elastic and inelastic scattering [269–271], and transfer reactions such as the  ${}^9\text{Be}({}^6\text{Li}, d){}^{13}\text{C}^*$  case [272–274].

Among the various possible reactions channels,  $\alpha + {}^9\text{Be}$  scattering has been suggested to be one of the best ways to populate molecular states in  $^{13}\text{C}$  [265] because of the well pronounced molecular structure of  ${}^9\text{Be}$  target nucleus [55, 118]. In Ref. [260], the structure of  $^{13}\text{C}$  in the  $E_x \approx 13.3\text{--}14.5$  MeV range has been explored, with this reaction, by performing fits of experimental excitation functions at several angles with predictions based on the Blatt-Biedenharn formalism [36]. In more recent times  $R$ -matrix calculations have been performed by Freer et al [265] to understand the complexity of the  $^{13}\text{C}$  spectroscopy above the  $\alpha$ -threshold. They succeeded in measuring the  ${}^9\text{Be} + {}^4\text{He}$  elastic scattering in inverse kinematics. The  $R$ -matrix fit of one excitation function at  $\theta_{cm} \approx 180^\circ$  allowed to revise the  $J^\pi$  assignments and the partial width values of several  $^{13}\text{C}$  states in the  $E_x \approx 13.3\text{--}16.2$  MeV range. In particular no clear evidences of the  $\frac{9}{2}^\pm$  members of the molecular bands suggested in Ref. [127] have been found.

### 2.4.1 Selection of reaction data-set

In the context of the present thesis, we perform, for the first time, a comprehensive  $R$ -matrix calculation of several reaction channels involving the structure of  $^{13}\text{C}$  as a compound system. We included in our calculations elastic scattering ( $\alpha_0$ ) differential cross sections (DCS) obtained at several backward angles, inelastic scattering DCS to the first excited state ( $\alpha_1$ , corresponding to  $E_x = 1.684$  MeV) in  ${}^9\text{Be}$  obtained at  $\theta_{lab} = 70^\circ$ , and integrated cross sections of  ${}^9\text{Be}(\alpha, n_0){}^{12}\text{C}$  and  ${}^9\text{Be}(\alpha, n_1){}^{12}\text{C}$  reactions.

The largest part of data used in the present  $R$ -matrix analysis derives from an experiment performed at the TTT3 tandem accelerator in Napoli, Italy [229]. Beams of doubly-ionized  ${}^4\text{He}$  bombarded a self-supporting  ${}^9\text{Be}$  target ( $122 \mu\text{g}/\text{cm}^2$  thick). The beam energy was varied in 60 keV steps, covering the  $E_\alpha \simeq 3.5\text{--}10$  MeV domain. An array of collimated silicon detectors placed at various angles was used as a detection apparatus. With this apparatus, elastic scattering DCS were measured at  $160^\circ$ ,  $150^\circ$ ,  $135^\circ$ ,  $110^\circ$  in the laboratory frame. In the present dissertation we are interested in the details concerning the  $R$ -matrix description of the data. For

---

<sup>8</sup>A review of results concerning  $^{13}\text{C}$  spectroscopy is reported in Ref. [258].

## 2.4 Clustering in $^{13}\text{C}$ with $\alpha + ^9\text{Be}$ reactions

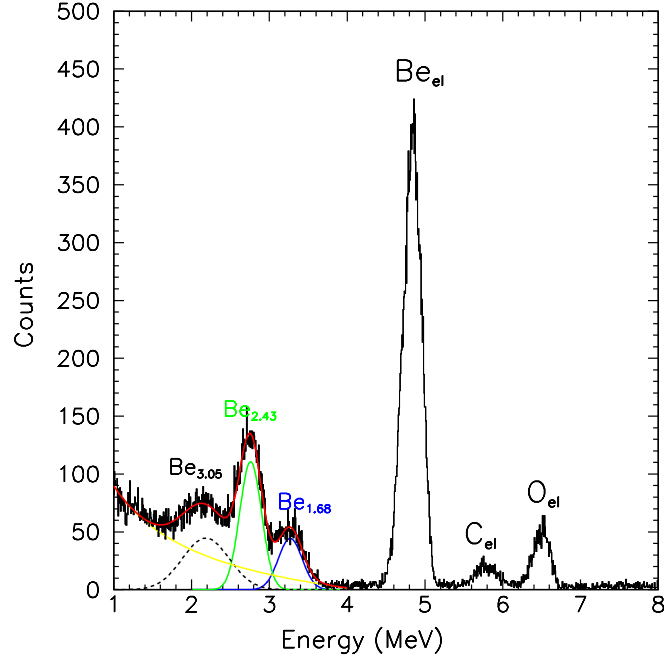


Figure 2.19: Ejectile energy spectrum observed in  $\alpha + ^9\text{Be}$  collisions at  $E_\alpha = 9.24$  MeV and  $\theta_{lab} = 70^\circ$ . The small peaks at high energies are due to contaminants in the target. The group of peaks at 1.5-4 MeV is attributed to the inelastic scattering channels  $\alpha_1$  ( $^9\text{Be}$  at  $E_x = 1.684$  MeV, blue line),  $\alpha_2$  ( $^9\text{Be}$  at  $E_x = 2.429$  MeV, green line) and  $\alpha_4$  ( $^9\text{Be}$  at  $E_x = 3.049$  MeV, black dashed line). The yellow line represents the assumed background. The red solid line shows the fit of inelastic peaks.

this reason we will not give further details about the experiment, which have been reported in Ref. [229]. As an example, a typical ejectile energy spectrum obtained at  $E_\alpha = 9.24$  MeV and  $\theta_{lab} = 70^\circ$  is shown in Figure 2.19. The most intense peak is associated to the elastic scattering of  $\alpha$  particles on  $^9\text{Be}$  nuclei. The two small peaks at higher energies are due to scattering events on carbon and oxygen contaminants in the target, as discussed in Ref. [229]. Particularly interesting is the low-energy group of peaks ( $E \approx 2-4$  MeV). It is attributed to inelastic scattering processes on  $^9\text{Be}$ . The energy positions of peaks at  $E \approx 3.3$ , 2.7 and 2.2 MeV agree with predictions based on kinematics and energy loss calculations for  $\alpha + ^9\text{Be}$  inelastic scattering events, exciting the 1.684 ( $\alpha_1$ ), 2.429 ( $\alpha_2$ ) and 3.049 MeV ( $\alpha_4$ ) states of  $^9\text{Be}$ . Contributions due to  $\alpha + ^{16}\text{O}$  inelastic scattering to this part of the energy spectrum are ruled out because of kinematics, while contributions due to  $\alpha + ^{12}\text{C}$  are expected to be observed up to  $E \approx 1.9$  MeV. Furthermore, we verified via a detailed kinematic calculation that the maximum energy of  $\alpha$  particles coming from the break-up of excited  $^9\text{Be}$  nuclei is outside the region of inelastic scattering peaks. The yield of the  $^9\text{Be}(\alpha, \alpha_1)^9\text{Be}_{1.68}$  inelastic scattering channel is deduced by fitting the low energy

## Chapter 2. Clustering in light systems: an experimental campaign

---

part of the spectrum in Figure 2.19. We assumed the presence of inelastic peaks (parameterized with gaussian functions) due to the 1.684 (blue line), 2.429 (green line) and 3.049 MeV (dashed line) states in  ${}^9\text{Be}$ , summed on a smoothly-varying background of exponential shape (yellow line)<sup>9</sup>. The result of the fit procedure is reported in Figure 2.19 as red solid line. With this procedure we succeeded in measuring DCS for the  ${}^9\text{Be}(\alpha, \alpha_1){}^9\text{Be}_{1.68}$  inelastic scattering. It is also possible to estimate DCS for  ${}^9\text{Be}(\alpha, \alpha_2){}^9\text{Be}_{2.43}$  and  ${}^9\text{Be}(\alpha, \alpha_4){}^9\text{Be}_{3.05}$  inelastic channels, but because of the possible contamination due to the 2.78 MeV state, they have not been included in the present fit procedure. Uncertainties in elastic scattering DCS are taken from Ref. [229], while for inelastic scattering we evaluated uncertainties by summing in quadrature statistical and non-statistical errors. Since low energy states can play a role also in the high energy part of excitation functions [242], we complemented our elastic scattering DCS data-set with data at  $\theta_{cm} = 160^\circ, 150^\circ$  taken from Ref. [261] and covering the energy range  $E_\alpha \simeq 1.0\text{-}1.7$  MeV. During the  $R$ -matrix fit procedure, we allowed the presence of small normalization factors (within 15% from unity) to take into account for eventual absolute normalization errors in the original data set of Ref. [261].

To give firm constraints to our  $R$ -matrix fit, we included in the fit  ${}^9\text{Be}(\alpha, n){}^{12}\text{C}$  reaction cross section data. We used absolute integrated cross section data for  $n_0$  (i.e. associated with the  ${}^{12}\text{C}$  in the ground state) and  $n_1$  (i.e.  ${}^{12}\text{C}$  in the 4.44 MeV state) channels taken from Ref. [275] for the energy range  $E_\alpha \simeq 1.4\text{-}3.5$  MeV, and from Ref. [276] for the energy range  $E_\alpha \simeq 2\text{-}7.5$  MeV. In the case of the  $n_0$  channel, the two data sets of Refs. [275, 276] are in reasonable agreement in their overlap region, while for the  $n_1$  channel a disagreement in the absolute cross section scales is seen. To match the two datasets at low energies, we normalized the  $n_1$  data of Ref. [276] by a 0.52 factor.

### 2.4.2 Results of $R$ -matrix fit of data

In this paragraph we discuss the  $R$ -matrix fit of the experimental data sets described in paragraph 2.4.1. As for the  ${}^{11}\text{C}$  case discussed in Section 2.2, we used the multi-channel, multi-level  $R$ -matrix code AZURE2 [147, 242] to fit the data. The maximum order of partial waves contributing to the reaction or scattering events was set to  $\ell = 8$ . The channel radii used in the  $R$ -matrix calculation are computed by the formula  $R = 1.4 \times (A_1^{1/3} + A_2^{1/3})$ , being  $A_1$  and  $A_2$  the mass number of the two particles constituting the reaction channel. Concerning the DCS obtained with the Naples experiment, we included within the fit procedure the effects due to the finite target thickness, as implemented into AZURE2 [147]; for this reason, the energy scale

---

<sup>9</sup>Concerning inelastic scattering events populating the very broad state at 2.78 MeV in  ${}^9\text{Be}$ , it is very difficult to distinguish them in the present analysis because of the limited energy resolution. After all, this state was never observed in inelastic scattering experiment of  $\alpha$  particles on  ${}^9\text{Be}$  according to the NNDC database [196].

## 2.4 Clustering in $^{13}\text{C}$ with $\alpha + ^9\text{Be}$ reactions

$E_x^{lit}$	$J_{lit}^\pi$	$E_x$	$J^\pi$	$\Gamma$	$\Gamma_{\alpha_0}$	$\Gamma_{\alpha_1}$	$\Gamma_n$	Refs.
11.75	$3/2^-$	11.75	$3/2^-$	116	3	-	113	[258]
11.97	$5/2^+$	11.97	$5/2^+$	152	65	-	87	[258, 261]
12.13	$5/2^-$	12.17	$5/2^-$	199	28	-	171	[258]
12.14	$1/2^+$	12.33	$1/2^+$	230	40	-	190	[258]
12.44	$7/2^-$	12.45	$7/2^-$	222	16	-	206	[258, 271]
13.28	$3/2^-$	13.05	$3/2^-$	546	153	-	393	[258, 260, 265]
13.41	$9/2^-$	13.41	$9/2^-$	84	21	-	63	[258, 260, 265]
13.57	$7/2^-$	13.49	$7/2^-$	417	114	-	303	[258, 265]
13.76	$(3/2, 5/2)^+$	13.63	$5/2^+$	743	623	-	120	[258, 260]
14.13	$3/2^-$	14.13	$5/2^-$	94	94	-	-	[258, 260, 265]
		14.17	$7/2^+$	6	6	-	-	[260]
14.39	$(1/2, 5/2)^-$	14.27	$7/2^-$	392	185	-	207	[258, 265]
14.58	$(7/2, 9/2)^+$	14.36	$9/2^+$	322	70	-	252	[258, 265]
14.63		14.64	$7/2^-$	361	279	-	82	[258, 268]
14.98	$(7/2^-)$	15.04	$5/2^+$	964	830	-	134	[258, 267]
15.27	$9/2^+$	15.27	$3/2^+$	1201	1061	-	140	[258, 268]
16.08	$(7/2^+)$	16.09	$3/2^+$	365	233	55	77	[258]
		16.27	$5/2^-$	1596	1503	87	6	
		16.40	$5/2^+$	17	2	14	1	
		16.64	$5/2^-$	1501	1294	10	152	
		16.67	$7/2^+$	904	633	2	-	
16.95		16.89	$9/2^+$	635	501	86	4	[258]
		16.91	$3/2^-$	1080	703	257	120	
		17.23	$3/2^+$	393	280	-	113	
17.36		17.24	$3/2^-$	215	184	20	11	[258]
		17.52	$5/2^+$	2153	1834	86	233	
17.92		17.86	$7/2^-$	477	457	-	20	[258]

Table 2.3:  $^{13}\text{C}$  level structure derived from the  $R$ -matrix best-fit of  $^4\text{He} + ^9\text{Be}$  elastic and inelastic scattering data and  $^9\text{Be}(\alpha, n)^{12}\text{C}$  reactions. First two columns: summary of literature data, published before 1990, as reported in Ref. [258]. Third, fourth and fifth columns:  $E_x$ ,  $J^\pi$  and  $\Gamma_{tot}$  values of  $^{13}\text{C}$  excited states as obtained in the present work. Sixth, seventh and eighth columns:  $\Gamma_{\alpha_0}$ ,  $\Gamma_{\alpha_1}$  and  $\Gamma_n$  partial width values obtained in the present work. Nine-th column: references to states already reported in the literature.

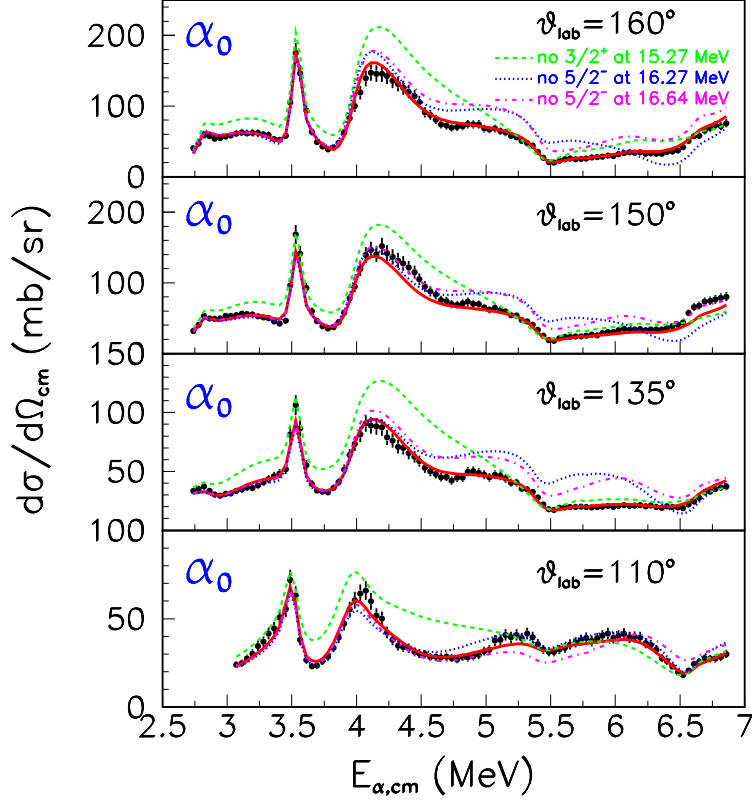


Figure 2.20:  ${}^9\text{Be}(\alpha, \alpha_0){}^9\text{Be}$  DCS at laboratory angles of  $160^\circ$ ,  $150^\circ$ ,  $135^\circ$  and  $110^\circ$ . Data are taken from [229]. The energy scale here shown represents the center of mass energy calculated starting from the  $\alpha$  particle bombarding energy. Effects of finite target thickness have been taken into account in the  $R$ -matrix fit. Red lines represents the results of the simultaneous multi-channel  $R$ -matrix best-fit on the whole data set here investigated. Green dashed line:  $R$ -matrix best-fit without the  $3/2^-$  state at 15.27 MeV. Blue dotted line:  $R$ -matrix best-fit without the  $5/2^-$  state at 16.27 MeV. Magenta dash-dot line:  $R$ -matrix best-fit without the  $5/2^-$  state at 16.64 MeV.

of DCS obtained from the Naples experiment here reported is directly derived from the bombarding energy, without taking into account the energy loss at mid-target.

The starting parameters of our fit were set by using the ones suggested by the table of states reported in Ref. [258], updated with the more recent findings described in Ref. [265]. The presence of several angles and of a wide energy range of elastic scattering DCS and the inclusion of inelastic scattering and neutron reaction channels allow us to discriminate between contrasting  $J^\pi$  assignments reported in the literature. Furthermore, the large body of data here used allows us to unveil the presence of broad states that can be missed when only one reaction channel

## 2.4 Clustering in $^{13}\text{C}$ with $\alpha + {}^9\text{Be}$ reactions

---

and data in small energy and angular ranges are analyzed. When necessary,  $J^\pi$  assignments tentatively reported in the literature have been changed to describe in the best possible way all the details of excitations functions.

Results of the best fit procedure are summarized in Table 2.3, together with previous findings reported in the literature. Red solid lines drawn in Figures 2.20, 2.21, 2.22, 2.23, 2.24, 2.25 of this thesis show the results of the best-fit procedure. The overall agreement with data is quite satisfactory, also in consideration of the high complexity of  $^{13}\text{C}$  level scheme. Depending on the reaction channel, the reduced  $\chi^2$  goes from  $\approx 0.6$  up to  $\approx 2$ . In the next paragraphs we discuss in more details the spectroscopy of  $^{13}\text{C}$  as obtained from the present  $R$ -matrix fit procedure.

### 2.4.2.1 Resonances in the $E_{cm} = 1\text{-}2$ MeV region

In the  $E_{cm} = 1\text{-}2$  MeV region, the presence of excited states in  $^{13}\text{C}$  leads to the appearance of a marked local minimum in the  $\alpha_0$  channel (Figure 2.21) and to the presence of several peaks in the  $n_0$  and  $n_1$  neutron channels (Figure 2.22). The small peak seen at  $E_{cm} \simeq 1.11$  MeV in the  $n_0$  excitation function is attributed to the presence of a  $3/2^-$  state at 11.75 MeV, already seen in  $n + {}^{12}\text{C}$  scattering experiment [258]. Ref. [258] reports for this state a neutron branching ratio  $\frac{\Gamma_n}{\Gamma_{tot}} = 0.80 \pm 0.08$  and a total width of  $129 \pm 40$  keV. In our fit procedure, we found  $\frac{\Gamma_{n_0}}{\Gamma_{tot}} = 0.97$  and  $\Gamma_{tot} = 116$  keV, in reasonable agreement with the literature.

At  $E_{cm} \simeq 1.33$  MeV, both the  $n_0$  and  $n_1$  cross sections show a maximum, while the elastic channel shows a marked dip. In the literature, Saleh et al [261] have attributed the dip in the elastic cross section to the effect of a  $5/2^+$  state at 11.97 MeV. Also previous  $n + {}^{12}\text{C}$  scattering and  ${}^9\text{Be}(\alpha, n){}^{12}\text{C}$  reactions experiments report such a state, even if with a tentative  $7/2^-$  assignment in the latter case. The data here considered are very well reproduced with a  $5/2^+$  state at 11.97 MeV. Our total neutron branching ratio ( $\frac{\Gamma_n}{\Gamma_{tot}} \approx 0.57$ ) is in good agreement with the value quoted in the literature ( $0.51 \pm 0.06$ , [258]). The width of this state (152 keV) and the  $\Gamma_\alpha$  partial width (65 keV) are in agreement with the values reported in Ref. [261] (180 and 72 keV respectively).

At  $E_{cm} \simeq 1.53$  MeV, the  $n_0$  cross section shows a bump that has been attributed, in our analysis, to the presence of a  $5/2^-$  state at 12.17 MeV. In this energy region, the literature reports four states (with different  $J^\pi$  and  $\Gamma_{tot}$  values) separated by just few tens of keV [258]. Among them, we can find also a  $5/2^-$  state at 12.13 MeV, even if its total width ( $80 \pm 30$  keV) and neutron branching ratio ( $0.43 \pm 0.06$ ) are different from our estimates. Interestingly, in a more recent work, Wheldon et al [272] measured with a refined coincidence technique the total width and branching ratios of this state, finding  $\Gamma_{tot} = 219$  keV and  $\frac{\Gamma_n}{\Gamma_{tot}} \approx 1$ , values in agreement with the present ones.

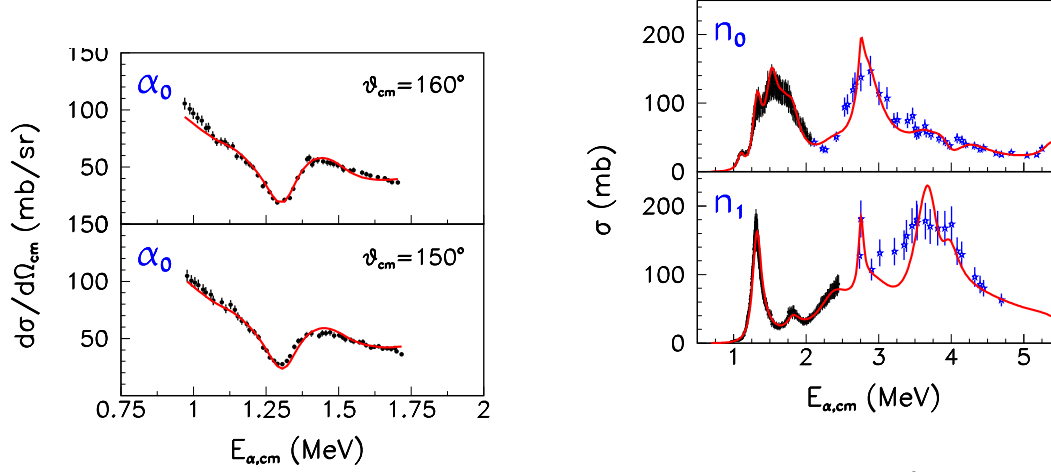


Figure 2.21: Low-energy  ${}^9\text{Be}(\alpha, \alpha_0){}^9\text{Be}$  DCS at center of mass angles  $160^\circ$  and  $150^\circ$ . Data are taken from Ref. [261]. Red lines are the results of the  $R$ -matrix best-fit on the whole data set here investigated.

Figure 2.22: Excitation functions of the  ${}^9\text{Be}(\alpha, n_0){}^{12}\text{C}_{GS}$  and  ${}^9\text{Be}(\alpha, n_1){}^{12}\text{C}_{4.44}$  angle integrated reaction cross section. Black dots: data from [275]; blue stars: data from [276]. 15% average uncertainties have been used for both data sets. Red lines are the results of the simultaneous multi-channel  $R$ -matrix fit on the whole data set here investigated.

At slightly higher energies ( $E_{cm} \simeq 1.79$  MeV), a shoulder appears on the  $n_0$  excitation function. A good reproduction of data is achieved by including a  $1/2^+$  excited state at 12.33 MeV having only  $\alpha$  and  $n_0$  branches. The effect of adding this state can be seen in Figure 2.23, where the green dashed line shows the results of the best fit without including this state. We see a pronounced disagreement with the  $n_0$  data, while the effect is less evident in the elastic channel. A  $1/2^+$  state at 12.14 MeV has been reported in the literature, even with a total width larger and a neutron branching ratio smaller than the present ones.

Finally, the last state contributing to this energy region is a  $7/2^-$  at 12.45 MeV. It is responsible of the bump clearly visible in the  ${}^9\text{Be}(\alpha, n_1){}^{12}\text{C}_{4.44}$  excitation function at  $E_{cm} \simeq 1.83$  MeV. A  $7/2^-$  state at 12.43 MeV was reported in the literature [258]. The quoted total width ( $114 \pm 40$  keV, [258]) is not far from the present result (222 keV), even if the neutron-decay branching ratio is lower than the present one. It is anyway interesting to underline that in an older work studying the  ${}^{12}\text{C}(n, n'\gamma){}^{12}\text{C}_{4.44}$  reaction [271], a value  $\Gamma_{tot} = 220$  keV was reported, in nice agreement with the present one.

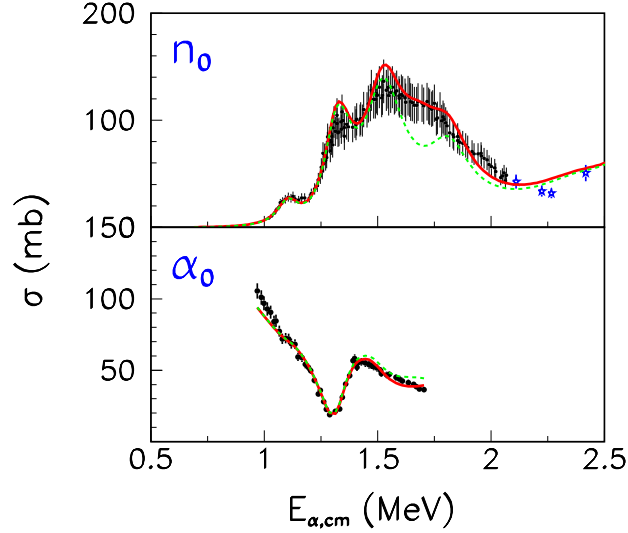


Figure 2.23: (upper panel) Zoom of  $^9\text{Be}(\alpha, n_0)^{12}\text{C}$  integrated cross section data (see Figure 2.22). Green dashed line:  $R$ -matrix best-fit without the inclusion of the  $1/2^+$  state at 12.33 MeV. Red solid line:  $R$ -matrix best-fit with all the parameters of Table 2.3. (lower panel) The same of upper panel, but for the  $^9\text{Be}(\alpha, \alpha_0)^9\text{Be}$  DCS at  $\theta_{cm} = 160^\circ$ .

#### 2.4.2.2 Resonances in the $E_{cm} = 2\text{-}3$ MeV region

This energy domain is mainly dominated by structureless shapes of both elastic (see [260]) and neutron cross sections. This fact, coupled to the use of the rarefied data points of Ref. [276] for the  $n_0$  and  $n_1$  channels, makes the spectroscopic investigation quite difficult. A broad  $3/2^-$  13.05 MeV state has to be included to reproduce the hole in the  $n_0$  cross section around  $E_{cm} \approx 2.6$  MeV and to explain the corresponding shoulder in the  $n_1$  channel at similar energies. The need to include a broad  $3/2^-$  state at 13.28 MeV was pointed out by Ref. [260] and subsequently also in the more recent Ref. [265] by analyzing  $\alpha + ^9\text{Be}$  elastic scattering data. The total width obtained with the present  $R$ -matrix analysis (548 keV) is larger than the previous estimates of Refs. [260, 265].

At  $E_{cm} \simeq 2.76$  MeV, a peculiar shape of  $\alpha_0$  and  $n_1$  excitation functions appears, as it can be seen in Figures 2.24 and 2.22. By analyzing their  $\alpha + ^9\text{Be}$  elastic scattering data, Goss et al [260] attributed this effect to the excitation of a high spin state (tentatively  $9/2^-$ ) in  $^{13}\text{C}$  at 13.41 MeV (with a  $\Gamma_{tot} = 58$  keV). The appearance of a resonance at this excitation energy with similar width was also reported in  $^{12}\text{C}(n, n'\gamma)^{12}\text{C}_{4.44}$  experiments [271]. In their more recent analysis, Freer et al [265] included a  $9/2^-$  state at 13.43 MeV, but with a width much smaller than the present one. They also suggested that a  $7/2^+$  assignment for this state could

## Chapter 2. Clustering in light systems: an experimental campaign

---

reproduce a resonance having  $\approx 60$  keV width at  $E_{cm} \simeq 2.76$  MeV, in agreement with the experimental data. Thanks to the use of DCS at different angles, we can investigate this question in more detail. A nice reproduction of elastic scattering DCS at all angles and of the narrow peak in the  $n_1$  integrated cross section is obtained by including in the level scheme a  $9/2^-$  state at 13.41 MeV, having  $\Gamma_{tot} = 84$  keV, and branching ratios  $\frac{\Gamma_{\alpha_0}}{\Gamma_{tot}} \approx 0.25$ ,  $\frac{\Gamma_{n_0}}{\Gamma_{tot}} \approx 0.29$ ,  $\frac{\Gamma_{n_1}}{\Gamma_{tot}} \approx 0.46$ . The  $\alpha_0$  and the  $n_0 + n_1$  branching ratios quoted in [260] are in nice agreement with the present ones. Finally, we checked the possibility that the 13.41 MeV state could have  $7/2^+$  assignment. If we adopt such a  $J^\pi$  value for the state at 13.41 MeV, having  $\Gamma_{tot}$  and partial widths equal to the previously mentioned ones, the associated  $R$ -matrix calculations are reported as blue dashed lines in Figure 2.24. The disagreement with experimental DCS  $\alpha_0$  data at two representative angles<sup>10</sup> is evident. We checked also the possibility that, in the case of a  $7/2^+$  assignment,  $\Gamma_{\alpha_0} > \Gamma_{n_0}, \Gamma_{n_1}$  with the constraint  $\Gamma_{tot} = 84$  keV; also in this case calculations and experimental data for the  $\alpha_0$ ,  $n_0$  and  $n_1$  channels largely disagree. Therefore, from the present work, a  $9/2^-$  assignment is deduced for the state at 13.41 MeV.

### 2.4.2.3 Resonances in the $E_{cm} = 3-3.75$ MeV region

$\alpha + {}^9\text{Be}$  elastic scattering data in this energy region are characterized by a very broad bump ( $E_{cm} \simeq 2.9-3.4$  MeV), followed by a narrower peak ( $E_{cm} \simeq 3.5$  MeV) and a broad local minimum ( $E_{cm} \simeq 3.85$  MeV), as clearly visible in Figure 2.20. The evolution with the angle of the broad bump is very evident, and it is a useful tool to determine  $J^\pi$  values of states contributing in this energy region. We find that two broad states are needed to simultaneously reproduce the  $\alpha_0$ ,  $n_0$  and  $n_1$  excitation functions: a  $7/2^-$  state at 13.55 MeV and a  $5/2^+$  state at 13.64 MeV. Similar findings are reported by Freer et al [265], even if the  $\Gamma_{tot}$  and the branching ratio values seem to be inverted between the two states.

A good reproduction of the  $\alpha_0$  channel data is seen at all angles, as well as a reasonable reproduction of the  $n_0$  and  $n_1$  channels is seen. Probably the small gap between data and fit in the  $n_1$  channel could be reduced by taking into account also a non-zero branching to the  $n_2$  reaction channel. In this energy region, Wheldon et al [272] reported the presence of a state at 13.78 MeV having a quite narrow width (117 keV). According to [272], this state has sizable branches to the  $\alpha_0$  and  $n_1$  channels. In principle, the presence of such a state can help to reduce the gap in the  $n_1$  channel mentioned before, especially in the  $E_{cm} \simeq 3.11$  MeV region. The absence of a pronounced (and narrow) structure near this energy value in the  $\alpha_0$  channel data makes quite difficult to evince the presence of such a state from the present analysis.

The peak at  $E_{cm} \simeq 3.5$  MeV has been reproduced, following the suggestions by Goss et al, by using two close-lying states at 14.13 MeV ( $5/2^-$ ) and 14.17 MeV

---

<sup>10</sup>Data at  $137.9^\circ$  in the center of mass frame are taken from the relative data by Goss et al. [260] and normalized to match our cross section scale.

## 2.4 Clustering in $^{13}\text{C}$ with $\alpha + ^9\text{Be}$ reactions

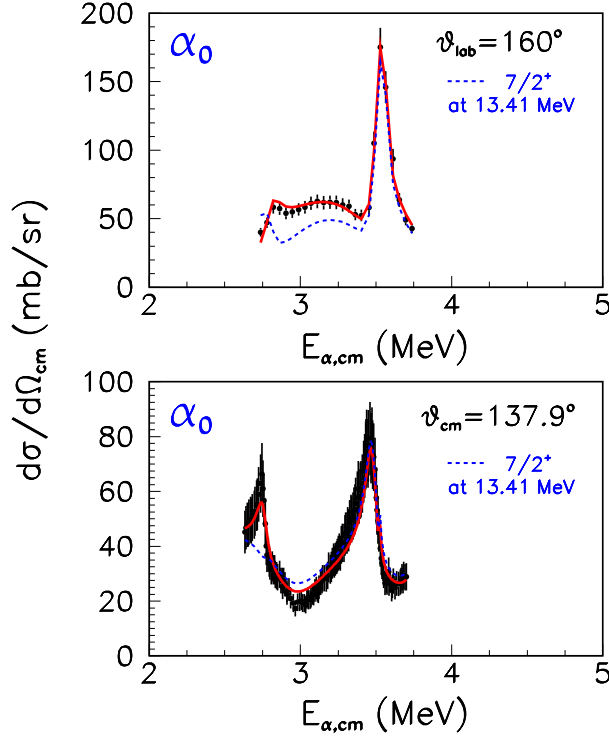


Figure 2.24: (upper panel) Zoom of  $^9\text{Be}(\alpha, \alpha_0)^9\text{Be}$  DCS data at  $\theta_{lab} = 160^\circ$  (see Figure 2.20). Blue dashed line:  $R$ -matrix best-fit where we changed the  $J^\pi$  value of the 13.41 MeV state from  $9/2^-$  to  $7/2^+$ . Total and partial width values used in the case of a  $7/2^+$  assignment for the 13.41 MeV state are the same as those reported in Table 2.3 for the 13.41 MeV  $9/2^-$  state. Red solid line:  $R$ -matrix best-fit with all the parameters of Table 2.3. (lower panel) The same as upper panel, but for the  $^9\text{Be}(\alpha, \alpha_0)^9\text{Be}$  DCS at  $\theta_{cm} = 137.9^\circ$ , data taken from Goss et al. [260].

( $7/2^+$ ). Concerning the  $5/2^-$  state, its  $\Gamma_{tot}$  value (94 keV) is in reasonable agreement with the ones quoted by Goss et al (75 keV) and Freer et al (124 keV). Furthermore, a vanishingly small neutron width is observed in all the investigations. In agreement with Goss et al, we found that the largest part of the  $\alpha_0$  width is due to the  $\ell = 4$  partial wave. Concerning the  $7/2^+$  state, as suggested by Goss et al, we included it to reproduce the shape of the  $E_{cm} \simeq 3.5$  MeV peak at all angles. Anyway, we find a width much smaller than Ref. [260] one.

The broad local minimum ( $E_{cm} \simeq 3.85$  MeV) seen in the  $\alpha_0$  excitation functions at all angles is due to the presence of a  $7/2^-$  state at 14.27 MeV, interfering with the neighboring states and with the Coulomb background amplitudes. In Ref. [258], a negative parity state is reported at a close energy (14.39 MeV), with  $J = 1/2$  or  $5/2$  tentative assignments. In more recent times, a  $7/2^-$  state at 14.4 MeV was reported in Ref. [265] but with a  $\Gamma_{tot}$  value quite smaller than the present one. Our value

## Chapter 2. Clustering in light systems: an experimental campaign

---

( $\Gamma_{tot} = 392$  keV) agrees with the one quoted in Ref. [258] ( $\Gamma_{tot} = 280 \pm 70$  keV) within two standard deviations.

### 2.4.2.4 Resonances in the $E_{cm} = 3.75\text{-}5.5$ MeV region

In this region, the  $\alpha_0$  elastic scattering data show two very broad bumps. In the neutron emission channels also some broad structures appear. To simultaneously describe all the data, we used four (mainly broad) states. The first two ones are a  $9/2^+$  state at 14.36 MeV and a  $7/2^-$  state at 14.64 MeV (the last one with a dominant  $\ell = 4$  component in the  $\alpha_0$  channel). Two states with the same  $J^\pi$  assignments and similar  $\Gamma_{tot}$  values are reported in Ref. [265], even if their resonance energies are shifted back by  $\approx 300$  keV. Signals of the existence of a state near 14.63 MeV were reported in the study of  $\alpha + {}^9\text{Be} \rightarrow n_1 + {}^{12}\text{C}^*$  DCS [268]. In our investigations we found  $\Gamma_{n_1} \gg \Gamma_{n_0}$ , in qualitative agreement with the findings of [268]. A narrow resonance having  $\ell = 4$  has been observed at 14.7 MeV in  ${}^9\text{Be}({}^6\text{Li},d){}^{13}\text{C}$  transfer reactions [277, 278]; also these findings could be in qualitative agreement with present ones concerning the existence of a  $7/2^-$  state at 14.64 MeV.

Two very broad states (a  $5/2^+$  state at 15.04 MeV and a  $3/2^+$  state at 15.27 MeV) are needed to reproduce the behavior of elastic scattering DCS in the region  $E_{cm} \simeq 4\text{-}5.5$  MeV. The interference of these two states reproduces very well the bump in the  $E_{cm} \approx 4.7\text{-}5.4$  MeV region. The green dashed line of Figure 2.20 shows the behavior of the  $R$ -matrix best fit if the  $3/2^+$  state at 15.27 MeV is not included in the level scheme; the disagreement at all angles is evident. Both such states show large  $\Gamma_\alpha$  partial width, but the associated reduced width  $\gamma_\alpha^2$  are well lower than the single-particle limits ( $\ell=3$ ,  $\theta_\alpha^2 \simeq 0.33$  for the 15.04 MeV state; and  $\ell = 1$ ,  $\theta_\alpha^2 \simeq 0.22$  for the 15.27 MeV state).

### 2.4.2.5 Resonances in the $E_{cm} = 5.5\text{-}6.8$ MeV region

In this high energy region,  $\alpha_0$  DCS show a quite smooth behavior, with the exception of two pronounced dips at  $E_{cm} \simeq 5.52$  MeV and  $E_{cm} \simeq 6.5$  MeV. Also the  $\alpha_1$  channel shows some structures, see Figure 2.25 (e.g. a wing at  $E_{cm} \simeq 5.8$  MeV) that are very useful to study the high energy part of  ${}^{13}\text{C}$  level scheme. In this high energy region, the spectroscopy of  ${}^{13}\text{C}$  reported in the literature is particularly poor [258]. Eleven states have been introduced in the present work to simultaneously fit all the reaction and scattering channels here studied. For some of the states, we allowed the possibility of having non-zero strength in the  $\alpha_2$  inelastic channel.

The dip at  $E_{cm} \simeq 5.52$  MeV is due to the 16.09 MeV  $3/2^+$  state. In the literature, the presence of a state at  $E_x \simeq 16.1$  MeV with  $\Gamma_{tot}$  of the order of 200-300 keV has been reported by analyzing both the  ${}^9\text{Be}(\alpha,n){}^{12}\text{C}$  reaction and  ${}^{12}\text{C}(n,n){}^{12}\text{C}$  scattering data. The deep minimum, seen in the  $\alpha_0$  channel at  $\theta_{lab} = 110^\circ$  at  $E_{cm} \simeq 6.51$  MeV, is due to the interferences between two close-lying states at 17.23 ( $3/2^+$ ) and 17.24 ( $3/2^-$ ) MeV. We verified this finding by removing them from the

## 2.4 Clustering in $^{13}\text{C}$ with $\alpha + ^9\text{Be}$ reactions

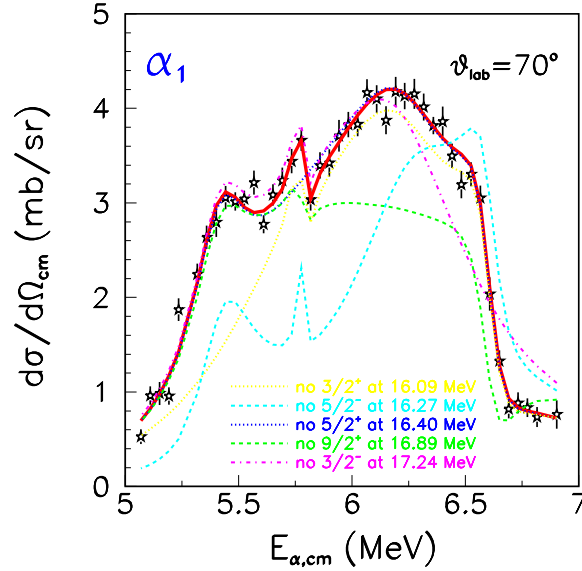


Figure 2.25:  $^9\text{Be}(\alpha, \alpha_1)^9\text{Be}_{1.68}$  DCS data at  $\theta_{lab} = 70^\circ$ . The red line represents the  $R$ -matrix best-fit on the whole data set here investigated. The dotted yellow line is the  $R$ -matrix best-fit without the inclusion of the  $3/2^+$  state at 16.09 MeV. The dashed azure line is the  $R$ -matrix best-fit without the inclusion of the  $5/2^-$  state at 16.27 MeV. The dotted blue line is the  $R$ -matrix best-fit without the inclusion of the  $5/2^+$  state at 16.40 MeV, responsible of the wing at  $E_{cm} \simeq 5.8$  MeV. The dashed green line is the  $R$ -matrix best-fit without the inclusion of the  $9/2^+$  state at 16.89 MeV. Finally, the dash-dotted magenta line is the  $R$ -matrix best-fit without the inclusion of the  $3/2^-$  state at 17.24 MeV.

level list in the  $R$ -matrix calculation; in this case, the deep minimum will be not reproduced at all.

The wing at  $E_{cm} \simeq 5.8$  MeV in the  $\alpha_1$  inelastic channel can be attributed to a narrow  $5/2^+$  state at 16.40 MeV. The blue dotted line of Figure 2.25 represents the result of the  $R$ -matrix best-fit without the 16.40 MeV state: the wing in the excitation function disappears.

Apart from the presence of such dips and wings, the global behavior of  $\alpha_0$  and  $\alpha_1$  excitation functions in this energy region is determined by the contributions of four broad states ( $\Gamma_{tot} > 1$  MeV). Their mutual interference and their interference with Coulomb amplitudes allow to describe the overall trend of data. In Figure 2.20 we report, in different colors, the effect of removing some of these states from the  $R$ -matrix calculation. A much poorer agreement with data is seen in all cases. Furthermore, we checked the possibility that the two broad  $5/2^-$  states at 16.27 and 16.64 MeV can balance out their effects. Results of the present  $R$ -matrix calculation

## Chapter 2. Clustering in light systems: an experimental campaign

---

performed without including both these states do not reproduce the high energy part of the data.

The spectroscopic information on the highest excitation states obtained with the present  $R$ -matrix analysis is not fully reliable, since the range of the present data is limited. At bombarding energies larger than the ones here investigated,  $E_\alpha > 10$  MeV,  $\alpha + {}^9\text{Be}$  elastic scattering DCS have been reported at several backward angles in Ref. [259]. The presence of broad resonant-like structures characterizes the DCS pattern up to  $E_\alpha \approx 20$  MeV. Even if their nature was not definitely understood, they were attributed to direct reaction mechanisms, such as the optical model resonance phenomenon [259]. In this frame, it is also possible that the broad states appearing in the high excitation energy domain of our  $R$ -matrix analysis indicates the onset of such direct effects. New investigations of  $\alpha + {}^9\text{Be}$  reactions at high energies can help to better clarify this aspect.

### 2.4.3 Impact of our data on molecular bands

The broad body of spectroscopic data obtained in the present work allows us to draw some considerations on the structure of  ${}^{13}\text{C}$ , in particular on the existence of molecular rotational bands. Our findings can be indeed compared with theoretical predictions regarding the structure of such bands, which are described in paragraph 1.4.3. As a first point, we fix our attention on negative parity states on the light of the proposed molecular rotational band of Ref. [127]. In our measurement we do not have access to the first two members of such a rotational band ( $3/2^-$  at 9.897 MeV, sub-threshold, and  $5/2^-$  at 10.818); at variance, we see well the contribution of the  $7/2^-$  state at 12.45 MeV. For this state, we found a relatively small value of the dimensionless reduced  $\alpha$  width  $\theta_\alpha^2 = \frac{\gamma_\alpha^2}{\gamma_{\alpha W}^2}$  ( $\gamma_{\alpha W}^2 = \frac{3\hbar^2}{2\mu R}$  is the Wigner single-particle limit, as already defined in Section 2.2 for the  ${}^{11}\text{C}$  case), of the order of 0.05. Concerning the 14.13 MeV state, we discard the possibility, suggested in Ref. [127], to be a  $9/2^-$  state. The  $5/2^-$  assignment here reported, in agreement with Refs. [260, 265], appears to be very solid. Otherwise, a closer inspection of states in Table 2.3, points out the presence of a  $9/2^-$  state at 13.41 MeV. This state has a sizable dimensionless reduced  $\alpha$  width ( $\theta_\alpha^2 = 0.26$ ) and we could suppose that it belongs to the negative parity molecular bands, as shown in Figure 2.26. In this hypothesis, a reasonable fulfilment of the rotational band rule  $E_x = \frac{\hbar^2 J(J+1)}{2\mathfrak{I}} + \text{const.}$  is seen (the coefficient of determination is  $r^2 = 0.973$  in our hypothesis and  $r^2 = 0.998$  for the suggested molecular band of Ref. [127]). It is interesting to note that, if our hypothesis is true, such a molecular band will have a slope coefficient  $\frac{\hbar^2}{2\mathfrak{I}} \simeq 171$  keV. This value is very close to the one ( $\frac{\hbar^2}{2\mathfrak{I}} \simeq 163$  keV) that can be extracted by a linear fit of theoretical data related to the  $K^\pi = 3/2_2^-$  molecular band of Ref. [129]. The GCM model used in Ref. [129] suggests that the large value of the moment of inertia associated to the  $K^\pi = 3/2_2^-$  band could be related to the presence of an obtuse-triangle configuration of the three  $\alpha$ -particles

## 2.4 Clustering in $^{13}\text{C}$ with $\alpha + {}^9\text{Be}$ reactions

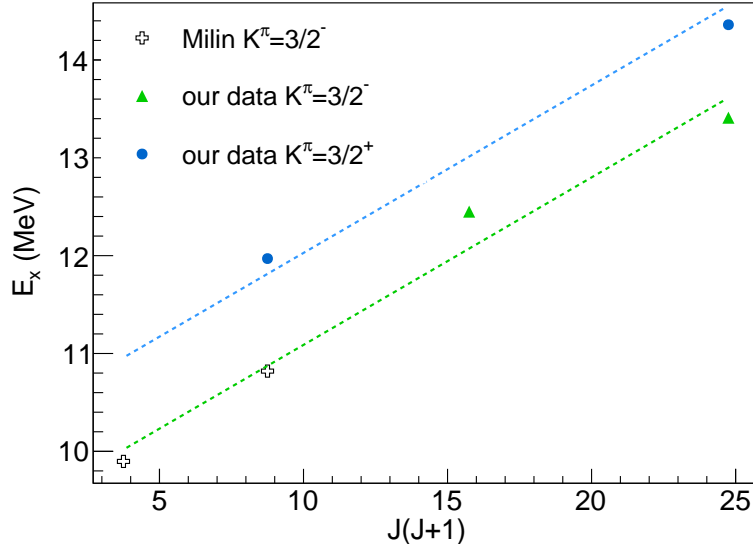


Figure 2.26:  $^{13}\text{C}$   $K^\pi = 3/2^-$  band and the hypothetical  $K^\pi = 3/2^+$  band as obtained from our  $R$ -matrix fit of data. The open symbols represent the  $3/2^-$  and  $5/2^-$  members of the  $K^\pi = 3/2^-$  molecular band suggested in [127], which lie outside from the energy region here explored. The green and blue symbols represent, respectively, the states here associated to the negative parity  $K^\pi = 3/2^-$  band and to an hypothetical positive-parity molecular band. The green dashed line is obtained by a best-fit of the  $K^\pi = 3/2^-$  states, while the blue one is a simple translation of the previous.

constituting the nuclear molecule. Being this hypothesis very intriguing, it certainly deserves further attention both from experimental and theoretical points of view. Finally, contrary to the conjecture of [127], no evidence of high-energy states with  $J^\pi = 11/2^-$  is seen in our work.

The situation is more complicated for positive parity states. Of all the states belonging to the positive parity molecular band of Ref. [127], only the  $5/2^+$  level at 11.97 MeV is seen. This state has a sizable dimensionless reduced  $\alpha$  width,  $\theta_\alpha^2 = 0.27$ , and therefore it could have an  $\alpha$ -cluster nature. A  $9/2^+$  state ( $\theta_\alpha^2 \approx 0.1$ ) is reported at 14.36 MeV (see Table 2.3). If we suppose that both such states belong to an hypothetical positive parity molecular band, as suggested in Figure 2.26, a slope parameter  $\frac{\hbar^2}{2\mathcal{I}} \simeq 150$  keV is found, similar to the one reported for the negative parity band. If this naive hypothesis would be true, the missing  $7/2^+$  member should be at around 13 MeV, corresponding to  $E_{cm} \approx 2.35$  MeV. Indeed, the  $E_{cm} \approx 2$ -2.5 MeV energy domain corresponds to a quite delicate region of the data set used for the present  $R$ -matrix analysis. This energy domain is at the matching between the two neutron data sets of Refs. [275, 276]. Furthermore, if one looks to the  $\alpha + {}^9\text{Be}$  elastic scattering DCS from Refs. [260, 262–264] (the only that cover this energy region), a

## Chapter 2. Clustering in light systems: an experimental campaign

---

structureless behavior is seen, making challenging the observation of (broad) states. New accurate measurements of  $\alpha + {}^9\text{Be}$  elastic scattering DCS and of  ${}^9\text{Be}(\alpha, n){}^{12}\text{C}$  reaction cross sections in the energy region  $E_\alpha \approx 2.0\text{-}3.5$  MeV are clearly required to improve the spectroscopic picture reported in the present work.

### 2.5 Clustering in ${}^{16}\text{C}$ : towards the dripline

In Chapter 1, the importance played by valence neutrons in giving more stability to cluster structures in light nuclear systems was discussed. A quite interesting example of such phenomena is constituted by neutron-rich isotopes of carbon, and, in particular, by  ${}^{16}\text{C}$ . This nucleus has recently attracted a large interest because of the possible appearance of linear and triangular molecular structures, which have been predicted by means of AMD calculations [132], see also Section 1.4.3. Unfortunately, on the experimental point of view, the spectroscopy of  ${}^{16}\text{C}$  is practically unknown above the  $\alpha$  disintegration threshold [109, 135, 136]. Very few experimental data (and with low statistics) have been reported at excitation energy values around the cluster disintegration thresholds at 16.5 MeV ( ${}^6\text{He}+{}^{10}\text{Be}$ ) and 22.9 MeV ( ${}^8\text{He}+{}^8\text{Be}$ ) [196, 279]. We are therefore not able to understand the structure of  ${}^{16}\text{C}$  by comparing the theoretical calculations with the present experimental data. For this reason, we decided to study the spectroscopy of  ${}^{16}\text{C}$  via sequential breakup into its cluster components at the FRIBs facility of INFN-LNS. The results of this work are reported in the following paragraphs of the present section.

#### 2.5.1 Experimental results

The experimental apparatus here used was identical to the one used for the present studies of  ${}^{10}\text{Be}$  spectroscopy. It is described in detail in Section 2.1.  ${}^{16}\text{C}$  beams were delivered by the FRIBs facility of LNS; the breakup fragments due to reactions on  $\text{CH}_2$  target were detected by the CHIMERA array. In our experiment, we investigated the following breakup channels:  ${}^1\text{H}, {}^{12}\text{C}({}^{16}\text{C}, {}^6\text{He}{}^{10}\text{Be})$ ,  ${}^1\text{H}, {}^{12}\text{C}({}^{16}\text{C}, {}^6\text{He}{}^6\text{He}{}^4\text{He})$ . They involve both two-body and three-body decompositions of  ${}^{16}\text{C}$ .

As discussed for the  ${}^{10}\text{Be}$  case, the excitation energy of  ${}^{16}\text{C}$  before decaying can be deduced from the invariant mass of the breakup fragments. Inspecting  ${}^6\text{He}$ - ${}^{10}\text{Be}$  correlations, we found the spectrum reported in Figure 2.27(a). In this case, due to the very low accumulated statistics, we cannot reasonably estimate the background contribution with the event-mixing procedure as in the case of  ${}^{10}\text{Be}$ . Indeed, a similar analysis on a so limited data set would result in the possible creation of *artificially induced correlations* and the following appearance of spurious peaks in the simulated background spectrum. The presence (even with a poor statistics) of a narrow peak at about 20.6 MeV represents the possible signature of an unreported excited state in  ${}^{16}\text{C}$ . The red and orange dashed curves are the simulated detection efficiency by assuming hydrogen or carbon recoil respectively. To evaluate such efficiencies, we

## 2.5 Clustering in $^{16}\text{C}$ : towards the dripline

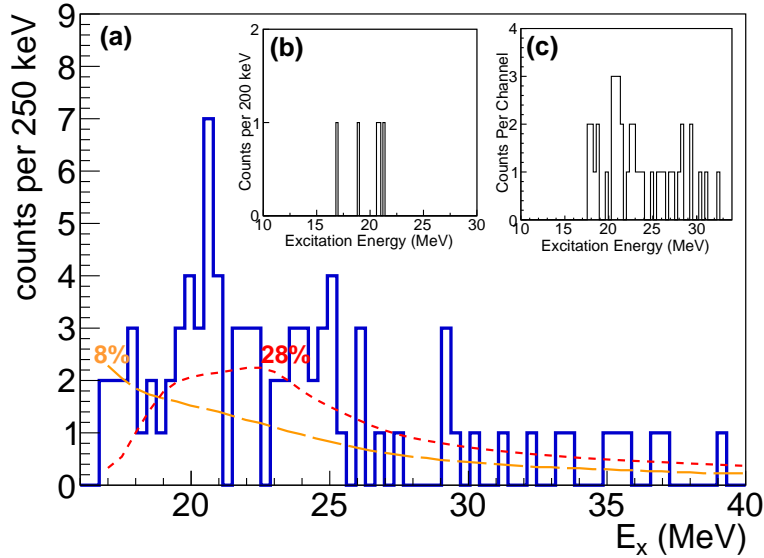


Figure 2.27: (a)  $^{16}\text{C}$  excitation energy spectrum obtained from the  $^{10}\text{Be}+^6\text{He}$  break-up channel. Orange dashed line: Monte Carlo simulated detection efficiency obtained by assuming  $^{12}\text{C}$  recoils. Red dotted line: Monte Carlo simulated detection efficiency obtained by assuming  $^1\text{H}$  recoils. Details on the Monte Carlo calculations are discussed in the text. (b)  $^{16}\text{C}$  excitation energy spectrum obtained from the  $^{10}\text{Be}+^6\text{He}$  break-up channel, as reported in Ref. [136]. (c)  $^{16}\text{C}$  excitation energy spectrum obtained from the  $^{10}\text{Be}+^6\text{He}$  break-up channel, as reported in Ref. [135].

developed a Monte Carlo code based on the generation of breakup events, by using an exponential functional form of the inelastic scattering angular distribution [183]. Simulated events are then filtered with a software replica of the CHIMERA detector in the configuration used in the present experiment. The efficiency curves exhibit quite smooth trends. Therefore the peak at  $E_x = E_{rel} + E_{th} \approx 20.6$  MeV should not be caused by effects related to the detection efficiency. Another interesting point is that also previous works [135, 136] show a yield enhancement at about 21 MeV of  $^{16}\text{C}$  excitation energy, as evident in the insert of Figure 5. Our data are characterized by higher statistics as compared to previous experiments. In this excitation energy region, theoretical calculations of Ref. [132] have predicted the possible presence of various  $6^+$  states, members of two triangular bands and of a linear chain band. Unfortunately, given the low statistics collected in our experiment, we cannot completely rule-out a phase-space decay without assumption of any resonance in  $^{16}\text{C}$  and we are unable to investigate the angular correlation for the 20.6 MeV bump.

Finally, it is also possible to explore the structure of  $^{16}\text{C}$  via three-body cluster break-up channels. Following the suggestions of the literature [135], we studied the  $^6\text{He}+^6\text{He}+^4\text{He}$  break-up channel, which gives a very small number of coincidences. We made a  $Q$ -value analysis of these counts. It consists in the construction of the

## Chapter 2. Clustering in light systems: an experimental campaign

---

corresponding  $Q$ -value spectrum, i.e. the spectrum of the kinetic energy difference between the final channel  ${}^6\text{He}+{}^6\text{He}+{}^4\text{He}+\text{recoil}$  and the initial channel  ${}^{16}\text{C}+\text{target}$ . Such spectrum should peak at the  $Q_{gggg}$  ( $-23.914$  MeV), which represents the  $Q$ -value in the case the four final fragments are left in their ground states. The  $Q$ -value spectrum for these events, obtained by assuming hydrogen recoils, shows a broad bump centred around the  $Q_{gggg}$  value. Including all the selected  ${}^6\text{He}+{}^6\text{He}+{}^4\text{He}$  triple coincidences, without any cut on the  $Q$ -value spectrum, we found the invariant mass spectrum shown with blue dashed line in Figure 2.28. In the same Figure, we show as a green filled histogram the same relative energy spectrum gated within the  $Q$ -value window  $Q = Q_{gggg} \pm 30$  MeV. Despite the very low statistics, the excitation energy spectrum shows an enhanced yield at about 34 MeV. The effect of the gate on the  $Q$ -value seems to slightly reduce the yield in proximity of the 34 MeV peak and completely cut the coincidence yield over 40 MeV. This finding could point out, very tentatively, the possible presence of resonant structures of  ${}^{16}\text{C}$  around 34 MeV characterized by a non-vanishing  $\alpha$  decay width. This high-energy region has been also studied in Ref. [132], indicating the possible presence of the  $12^+$  member of the linear chain bands discussed in Section 1.4.3 of Chapter 1.

Because of the very low statistics, this finding needs (and stimulates) further investigations. If the existence of a high-energy state in  ${}^{16}\text{C}$ , visible via three body break-up, will be confirmed, it would be the first indication of three-body cluster disintegration of  ${}^{16}\text{C}$ , since the literature does not provide the evidence of this extremely rare process [135].

### 2.5.2 Consequences of our investigation on successive works

The above discussed findings and the publication of Ref. [199] triggered the development of a new, higher statistics, experiment at the FRIBs facility [280]. In this experiment, whose analysis is still in progress, we improved the invariant mass reconstruction by coupling CHIMERA with a new high granularity hodoscope, FAR-COS [281], placed at forward angles. This angular region is of extreme importance because of the inverse kinematics. From the new experiment we expect to obtain firmer spectroscopic information on light nuclei far from the stability line and to confirm the present findings.

The present work was mentioned also in subsequent theoretical papers as a confirmation of the findings of the AMD model regarding linear chain configurations in  ${}^{16}\text{C}$  [282–284]. Finally, in a recent experiment [285] by means of the SAMURAI spectrometer at RIKEN, the disintegration of  ${}^{16}\text{C}$  in the  ${}^{12}\text{Be} + {}^4\text{He}$  channel was studied. Preliminary results of invariant mass analysis starting from  ${}^{12}\text{Be} + {}^4\text{He}$  fragments point out the formation of a possible level of  ${}^{16}\text{C}$  at about 21 MeV excitation energy, which would be compatible with our result.

## 2.6 Cluster structures in $^{20}\text{Ne}$ and $^{19}\text{F}$ and their role in the $^{19}\text{F}(\text{p},\alpha)^{16}\text{O}$ reaction

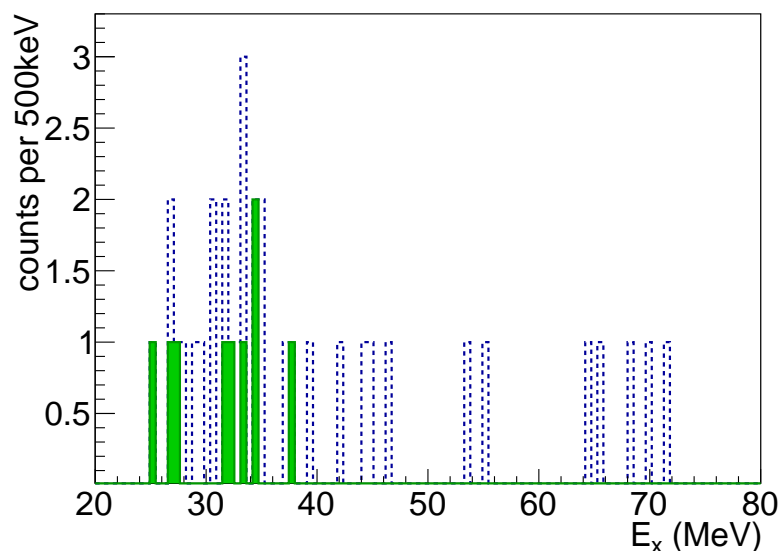


Figure 2.28:  $^{16}\text{C}$  excitation energy spectrum for the three body  $^6\text{He}+^6\text{He}+^4\text{He}$  break-up channel. The black dashed histogram represents the excitation energy spectrum obtained without cuts on the  $Q$ -value. The green filled histogram is obtained by gating the reconstructed  $Q$ -value (assuming hydrogen recoils) in the range  $Q = Q_{gggg} \pm 30$  MeV.

## 2.6 Cluster structures in $^{20}\text{Ne}$ and $^{19}\text{F}$ and their role in the $^{19}\text{F}(\text{p},\alpha)^{16}\text{O}$ reaction

$^{20}\text{Ne}$  is one of the self-conjugated nuclei for which many investigations have been performed in both very old and recent times. In particular, cluster structures of the type  $^{16}\text{O} + \alpha$  and  $^{12}\text{C} + ^8\text{Be}$  have been predicted for different  $0^+$  states [286]. Furthermore, it is particularly remarkable the fact that the emission thresholds of  $1\alpha$  (4.73 MeV) and  $2\alpha$  (11.89 MeV) are much lower than the proton and neutron emission thresholds (12.884 MeV and 16.864 MeV, respectively). The shell closure of the  $^{16}\text{O}$  core (doubly magic) and the residual interaction of the further 4 nucleons ( $2p$  and  $2n$ ) of the Nilsson sub-shell  $(1/2)^+$  make such 4 nucleons strongly bounded. For this reason, even for low excitation energies of  $^{20}\text{Ne}$  ( $E_x > 4.73$  MeV), the simultaneous emission of this strongly correlated system of 4 nucleons is energetically more convenient respect of a single nucleon to be excited to a superior shell (e.g. the  $2s_{1/2}$  or  $1d_{3/2}$ ). In fact, the only bound states of  $^{20}\text{Ne}$  (below the  $\alpha$ -emission threshold) are the  $2^+$  and the  $4^+$  states, lying respectively, at 1.63 MeV and 4.25 MeV excitation energy, which are due to a collective rotation of the  $^{20}\text{Ne}$  deformed ground state rather than single-particle excitations. Similar arguments can be discussed for  $^{19}\text{F}$  (see the *cluster model joke*, paragraph 1.2.4 of Chapter 1), which has the  $\alpha$ -

## Chapter 2. Clustering in light systems: an experimental campaign

---

emission threshold at only 4.01 MeV, while 8 MeV and 10.43 MeV are respectively required to emit a proton or a neutron.

The study of the  $^{19}\text{F}(p,\alpha)^{16}\text{O}$  reaction ( $Q = 8.114$  MeV), where both  $^{19}\text{F}$ , as target nucleus, and  $^{20}\text{Ne}$ , as a compound nucleus, are involved, allows to obtain crucial information on the above discussed aspects. In particular, it allows to explore the influence of clustering phenomena both in the population of resonant states in  $^{20}\text{Ne}$  and in the appearance of direct effects (which can be related to the cluster structure of the  $^{19}\text{F}$  nucleus) affecting the reaction cross section [149, 287]. Indeed, as previously mentioned in paragraph 1.2.4, two possible cluster sub-structures of  $^{19}\text{F}$  characterize its ground state and its first excited state, namely the  $^{16}\text{O}-^3\text{H}$  and the  $\alpha-^{15}\text{N}$  ones. When  $^{19}\text{F}$  is bombarded by very low energy protons, the presence of such low-lying cluster configurations could favour the direct capture of the proton by the  $^{19}\text{F}$  nucleons outside of the core. This would result in the direct formation of  $\alpha-^{16}\text{O}$  substructures, with the appearance of a forward-backward asymmetry in the  $(p, \alpha)$  angular distributions. Moreover, at such low bombarding energy, one can even expect that the  $^{16}\text{O}-^3\text{H}$  cluster structure of the  $^{19}\text{F}$  ground state could experience polarisation phenomena, resulting in a local decreasing of the  $p-^{19}\text{F}$  Coulomb barrier, with the consequence of an enhancement of the reaction cross section that can mimic the presence of a direct contribution.

Another interesting motivation which leads to an accurate investigation of the  $^{19}\text{F}(p,\alpha_0)^{16}\text{O}$  reaction at energies far below the Coulomb barrier is related to its astrophysical importance [103, 138]. In massive stars, the competition between  $^{19}\text{F}(p,\gamma)^{20}\text{Ne}$  and  $^{19}\text{F}(p,\alpha)^{16}\text{O}$  in the hydrogen burning phase determines the quantity of catalytic material that is lost in the CNO cycles and becomes available for the NeNa one [103, 288, 289]. The most recent experimental work on this subject is Ref. [289], suggesting that at the lowermost energies ( $T < 0.1$  GK) the  $\alpha_0$  channel dominates over the other open reaction channels (i.e.  $\alpha_\pi$ , where the residual  $^{16}\text{O}$  nucleus is left in its first excited state, and  $\alpha\gamma$ , where the  $\alpha$  emission is accompanied by the subsequent  $\gamma$  de-excitation of the residual  $^{16}\text{O}^*$ ). Furthermore, fluorine nucleosynthesis is an open issue of modern astrophysics, and it has been suggested that  $^{19}\text{F}(p,\alpha)^{16}\text{O}$  reactions can play an important role in the destruction of fluorine in hydrogen-rich environments like for example Asymptotic Giant Branch (AGB) stars<sup>11</sup> [290, 292, 294]. The accurate knowledge of the  $^{19}\text{F}(p,\alpha)^{16}\text{O}$  reaction rate around the AGB Gamow window ( $E_{cm} \approx 27\text{-}94$  keV at  $T \simeq 0.04$  GK) is therefore of crucial importance for modeling nucleosynthesis in these stars [292] and may help to solve large discrepancies between stellar model predictions and experimental observations [290].

---

<sup>11</sup>Nowadays, the AGB stars are believed to be the main sites of fluorine production [290]. Anyway, in the case of thermally-pulsing AGB stars, extra-mixing of material through the zone of radiative energy transport above the hydrogen shell (often referred as *deep mixing* or *cool bottom processing* phenomena) can occur [291]. This may lead to important alteration of the isotopic composition of stellar outer layers [292], exposing material at temperatures high enough to activate the  $^{19}\text{F}(p,\alpha)^{16}\text{O}$  reaction [293, 294].

## 2.6 Cluster structures in $^{20}\text{Ne}$ and $^{19}\text{F}$ and their role in the $^{19}\text{F}(\text{p},\alpha)^{16}\text{O}$ reaction

---

Despite its relevance in studying clustering phenomena in nuclei and its importance in astrophysics, the behaviour of the  $^{19}\text{F}(\text{p},\alpha_0)^{16}\text{O}$  cross section is largely uncertain, especially at low energies, as early noted in Refs. [295, 296]. The Nuclear Astrophysics Compilation of Reaction Rates (NACRE) [109] extrapolated the  $S$ -factor from direct data available in the literature in the  $E_{cm} = 0.46\text{--}2.54$  MeV energy domain [297–301]. At lower energies, unpublished data [302] referred in [148, 149] exist, and were not included in the NACRE compilation as possibly affected by normalization problems [109]. More recently, two experimental works have been reported. The first one explores the low energy region by using the Trojan Horse Method (THM) [220, 292]. The authors argue the possible existence of resonances leading to a significant increase of the reaction rate at energies of stellar interest [292]. The second one is a direct measurement carried out in the energy range  $E_{cm} = 0.577\text{--}0.982$  MeV [228], that partially covers the lowermost energy data by Breuer [299]. In that work, a good agreement with Breuer [299] and Caracciolo et al [300] direct data was observed [228] suggesting that the non-resonant part of the  $S$ -factor at low energies might be larger than the NACRE extrapolation.

In the following paragraphs, our direct experimental measurement of  $^{19}\text{F}(\text{p},\alpha_0)^{16}\text{O}$   $S$ -factor in the  $E_{cm} = 0.18\text{--}0.60$  MeV range is described. In this low-energy region, to our knowledge, no direct experimental data have been previously published. The lowermost energy region of the new experimental data set is close to the upper limit of the Gamow window at  $T = 0.04$  GK, and partially covers the  $E_{cm} \approx 50\text{--}300$  keV energy interval needed for accurate modeling of the nucleosynthesis scenarios in post-AGB stars [292].

### 2.6.1 Experimental details

The experiment was performed at the AN2000 Van de Graaf accelerator of Laboratori Nazionali di Legnaro (LNL) of Padova, Italy. The energy calibration of the proton beam was determined by measuring with a  $\text{LaBr}_3(\text{Ce})$  crystal the  $\gamma$ -ray yield of the  $^{19}\text{F}(\text{p},\alpha\gamma)^{16}\text{O}$  reaction around the resonance at 340 keV, and by using a previous calibration point obtained by studying the  $\gamma$ -ray yield of the  $^{27}\text{Al}(\text{p},\gamma)^{28}\text{Si}$  reaction around the resonance at 992 keV. This calibration has been frequently checked during the experiment and further benchmarked by considering the position of 0.484, 0.594 and 0.669 keV resonances in the yield curve of the  $\alpha_2$  line (associated with the 6.13 MeV state in  $^{16}\text{O}$ ) measured with a silicon detector at  $\theta_{lab} = 160^\circ$ . A further check was the shape analysis of the dip in the elastic scattering differential cross sections  $^{12}\text{C}(\text{p},\text{p}_0)^{12}\text{C}$  at  $\theta_{lab} = 160^\circ$  in the  $E_p = 450$  keV region. The two methods give consistent results within  $\approx 1$  keV. From the measured width of the 340 keV resonance ( $\Gamma = 2.4$  keV [93]) in the  $^{19}\text{F}(\text{p},\alpha_2)^{16}\text{O}$  yield it is possible to estimate a beam energy resolution of  $\approx \pm 2.5$  keV.

In this experiment, the proton beam intensity ranged from 0.3 to 0.9  $\mu\text{A}$ . The target consisted of a  $\text{CaF}_2$  layer (30  $\mu\text{g}/\text{cm}^2$  thick) evaporated onto a natural carbon backing (20  $\mu\text{g}/\text{cm}^2$  thick) and was frequently changed to avoid degradation. Tar-

## Chapter 2. Clustering in light systems: an experimental campaign

---

get thickness was determined during evaporation by means of the resonating quartz method and was subsequently cross-checked by means of elastic backscattering analysis with proton beams at several energies; the resulting overall accuracy is  $\approx 3\%$ . Repeated measurements at the same energy allowed to check the target stability all along the experiment. The elastic backscattering spectra indicate a natural stoichiometric ratio of the  $\text{CaF}_2$  layer, in agreement with [288, 303]. The effect of target thickness has been carefully taken into account according to the procedure outlined in Ref. [103].

The detection system consisted of 12 silicon detectors mounted at various polar angles and placed at 10-12 cm from the target center into a scattering chamber in which a copper rod cooled to liquid nitrogen temperature was placed in order to reduce carbon build up effects. The chamber was kept, during the whole experiment, at high vacuum conditions, i.e. better than  $10^{-6}$  mbar, while the beam current was measured by means of a Faraday cup placed behind the target and a  $-300$  V suppression voltage was applied to reduce secondary electron effects. The detectors,  $300 \mu\text{m}$  thick, have  $1 \times 1 \text{ cm}^2$  active area. The angular resolution was estimated to be  $\simeq 2.8^\circ$ , similar to the one in Ref. [298]. Solid angles were determined by geometry with an accuracy better than 3%. A thin aluminium absorber ( $8 \mu\text{m}$  thick) was placed in front of the silicon detectors in order to suppress scattered protons [228, 298]. Figure 2.29 shows, as an example, the spectrum obtained at a detection angle  $\theta_{lab}=20^\circ$  for proton energy  $E_p = 0.347 \text{ MeV}$ . A very low background is seen in proximity of the  $^{19}\text{F}(p,\alpha_0)^{16}\text{O}$  peaks, and analogous results are obtained in the whole bombarding energy domain here investigated. Peaks due to reactions on the main target contaminants are indicated in the figure. In particular, no appreciable contamination is due to the close-lying  $^{11}\text{B}(p,\alpha_0)^8\text{Be}$  reaction. In this case, indeed, the energy resolution of experimental spectra ( $\approx 0.2 \text{ MeV}$  FWHM) is better than the energy separation of the  $^{11}\text{B}(p,\alpha_0)^8\text{Be}$  and  $^{19}\text{F}(p,\alpha_0)^{16}\text{O}$  peaks at all angles and bombarding energies ( $\approx 0.7 \text{ MeV}$  in the most unfavourable case).

As already mentioned, a tightly collimated ( $\approx 4 \text{ mm}^2$ ) detector was placed at  $\theta_{lab} = 160^\circ$  to detect backscattered protons. In the right panel of Figure 2.29 we show a spectrum obtained with this silicon detector at  $E_p = 0.347 \text{ MeV}$  bombarding energy. In this way it was possible to make a check of the absolute cross section scale for several bombarding energies. In fact, at low energies, the p+Ca elastic scattering cross section can be theoretically predicted [230]. The analysis of the p+Ca elastic backscattering peak at various energies (including low energy points in the 0.25-0.35 MeV domain) leads to elastic cross section estimates in agreement with Rutherford predictions (taking into account electron screening effects, of the order of 1% [230]) within  $\approx 7\%$ ; this number can be assumed as the maximum overall non-statistical error on the absolute cross section scale.

Figure 2.30 (panels a-d) displays present experimental angular distributions (red dots) together with data available from the literature. In the  $E_p \approx 0.3\text{-}0.4 \text{ MeV}$  interval only the very old data (in arbitrary units) by McLean, Ellett and Jacobs [304] exist. Here, they have been normalized to our cross section and shown for com-

## 2.6 Cluster structures in $^{20}\text{Ne}$ and $^{19}\text{F}$ and their role in the $^{19}\text{F}(p,\alpha)^{16}\text{O}$ reaction

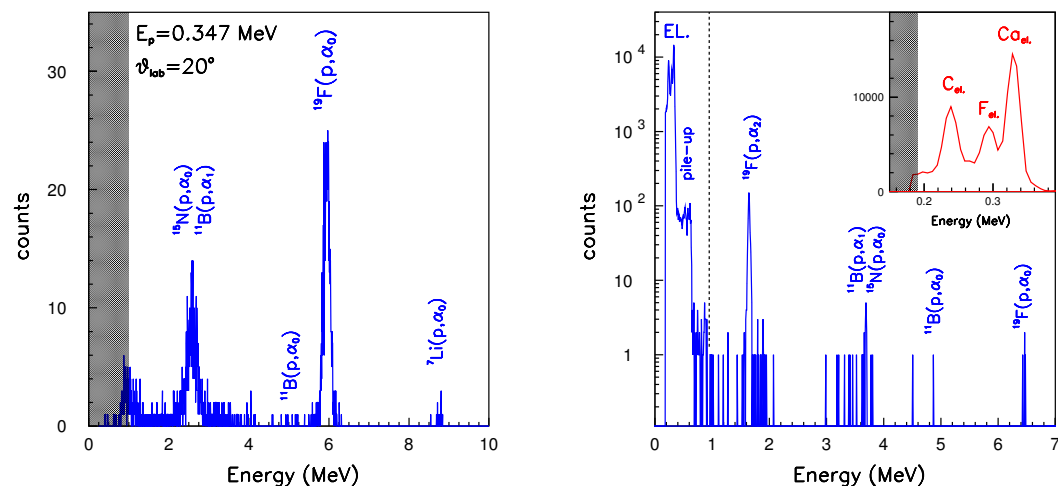


Figure 2.29: (Left panel) Experimental spectrum at  $\theta_{lab} = 20^\circ$  and  $E_p = 0.347$  MeV with the Al absorber. Kinematics and energy loss considerations allow to identify the peaks due to the various reactions. (Right Panel) Experimental spectrum obtained at  $\theta_{lab} = 160^\circ$  and  $E_p = 0.347$  MeV by using a tightly collimated unshielded silicon detector. For clarity, the elastic peak and the pile-up region is scaled by a  $\approx 500$  factor. A magnified view of elastic scattering peaks is reported in the insert. The shadow region indicates electronic threshold.

parison in Figure. The shapes of these angular distributions are in good agreement with our results. In the same energy region, unpublished results by Lorenz-Wirzba [302] have been quoted in Refs. [148, 149]. These data at  $E_p = 0.35$  MeV have been normalized (by a factor 2) to our cross section scale and are shown as blue triangles in Figure 2.30a. A good agreement between the shapes of angular distributions is observed. In Ref. [109] it was hypothesized that the cross section values of the low energy part of this data set could be underestimated. In Figure 2.30e, we show a comparison of the excitation functions at  $140^\circ$  and  $135^\circ$  from the present measurements and data from Refs. [148, 302], respectively. A reasonable agreement is seen at  $E_p > 0.4$  MeV, while at low energies the cross section data from Refs [148, 302] have a different slope. It is interesting to note that discrepancies respect to the cross section data of Ref. [302] have been reported also by other authors in unpublished works, see the review paper [296]. Finally, figures 2.30(c,d) show the angular distributions obtained at  $E_p = 0.482$  and  $0.612$  MeV, together with the data by Breuer [299] normalized to our cross section scale. The agreement between the two data sets is quite good.

## Chapter 2. Clustering in light systems: an experimental campaign

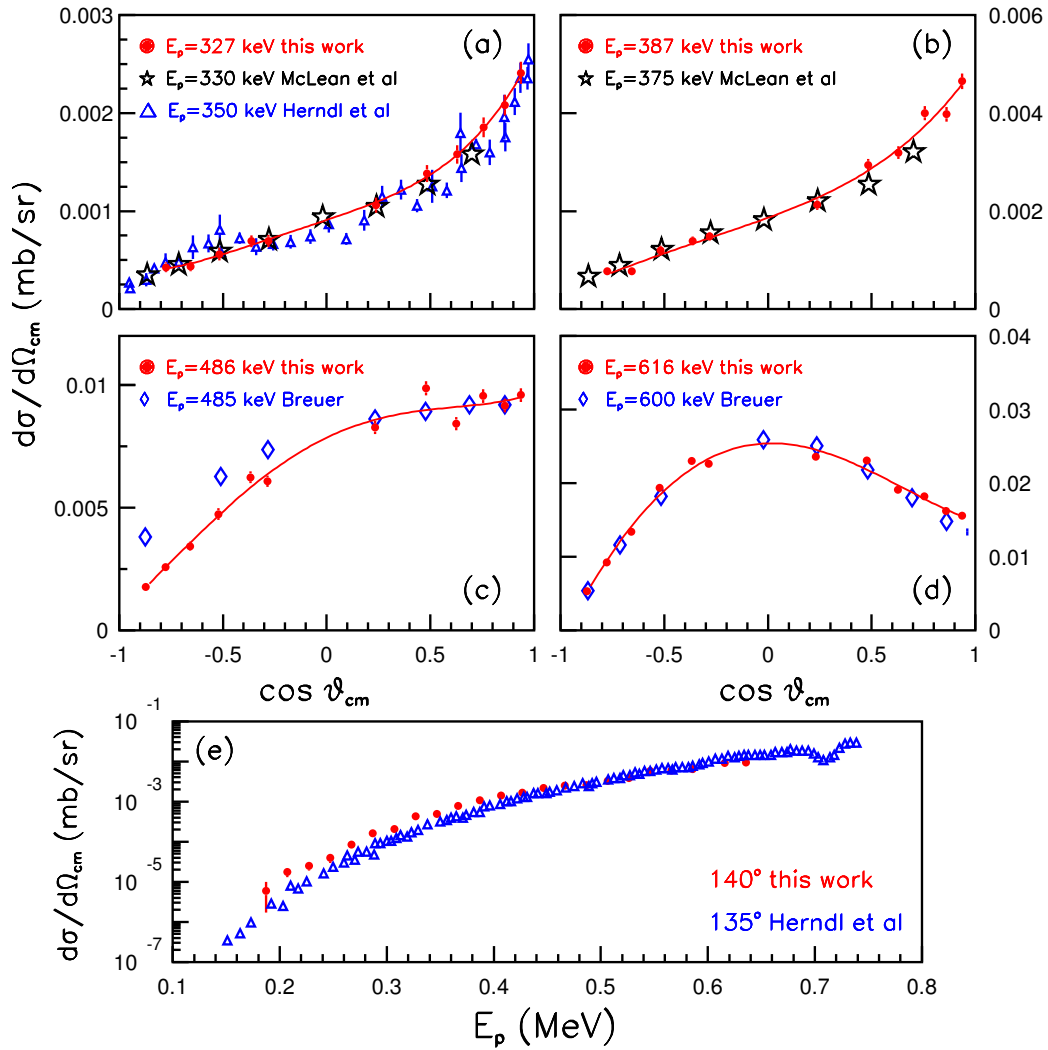


Figure 2.30: (Panels a-d) Angular distributions of the  $^{19}\text{F}(p, \alpha_0)^{16}\text{O}$  reaction at  $E_p = 0.327, 0.387, 0.486$  and  $0.616$  MeV. Red dots: Present data. Red lines: Legendre polynomial fits. Black stars: data from Ref. [304]. Blue diamonds: data from Ref. [299]. Blue triangles: data from Ref. [302]. Data from Refs. [299, 302, 304] have been normalized to our cross section scale as discussed in the text. (e) Excitation function obtained in this experiment at  $140^\circ$  (red dots) compared with data reported at  $135^\circ$  in Ref. [148] (blue triangles).

## 2.6 Cluster structures in $^{20}\text{Ne}$ and $^{19}\text{F}$ and their role in the $^{19}\text{F}(\text{p},\alpha)^{16}\text{O}$ reaction

---

### 2.6.2 Angular distribution analysis and $R$ -matrix fit of data

A strong forward-backward asymmetry of the angular distributions is seen in the  $E_p = 0.2\text{-}0.5$  MeV region. This effect can be explained in two different ways. It can be attributed to interference effects between opposite parity close-lying resonances [298–300] or to the onset of direct processes at sub-Coulomb energies; these direct effects could be triggered by cluster structures in the  $^{19}\text{F}$  target nucleus [148, 149, 305]. To investigate these aspects we analyzed angular distributions in terms of cosine polynomials [298, 300]. The trend of the  $A_i$  coefficients deduced from the fit of experimental data (truncated to the 4<sup>th</sup> order) is reported in Figure 2.31 (left and right panels). The smooth behavior of the  $A_0$  and  $A_2$  terms in the  $E_p = 0.3\text{-}0.5$  MeV region can be mainly due to direct processes, while the broad bump of the  $A_4$  term in the  $E_p = 0.3\text{-}0.5$  MeV region can be attributed to the excitation of the broad  $2^+$  cluster state in  $^{20}\text{Ne}$  ( $E_{cm} = 0.251$  MeV,  $E_x = 13.095$  MeV,  $\Gamma = 162$  keV [93, 306]). At variance, the overall forward anisotropy (see Figure 2.30 (a,b)) observed at low energies seems mainly due to direct reaction mechanisms, which could be triggered by the above mentioned cluster structure of  $^{19}\text{F}$ . In particular, on a naive way, we can expect that a strong  $t + ^{16}\text{O}$ -like configuration for the  $^{19}\text{F}_{gs}$  target would favour forward asymmetries in the  $^{19}\text{F}(\text{p},\alpha)$  angular distributions in a direct reaction scenario. Also the  $\alpha + ^{15}\text{N}$  cluster structure, predicted for the 0.11 MeV excited state of  $^{19}\text{F}$  (due to the *cluster model joke*) can play a role, if one assumes that the process involves more than one step, where one intermediate step passes through this low-lying state. It can lead to the appearance of a forward peaked contribution in the angular distributions at low energies, because of the strong exchange forces involved [149]. Anyway, the situation is more complicated if we go into the details of possible theoretical explanations. All these speculations, triggered by the observed anisotropies in the angular distributions, point out the importance of understanding the cluster structure of light nuclei and stimulate the need of detailed theoretical calculations that couple the cluster structure with the reaction mechanism at low energies.

The cross section  $\sigma(E)$  was obtained by integrating angular distributions over  $4\pi$  for each value of incident energy here explored. The analytical form of the angular distribution trend was taken to be the best-fit to experimental angular distributions in terms of 4<sup>th</sup> order Legendre polynomials. In fact, at these very low energies, only  $s$ ,  $p$  and  $d$  partial waves are expected to mainly contribute [298–300]. Figure 2.32 (upper panel) displays, as blue dots, the calculated astrophysical  $S$ -factor. Statistical errors are represented by error bars, while the grey band indicates non-statistical ones. Our results are plotted together with the ones from [298–300] as reported in NACRE [109], shown as triangles, diamonds and stars respectively. Empty blue circles show more recent data of Ref. [228]. The green dashed line is the non-resonant NACRE  $S$ -factor extrapolation [109]. Present results are in good agreement with the lowermost energy data of [228]. The inspection of Figure 2.32 suggests the appearance of several structures as a consequence of the excitation of

## Chapter 2. Clustering in light systems: an experimental campaign

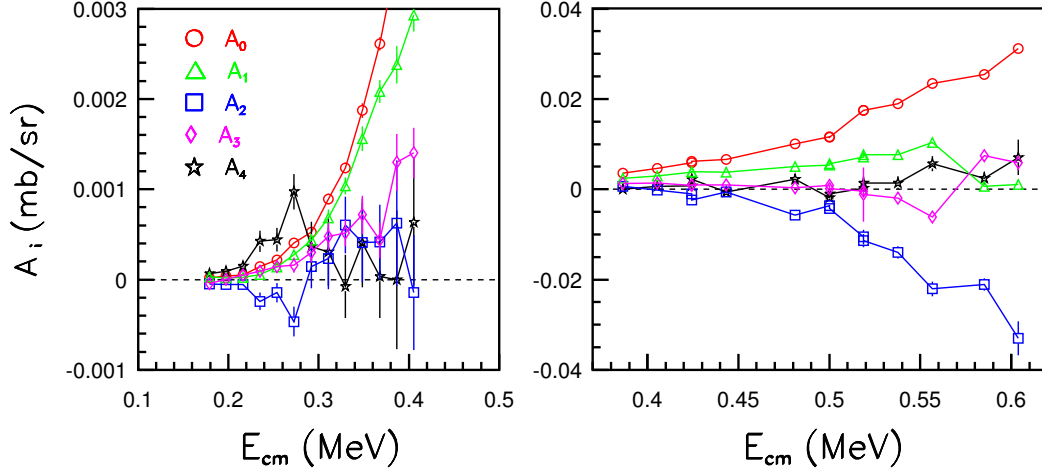


Figure 2.31: Evolution with the energy of the  $A_i$  coefficients of cosine power fit of experimental angular distributions obtained in the present experiment. Error bars are statistical. Note the change of vertical scale in the left and right panels.

various resonances in the compound nucleus, sitting on a continuous background given by direct processes.

We performed an  $R$ -matrix fit of present data and data from Ref. [228]. The  $E_x$ ,  $J^\pi$  and  $\Gamma_{cm}$  resonance parameters have been fixed to the literature values ([93, 228, 292]). As in Refs. [228, 292], the high energy part of  $S$ -factor data is described by the excitation of the  $E_{cm} = 0.801, 0.739, 0.697$  MeV states. The low energy part of data has been reproduced by considering the  $E_{cm} = 0.382$  MeV state ( $3^-$ ,  $\Gamma_{cm} = 53$  keV, [292]), the broad  $E_{cm} = 0.251$  MeV cluster state ( $2^+$ ,  $\Gamma_{cm} = 162$  keV) [93, 306], and the  $E_{cm} = 0.204$  MeV state ( $4^+$ ,  $\Gamma_{cm} = 18$  keV, [292]). We included in the fit the previously observed  $E_{cm} = 0.113$  MeV ( $2^+$ ,  $\Gamma_{cm} = 38$  keV, [292]) state. The resonances at  $E_{cm} = 0.113, 0.204$  and  $0.382$  MeV have been observed with the THM [292] while the resonance at  $E_{cm} = 0.251$  MeV has not been seen before. We assumed  $\Gamma_{tot} \approx \Gamma_\alpha$ , which is a good approximation since at energies well below the Coulomb barrier,  $\Gamma_p$  are severely suppressed by penetrability and, consequently, can be neglected in the calculation of the  $\Gamma_{tot}$ . The shape of the non-resonant background has been taken from NACRE [109]. The only free parameters of the fit were the scaling factor of the non-resonant background and the  $\Gamma_p$  of the  $0.251$  MeV state. The result of fit procedure is reported as red solid line in Figure 2.32. The  $\chi^2$  is 0.97 with 36 d.o.f; the fit describes reasonably well the trend of experimental data in a wide energy domain. The partial widths and, in particular, the  $\Gamma_p$  values are given in [292]. The resonance parameters of the 251 keV peak, not observed in [292], are  $\Gamma_\alpha \approx 160$  keV and  $\Gamma_p \approx 1.4 \times 10^{-5}$  keV, as obtained from the fit procedure. The scaling factor of the non-resonant background is  $1.16 \pm 0.04$ .

## 2.6 Cluster structures in $^{20}\text{Ne}$ and $^{19}\text{F}$ and their role in the $^{19}\text{F}(p,\alpha)^{16}\text{O}$ reaction

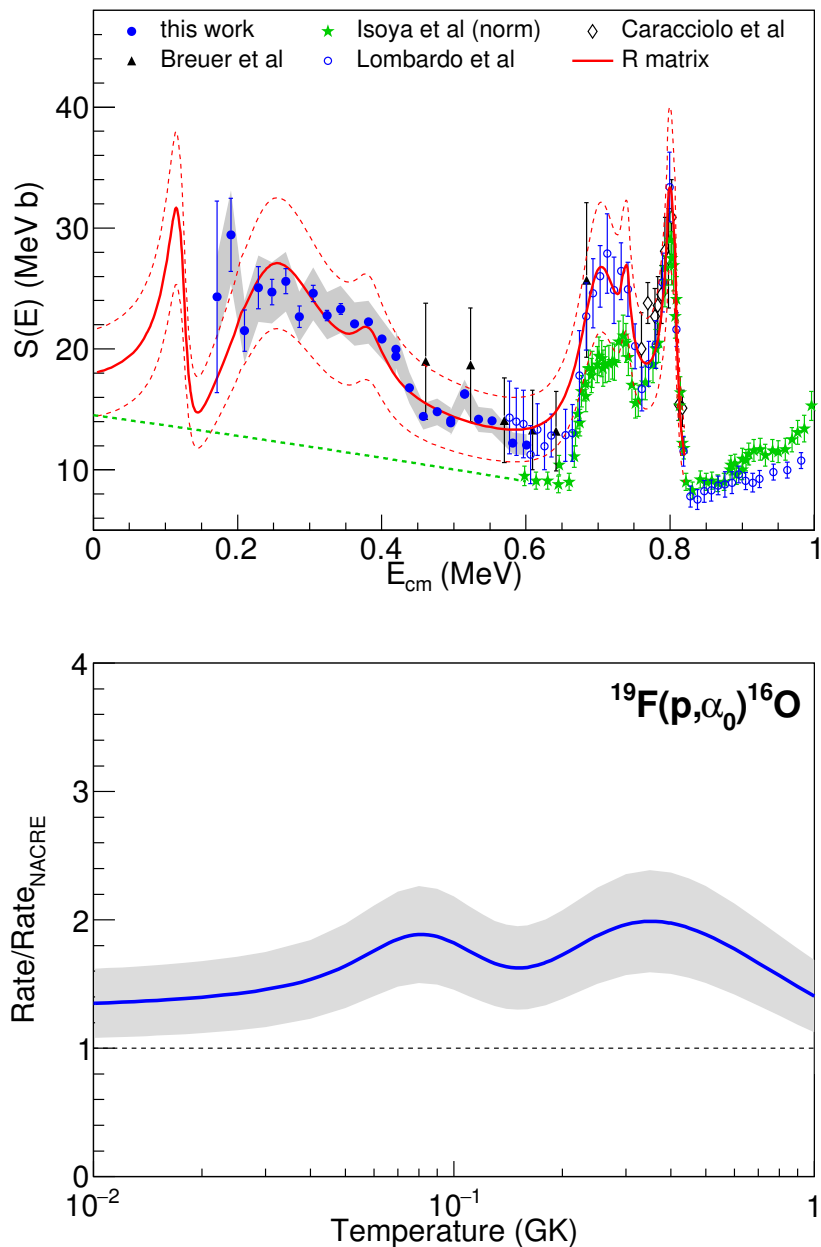


Figure 2.32: (Upper panel)  $S$ -factor of the  $^{19}\text{F}(p,\alpha_0)^{16}\text{O}$  reaction at low energies ( $\lesssim 1$  MeV). Blue solid dots: experimental data obtained in this work (error bars: statistical errors; grey band: non-statistical errors). Black triangles: direct data by [299]. Blue empty circles: data by [228]. Green stars: data by Isoya et al [298] as normalized by NACRE [109]. Black empty diamonds: data by [300]. Green dashed line: non-resonant extrapolation reported in NACRE [109]. Red line: result of  $R$ -matrix best-fit of present data and data by Ref. [228]. White band within the red lines: confidence band of the fit. (Lower panel) Reaction rate calculation (expressed as ratio to NACRE) obtained from the  $R$ -matrix fit of the  $S$ -factor.

## Chapter 2. Clustering in light systems: an experimental campaign

---

The broad bump in the 0.2-0.4 MeV region can be attributed to the constructive interference between the 0.113 and 0.251 MeV  $2^+$  states superimposed on the direct non-resonant background; the contribution of the 0.382 MeV  $3^-$  state is instead quite small. Our analysis allows to exclude the opposite interference pattern option (i.e. destructive interference in the 0.3-0.5 MeV region and constructive in the 0.1-0.2 MeV one) because in this case any attempt to better reproduce the experimental trend between 0.3 and 0.6 MeV would result in a worse agreement at energies below  $\approx 0.3$  MeV. Indeed, the reduction of the astrophysical factor due to the destructive interference above 0.3 MeV cannot be recovered by increasing the non-resonant contribution, as the fitting curve would dramatically overestimate the  $S$ -factor below 0.3 MeV, even taking into account the large errors affecting data in this energy region.

The present  $R$ -matrix fit of  $S$ -factor data allows us to compute the corresponding *stellar reaction rate* per couple of particle  $\langle\sigma v\rangle$ . This gives us an idea of the efficiency of such a reaction for various astrophysical environments. We evaluated the ratio of our calculated reaction rate to the one calculated by using the NACRE extrapolation [109] as a function of the temperature. This can be computed by using the following formulation [103]:

$$\langle\sigma v\rangle = \left(\frac{8}{\pi\mu}\right)^{\frac{1}{2}} \left(\frac{1}{k_B T}\right)^{\frac{3}{2}} \int_0^{+\infty} S(E) e^{-\frac{E}{k_B T}} e^{2\pi\eta(E)} dE \quad (2.1)$$

Here  $\mu$  is the reduced mass of the entrance channel,  $k_B$  is the Boltzmann constant and  $T$  is the temperature of the astrophysical site where the reactions occur. The two exponential factors are respectively the Maxwell-Boltzmann kinetic energy distribution and the barrier penetrability.  $S(E)$ , i.e. the astrophysical  $S$ -factor, is obtained by connecting the experimental point via a polygonal line. The result of this calculation is shown in the lower panel of Figure 2.32. To evaluate the errors due to ambiguities on the modelling of the non-resonant contribution adopted in the  $R$ -matrix fit, we fixed our attention on two different models, the  $s$ -wave proton capture estimation used by NACRE (green dashed line of Figure 2.32) and the finite-range DWBA calculations of Yamashita and Kudo [149]. If we perform the  $R$ -matrix fit by choosing the functional form given by the DWBA model respect to the NACRE one, the resonance parameters remain essentially unaltered, with the low-energy part of the  $S$ -factor differing by  $\approx 20\%$  from the fit obtained by assuming the NACRE non-resonant contribution. Taking into account this main source of ambiguity, we conservatively assumed a 20% error level on the  $S$ -factor evaluation and therefore on the reaction rate calculation. On average, the reaction rate is a factor  $\approx 1.4$  larger than the corresponding NACRE evaluation. Local enhancement at  $T \approx 0.4$  GK can be mainly attributed to the 0.251 MeV state and its interference with the 0.113 MeV state. The bump at  $T \approx 0.08$  GK is originated by the 0.113 MeV state, as seen with the indirect measurement of Ref. [292]. The larger reaction rate observed at temperatures typical of AGB stars should lead to a more efficient  $^{19}\text{F}$

## 2.6 Cluster structures in $^{20}\text{Ne}$ and $^{19}\text{F}$ and their role in the $^{19}\text{F}(\text{p},\alpha)^{16}\text{O}$ reaction

---

destruction by extra-mixing processes. This finding goes in the direction of recent experimental observations of fluorine abundance in metal-poor AGB stars [290, 293] and can contribute to solve the puzzle of fluorine nucleosynthesis in AGB stars [307].

### 2.6.3 Impact of our results on successive works

Now that these new direct data are available [308], the authors of [292] performed a new analysis of the indirect data assuming a different level identification, where the 0.251 MeV state plays a more important role. They show that the THM data can be reasonably fitted by introducing into the modified  $R$ -matrix code the 0.251 MeV resonance in spite of the 0.204 MeV one, by using the same reduced widths as in the present work for the 0.251 MeV state.

A more recent THM experiment succeeded to investigate the  $^{19}\text{F}(\text{p},\alpha)$  reaction with an improved energy resolution [309]. In these data, a more evident contribution of the 0.251 MeV state to the cross section is seen, in nice agreement with our findings.

It is worth nothing that our work stimulated a scientific proposal to the new Jinping Underground laboratory for Nuclear Astrophysics (JUNA) facility that is currently under development in the *Jinping Mountains of Sichuan*, China [310]. The extremely low background of this laboratory makes it a perfect place to explore the  $^{19}\text{F}(\text{p},\alpha)$  reaction at very low bombarding energies ( $E_{cm} < 0.2$  MeV). This will allow to obtain a better knowledge of the reaction rate at temperatures lower than 0.1 GK.



## Chapter 3

# Clustering in HICs as a link between structure and dynamics

In paragraph 1.5.4 of Chapter 1, it has been mentioned how particle-particle and multi-particle correlations in heavy ion collisions can represent a powerful probe to study structure and clustering in light systems and their interplay with nuclear dynamics. In the present chapter, we describe the development of a thermal model to reproduce the formation and the *in-flight decay* of resonances in HICs at intermediate energies. This model, which is valid under the assumption of a unique source of particle emission in thermal equilibrium, allowed us to perform a systematic particle-particle correlation analysis of  $^{36}\text{Ar} + ^{58}\text{Ni}$  collisions at bombarding energies from 32 AMeV to 95 AMeV. The here discussed methods can provide fundamental information on the behaviour of the nuclear force under different conditions of density and temperature, i.e. on the Equation of State (EoS) of nuclear matter.

We organize the present chapter as follows. In Section 3.1, we introduce the concept of *correlation function* in the general case of multi-particle correlation studies and we give a further characterization of the expected dynamics for a central HIC, which is the scenario of the present investigation. After introducing a thermal model for correlations in HICs, we briefly discuss the role of final state interactions and *HBT* effects. In Section 3.2, we describe an in-flight decay simulation code in a specific experimental case. Finally, predictions of the model are compared to experimental  $\alpha$ - $\alpha$  correlations in  $^{36}\text{Ar} + ^{58}\text{Ni}$  collisions from 32 AMeV to 95 AMeV studied with the INDRA  $4\pi$  multi-detector.

### 3.1 Further details on correlations in HICs

Heavy Ion Collisions at intermediate energies are often used to produce states of nuclear matter at densities and temperatures far from saturation. Such conditions do not occur in ordinary terrestrial environments and characterize more extreme scenarios like *supernovae* explosions [311], *neutron stars* [312] or other fascinating

### Chapter 3. Clustering in HICs as a link between structure and dynamics

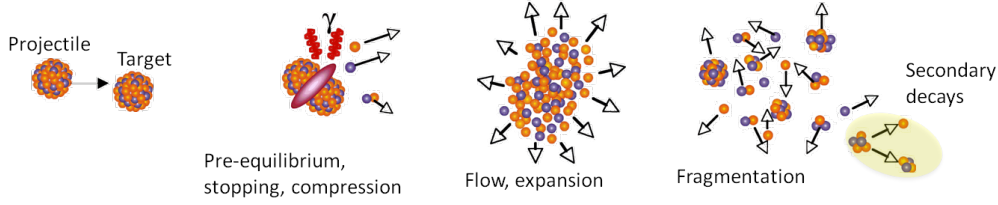


Figure 3.1: Schematic qualitative description of a central HIC at intermediate energies. A unique system, source of particles, is expected to be formed, after a first stage of fast pre-equilibrium emission. The compact object experiences then an expansion, which allows to study, by means of the secondary decays of unbound nuclear states, hot and diluted phases of nuclear matter.

objects in the cosmos. The qualitative schematic description of Figure 3.1 helps understanding such a complex picture. In the figure, a typical central HIC at intermediate energies is schematically shown. Nuclear matter which is formed in the overlapping zone between projectile and target is initially compressed and nuclear *stopping* occurs. In this hot phase, *pre-equilibrium* emission of particles and  $\gamma$ s, which occurs over a short time scale (of the order of 10-50 fm/c), anticipates the expansion of a thermally equilibrated nuclear medium. Such a system experiences decreasing temperatures and densities, finally leading to a hot ( $T \approx 4-6$  MeV) and diluted ( $\rho \lesssim /2\rho_0$ ) nuclear medium. In this stage of the collision complex fragments are produced and carry information about the sub-saturation density regions of nuclear matter under laboratory controlled conditions. Produced fragments can be excited to unbound states, which can subsequently decay inducing the so-called *secondary decays*. These emissions are characterized by time scales significantly longer and, typically, of the order of several thousands and millions of fm/c. Correlation studies involving the decay of resonances for fragments produced *in-medium* may give the opportunity to study unbound states of stable and unstable light nuclei, as well as the *space-time* and *thermal* properties of the medium in which such resonances are produced.

It is useful to define the two-particle correlation function. Assuming two particles 1 and 2 having momenta  $\vec{p}_1$  and  $\vec{p}_2$  (in the center of mass of the couple), the two-particle coincidence yield  $\sum Y_{12}(\vec{p}_1, \vec{p}_2)$  represents the yield of two particles having momentum  $\vec{p}_1$  and  $\vec{p}_2$  detected in coincidence in the same event with relative momentum  $\vec{q}$  and total momentum  $\vec{P}$ :

$$\sum Y_{12}(\vec{p}_1, \vec{p}_2) = C_{12}[1 + R(\vec{q}, \vec{P})] \sum Y_1(\vec{p}_1)Y_2(\vec{p}_2) \quad (3.1)$$

where  $R$  is the so-called *correlation function*, a function of the relative momentum  $\vec{q} = \frac{1}{2}(\vec{p}_1 - \vec{p}_2)$  and of the total momentum  $\vec{P} = \vec{p}_1 + \vec{p}_2$ . The two-particle coincidence yield  $Y_{12}(\vec{p}_1, \vec{p}_2)$  is summed over all the couples of detectors 1 and 2 and the couples  $\vec{p}_1, \vec{p}_2$  which provide the vector  $\vec{q}$ .  $\sum Y_1(\vec{p}_1)Y_2(\vec{p}_2)$  represents the production of the

### 3.1 Further details on correlations in HICs

single yields,  $Y_1$  and  $Y_2$ , if particle 1 and 2 being detected with momenta  $\vec{p}_1$  and  $\vec{p}_2$ , respectively. It is therefore expressed as the sum, with the same prescription of the previous, of products of single-particle yields.  $C_{12}$  is a normalization constant chosen so that  $R = 0$  at large relative momentum values. The most common way to perform particle-particle and multi-particle correlation studies is the use of the so-called *angle-averaged* correlation function, that consists in integrating equation 3.1 over the relative angle between the vectors  $\vec{q}$  and  $\vec{P}$ . The corresponding correlation functions only depend on the magnitude of the relative momentum if one also integrates over the magnitude of the total momentum  $P$ :

$$\sum Y_{12}(\vec{p}_1, \vec{p}_2) = C_{12}[1 + R(q)] \sum Y_1(\vec{p}_1)Y_2(\vec{p}_2) \quad (3.2)$$

From an experimental point of view, the product of single-particle yields  $\sum Y_1(\vec{p}_1)Y_2(\vec{p}_2)$  is constructed via an *event-mixing* procedure: particles 1 and 2 are taken from two different events. The corresponding correlation function assumes therefore the form:

$$R(q) + 1 = \frac{Y^{coinc}(q)}{Y^{mix}(q)} \quad (3.3)$$

which is different than unity in the presence of correlations between particles 1 and 2, while it assumes value equal to unity in the absence of correlations. Correlations between coincident particle pairs can be induced by their mutual nuclear and Coulomb interaction and by their quantum statistical symmetries in they are identical.

#### 3.1.1 The thermal model for correlations in central HICs at low and intermediate energies

We developed a simulation code for the description of two-body in-flight resonance decays in central heavy ion collisions based on a thermal model of two-particle correlations.

The basic assumption of the model is that a *unique* source is created in the central collision and such a source is at thermal equilibrium. Then one can assume a temperature  $T$  for the source itself. A certain amount of light nuclei resonances is produced in the thermally equilibrated medium. In our model, the population of internal states in the decaying nuclides is determined by the temperature of the system. We call this temperature *excited state temperature* [162, 313–315]. It is important to point out, as discussed in Ref. [313], that such a temperature may differ from the one measured by means of other techniques such as the double isotopic yield ratios [170]. Also, excited state temperatures determined from the decay of different nuclear species may differ from another. Indeed, thermometers in HICs may be sensitive to different stages of the fragment formation and emission.

Let us consider a system contained in a volume  $V$ ; the corresponding two-particle density of states is approximated by the equation [316]:

$$\rho(P, q) \approx \rho_0(P) \cdot \rho(q) \quad (3.4)$$

### Chapter 3. Clustering in HICs as a link between structure and dynamics

---

As in the previous paragraphs,  $P$  and  $q$  are, respectively, the amplitude of the total and relative momentum of a generic pair of particles.  $\rho_0(P) = VP^2/2\pi^2$  is the density of states associated with the motion of their center of mass, while  $\rho(q)$  depends only on relative motion. The latter, at the first order of approximation, can be written as:

$$\rho(q) = \rho_0(P) + \Delta\rho(q) \quad (3.5)$$

The first component,  $\rho_0(P)$ , is a plane-wave density of states for particles with spins  $s_1$  and  $s_2$ . It is given by the equation

$$\rho_0(q) = (2s_1 + 1)(2s_2 + 1) \frac{Vq^2}{2\pi^2} \quad (3.6)$$

The latter term,  $\Delta\rho$ , is an interaction term. It can be written, in the simplified case of non-identical particles, as [316]:

$$\Delta\rho(q) = \frac{1}{\pi} \sum_{J,\alpha} (2J + 1) \frac{\partial\delta_{J,\alpha}}{\partial q} \quad (3.7)$$

Here,  $J$  represents the total angular momentum of the interaction of the two particles, while  $\delta_{J,\alpha}$  is the scattering phase shift for each channel  $\alpha$ . This term, differently from the plane-wave density of states, does not depend on the volume of the system. Equation 3.4 can be rewritten introducing the previous prescription as follows:

$$\rho(P, q) \approx \rho_0(P)\rho_0(q)[1 + R(q)] \quad (3.8)$$

The two-particle correlation function  $R(q)$  is here defined by:

$$R(q) = \frac{2\pi}{(2s_1 + 1)(2s_2 + 1)Vq^2} \sum_{J,\alpha} (2J + 1) \frac{\partial\delta_{J,\alpha}}{\partial q} \quad (3.9)$$

Equation 3.9 does not depend on the temperature of the system. Under the above discussed thermal equilibrium hypothesis, the single-particle yield of the  $i$ -th particle of the system with a momentum  $p_i$  follows instead a Boltzmann distribution of the type:

$$Y_i(p_i) \propto \rho_0(p_i)e^{-E_i/T} \quad (3.10)$$

while, for the probability to find simultaneously a particle 1 with momentum  $p_1$  and a particle 2 with momentum  $p_2$ , having total momentum  $P$  and relative momentum  $q$ , one finds:

$$Y_{12}(p_1, p_2) \propto \rho_0(P, q)e^{-(E_1+E_2)/T} \quad (3.11)$$

### 3.1 Further details on correlations in HICs

Within this thermal model, the two-particle correlation function therefore depends only on the volume of the system and it is independent on the temperature<sup>1</sup>, while the two-particle coincidence yield is affected by the temperature of the system. In the thermal model, the probability that a nucleus is at an excitation energy  $E$  is given by:

$$\frac{dn(E)}{dE} \propto e^{-E/T} \Delta\rho(E) \quad (3.12)$$

where  $\Delta\rho(E)$  is the above discussed density of states and  $e^{-E/T}$  is the so-called Boltzmann factor. In the case of resonances dominating the energy dependence of the partial-wave scattering phase shift, the density for the unbound states can be written as a sum of Breit-Wigner terms and equation 3.7 can be rewritten as:

$$\Delta(\rho)(E) \propto \sum_i \frac{(2J_i + 1)\Gamma_i/2\pi}{(E - E_i)^2 + \Gamma_i^2/4} \quad (3.13)$$

where the sum is extended to all nuclear levels  $i$  contributing to the formation of the particular nucleus under study. The probability to observe the nucleus populated at an excitation energy in the interval  $E, E + dE$  decaying into the channel  $c$  is finally:

$$\left[ \frac{dn(E)}{dE} \right]_c \propto e^{-E/T} \sum_i \frac{(2J_i + 1)\Gamma_i/2\pi}{(E - E_i)^2 + \Gamma_i^2/4} \frac{\Gamma_{c,i}}{\Gamma_i} \quad (3.14)$$

where  $\Gamma_{c,i}$  is the partial decay width of the state  $i$  into the channel  $c$  and  $\frac{\Gamma_{c,i}}{\Gamma_i}$  is the decay branching ratio into this channel. In the case of two non-overlapping states,  $H$  and  $L$ , separated by an energy  $\Delta E = E_H - E_L$ , the ratio of their populations before decaying will be, according to this model:

$$R_{L,H} = \frac{Y_L}{Y_H} = \frac{2J_L + 1}{2J_H + 1} e^{-\Delta E/T} \quad (3.15)$$

In other words, the ratio of the population of the low energy state to the one of the high energy state depends only on structure properties of the two states (i.e. their spins,  $J_L$  and  $J_H$ , and their energy separation,  $\Delta E$ ) and on the temperature,  $T$ , of the medium in where the levels are populated.

#### 3.1.2 The In-Flight Decay Simulation Code

The following step consists in studying how the initial population of the states prior to decay affects the yields of the experimentally observed peaks. In other words, a

<sup>1</sup>It is important to point out that this represents only a rough approximation, since it has been proved that the correlation function can depend on the temperature in the case of *collective motion* [164, 317]. In fact, the presence of a collective motion, e.g. a radial expansion which depends on the position coordinates of the particles in the medium, may induce the appearance of an artificial effective temperature in the uncorrelated background which can lead, in the presence of resonances, to an alteration of the corresponding correlation function. This effects are not taken into account in our model and will be introduced in a successive improved version.

### Chapter 3. Clustering in HICs as a link between structure and dynamics

---

detailed simulation code which explicitly describes the in-flight decay of resonances produced under the thermal model assumption, accounting also the configuration of the used detector, is required to predict the yields in eq. 3.15. They can be reconstructed by studying the corresponding two-particle correlation function of the particular exit channel involved. Let us assume, to clarify this step, that a nuclear specie X is produced in a nuclear medium at temperature  $T$ . The states of the unbound system which contribute to the formation of X are numbered from 1 to  $M$ , and their corresponding spectroscopic properties are indicated as  $E_i$ ,  $\Gamma_i$ ,  $\Gamma_{i,c}$ . Here,  $E_i$  represents the energy of the  $i$ -th state of  $\Gamma_i$  total width.  $\Gamma_{i,c}$  is instead the partial width of the  $i$ -th state into the decay channel  $c$ . The observed yield  $Y_N^C(E)$ , as a function of the excitation energy of the emitting nuclei, can be easily written, with this prescription, in the following way:

$$Y_N^C(E) = N \int \left[ \eta_c(E, E') e^{-E'/T} \right] \sum_{i=1}^N \frac{(2J_i + 1) \Gamma_i / 2\pi}{(E - E_i)^2 + \Gamma_i^2 / 4} \frac{\Gamma_{i,c}}{\Gamma_i} dE' \quad (3.16)$$

In equation 3.16,  $N$  is an arbitrary constant and the integral is extended over all excitation energies  $E'$  that contribute to the formation of the unbound system. The factors in square parenthesis is the product of the Boltzman factor, which gives a weight to any possible excitation energy according to the thermal hypothesis, and the matrix elements  $\eta_c(E, E')$ . The latter, as it will be discussed in more detail in the following paragraph for the case of the INDRA  $4\pi$  multi-detector, connects theoretical values of excitation energy  $E'$  of the nucleus to the corresponding experimentally reconstructed value  $E$  in the emitting channel  $c$  by means of the corresponding detection efficiency. In other words, if one assumes an excitation energy  $E'$  of the emitting nucleus before decaying in the channel  $c$ , this will be reconstructed by the detector as  $E$  (taking into account any possible distortion introduced by the detector to the observed particles, according to reaction kinematics and the energy and angular resolution of the detector itself) with an efficiency  $\eta_c(E, E')$ . The second part contains all the structure properties of the states involved in the formation of the decaying system. It is the sum, over each state of the X nucleus, of the product of the probability that the  $i$ -th state decays through the channel  $c$ ,  $\Gamma_{i,c}/\Gamma_i$ , weighted for the probability that it is populated at an excitation energy  $E'$ .

#### 3.1.3 HBT interferometry in Nuclear Physics

Two-particle correlations at low relative momentum provide information on a number of properties of collisions between heavy nuclear systems. Besides the possibility of deducing temperatures via the above-mentioned thermal model approach, one can study also the space-time properties of the collision system. This research field, usually named *intensity interferometry* or *HBT femtoscopy*, has been the object of a large number of investigations in the last decades.

HBT interferometry was originally introduced in astronomy (in 1950s by Hanbury Brown and Twiss, HBT). Such techniques were extensively used to extract

### 3.1 Further details on correlations in HICs

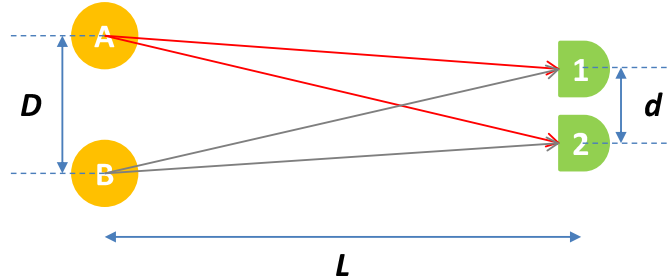


Figure 3.2: A schematic explanation of the HBT effect in astronomy. Two sources of photons A and B are separated by a distance  $D = |\vec{r}_a - \vec{r}_b|$  and are seen at a distance  $L$  by the detectors 1 and 2 (at a mutual distance  $d$ ). The interference pattern observed at the detectors allows to infer the distance between the stellar sources.

unknown separations (*source size*) of astrophysical objects. Differently from amplitude interferometry that suffers uncontrollable contributions from atmospheric distortions, HBT is based on intensity interferometry [318]. Let us assume that two sources of photons A and B are located at a relative distance  $D$  as it is schematically illustrated on Figure 3.2. If one detects the emitted photons by means of the detectors 1 and 2, placed at a distance  $L$  from the sources and at a mutual distance  $d$ , one can define the following quantity:

$$R(\vec{k}_1, \vec{k}_2) = \frac{\langle n_{12} \rangle}{\langle n_1 \rangle \langle n_2 \rangle} - 1 \quad (3.17)$$

Here  $\langle n_{12} \rangle$  is the two-photon coincidence yield, i.e. the probability to detect two photons with wave numbers  $\vec{k}_1$  and  $\vec{k}_2$  respectively in the detectors 1 and 2. The denominator of eq. 3.17 represents instead the product of single-photon yield in the detectors 1 and 2. All the quantities which contribute to this equation are proportional to the absolute square of the amplitudes, and, therefore, HBT interferometry is insensitive to phase shifts introduced by atmospheric disturbances [319]. The quantity described in the equation 3.17 is called *two-photon correlation function*. The physical basis of the HBT is that two photons may have a non-zero correlation function because of the symmetrization of their wave-functions. This is a consequence of the quantum nature of identical particles [141, 320]. The link between the correlation function for two-photons and the spatial properties of the emitting source is clear if one considers the simplified case of simultaneous photon emission from two distant point sources located at  $\vec{r}_a$  and  $\vec{r}_b$ . Assuming that the propagation occurs in vacuum, the coincidence rate of two photons  $\vec{k}_1$  and  $\vec{k}_2$  in the detectors 1 and 2 is proportional to the symmetrized two-photon wave-function, normalized to

### Chapter 3. Clustering in HICs as a link between structure and dynamics

---

the incident fluxes:

$$\begin{aligned} \langle n_{12} \rangle(\vec{k}_1, \vec{k}_2) &= \frac{1}{2} \left| e^{i\vec{k}_1 \cdot \vec{r}_a + i\vec{k}_2 \cdot \vec{r}_b} + e^{i\vec{k}_1 \cdot \vec{r}_b + i\vec{k}_2 \cdot \vec{r}_a} \right|^2 \\ &= 2\cos^2 \left[ \frac{1}{2}(\vec{k}_1 - \vec{k}_2) \cdot (\vec{r}_a - \vec{r}_b) \right] \end{aligned} \quad (3.18)$$

The correlation function therefore depends on the relative momentum of the two detected photons  $\vec{q} = \frac{1}{2}(\vec{k}_1 - \vec{k}_2)$  and on the spatial separation of the two sources  $\vec{D} = (\vec{r}_a - \vec{r}_b)$ . The correlation function in the case of a simultaneous emission from an extended and incoherently emitting source is finally obtained by integrating eq. 3.18 over the spatial extent of the source.

The ideas of Hanbury Brown and Twiss have been extended later to subatomic particles such as photons, pions and various fermions and bosons. There is an essential difference between HBT in astronomy and in subatomic physics: whereas in astrophysics the emission can be assumed to be stationary during the observation time, in nuclear physics the system is evolving with time. Therefore the study of correlations between particles probes both the spatial and time extension of a subatomic source. As an example, intensity interferometry has been successfully applied to the study of angular correlations between pions emitted in proton-antiproton annihilation processes at energies of 1 GeV by Goldhaber and collaborators [321]. They found that the probability of coincident identical pions was strongly affected by their quantum mechanical properties, i.e. the Bose-Einstein statistics. The corresponding correlation function showed indeed an enhancement corresponding to zero relative momentum  $q = 0$ , and the width of such a maximum was linked to the interaction volume [322]. These measurements further stimulated efforts in the development of HBT interferometry to nuclear cases. Shuryak [323] showed that the effects observed by Goldhaber et al. in the pion-pion correlation function could be interpreted in terms of HBT intensity interferometry. The shape of the correlation function depends not exclusively on the geometrical size of the emitting source, but also on the dynamics of the source. More in details, the mean-life of the emitting pion source affects such a correlation function. Sources of particle emission evolve indeed in extremely short time-scales (of the order of  $10^{-22}$ - $10^{-18}$  s) when compared to the time required for the particles to be detected. An historical step in such a development was made by S.E. Koonin with his seminal work [324]. He proposed in 1977 that proton-proton correlation functions could be used as a tool to explore the emission sources in nuclear collisions involving heavy systems at intermediate energies ( $E = 20$ - $100$  AMeV). Since protons are *fermions*, an effect opposite to the one pointed out in the case of pairs of pions was observed, resulting in a reduction of the coincidence yield at small values of relative momenta, as a result of the antisymmetrization properties of the two-fermion wave-function. The two-proton correlation function depends also on the Coulomb and nuclear final state interactions (FSI) between them. While the Coulomb FSI is repulsive, the second is attractive at very short ranges and vanishes when the relative distance exceeds a

### 3.1 Further details on correlations in HICs

certain range of few fm's. These effects modify the shape of the correlation function. They depend on the relative distance between the particles and therefore they are more effective when the emission points of the two particles are close enough in the source. FSI contribute to increase the sensitivity of correlation functions to the size of the emitting source as well as to a detailed description of multi-fragmentation phenomena and the liquid-gas *phase transition* in nuclear matter. In 1990s, correlation studies have been extended to the case of complex particles such as deuterium- $\alpha$ ,  $\alpha$ -proton,  $\alpha$ - $\alpha$  or even to the case of the so-called Intermediate Mass Fragments<sup>2</sup> (IMFs) [317, 325, 326].

#### 3.1.4 Characterization of the emitting source

Since the nuclear and Coulomb interactions depend on the relative position between the two interacting particles, the shape of the correlation function peaks is strongly sensitive to the size of the two-particle emitting source. To be more precise, the shape of correlation function peaks due to the nuclear FSI and of the *anti-correlation hole*<sup>3</sup> at small relative momentum due to the Coulomb FSI, are determined by the space-time extent spanned by the two-body system in the fragmenting system. Thanks to these properties, intensity interferometry, for example involving two-proton correlations, have been largely used to probe the space-time properties of sources produced in HICs. Protons are indeed the most abundantly produced particles in a HIC at intermediate energies and for this reason one can expect to study their correlation function with high statistics at all incident energies. From a theoretical point of view, the two-proton correlation function can be computed by means of the so-called Koonin-Pratt equation [327]:

$$R(q) + 1 = \int d\vec{r} S(\vec{r}) K(\vec{r}, \vec{q}) + 1 \quad (3.19)$$

here  $S(\vec{r})$  represents the probability that two particles are emitted at a mutual space-time distance  $r$ , calculated at the time when the last particle is emitted. This quantity is connected to the spatial extension of the emitting source.  $K(\vec{r}, \vec{q})$  is the so-called angle-averaged kernel. It is obtained from the radial part of the antisymmetrized two-proton relative wave-function by using the following relation:

$$K(\vec{r}, \vec{q}) = |\Psi_q(r)|^2 - 1 \quad (3.20)$$

where  $\Psi_q(r)$  is the radial part of the proton-proton scattering wave-function [328]. The kernel contains all the information about the antisymmetrization of the proton-proton wave function, as well as their mutual Coulomb and nuclear final-state interactions.

<sup>2</sup>With Intermediate Mass Fragments (IMFs) we define charged fragments with  $3 \leq Z \leq 30$ .

<sup>3</sup>The anti-correlation hole consists in a reduction of the two-particle coincidence yields at small values of relative momentum due to their mutual Coulomb repulsion.

## Chapter 3. Clustering in HICs as a link between structure and dynamics

---

One can obtain information on the space-time extent of a nuclear emitting source basically solving equation 3.19, namely extracting the profile of the source function,  $S(\vec{r})$ . One can then obtain the geometrical extension of the emitting source function once the kernel is known theoretically. Since the emission of particles is generally distributed over a finite time window, the source function is affected by a space-time ambiguity and will appear deformed in the direction defined by the total momentum vector [329]. In angle-averaged approaches one can use the source function to infer the relative contributions from dynamical emissions (occurring over short time scales and at early stages of the collisions) and from evaporative and secondary decay contributions (which slowly characterize the later stages of the collisions) [330].

Even if different approaches have been used in the literature to extract information on the source function, a commonly adopted strategy is to consider  $S(r)$  as a normalized single gaussian function, where the width  $\sigma$  of the distribution is an estimate of the space-time extent of the source. These gaussian approaches are rather simple, since they depend only on the source radius. Another approach that allows to study the shape of the correlation function is the *imaging technique* [331]. The basic idea behind it is to extract the source function  $S(\vec{r})$  by a numerical inversion of the Koonin-Pratt equation 3.19, without any a-priori assumption about its profile. Theoretical attempts have been performed in order to extend the Koonin-Pratt formalism to cases involving the emission of more complex particles like  $\alpha$ -particles.  $\alpha$ - $\alpha$  correlation studies offer important future perspectives in this respect.

### 3.2 Application of the thermal model to $\alpha$ - $\alpha$ correlations in $^{36}\text{Ar} + ^{58}\text{Ni}$ with the INDRA $4\pi$ multi-detector

The developed thermal model is useful to study the decay of resonances measured by high resolution arrays, such as FAZIA [332] and HiRA [333]. The latter is characterized by high angular resolution. The analysis that we performed with INDRA is limited by its geometry (e.g. its angular resolution). However, it represents a good starting point for future high resolution analyses. With this premise, in the following paragraphs of the present section, dynamical properties of HICs at intermediate energies will be studied by means of  $\alpha$ - $\alpha$  correlations in  $^{36}\text{Ar} + ^{58}\text{Ni}$  reactions and with the previously discussed thermal-model simulation code.

#### 3.2.1 The INDRA experimental filter

The in-flight resonance decay model described in the previous paragraph allows us to characterize the emission and decay of light nuclei resonances produced in HICs (under a thermal equilibrium assumption) for an arbitrary couple of emitted fragments. The model also accurately describes the detector distortions induced to the

### 3.2 Application of the thermal model to $\alpha$ - $\alpha$ correlations in $^{36}\text{Ar} + ^{58}\text{Ni}$ with the INDRA $4\pi$ multi-detector

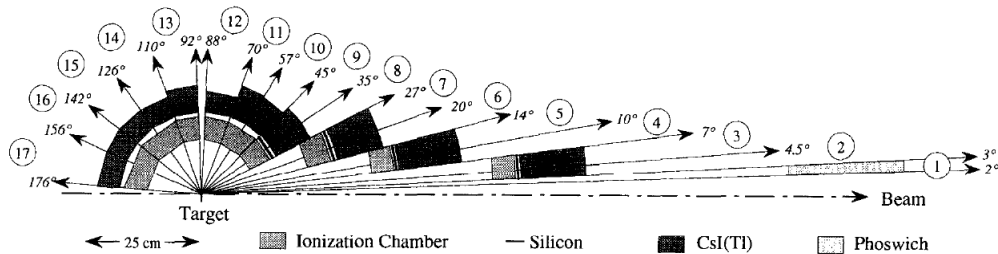


Figure 3.3: Geometrical scheme of the INDRA  $4\pi$  multi-detector (cut along the beam axis). Rings of detectors, coaxial with the beam axis, cover specific region of polar angle. Rings are numbered from 1 to 17 and the minimum and maximum polar angle covered by each ring is indicated. From [334].

observed phenomenon when experimentally reconstructed, allowing a direct comparison of simulated data to experimental ones. The effect of the detector is included in the  $\eta_c(E, E')$  matrix introduced in equation 3.16. To adapt the model to a specific case of interest it is therefore needed to build such a matrix. In this paragraph, a specific example of  $\alpha$ - $\alpha$  correlations reconstructed in  $^{36}\text{Ar} + ^{58}\text{Ni}$  collisions from 32 AMeV to 95 AMeV with the INDRA  $4\pi$  multi-detector is discussed. Such a systematics is important since it allows us to deduce information on how  $\alpha$ -clustering phenomena may affect the production of light particles at various conditions of density and temperature of the medium, and what one can learn about the reaction dynamics from light particle correlation studies.

The experiment was performed at the Grand Accélérateur National d'Ions Lourds (GANIL) laboratory to study  $^{36}\text{Ar} + ^{58}\text{Ni}$  collisions at 32, 40, 52, 63, 74, 84 and 95 AMeV. The INDRA multi-detector was used to detect the produced particles and fragments. It is constituted by 336 independent detection cells which cover geometrically 90% of the  $4\pi$  solid angle. These detectors are grouped in a series of 17 rings, each of them containing a number of cells from 8 to 24 arranged in an axially-symmetric configuration around the beam axis, as outlined by Figure 3.3. Except for the detectors of the first ring, which cover smaller polar angles (from  $2^\circ$  to  $3^\circ$ ) and which are constituted by phoswich scintillators, each detection unit is composed by three detection stages: an ionization chamber, a silicon layer and a CsI(Tl) scintillator. The thickness of such layers depends on the polar angle. This apparatus allows us to track and identify the charge of particles and fragments with a low detection threshold ( $\approx 1$  AMeV) and up to  $Z = 50$ . Isotopic separation is obtained up to  $Z = 3$ . A photograph of the apparatus is shown in Figure 3.4, where the ring arrangements of the detectors are clearly visible. More details about the present apparatus can be found in Ref. [334].

The in-flight resonance decay model can be applied to the case under investigation, by building the  $\eta(E, E')$  matrix. It is affected clearly by the geometrical arrangement of the detectors and their intrinsic energy resolution, but also by the

### Chapter 3. Clustering in HICs as a link between structure and dynamics

---

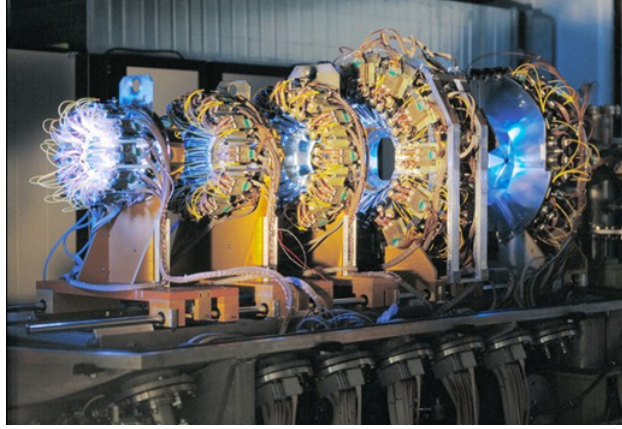


Figure 3.4: A photo of the INDRA  $4\pi$  multi-detector.

kinematic of resonance emission and by the specific decay channel chosen. For this reason, the starting point of the construction of the detector matrix consists in the development of an event generator which is able to reproduce the observed resonance emission in the case here considered.

One can assume that, in the collision events to be investigated,  $^8\text{Be}$  nuclei are statistically emitted. They subsequently decay into a couple of  $\alpha$ -particles which are then reconstructed by the detector. To study how the detector affects the *ideal* relative momentum spectrum of the couples of  $\alpha$ -particles, one can start from the  $^8\text{Be}$  (emitting nucleus) energy and angular distributions expected for the present collision. They can be obtained by inspecting the experimental data, assuming that they do not differ significantly from the ones observed for other detected beryllium stable isotopes such as  $^7\text{Be}$  and  $^9\text{Be}$ . According to the suggestions of literature, the energy spectrum of a nuclear species produced in a collision at a particular angle  $\theta$  can be parametrized in terms of the sum of Maxwellian *moving sources* [335, 336]. In other words, we are assuming that a certain number of different emission sources in thermal equilibrium are created in the collision and that they evaporate according to the Maxwell-Boltzmann statistics. Since they are not produced at rest, the evaporated particles and fragments have to be *boosted* with a velocity which depends on the source motion. The yield of beryllium isotopes emitted at an angle  $\theta$  in the laboratory frame within an elementary solid angle  $d\Omega$  and with kinetic energy  $E \in [E_{lab}, E_{lab} + dE_{lab}]$  can be thus described by the equation:

$$Y(E_{lab}, \theta) = \sum_{i=1}^3 N_i \sqrt{E_{lab} - E_C} \times \exp \left[ - \frac{E_{lab} - E_C + E_{S,i} - 2\sqrt{(E_{lab} - E_C)E_{S,i}} \times \cos\theta}{T_i} \right] \quad (3.21)$$

### 3.2 Application of the thermal model to $\alpha$ - $\alpha$ correlations in $^{36}\text{Ar} + ^{58}\text{Ni}$ with the INDRA $4\pi$ multi-detector

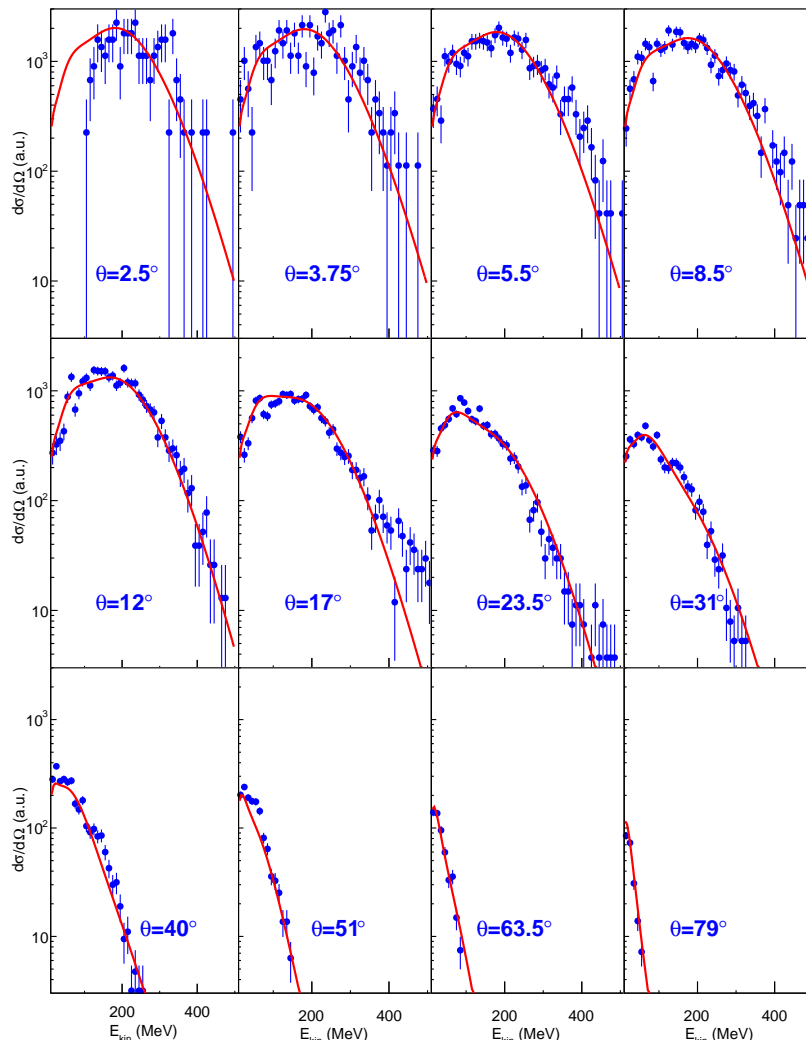


Figure 3.5: Maxwellian moving-source fit of Be energy spectra, obtained at various angles with the INDRA  $4\pi$  multi-detector measured in  $^{36}\text{Ar} + ^{58}\text{Ni}$  collisions at 74 AMeV. The experimental data are shown by blue points with statistical error. Each panel is relative to a different ring of the INDRA multi-detector. The red line is the result of the simultaneous fit with the formula shown in equation 3.21.

where the sum is extended over three different emitting sources<sup>4</sup>. Here  $T_i$  indicates the apparent temperature of the  $i$ -th source emitting particles of charge  $Z$  while

<sup>4</sup>In the present analysis, we are assuming that only one emission source is created in such central collisions. Anyway, since the result of the Maxwellian moving-source analysis is here used only as event generator, without any intent of proving the physical properties of the collision, and to obtain a better fit of the data, we extended the number of emission sources to three, similarly to the case of less dissipative collisions studied in Refs. [335, 336].

### Chapter 3. Clustering in HICs as a link between structure and dynamics

---

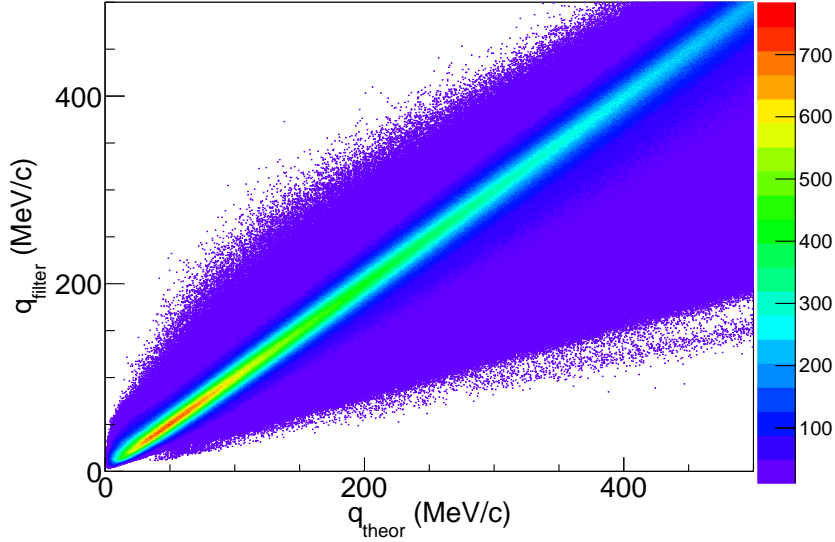


Figure 3.6:  $\eta(E, E')$  matrix used to simulate the effect of the detector for  $\alpha$ - $\alpha$  correlations in  $^{36}\text{Ar} + ^{58}\text{Ni}$  collisions at 74 AMeV. For convenience, it is shown in terms of the relative momenta. The one-dimensional efficiency distribution, as a function of  $q_{\text{filter}}$ , obtained for a fixed value of theoretical momentum  $q_{\text{theor}}$ , allows to estimate the resolution with which the relative momentum  $q_{\text{theor}}$  is reconstructed by INDRA.

$E_{S,i} = (1/2)mv_{S,i}^2$  is the non-relativistic kinetic energy of a particle having mass  $m$  and velocity equal to the one ( $v_{S,i}$ ) of the  $i$ -th source in the laboratory frame.  $E_C = ZE_{\text{coul}}$  is a term representing the energy needed by the particle to overcome the Coulomb barrier.  $N_i$  is finally a normalization coefficient which determines the weight of each contribution to the emission spectrum. Equation 3.21 is used to reproduce the trend of the experimental data obtained at various angles with the INDRA multi-detector by selecting a specific class of collisions events (see the next paragraph for further details of the event selection). An example of the result of our multi-parametric fit is reported in Figure 3.5 for the case of  $^7\text{Be}$  energy spectra measured in  $^{36}\text{Ar} + ^{58}\text{Ni}$  collisions at 74 AMeV incident energy. Here each panel is representative of a particular ring of the INDRA multi-detector and, therefore, of a specific angle in the laboratory frame. The energy spectra for each ring shown in the picture are normalized to the solid angle covered by the ring to be directly compared with the formula 3.21. The red lines, which represent the results of our best-fit procedure, reasonably reproduce the trend of the data for each detection angle. The formula is more general as it allows us to extend the expected angular and energy distributions also outside from the measured regions.

The result obtained via the best-fit procedure on the beryllium energy spectra

### 3.2 Application of the thermal model to $\alpha$ - $\alpha$ correlations in $^{36}\text{Ar} + ^{58}\text{Ni}$ with the INDRA $4\pi$ multi-detector

data are here used to generate randomly extracted  $^8\text{Be}$  fragments. For a theoretical excitation energy  $E'$  of a generated  $^8\text{Be}$ , one can simulate the decay in two  $\alpha$ -particles according to the available phase space. The momenta of the so obtained  $\alpha$ -particles are then processed by a detailed geometrical simulation of the INDRA multi-detector. In this simulation we take into account any dead zone of the detector and we reject events in which two  $\alpha$ -particles hit the same detection cell. The detector matrix  $\eta$  is shown in Figure 3.6 in terms of the relative momenta for  $\alpha$ - $\alpha$  correlations in  $^{36}\text{Ar} + ^{58}\text{Ni}$  collisions at 74 AMeV.  $q_{theor}$  represents the theoretical value of relative momentum while  $q_{filter}$  is the reconstructed one. A locus corresponding to  $q_{theor} \approx q_{filter}$ , where the majority of the counts lie, is clearly visible. Minor contributions are also localized outside this band reflecting possible discontinuities in the emission direction reconstruction due to the finite number of detection cells. This matrix is particularly useful even for a rapid evaluation of the effect of the detector in the invariant mass reconstruction of such pairs of particles. In fact, for a fixed value of theoretical relative momentum  $\overline{q_{theor}}$ , one can inspect the corresponding  $\eta(q_{filter}, \overline{q_{theor}})$  distribution. The width of this distribution is a measurement of the resolution of the detector in measuring the  $\overline{q_{theor}}$  relative momentum in the selected break-up channel. Figure 3.6 shows that the INDRA detector tends to deform significantly the reconstructed  $q_{rel}$  values due to its very limited angular resolution. Significant improvements of these techniques can be obtained with more segmented detector arrays such as LASSA [337] or HiRA [333].

By means of the detector matrix shown in Figure 3.6, we computed formula 3.16. As structure parameters we considered the ground state ( $E_x = 0$ ,  $J^\pi = 0^+$ ,  $\Gamma = 0.0068$  MeV,  $\Gamma_\alpha/\Gamma = 1.00$ ,  $q_{rel} = 18.49$ ) and the first excited state of  $^8\text{Be}$  ( $E_x = 3.04$ ,  $J^\pi = 2^+$ ,  $\Gamma = 1.5$  MeV,  $\Gamma_\alpha/\Gamma = 1.00$ ,  $q_{rel} = 108.0$ ). The result of the calculation is shown in Figure 3.7 for different values of temperature  $T$  from 1 to 12 MeV. Each line, in a different colour, represents the expected  $\alpha$ - $\alpha$  correlation, as observed by INDRA considering  $^{36}\text{Ar} + ^{58}\text{Ni}$  collisions at 74 AMeV, for a specific value of temperature. As it is clearly visible, the second peak, which is associated to  $\alpha$  decays of the first excited state of  $^8\text{Be}$ , becomes more pronounced as the temperature increases. For higher values of temperature (starting from  $T \approx 6$  MeV) the shape of the  $\alpha$ - $\alpha$  correlation yield saturates, making it difficult to distinguish between different temperatures. These calculations can be easily used in order to construct a calibration curve of the excited-state thermometer based on the population of  $^8\text{Be}$  ground state and its first excited state. By using equation 3.15, we can finally replace the initial population  $Y_L$  and  $Y_H$  of the lower and higher energy states here considered with the reconstructed ones  $N_L$  and  $N_H$ , as they are experimentally determined. They can be deduced by a simple integration<sup>5</sup> of the spectrum of Figure 3.7 for different values of temperature. The result is shown in Figure 3.8,

<sup>5</sup>For the present analysis we used reasonable integration limits deduced from Figure 3.7. The corresponding intervals are [0MeV/c, 50MeV/c] for the  $^8\text{Be}$  ground state peak and [50MeV/c, 304MeV/c] for the 3.04 MeV state peak.

### Chapter 3. Clustering in HICs as a link between structure and dynamics

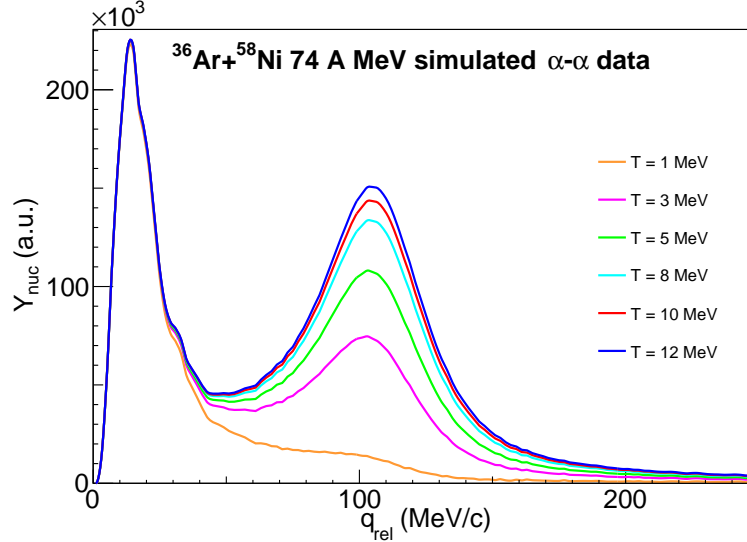


Figure 3.7: Simulated  $\alpha$ - $\alpha$  relative momentum spectrum in  $^{36}\text{Ar} + ^{58}\text{Ni}$  collisions at 74 A MeV via the model here described. The detector distortions introduced by the detection with INDRA are carefully taken into account via our detailed event filter. The calculation is repeated for different values of temperature, shown in different colours.

where black points represent the simulated values above discussed and the red line is the result of a best-fit using equation 3.15. The calibration curve, which has been constructed for each colliding system of our systematics, allows us to extract the temperature of the medium in which the resonances are produced by experimental measurement of the yields of the observed peaks in the  $\alpha$ - $\alpha$  correlations. Finally, as previously pointed out, the present thermometer becomes less sensitive to high values of temperatures. This fact is even more clear considering the trend of the calibration curve shown in Figure 3.8. While for high  $N_L/N_H$  values, i.e. low temperatures, the calibration curve is only smoothly variable, indicating a good sensitivity of the thermometer, for high temperatures the curve is almost vertical. In other words, a large variation in temperature results in a negligible variation for the relative ratio of the two peaks, making this thermometer poorly sensitive to high values of temperature. The sensitivity of the thermometer to such temperature values can be increased, for example, by considering a couple of states with a larger energy distance  $\Delta E$ . Among them, we mention the  $^5\text{Li}$  thermometer [162, 171, 313], whose ground and first excited states differ by about  $\Delta E = 16$  MeV. We do not use this thermometer due to the limited statistics for  $d$ - $^3\text{He}$  correlations, which makes it difficult to extract the population of the first excited state of  $^5\text{Li}$ . Also the limited angular resolution and granularity of the INDRA array make it difficult to well isolate the peaks corresponding to the decay of  $^5\text{Li}$  states.

### 3.2 Application of the thermal model to $\alpha$ - $\alpha$ correlations in $^{36}\text{Ar} + ^{58}\text{Ni}$ with the INDRA $4\pi$ multi-detector

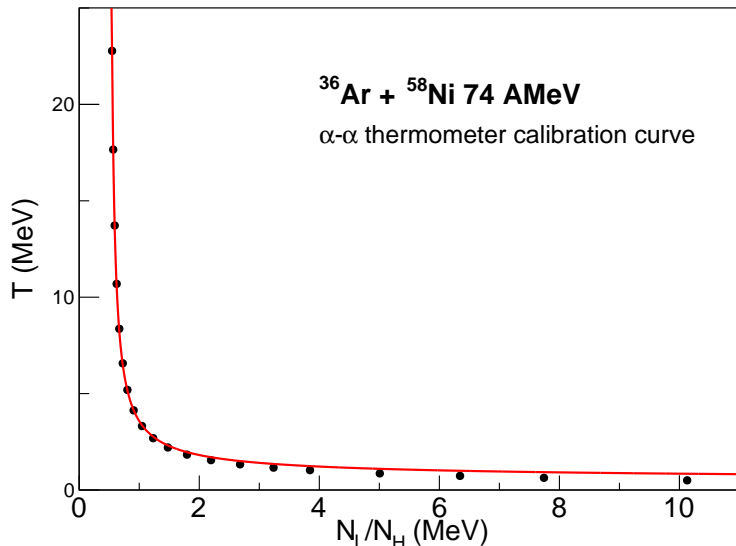


Figure 3.8: Calibration curve of the excited-state thermometer of  $^8\text{Be}$  ground state and first excited state ( $\alpha$ - $\alpha$  correlations).  $N_L/N_H$  is the ratio of the observed peak integrals of respectively low and high energy peak here considered, obtained by means of our simulation code. The thermometer is less sensitive to high values of temperature.

#### 3.2.2 Analysis of $\alpha$ - $\alpha$ correlations in $^{36}\text{Ar} + ^{58}\text{Ni}$ systematics from 32 AMeV to 95 AMeV

The above discussed method has been used to perform a systematic analysis of  $\alpha$ - $\alpha$  correlations in  $^{36}\text{Ar} + ^{58}\text{Ni}$  collisions. As it was previously anticipated, *central* collision events are selected. The centrality selection has been obtained by means of a cut on the transverse energy spectra of  $Z = 1, 2$  particles. This cut is based on an intuitive fact: as the impact parameter decreases (more central collisions), the dissipation of energy increases with the effect of releasing much more energy in the direction orthogonal to the beam axis and with a more abundant emission of light particles. This can be studied by summing all the kinetic energies of hydrogen and helium particles associated to their motion on a plane orthogonal to the beam axis,  $E_{t12}$ . The cuts we used on  $E_{t12}$  are shown in table 3.1 for each of the incident energies here considered; we report also the minimum values of such observable,  $E_{t12}^*$ . Events are selected by means of the condition  $E_{t12} > E_{t12}^*$ , where  $E_{t12}^*$  increases with the incident energy as shown in table 3.1. These cuts are determined by means of the

### Chapter 3. Clustering in HICs as a link between structure and dynamics

---

Colliding system	$E_{t12}^*$ (MeV)
$^{36}\text{Ar} + ^{58}\text{Ni}$ 32 AMeV	183
$^{36}\text{Ar} + ^{58}\text{Ni}$ 40 AMeV	221
$^{36}\text{Ar} + ^{58}\text{Ni}$ 52 AMeV	285
$^{36}\text{Ar} + ^{58}\text{Ni}$ 63 AMeV	352
$^{36}\text{Ar} + ^{58}\text{Ni}$ 74 AMeV	421
$^{36}\text{Ar} + ^{58}\text{Ni}$ 84 AMeV	479
$^{36}\text{Ar} + ^{58}\text{Ni}$ 95 AMeV	550

Table 3.1: Centrality selection cuts for the  $^{36}\text{Ar} + ^{58}\text{Ni}$  collisions here investigated. The second column reports the minimum  $E_{t12}$  values here selected calculated with the Cavata method and relative to a reduced impact parameter  $\tilde{b} \leq 30\%$ .

Cavata method<sup>6</sup> [338], and they correspond to a sufficiently high degree of centrality ( $\tilde{b} \leq 30\%$ ).  $\tilde{b}$  is here the so-called *reduced impact parameter*, calculated as the ratio of the impact parameter to the sum of the nuclear radii in the entrance channel  $\tilde{b} = b/(R_t + R_p)$ .

We constructed  $\alpha$ - $\alpha$  correlation functions for each value of the incident energy. As an example, in Figure 3.9 we show the experimental two- $\alpha$  coincidence yield obtained in central collisions at 74 AMeV as a function of the relative momentum  $q_{rel}$ . The spectrum shows a maxwellian-like overall shape fall off due to couplings of non-resonant pairs of particles. Two yield enhancements are visible in the left side of the spectrum, which correspond to low relative momentum values, for which one can expect the appearance of resonances in the  $^8\text{Be}$  emitting nuclei. Such enhancements are better visible in the insert, where a zoom of the left side is reported. In this plot, together with the two-particle coincidence yield spectrum (blue line) we plot the expected non-resonant background (red dashed line). This is evaluated by means of event-mixing techniques and is normalized as previously discussed (see paragraph 3.1.3). We attribute the yield of the blue spectrum exceeding the one of the uncorrelated spectrum to the  $\alpha$  decays respectively from the ground state of  $^8\text{Be}$  and its first excited state ( $E_x = 3.04$  MeV). The first of the two peaks is deformed, and it could be the superposition of the ground state contribution with the  $^9\text{Be}$  ghost peak (as previously observed in the analysis of paragraph 2.1 in Chapter 2 of the present dissertation). Finally, we used labels to indicate the expected position of such peaks in the insert.

In Figure 3.10 we report the corresponding correlation function, obtained with equation 3.3, at the same incident energy of Figure 3.9. It is obtained by the ratio of the two- $\alpha$  coincidence yield to the event-mixing spectrum. The error bars are

---

<sup>6</sup>The Cavata method links the reduced impact parameter  $\tilde{b}$  to the sum of the  $E_{t12}$  yield spectra in the following way:  $\tilde{b} = \sqrt{\frac{1}{N} \int_{E_{t12}^{max}}^{E_{t12}^*} Y(E_{t12}) dE_{t12}}$ , where the integral is extended from the maximum of the spectrum  $E_{t12}^{max}$  to the  $E_{t12}^*$  value.

### 3.2 Application of the thermal model to $\alpha$ - $\alpha$ correlations in $^{36}\text{Ar} + ^{58}\text{Ni}$ with the INDRA $4\pi$ multi-detector

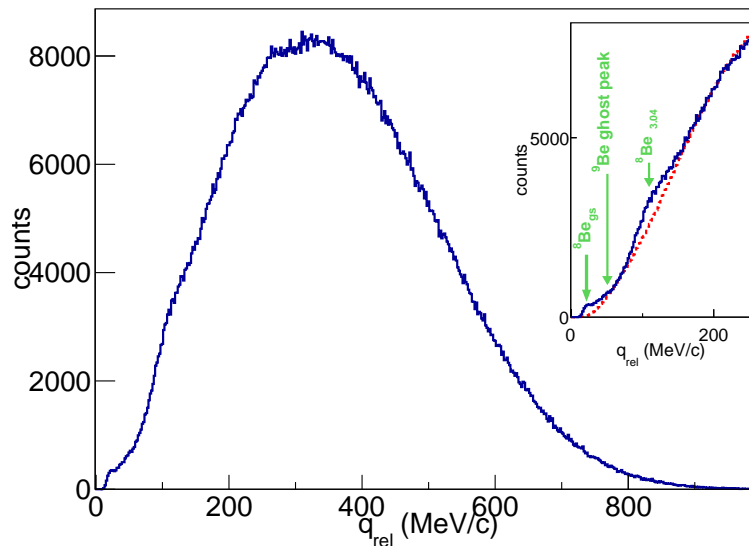


Figure 3.9: Experimental two- $\alpha$  coincidence yield, as a function of the relative momentum, for  $^{36}\text{Ar} + ^{58}\text{Ni}$  collisions at 74 AMeV obtained for central events with the INDRA  $4\pi$  multi-detector. The insert shows a zoom of the low relative momentum part of the spectrum. Here the red line is the evaluated non-correlated background estimated via our event-mixing procedure. Arrows and labels indicate the position of expected peaks.

only due to statistical errors in the numerator of equation 3.3, since the error on the uncorrelated background is made arbitrarily small by increasing its statistics in the event-mixing spectrum. This figure allows to clearly observe contributions of nuclear-interaction correlations. In particular, the insert in figure reports a zoom of the region of the peak corresponding to the decays from the 3.04 MeV state in  $^8\text{Be}$ .

A more detailed analysis of the observed two-particle coincidence yield is anyway required in order to disentangle the nuclear correlation yield from any other contribution which dominates the experimental yield reported in Figure 3.9. It can be reasonably assumed that it is constituted by the overlap of the following contributions:

$$\sum Y_{12}(\vec{p}_1, \vec{p}_2) = Y_{nuc}(q) + Y_{uncorr}(q) + Y_{coul}(q) \quad (3.22)$$

In equation 3.22,  $Y_{nuc}(q)$  represents the yield of nuclear correlated pairs of particles, i.e. the two-particle coincidence yield that would be obtained in the presence of resonance decay only without Coulomb repulsion between them. This is the quantity which has to be obtained in order to make comparisons with the one simulated by using equation 3.16. A certain number of particle pairs which do not belong to  $^8\text{Be}$  in-flight decays are even present in the total yield. They are represented by the second term of equation 3.22. As it was discussed above, we estimate this contribution

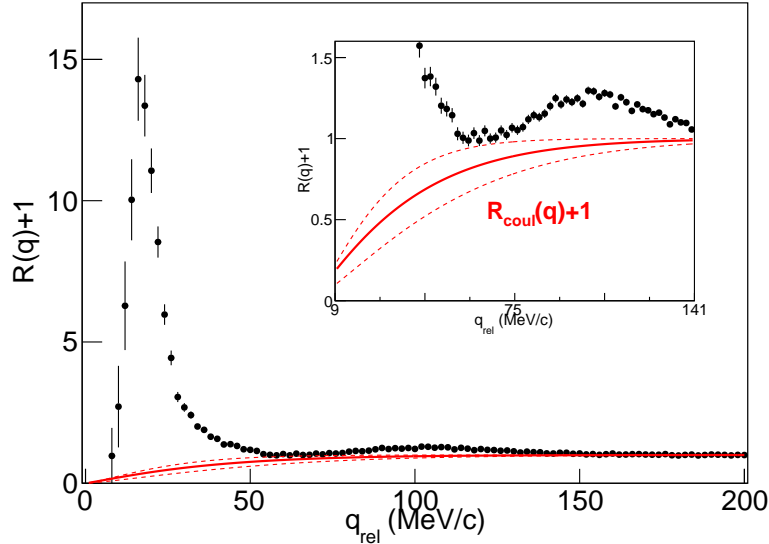


Figure 3.10: Two- $\alpha$  correlation function, as a function of the relative momentum, obtained for  $^{36}\text{Ar} + ^{58}\text{Ni}$  at 74 AMeV with the INDRA multi-detector. The red solid line corresponds to the Coulomb anti-correlation function  $R_{coul}(q) + 1$  as obtained from the analysis of Figure 3.11. Dashed red lines represent the upper and lower limits of such contributions. The insert is a zoom of the relative momentum region of the 3.04 MeV state in  $^8\text{Be}$ .

by using the event mixing analysis of pairs of  $\alpha$ s. A last term,  $Y_{coul}$  has to be taken into account in the analysis of the two-particle coincidence yield. It corresponds to the spectrum one would obtain for independently emitted  $\alpha$ -pairs mutually interacting via Coulomb FSI. Such repulsive interaction induces a suppression of the particle-particle coincidence yield at small values of relative momentum. This effect plays an important role as it overlaps with those regions of spectrum where resonances are observed. This term has been estimated by using the phenomenological expression [339]:

$$R_{coul}(q) + 1 = 1 - e^{-\left(\frac{q^2}{b}\right)^d} \quad (3.23)$$

Here, it is given in terms of the corresponding correlation function, which has values  $\leq 1$ . This expression represents a Coulomb anti-correlation term, since it tends to 1 for large values of  $q$  and it is smaller than 1 at small relative momenta.  $b$  and  $d$  are two free parameters that can be fixed in order to reproduce the trend of experimental data. Since the spectrum of Figure 3.10 is clearly dominated by resonances, the use of such a correlation channel to constrain the Coulomb term of the correlation function makes the convergence of formula 3.23 difficult. Instead, one can use such formulation to reproduce the correlation function of non-resonant pairs

### 3.2 Application of the thermal model to $\alpha$ - $\alpha$ correlations in $^{36}\text{Ar} + ^{58}\text{Ni}$ with the INDRA $4\pi$ multi-detector

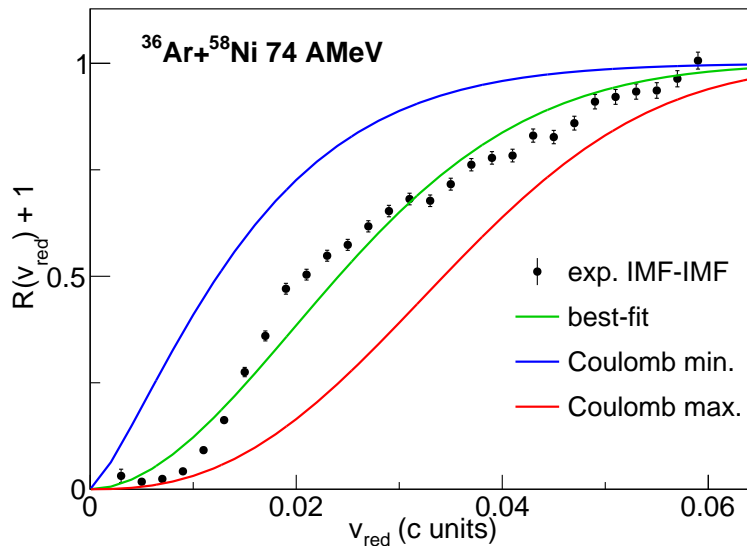


Figure 3.11: IMF-IMF correlations in  $^{36}\text{Ar} + ^{58}\text{Ni}$  central collisions at 74 AMeV, in terms of the reduced velocity. The green line represents the result of a best-fit of data using the empirical formulation of equation 3.23. Blue and red lines are the limit of the confidence band resulting from the fit.

of particles, which are therefore exclusively dominated by the Coulomb interaction. Correlation involving couples of IMFs are suited for that purpose, since they do not exhibit marked resonant behaviours. In Figure 3.11 we show the IMF-IMF correlation for central  $^{36}\text{Ar} + ^{58}\text{Ni}$  collisions at 74 AMeV. The typical Coulomb hole is clearly visible, as an effect of the above discussed mutual repulsion at small values of relative momenta. Data are here reported as a function of the *reduced velocity*,  $v_{\text{red}} = \frac{q}{\mu\sqrt{Z_1+Z_2}}$ , which represents the amplitude of the relative velocity to the square root of the sum of the charges. The advantage of such a representation of the data is that the corresponding correlation function, which is only affected by the charge of the fragments, does not depend on the particular couple of IMFs considered and can be extended to any different couple of particles simply transforming the  $v_{\text{red}}$  in the relative velocity. Other approaches used to determine the line-shape of the purely Coulomb correlation function consist of studying non-resonant light particle correlations. On the one hand, such approach would be more appropriate to extract the  $\alpha$ - $\alpha$  Coulomb background. On the other hand, the limited angular resolution of INDRA makes it difficult to measure the shape of the Coulomb anti-correlation in light particle correlations. Heavier particle pairs with  $Z > 2$  undergo stronger mutual Coulomb repulsion, inducing wider Coulomb holes in the correlation functions extending over larger  $q_{\text{rel}}$  values that are more easily measured. The green line shown in Figure 3.11 represents the best-fit obtained by using equation 3.23 and

### Chapter 3. Clustering in HICs as a link between structure and dynamics

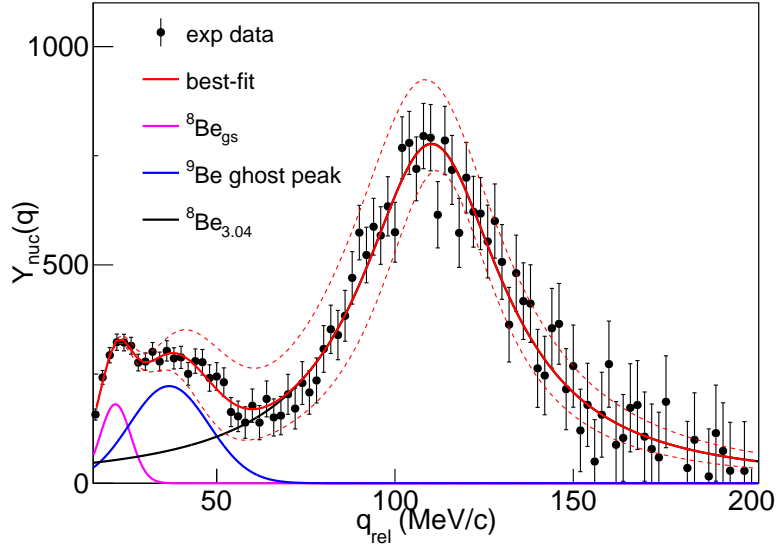


Figure 3.12:  $\alpha$ - $\alpha$  coincidence yield obtained by subtracting the uncorrelated yield and the coulomb anti-correlation effects. Error bars reflect the usual error propagation procedure applied to equation 3.24. The red solid line is the result of a best-fit including the sum of two gaussians and a lorentzian. Dashed lines are the extremes of confidence of our indetermination band due to the uncertainty in the estimation of the Coulomb effects. Lines of different colours are finally used to show, separately, the contribution of each of the peaks considered.

the above discussed prescriptions. A weaker or stronger assumption on the Coulomb strength results, respectively, in the blue and red lines shown in figure. They can be considered as delimiting a confidence band which includes the assumed Coulomb correlation function. The result of the best-fit, together with its confidence band, is shown in terms of  $\alpha$ - $\alpha$  relative momentum in Figure 3.10 with solid and dashed red lines.

One can finally disentangle the nuclear part of the observed two-particle coincidence yield from the ones associated to uncorrelated pairs of particles and the Coulomb anti-correlation by a simple application of the following equation:

$$Y_{nuc}(q) = \sum Y_{12}(\vec{p}_1, \vec{p}_2) - [R_{coul}(q) + 1]Y_{uncor}(q) \quad (3.24)$$

Figure 3.12 shows the result of this analysis. In the figure, the solid black points represent the trend of the estimated nuclear yield by using the average value of the calculated Coulomb background. Error bars are calculated via the usual error propagation applied to equation 3.24. Peaks are here clearly visible. They are associated to the ground state and first excited state of  ${}^8\text{Be}$ , while the peak at around 35 MeV/c is the previously mentioned ghost peak due to  ${}^9\text{Be}$  decay. A

### 3.2 Application of the thermal model to $\alpha$ - $\alpha$ correlations in $^{36}\text{Ar} + ^{58}\text{Ni}$ with the INDRA $4\pi$ multi-detector

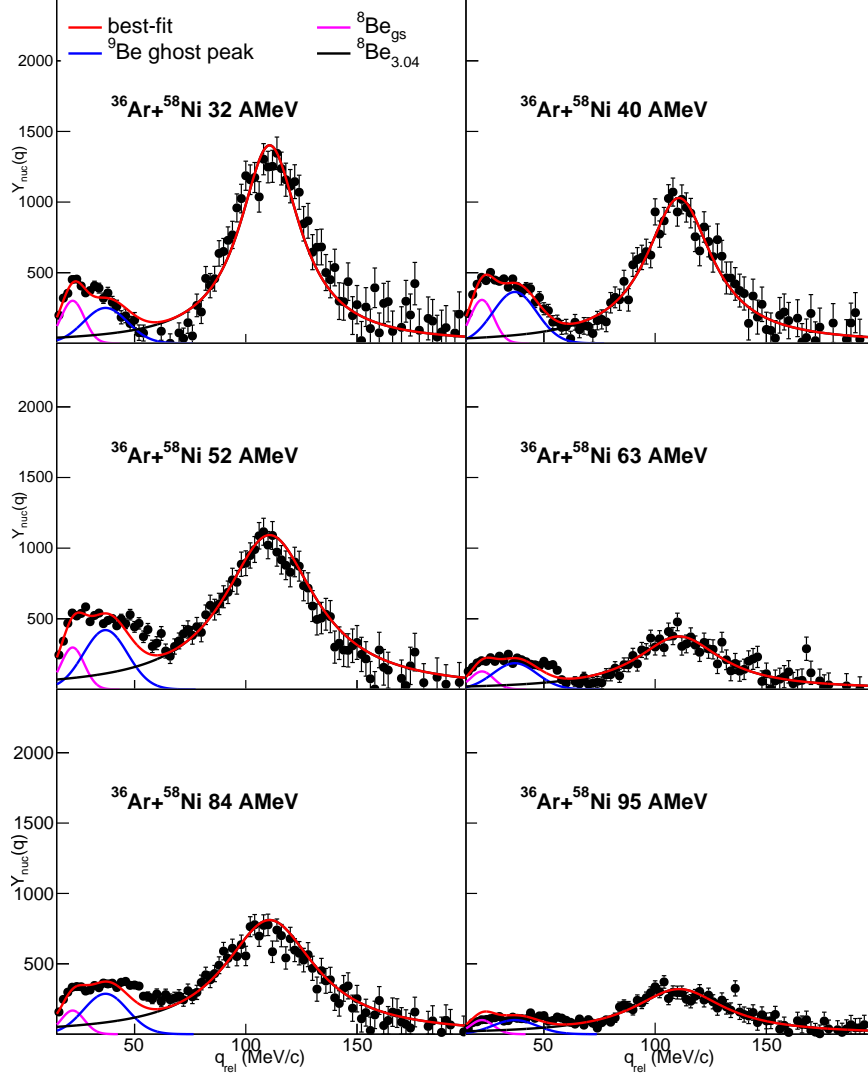


Figure 3.13:  $\alpha$ - $\alpha$  coincidence yield from the method of equation 3.24. Data are shown in different panels for each of the energies here explored (the case of 74 AMeV is reported, separately, in Figure 3.12). The line representing the best-fit of the data (for an average Coulomb strength assumption) is shown.

superposition of two gaussians, to account for the shape of the first two peaks, and a lorentzian are used to reproduce the trend of the data. The choice of different curves reproducing different peaks is imposed by the largely different peak widths. In fact, while the experimental resolution clearly dominates the two narrow low energy peaks, altering the original lorentzian-like shape, the width 3.04 MeV state of  $^8\text{Be}$  is sufficiently large to make the effect of the detector on its shape less significant. Lines of different colours are used in the figure to show separately the single-state

## Chapter 3. Clustering in HICs as a link between structure and dynamics

---

contributions which better reproduce the data. The red solid line is the result of our best fit procedure, in good agreement with the experimental points. Red dashed lines represent the result of an analogous best-fit procedure but considering minimum and maximum Coulomb background. They give the idea of the confidence band here introduced, reflecting the uncertainty in the estimation of the Coulomb effects.

Finally, to complete our systematics, in Figure 3.13 we show the results of a similar analysis for all the other energies explored here. The same horizontal and vertical scales are here used to allow an easier comparison of all the spectra. By looking at the entire systematics, one clearly observes an average decreasing of the total yield of  $\alpha$ - $\alpha$  correlation. This may be consistent with a preferential production, as the energy increases, of lighter particles instead of more complex fragments like beryllium, with a subsequently reduction of the accumulated statistics.

### 3.2.3 Discussion on the reaction dynamics

By inspecting the best-fits of the systematics of Figs. 3.12 and 3.13, one can extract the population of the observed  $\alpha$ - $\alpha$  peaks associated, respectively, to the ground state and the 3.04 MeV state in the decaying  ${}^8\text{Be}$ . Thanks to the calibration curves constructed by our model (Figure 3.8 gives as an example, the thermometer calibration curve at 74 AMeV incident energy) one can infer, as previously stated, the excited-state temperature of the  ${}^8\text{Be}$ . Quite interestingly, we find that the observed  $N_L/N_H$  ratio is not consistent, for any of the bombarding energies here explored, with a thermal model description. More in details, we observe an extra-population of the peak associated to the 3.04 MeV state with respect to the ones predicted by the model for such a mechanism. This is clearly visible in Figure 3.14, where we report the experimental  $N_H/N_L$  yield ratio as a function of the incident energy. The red stars, which represent the experimental data, do not agree with any excited state temperatures extracted via the thermal model, that are shown in the figure as solid lines of different colours. We observe, as previously stressed, a saturation of the thermometer sensitivity for high temperatures, which results in a reduced distance between the theoretical lines close to  $T = 5$  MeV. This evidence pushes us to formulate some hypothesis, which help us in understanding how the production of  $\alpha$ -cluster states is affected by the reaction mechanism and to infer about the properties of the medium in which the explored resonances are produced.

The thermal model seems to under-predict the population of the second peak in the  $\alpha$ - $\alpha$  correlation function in a way that cannot be explained by a temperature effect. It is difficult to provide an explanation for such an effect. Previous studies have attributed difficulties in predicting simultaneously more than one peak in a correlation function to an effect of collective motion [317]. In that work, however, correlation functions, rather than coincidence yields, were studied. Furthermore, it was shown that the line-shape distortion consisted of over-predicting lower-lying resonances, opposite to what is observed here in  $\alpha$ - $\alpha$  correlations. This was the

### 3.2 Application of the thermal model to $\alpha$ - $\alpha$ correlations in $^{36}\text{Ar} + ^{58}\text{Ni}$ with the INDRA $4\pi$ multi-detector

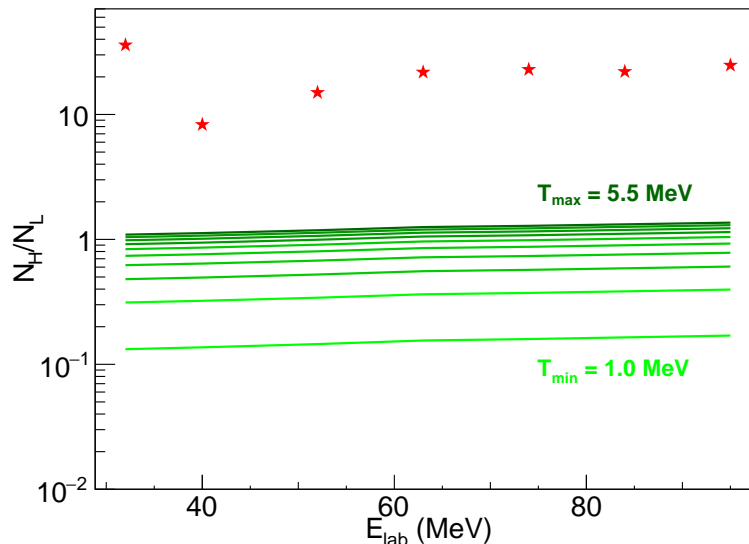


Figure 3.14: Experimental  $\alpha$ - $\alpha$  yield ratios ( $N_H/N_L$ ) as a function of the incident energy compared with the results of the pure thermal model. The experimental points are represented by red stars while in different tonality of green we show the present theoretical predictions for medium-temperatures in the range  $1.0 \text{ MeV} \leq T \leq 5.5 \text{ MeV}$ .

case of the  $d$ - $\alpha$  correlation function measured in Xe+Au collisions at 50 AMeV, where standard intensity interferometry techniques require a modification including effects of position-momentum correlations due to collective motion [317]. In the case explored in the present thesis, the difficulty in reproducing the overall line-shape of the nuclear two-alpha coincidence yield may arise from the hypotheses behind the thermal model described at the previous section. From the point of view of HBT prescriptions of the correlation function, the shapes of wide resonance peaks are the most suited to probe the space-time extent of the source profiting from FSI. This is the case, for example, of the peak at 20 MeV/c relative momentum in p-p correlations and the one at 84 MeV/c in d- $\alpha$  correlations. Very narrow peaks are difficult to be treated as a probe of the space-time extent of the two-particle emitting source because their shape is almost entirely determined by the finite angular resolution of the experimental setup. The same is true for the first peak in the  $\alpha$ - $\alpha$  correlation function, shown on Figure 3.10. In contrast, the wide peak corresponding to the short-lived resonance at 3.04 MeV has a shape that can be used to deduce space-time information on the emitting source via the Koonin-Pratt model. In this work we do not proceed on using this interferometry technique. This would require solving the Koonin-Pratt equation after having calculated the uneasy two- $\alpha$  scattering wave function,  $K(\vec{r}, \vec{q})$  of eq. 3.19. We consider this as an opportunity

### Chapter 3. Clustering in HICs as a link between structure and dynamics

---

for future investigations that require higher statistics (best interferometry analyses require gate on total momentum magnitude and on the angle between relative and total momentum vectors, thus being very demanding in statistics) and important theoretical implementations. However, we still use the concept of nuclear FSI to try to speculate on the  $\alpha$ - $\alpha$  correlation spectra measured at various energies.

In the above discussed thermal model, it is supposed that a certain number of  ${}^8\text{Be}$  nuclei is statistically present in the nuclear medium and at thermal equilibrium. Their emission is therefore statistical and what we observe is their subsequent decay into couples of  $\alpha$ -particles. Anyway, being the colliding nuclei relatively light, and given the possible intrinsic cluster nature of the self-conjugated projectile  ${}^{36}\text{Ar}$ , one can image that  $\alpha$ -like-particles are abundantly emitted. Moreover,  $\alpha$ -particles are known to be produced by other resonances and secondary decays. A number of free  $\alpha$ -particles may then exist within the thermally equilibrated medium. If the density of these  $\alpha$ -particles is sufficiently high, one may imagine that they could experience a resonant scattering process in the medium. In other words, two  $\alpha$ -like-particles may collide to populate one of the states of  ${}^8\text{Be}$  that then decays into a couple of  $\alpha$ -particles. This elastic scattering process is resonant (RES) since an intermediate resonant state is produced, and it is formally not distinguishable from the decay process of a thermally equilibrated  ${}^8\text{Be}$  that we supposed in our model. These rescattering and resonance regeneration effects, due to  $\alpha$ - $\alpha$  final state interactions, have also been discussed in ultra-relativistic HICs to describe resonance decays [340]. They are also the basis of using HBT with peaks generated by the nuclear FSI. One can imagine that a certain contribution to the peaks integral shown in Figs. 3.12 and 3.13 could be ascribed to RES processes instead of to the mechanism supposed in our model. The cross section of two- $\alpha$ s RES through a state in  ${}^8\text{Be}$  characterized by spin  $J$ , resonance energy  $E_r$  and total width  $\Gamma = \Gamma_\alpha$  is given, in a simplified way, by [142]:

$$\sigma_{RES}(E) = \frac{2J+1}{(2S+1)(2I+1)} \frac{\pi}{k^2} \frac{\Gamma_\alpha(E)\Gamma_\alpha(E)}{(E-E_r)^2 + \Gamma^2/4} \quad (3.25)$$

where spin of projectile and target  $S = 0$  and  $I = 0$  in the case of two  $\alpha$ -particles.  $E$  represents here the energy of the relative motion  $\alpha$ - $\alpha$  of the entrance channel while  $k/\sqrt{E} = \mu/\sqrt{A} \times 0.2187 \times 10^{13} \text{cm}^{-1} \text{MeV}^{-1/2}$  gives the wave-number associated to the two- $\alpha$ s. The reduced mass  $\mu$  is expressed in units of a.m.u. and  $E$  in units of MeV,  $A = 4$  is the mass number of the  $\alpha$ . To take into account the Coulomb penetrability, we included in the partial width the factor  $e^{-2\pi\eta(E)}$ , where  $\eta(E) = (1/137)Z_\alpha Z_\alpha \sqrt{\frac{\mu c^2}{2E}}$  is the Sommerfeld parameter, which represents the probability of two  $\alpha$ -particles to tunnel through the barrier<sup>7</sup>. Equation 3.25 can then be used to compute the expected reaction rate per couple of particle of the RES process  $\langle\sigma v\rangle$  separately for each of the two states of  ${}^8\text{Be}$  here involved. In Figure 3.15 we show

---

<sup>7</sup>As a first approximation, we neglect the centrifugal barrier present when two  $\alpha$ -particles populate the 3.04 MeV  $2^+$  state, that would require a  $R$ -matrix penetrability calculation as outlined in Chapter 1.

### 3.2 Application of the thermal model to $\alpha$ - $\alpha$ correlations in $^{36}\text{Ar} + ^{58}\text{Ni}$ with the INDRA $4\pi$ multi-detector

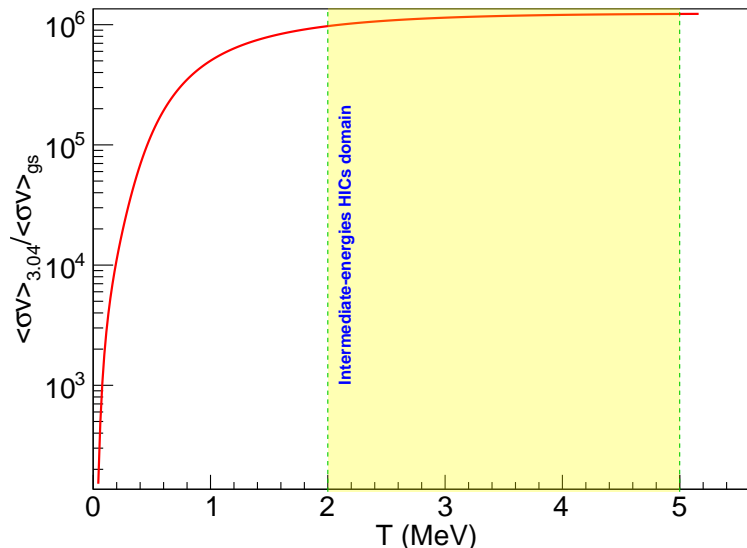


Figure 3.15: Ratio of the reaction rate  $\langle\sigma v\rangle$  for the  $\alpha$ - $\alpha$  resonant elastic scattering (RES) through the 3.04 MeV state to the one obtained assuming it occurs through the ground state of  $^8\text{Be}$ , as a function of the temperature of the medium. In the region of temperatures explored in HICs at intermediate energies, the  $\alpha$ - $\alpha$  RES via the 3.04 MeV state of  $^8\text{Be}$  is more than  $5 \times 10^5$  times favoured than the one passing through the ground state.

the ratio  $\langle\sigma v\rangle_{3.04}/\langle\sigma v\rangle_{gs}$  of such values computed, respectively, for the 3.04 MeV state and the ground state of  $^8\text{Be}$  as a function of the medium temperature. In the whole temperature domain that one can expect to explore in intermediate-energy HICs ( $2 \text{ MeV} < T < 5 \text{ MeV}$ ), the value of this ratio is of the order of  $10^6$ . In other words, if two  $\alpha$ -particles experience a RES in these conditions of temperature, the probability to populate the 3.04 MeV as intermediate stage is  $10^6$  times larger than the one associated to the ground state. This would result, clearly, in an increasing of the  $\alpha$ - $\alpha$  correlation yield in correspondence of the 3.04 MeV state in  $^8\text{Be}$ . Secondary decays of heavier isotopes may also contribute in populating states in  $^8\text{Be}$  nuclei, thus introducing some additional complication to the problem. However, the presented result may be used to explore more detailed properties of the nuclear medium. As an example, if one knows the temperature of  $^8\text{Be}$  from an independent technique, one can quantitatively estimate, by means of the present prescription of eq. 3.25, the extra-yield observed for the 3.04 state with respect to the one predicted by our thermal model approach. Taking into account the time of disintegration of the nuclear medium, as well as its volume, one may deduce the  $\alpha$ -particle density in the medium, which is involved in the absolute reaction rate calculation. Due to limited statistics, it is difficult to investigate further the observed effects. For example,

### Chapter 3. Clustering in HICs as a link between structure and dynamics

---

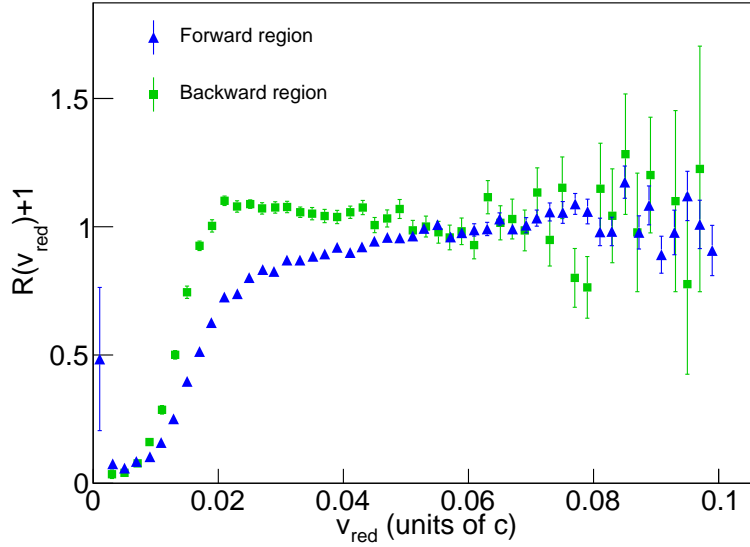


Figure 3.16: IMF-IMF correlation function, as a function of the reduced velocity, for central  $^{36}\text{Ar} + ^{58}\text{Ni}$  collisions at 40 AMeV. Data are separately shown for the forward ( $v_{\parallel} > v_{cm}$ , blue points) and the backward ( $v_{\parallel} \leq v_{cm}$ , green points) region of emission. The width of the Coulomb hole, at small values of relative velocity, indicates the different time-scale of the emission in the two separated regions. The bump observed at  $v_{red} \approx 0.03$  in the backward region correlation function is attributed to the evaporation of a large fragment, not present in the forward region.

these light collision systems may be characterized by non-equilibrium features and anisotropies in particle emissions that may require more stringent event selection criteria.

This can be seen for example inspecting IMF-IMF correlation functions produced in such collisions. Figure 3.16 shows, as an example, the IMF-IMF correlation function obtained at 40 AMeV, with the same central event selection used for the present analysis. The blue spectrum is relative to fragments associated to the forward emitting region while the green one is associated to the backward region. They are distinguished by the conditions  $v_{\parallel} > v_{cm}$  (forward part) and  $v_{\parallel} \leq v_{cm}$  (backward part), where  $v_{\parallel}$  is the component of the velocity vector of the fragments along the beam axis and  $v_{cm}$  is the velocity of the reaction system. The two correlation functions differ significantly. In the case of emissions occurring from the forward region, the corresponding Coulomb hole appears to be larger than the one observed in the backward region. This is the hint of a shorter forward disintegration time-scale as compared to the one observed in the backward region. These different observed time scales suggest non-isotropic emission that questions the validity of a purely thermal equilibrium. Also, the resonances studied are characterized by

### 3.2 Application of the thermal model to $\alpha$ - $\alpha$ correlations in $^{36}\text{Ar} + ^{58}\text{Ni}$ with the INDRA $4\pi$ multi-detector

---

different lifetimes. Their decay and recombination mechanisms may reasonably be affected by the different fragmentation time-scales revealed by Figure 3.16 and associated to different kinematic regions. Another interesting fact that one can deduce from Figure 3.16 is that a weak bump, not appearing in the IMF-IMF correlation function associated to the forward part, seems to appear in the backward correlation function at about  $v_{red} \approx 0.03$ . Similar bumps have been associated in the literature (see Ref. [341]) to the presence of charge asymmetry with a significantly large fragment which evaporates smaller fragments. Such an asymmetry in fragment emission is clearly not observed in the forward region. These findings agree with the recent analysis of Ref. [342] on the same data analyzed here, where it has been shown that  $^{36}\text{Ar} + ^{58}\text{Ni}$  collisions at central impact parameters are characterized by a fast-disassembling (named *jet-crumbling* effect) of the forward direction (projectile rapidity) through the target, without strongly perturbing the latter. In this scenario, while the projectile would experience a dissipative transparency effect, the target would be characterized, after the collision, by a heavy system which can evaporate light fragments. Such a mechanism clearly differs from the hypothesis of full stopping and equilibrium, implicit in our model assumptions. These dynamical aspects stimulate efforts also in transport model implementations in order to improve both  $\alpha$ -production and multi- $\alpha$  interactions and correlations. As already discussed in paragraph 1.5.4, investigations on the EoS and on the density dependence of the symmetry energy may profit from such efforts aimed at implementing dynamics/structure interplays in the time evolution of the system.



# Conclusions

Omnium hominum quos ad amorem  
veritatis natura superior impressit  
hoc maxime interesse videtur: ut,  
quemadmodum de labore antiquorum  
ditati sunt, ita et ipsi posteris  
prolaborent, quatenus ab eis  
posteritas habeat quo ditetur.

---

Dante Alighieri  
*De Monarchia, I 1*

In the present thesis we explored clustering phenomena in light nuclear systems with a multi-method approach. We performed an experimental campaign to probe such aspects in a variety of light nuclei for which the experimental information is not well established in the literature and which represent particularly remarkable examples of clusters in nuclei.

Possible evidences of  $\alpha$  molecular structure have been obtained by studying the neutron-rich isotope  $^{10}\text{Be}$ . It has been investigated at the FRIBs facility of INFN-LNS by using a fragmentation beam at intermediate energies. As experimental technique we used particle-particle correlations in sequential breakup events and the CHIMERA  $4\pi$  multi-detector.  $^6\text{He}$ - $^4\text{He}$  correlations allow us to link peaks in the reconstructed invariant mass spectrum to previously known excited states of  $^{10}\text{Be}$  and to suggest the existence of a new (tentatively assigned)  $6^+$  state at about 13.5 MeV. This state can represent a possible member of a molecular band associated to the  $\alpha:2n:\alpha$  structure in  $^{10}\text{Be}$ .

Carbon isotopes  $^{11,12,13,16}\text{C}$  are studied in different experiments with the aim to contribute in the understanding of how clustering phenomena are affected by the neutron-excess. The neutron-poor  $^{11}\text{C}$  isotope was investigated via the  $^{10}\text{B}(p,\alpha)$  reaction at bombarding energies  $E_p = 0.6\text{-}1.0$  MeV, where very few and fragmentary data have been reported in the literature. The experiment was performed at the Laboratorio dell'Acceleratore (LdA) of the University of Naples Federico II. Results of our measurements were interpreted by comprehensive  $R$ -matrix analysis of differential cross section and angular distributions. A good description of both  $S$ -factor and angular distributions in the  $E_x \approx 9.3\text{-}9.5$  MeV domain is achieved by including a  $(5/2^-)$  9.36 MeV state in the previously used level scheme. This state, never observed in previous works and which seems characterized by a pronounced  $\alpha$  struc-

## Conclusions

---

ture, allows to reach a satisfactory description of shapes of angular distributions and absolute cross sections data.

The neutron-rich  $^{13}\text{C}$  is investigated via  $^9\text{Be}(\alpha,\alpha)$  resonant elastic and inelastic scatterings at the LdA of Naples in the  $E_\alpha = 3.3\text{-}10$  MeV bombarding energy domain. A comprehensive  $R$ -matrix analysis of several reaction channels involving  $\alpha$  and neutron emission has been performed. For the first time, we succeeded in simultaneously fitting  $\alpha_0$  resonant elastic scattering data at four angles,  $\alpha_1$  inelastic scattering data and  $^9\text{Be}(\alpha,n_0)^{12}\text{C}$ ,  $^9\text{Be}(\alpha,n_1)^{12}\text{C}$  reaction cross section data. Our analysis provides refined information on the  $^{13}\text{C}$  spectroscopy in a quite large energy range where previous spectroscopic information was poorly known and giving a contribution in the understanding of  $^{13}\text{C}$   $K^\pi = 3/2^\pm$  parity doublet molecular bands.

To study the structure of  $^{16}\text{C}$ , for which almost no information is previously reported in the literature above the  $\alpha$ -threshold, we benefited of the presence of various nuclear species in the fragmentation beam used for the  $^{10}\text{Be}$  investigation. In particular, the intensity of the  $^{16}\text{C}$  present in our beam is the largest available for nuclear physics experiments at these energies. We used the same technique and apparatus of the above discussed  $^{10}\text{Be}$  case. In this case we report evidence of a possible molecular state in  $^{16}\text{C}$  at about 20.6 MeV excitation energy in the  $^6\text{He}\text{-}^{10}\text{Be}$  correlations. A small but non-vanishing yield is also observed in the  $^6\text{He}+^6\text{He}+^4\text{He}$  three-body correlation.

We investigated the Hoyle state (7.654 MeV,  $0^+$ ) in  $^{12}\text{C}$  via a high-precision and high-sensitivity experiment. We performed the up to date largest statistics measurement of the direct decay width of such state by using the  $^{14}\text{N}(\text{d},\alpha)^{12}\text{C}$  reaction at 10.5 MeV incident energy at the Tandem accelerator of INFN-LNS. To reach an extremely low background level, which is a requirement to disentangle direct decays of the Hoyle state, we developed a new hodoscope detector of independent silicon cells. We succeed to place an upper limit to direct decays of the Hoyle state of 0.043% (95% C.L), which is almost 5 times lower than previous state of the art measurements. Such a result provides a stringent constraint to theoretical models attempting to describe the structure of the Hoyle state and clustering phenomena in light systems as well as to nuclear astrophysics, where this state is involved as key state in the nucleosynthesis of carbon and heavier elements in the universe.

Clustering phenomena in  $^{19}\text{F}$  and  $^{20}\text{Ne}$  are explored with the  $^{19}\text{F}(\text{p},\alpha)^{16}\text{O}$  reaction in the energy range  $E_{cm} = 0.18\text{-}0.60$  MeV at the AN-2000 Van der Graff accelerator of INFN-LNL. A systematic analysis of the measured angular distributions at very low energies points out the appearance of direct reaction mechanisms possibly triggered by the presence of cluster  $^{16}\text{O}\text{-}^3\text{H}$  and  $\alpha\text{-}^{15}\text{N}$  structures of  $^{19}\text{F}$  in its ground state. The spectroscopy of the compound nucleus  $^{20}\text{Ne}$  is significantly improved thanks to a  $R$ -matrix analysis of data that we obtained in the experiment. In particular the present data point out the role played at low energies by the 0.251 MeV state (not observed before and characterized by a large  $\alpha$ -decay partial width) and by the 0.113 MeV state. The corresponding stellar reaction rate turns out to be significantly

larger (1.5-2 times larger) than currently adopted low-energy extrapolations.

Finally, to probe the role played by clusters in the interplay between nuclear structure and dynamics, we studied the production of light clusters in  $^{36}\text{Ar} + ^{58}\text{Ni}$  heavy ion central collisions. They have been detected with the INDRA  $4\pi$  multi-detector at various incident energies from 32 to 95 AMeV at GANIL. We analyzed  $\alpha$ - $\alpha$  correlations, produced in such collisions, by using a thermal model which describes the production and decay of resonant states produced in the overlapping region between projectile and target. We observe a significant extra-population of the 3.04 MeV state in the emitting  $^8\text{Be}$  that we attribute to  $\alpha$ - $\alpha$  final state interactions occurring in the hot and diluted nuclear medium produced in the collisions.



# Bibliography

- [1] E.P. Hubble, *Astrophys. J.* **79**, 8 (1934).
- [2] J.A. Peacock et al., *Nature* **410**, 169 (2001).
- [3] R. Olfati-Saber, J. A. Fax, and R. M. Murray, *Proc. IEEE* **95**, 215 (2007).
- [4] A. Arenas, A. Díaz-Guilera, J. Kurths, Y. Moreno, and C. Zhou, *Phys. Rep.* **469**, 93 (2008).
- [5] S.P. Borgatti, A.Mehra, D.J. Brass, and G. Labianca, *Science* **323**, 892 (2009).
- [6] D.J. Watts and S. Strogatz, *Nature* **393**, 6684 (1998).
- [7] M.E. Porter, *The Competitive Advantage of Nations*. (The Free Press, New York, 1990).
- [8] H. Milinski and R. Heller, *Nature* **275**, 642–644 (1978).
- [9] S. Singh, S.K. Srivastava, and D.K. Singh, *RSC Adv.* **4**, 1761 (2014).
- [10] M. Freer, *Rep. Prog. Phys.* **70**, 2149 (2007).
- [11] R.B. Wiringa, V.G.J. Stoks, and R. Schiavilla, *Phys. Rev.* **C51**, 38 (1995).
- [12] B. S. Pudliner, V. R. Pandharipande, J. Carlson, and Robert B. Wiringa, *Phys. Rev. Lett.* **74**, 4396 (1995).
- [13] H. Nagaoka, *Phyl. Mag.* **7**, 445 (1904).
- [14] Robley D. Evans, *The Atomic Nucleus*, 1st ed. (McGraw-Hill Book Company, Inc., New York, Toronto, London, 1955).
- [15] J.J. Thomson, *The Corpuscular Theory of Matter*, 1st ed. (Constable & Co., Ltd., London, 1907).
- [16] E. Rutherford, *Phyl. Mag.* **21**, 669 (1911).
- [17] K. Heide, *Basic Ideas and Concepts in Nuclear Physics: An Introductory Approach*, 2nd ed. (Institute of Physics Publishing, Bristol and Philadelphia, 1999).

## Bibliography

---

- [18] W.J. Huang, G. Audi, M.Wang, F.G. Kondev, S. Naimi, and X. Xu, *Chin. Phys. C* **41**, 030002 (2017).
- [19] W.J. Huang, G. Audi, M.Wang, F.G. Kondev, S. Naimi, and X. Xu, *Chin. Phys. C* **41**, 030003 (2017).
- [20] W.E. Burcham, *Nuclear Physics an introduction*, 2nd ed. (Longman, London, 1973).
- [21] A.N. James et al., *Nucl. Phys. A* **133**, 89 (1969).
- [22] Luc Valentin, *Noyaux et particules: modèles et symétries*, 2nd ed. (Hermann, Paris, 1989).
- [23] M.G. Mayer, *Phys. Rev.* **78**, 22 (1950).
- [24] O. Haxel, J.H.D. Jensen, and H.E. Suess, *Phys. Rev.* **75**, 1766 (1949).
- [25] A.P. Zuker, B. Buck, and J.B. McGrory, *Phys. Rev. Lett.* **21**, 39 (1968).
- [26] I.E. McCarty, *Introduction to Nuclear Theory*, 1st ed. (J. Wiley and Sons, New York, 1969).
- [27] C.F.v. Weizsacker, *Naturwiss* **26**, 209 (1938).
- [28] R. Rosenfeld, *Nuclear Forces*, 1st ed. (North-Holland Publishing Company, Amsterdam, 1948).
- [29] L. Hafstad and E. Teller, *Phys. Rev.* **54**, 681 (1938).
- [30] W. Wefelmeier, *Naturwiss* **25**, 525 (1937).
- [31] W. Wefelmeier, *Z. Physik* **107**, 332 (1937).
- [32] L.R.B. Elton, *Introductory Nuclear Theory*, 2nd ed. (Sir Isaac Pitman & Sons LTD., London, 1965).
- [33] J.A. Wheeler, *Phys. Rev.* **52**, 1083 (1937).
- [34] H. Margenau, *Phys. Rev.* **59**, 37 (1941).
- [35] H. Wergeland, *Norske Vidensk. Slsk. Skrifter* **1**, (1941).
- [36] John M. Blatt and Victor F. Weisskopf, *Theoretical Nuclear Physics*, 1st ed. (John Wiley & Sons, New York, New York, 1962).
- [37] A.A. Davydov, *Theory of the Atomic Nuclei*, 1st ed. (Nauka, Moscow, 1958).
- [38] E. Teller and J.A. Wheeler, *Phys. Rev.* **53**, 778 (1938).

- [39] J. Hiura and I. Shimodaya, *Progress of Theoretical Physics* **30**, 585 (1963).
- [40] K. Wildermuth and Th. Kanellopoulos, *Nuclear Physics* **7**, 150 (1958).
- [41] J.A. Wheeler, *Phys. Rev.* **52**, 1107 (1937).
- [42] P. Descouvemont, *Journal of Physics G: Nuclear and Particle Physics* **19**, S141 (1993).
- [43] S. Saito, S. Okai, R. Tamagaki, and M. Yasuno, *Progress of Theoretical Physics* **50**, 1561 (1973).
- [44] A.S. Solovyev et al., *J. Phys.: Conf. Ser.* **569**, 012020 (2014).
- [45] A. Arima, V. Gillet, and J. Ginocchio, *Phys. Rev. Lett.* **25**, 1043 (1970).
- [46] M. Sambataro and N. Sandulescu, *Phys. Rev. Lett.* **88**, 061303 (2013).
- [47] M. Sambataro and N. Sandulescu, *Phys. Rev. Lett.* **115**, 112501 (2015).
- [48] A. Ono and J. Randrup, *Eur. Phys. J.* **A30**, 109 (2006).
- [49] H. Horiuchi and Y. Kanada-En'yo, *Nucl. Phys. A* **616**, 394c (1997).
- [50] Y. Kanada-En'yo and H. Horiuchi, *Phys. Rev. C* **68**, 014319 (2003).
- [51] M. Freer et al., *arXiv* **1705**, 06192v1 (2017).
- [52] H. Feldmeier, *Nucl. Phys. A* **515**, 147 (1990).
- [53] M. Freer, R. R. Betts, and A. H. Wuosmaa, *Nucl. Phys.* **A587**, 36 (1995).
- [54] W. D. M. Rae, *Int. J. Mod. Phys.* **A3**, 1343 (1988).
- [55] W. von Oertzen, M. Freer, and Y. Kanada-En'yo, *Phys. Rep.* **432**, 43 (2006).
- [56] C. Beck (ed), *Lect. Not. Phys.* **818**, Vol. 1 (2010).
- [57] C. Beck (ed), *Lect. Not. Phys.* **848**, Vol. 2 (2012).
- [58] C. Beck (ed), *Lect. Not. Phys.* **875**, Vol. 3 (2014).
- [59] K. Ikeda, N. Tagikawa, and H. Horiuchi, *Prog. Theor. Phys. Suppl. E* **68**, 464 (1968).
- [60] N. Itagaki, W. von Oertzen, and S. Okabe, *Phys. Rev.* **C74**, 067304 (2006).
- [61] W. von Oertzen, *Zeitschrift für Physik A Hadrons and Nuclei* **357**, 355 (1997).
- [62] E. Uegaki, S. Okabe, Y. Abe, and H. Tanaka, *Prog. Theor. Phys.* **57**, 1262 (1977).

## Bibliography

---

- [63] M. Kamimura, Nucl. Phys. A **351**, 456 (1981).
- [64] S. Karataglidis et al., Phys. Rev. C **52**, 861 (1995).
- [65] M. Freer and H.O.U. Fynbo, Prog. Part. Nuc. Phys. **78**, 1 (2014).
- [66] K. Ogata, M. Kan, and M. Kamimura, Prog. Theor. Phys. **122**, 1055 (2009).
- [67] D.M. Brink and E. Boeker, Nucl. Phys. **A91**, 1 (1967).
- [68] H. Morinaga, Phys. Rev. **101**, 254 (1956).
- [69] Taiichi Yamada and Peter Schuck, Eur. Phys. J. **A26**, 185 (2005).
- [70] Y. Funaki, H. Horiuchi, W. von Oertzen, G. Röpke, P. Schuck, A. Tohsaki, and T. Yamada, Phys. Rev. C **80**, 064326 (2009).
- [71] A. Nakada, Y. Torizuka, and Y. Horikawa, Phys. Rev. Lett. **27**, 1102 (1971).
- [72] Y. Funaki, A. Tohsaki, H. Horiuchi, P. Schuck, and G. Ropke, Eur. Phys. J. **A28**, 259 (2006).
- [73] A. Tohsaki, H. Horiuchi, P. Schuck, and G. Röpke, Phys. Rev. Lett. **87**, 192501 (2001).
- [74] Y. Funaki, A. Tohsaki, H. Horiuchi, P. Schuck, and G. Ropke, Phys. Rev. **C67**, 051306 (2003).
- [75] T. Yamada and P. Schuck, Phys. Rev. C **69**, 024309 (2004).
- [76] S. Ishikawa, Phys. Rev. C **90**, 061604 (2014).
- [77] E. Epelbaum et al., Phys. Rev. Lett. **109**, 252501 (2012).
- [78] M. Freer and H.O.U. Fynbo, Physics **4**, 94 (2011).
- [79] Y. Kanada-En'yo, Prog. Theor. Phys. **117**, 655 (2007), [Erratum: Prog. Theor. Phys.121,895(2009)].
- [80] M. Itoh et al., Nucl. Phys. **A738**, 268 (2004).
- [81] D. J. Marin-Lambarri, R. Bijker, M. Freer, M. Gai, Tz. Kokalova, D. J. Parker, and C. Wheldon, Phys. Rev. Lett. **113**, 012502 (2014).
- [82] Tz. Kokalova Wheldon, Journal of Physics: Conference Series **569**, 012010 (2014).
- [83] R. Bijker and F. Iachello, Phys. Rev. **C61**, 067305 (2000).

- 
- [84] J.C. Slater, *Quantum Theory of Matter*, 1st ed. (McGraw-Hill, New York, 1968).
- [85] P. Cuzzocrea et al., *Lett. Nuovo Cim.* **22**, 257 (1978).
- [86] P. Cuzzocrea et al., *Nuovo Cim. A* **49**, 368 (1979).
- [87] M. Freer et al., *Phys. Rev.* **C80**, 041303 (2009).
- [88] W.R. Zimmermann et al., *Phys. Rev. Lett.* **110**, 152502 (2013).
- [89] M. Freer et al., *Phys. Rev. C* **83**, 034314 (2011).
- [90] D. J. Marin-Lambarri, M. Freer, Tz Kokalova, C. Wheldon, and D. J. Parker, *J. Phys. Conf. Ser.* **569**, 012071 (2014).
- [91] W. Bauhoff, H. Schultheis, and R. Schultheis, *Phys. Rev. C* **29**, 1046 (1984).
- [92] R. Bijker, *J. Phys. Conf. Ser.* **512**, 012007 (2014).
- [93] D.R. Tilley et al., *Nucl. Phys. A* **636**, 249 (1998).
- [94] S. J. Krieger, *Phys. Rev. Lett.* **22**, 97 (1969).
- [95] N. E. Reid, N. E. Davison, and J. P. Svenne, *Phys. Rev. C* **9**, 1882 (1974).
- [96] S. Åberg, I. Ragnarsson, T. Bengtsson, and R.K Sheline, *Nuclear Physics A* **391**, 327 (1982).
- [97] B. Buck, C. B. Dover, and J. P. Vary, *Phys. Rev. C* **11**, 1803 (1975).
- [98] R. Bijker and F. Iachello, *Phys. Rev. Lett.* **112**, 152501 (2014).
- [99] B. Buck, J. C. Johnston, A. C. Merchant, and S. M. Perez, *Phys. Rev. C* **52**, 1840 (1995).
- [100] H. Horiuchi and K. Ikeda, *Progress of Theoretical Physics* **40**, 277 (1968).
- [101] A. Arima, H. Horiuchi, and T. Sebe, *Phys. Lett.* **24B**, 129 (1967).
- [102] Y. Kanada-En'yo and H. Horiuchi, *Progress of Theoretical Physics* **93**, 115 (1995).
- [103] Claus E. Rolfs and William S. Rodney, *Cauldrons in the Cosmos: Nuclear Astrophysics*, fifth ed. (The University of Chicago Press, Chicago and London, 1997).
- [104] E.J. Opik, *Proc. R. Irish Acad. A* **54**, 49 (1951).
- [105] E.E. Salpeter, *Phys. Rev.* **88**, 547 (1952).

## Bibliography

---

- [106] F. Hoyle et al., Phys. Rev. **92**, 1095c (1953).
- [107] F. Hoyle, Astrophys. J. Suppl. Ser. **1**, 121 (1954).
- [108] C.W. Cook, W.A. Fowler, C.C. Lauritsen, and T. Lauritzen, Phys. Rev. **107**, 508 (1957).
- [109] C. Angulo et al., Nucl. Phys. A **656**, 3 (1999).
- [110] K. Nomoto, F.-K. Thielemann, and S. Miyaji, Astron. Astrophys. **149**, 239 (1985).
- [111] N.B. Nguyen, F.M. Nunes, I.J. Thompson, and E.F. Brown, Phys. Rev. Lett. **109**, 141101 (2012).
- [112] N.B. Nguyen, F.M. Nunes, and I.J. Thompson, Phys. Rev. **C87**, 054615 (2013).
- [113] K. Langanke, M. Wiescher, and F.K. Thielemann, Z. Physik A - Atomic Nuclei **324**, 147 (1986).
- [114] E. Garrido, R. de Diego, D. V. Fedorov, and A. S. Jensen, The European Physical Journal A **47**, 102 (2011).
- [115] K. Yabana and Y. Funaki, Phys. Rev. C **85**, 055803 (2012).
- [116] N. Itagaki and S. Okabe, Phys. Rev. **C61**, 044306 (2000).
- [117] T. Stovall M. Bernheim and D. Vinciguerra, Nucl. Phys. A **97**, 488 (1969).
- [118] D. Vinciguerra and T. Stovall, Nucl. Phys. A **132**, 410 (1969).
- [119] P. Raghavan, Atom. Data Nucl. Data Tabl. **42**, 189 (1989).
- [120] Y. Kanada-En'yo, H. Horiuchi, and A. Doté, Journal of Physics G: Nuclear and Particle Physics **24**, 1499 (1998).
- [121] D. Suzuki et al., Phys. Rev. **C87**, 054301 (2013).
- [122] Y. Kanada-En'yo, Phys. Rev. C **75**, 024302 (2007).
- [123] T. Kawabata et al., Phys. Rev. C **70**, 034318 (2004).
- [124] T. Kawabata et al., Phys. Lett. **B646**, 6 (2007).
- [125] N. Soic et al., Nucl. Phys. **A742**, 271 (2004).
- [126] I. Ragnarsson, S. Åberg, H. B. Hakansson, and R. K. Sheline, Nucl. Phys. **A361**, 1 (1981).

- [127] M. Milin and W. von Oertzen, *Eur. Phys. J. A* **14**, 295 (2002).
- [128] T. Yoshida, N. Itagaki, and T. Otsuka, *Phys. Rev.* **C79**, 034308 (2009).
- [129] N. Furutachi and M. Kimura, *Phys. Rev.* **C83**, 021303 (2011).
- [130] Y. Chiba and M. Kimura, *J. Phys. Conf. Ser.* **569**, 012047 (2014).
- [131] T. Yamada and Y. Funaki, *Phys. Rev.* **C92**, 034326 (2015).
- [132] T. Baba, Y. Chiba, and M. Kimura, *Phys. Rev.* **C90**, 064319 (2014).
- [133] N. Itagaki, S. Okabe, K. Ikeda, and I. Tanihata, *Phys. Rev. C* **64**, 014301 (2001).
- [134] D. R. Tilley, H. R. Weller, and C. M. Cheves, *Nucl. Phys.* **A564**, 1 (1993).
- [135] P J Leask et al., *J. Phys. G* **27**, B9 (2001).
- [136] N. I. Ashwood et al., *Phys. Rev.* **C70**, 064607 (2004).
- [137] Harald A. Enge, *Introduction to Nuclear Physics*, 1st ed. (Addison-Wesley Publishing Company, USA, Massachusetts, 1981).
- [138] Christian Iliadis, *Nuclear Physics of Stars*, 2nd ed. (Wiley-VCH Verlag GmbH & Co. KGaA, Weinheim, Germany, 2015).
- [139] M. Abramowitz and I. Stegun, *Nat. Bur. St. Appl. Math* **55**, 1 (1972).
- [140] Bernard L. Cohen, *Concepts of Nuclear Physics*, 1st ed. (McGraw-Hill Book Company, New York, 1971).
- [141] A. Messiah, *Mecanique Quantique*, 1st ed. (Dunod, Paris, 1959).
- [142] J.B. Marion and F.C. Young, *Nuclear Reaction Analysis*, 1st ed. (North Holland, Amsterdam, 1968).
- [143] A. M. Lane and R. G. Thomas, *Rev. Mod. Phys.* **30**, 257 (1958).
- [144] Ta-You Wu and Takashi Ohmura, *Quantum Theory of Scattering*, 1st ed. (Dover Publications Inc., Mineola, New York, 2011).
- [145] E.P. Wigner, *Phys. Rev.* **70**, 606 (1946).
- [146] E.P. Wigner and L. Eisenbud, *Phys. Rev.* **72**, 29 (1947).
- [147] R.E. Azuma et al., *Phys. Rev. C* **81**, 045805 (2010).
- [148] H. Herndl et al., *Phys. Rev. C* **44**, R952 (1991).

## Bibliography

---

- [149] Y. Yamashita and Y. Kudo, Prog. Theor. Phys. **90**, 1303 (1993).
- [150] Z.Q. Mao, H.T. Fortune, and A.G. Lacaze, Phys. Rev. C **53**, 1197 (1996).
- [151] A. Shotter, J. Phys. Soc. Jpn. (suppl.) **58**, 145 (1989).
- [152] S. Marsh and W. D. M. Rae, Phys. Lett. **153B**, 21 (1985).
- [153] M. Freer, Nucl. Instr. Meth. Phys. Res. A **383**, 463 (1996).
- [154] A. Cunsolo, A. Foti, G. Imme, G. Pappalardo, G. Raciti, and N. Saunier, Phys. Rev. **C21**, 2345 (1980).
- [155] R. H. Dalitz, Phil. Mag. Ser.7 **44**, 1068 (1953).
- [156] O. S. Kirsebom et al., Phys. Rev. Lett. **108**, 202501 (2012).
- [157] S. Typel, Journal of Physics: Conference Series **420**, 012078 (2013).
- [158] Y. Zhang et al., Phys. Lett. B **664**, 145 (2008).
- [159] W.G. Lynch et al., Prog. Part. Nucl. Phys. **62**, 427 (2009).
- [160] Akira Ono, Journal of Physics: Conference Series **420**, 012103 (2013).
- [161] S. Hudan et al., Phys. Rev. C **67**, 064613 (2003).
- [162] Josef Pochodzalla et al., Phys. Rev. **C35**, 1695 (1987).
- [163] R.J. Charity et al., Phys. Rev. **C52**, 3126 (1995).
- [164] W.P. Tan et al., Phys. Rev. C **69**, 061304 (2004).
- [165] F. Grenier et al., Nucl. Phys. **A811**, 233 (2008).
- [166] J. Pochodzalla, Prog. Part. Nucl. Phys. **39**, 443 (1997).
- [167] M.B. Tsang et al., Phys. Rev. C **53**, R1057 (1996).
- [168] J.B. Natowitz, K. Hagel, R. Wada, Z. Majka, P. Gonthier, J. Li, N. Mdeidayeh, B. Xiao, and Y. Zhao, Phys. Rev. C **52**, R2322 (1995).
- [169] J. Pochodzalla et al., Phys. Rev. Lett. **75**, 1040 (1995).
- [170] S. Albergo, S. Costa, E. Costanzo, and A. Rubbino, Nuovo Cim. **A89**, 1 (1985).
- [171] H. F. Xi et al., Phys. Rev. C **58**, R2636 (1998).
- [172] H.T. Fortune and R. Sherr, Phys. Rev. C **84**, 024304 (2011).

- [173] N.I. Ashwood et al., Phys. Rev. C **68**, 017603 (2003).
- [174] H.G. Bohlen et al., Phys. Rev. C **75**, 054604 (2007).
- [175] N. Soic et al., Europhys. Lett. **34**, 7 (1996).
- [176] N. Curtis et al., Phys. Rev. C **64**, 044604 (2001).
- [177] M. Freer et al., Phys. Rev. Lett. **96**, 042501 (2006).
- [178] G.V. Rogachev et al., J. Phys.: Conf. Ser. **569**, 012004 (2014).
- [179] R. Wolski et al., Phys. At. Nucl. **73**, 1405 (2010).
- [180] I. Lombardo et al., Nuc. Phys. Proc. Suppl. **215**, 272 (2011).
- [181] E. De Filippo and A. Pagano, Eur. Phys. J. A **50**, 32 (2014).
- [182] A. Pagano, Nucl. Phys. News **22**, 25 (2012).
- [183] M. Freer et al., Phys. Rev. C **63**, 034301 (2001).
- [184] A. Wagner et al., Nucl. Instr. and Meth. A **456**, 290 (2001).
- [185] D. Horn et al., Nucl. Instr. and Meth. A **320**, 273 (1992).
- [186] L. Acosta et al., Nucl. Instr. and Meth. A **715**, 56 (2013).
- [187] J. van Driel, Phys. Lett. B **98**, 351 (1981).
- [188] A.G. Artyukh et al., Nucl. Exp. Tech. **1**, 19 (2009).
- [189] N. I. Ashwood et al., Phys. Rev. C **70**, 024608 (2004).
- [190] G. Randisi et al., Phys. Rev. C **89**, 034320 (2014).
- [191] S. Ahmed et al., Phys. Rev. C **69**, 024303 (2004).
- [192] M.A. Lisa, W.G. Gong, C.K. Gelbke, and W. G. Lynch, Phys. Rev. **C44**, 2865 (1991).
- [193] H.G. Bohlen et al., Z. Phys. A **308**, 121 (1982).
- [194] G. R. Satchler, *Direct Nuclear Reactions* (Oxford University Press, New York, 1983), p. 553.
- [195] W.W. Wilcke et al., At. Data Nucl. Data Tab. **25**, 389 (1980).
- [196] Brookhaven National Laboratory, National Nuclear Data Center, <http://www.nndc.bnl.gov/>.

## Bibliography

---

- [197] N. Curtis et al., Phys. Rev. C **73**, 057301 (2006).
- [198] D. Carbone et al., Phys. Rev. C **90**, 064621 (2014).
- [199] D. Dell’Aquila et al., Phys. Rev. C **93**, 024611 (2016).
- [200] K. Amos, L. Canton, P. R. Fraser, S. Karataglidis, J. P. Svenne, and D. van der Knijff, Eur. Phys. J. **A53**, 72 (2017).
- [201] Wei Jiang et al., Science China Physics, Mechanics & Astronomy **60**, 062011 (2017).
- [202] H. Yamaguchi et al., Phys. Rev. C **87**, 034303 (2013).
- [203] Allan HR, Govindjee M, and Sarma N, Proc. Phys. Soc. A **69**, 350 (1956).
- [204] W.E. Burcham and J.M. Freeman, Phil. Mag. **41**, 337 (1950).
- [205] Bach G.C. and Livesey D.J., Phil. Mag. **46**, 824 (1955).
- [206] J. Szabo, J. Csikai, and M. Varnagy, Nucl. Phys. A **195**, 527 (1972).
- [207] R.J. Peterson et al., Ann. Phys. Energy **2**, 503 (1975).
- [208] M.C. Spraker et al., J. Fusion Energy **231**, 357 (2012).
- [209] V.S. Belyaev et al., Phys. Rev. E **72**, 026406 (2005).
- [210] S. Kimura et al., Phys. Rev. E **79**, 038401 (2009).
- [211] A. Kafkarkou et al., Nucl. Instrum. Meth. Phys. Res. B **316**, 48 (2013).
- [212] M. Wiescher et al., Phys. Rev. C **28**, 1431 (1983).
- [213] M. Freer et al., Phys. Rev. **C85**, 014304 (2012).
- [214] A.M. Boesgard et al., Astrophys. J. **621**, 991 (2005).
- [215] C. Spitaleri et al., Phys. Rev. C **90**, 035801 (2014).
- [216] S.M.R. Puglia et al., Mem. S.A.It. Suppl. **14**, 43 (2010).
- [217] L. Lamia et al., Nucl. Phys. A **787**, 309 (2007).
- [218] J.W. Cronin et al., Phys. Rev. **101**, 298 (1956).
- [219] G. Baur et al., Nucl. Phys. A **458**, 188 (1986).
- [220] C. Spitaleri et al., Phys. Rev. C **60**, 055802 (1999).

- [221] M. La Cognata, S. Palmerini, C. Spitaleri, I. Indelicato, A.M. Mukhamedzhanov, I. Lombardo, and O. Trippella, *Astrophys. J.* **805**, 128 (2015).
- [222] J.G. Jenkin, L.G. Earwaker, E.W. Titterton, et al., *Nucl. Phys. A* **50**, 516 (1964).
- [223] N.A. Roughton et al., *At. Data Nucl. Data Tables* **23**, 177 (1979).
- [224] Y. Xu et al., *Nucl. Phys. A* **918**, 61 (2013).
- [225] A.B. Brown et al., *Phys. Rev.* **82**, 159 (1951).
- [226] L. Campajola et al., *Nucl. Instrum. Meth. Phys. Res. B* **29**, 129 (1987).
- [227] I. Lombardo et al., *J. Phys. Conf. Ser.* **569**, 012068 (2014).
- [228] I. Lombardo et al., *J. Phys. G* **40**, 125102 (2013).
- [229] I. Lombardo et al., *Nucl. Instrum. Meth. Phys. Res. B* **302**, 19 (2013).
- [230] Tesmer J.R. and Nastasi M., *Handbook of Modern Ion Beam Material Analysis*, 1st ed. (Material Research Society, Pittsburgh PA, 1995).
- [231] Ziegler J.F., Biersack J.P., and Littmark U., *The Stopping and Range of Ions in Matter Vol. 1*, 1st ed. (Pergamon, New York, 1985).
- [232] J.H. Kelley et al., *Nucl. Phys. A* **880**, 88 (2012).
- [233] M. Chiari, L. Giuntini, P.A. Mandò, and N. Taccetti, *Nucl. Instrum. Meth. Phys. Res. B* **309**, 184 (2001).
- [234] M. Chiari, L. Giuntini, P.A. Mandò, and N. Taccetti, *Nucl. Instrum. Meth. Phys. Res. B* **343**, 70 (2015).
- [235] M. Youn et al., *Nucl. Phys. A* **533**, 321 (1991).
- [236] J.C. Overley and W. Whaling, *Phys. Rev.* **128**, 315 (1962).
- [237] M. Freer et al., *Phys. Rev. C* **85**, 014304 (2012).
- [238] R.J. De Boer et al., *Phys. Rev. C* **91**, 045804 (2015).
- [239] T. Rauscher and G. Raimann, *Phys. Rev. C* **53**, 2496 (1996).
- [240] I. Lombardo et al., *J. Phys. G.* **43**, 45109 (2016).
- [241] A. Caciolli et al., *Eur. Phys. J.* **A52**, 136 (2016).

## Bibliography

---

- [242] M. Wiescher, R. J. deBoer, J. Görres, and R. E. Azuma, *Phys. Rev. C* **95**, 044617 (2017).
- [243] C. Spitaleri et al., *Phys. Rev. C* **95**, 035801 (2017).
- [244] M. Freer et al., *Phys. Rev. C* **49**, R1751 (1994).
- [245] Ad.R. Raduta et al., *Phys. Lett.* **B705**, 65 (2011).
- [246] J. Manfredi et al., *Phys. Rev. C* **85**, 037603 (2012).
- [247] T.K. Rana et al., *Phys. Rev. C* **88**, 021601(R) (2013).
- [248] L. Morelli et al., *J. Phys.* **G43**, 045110 (2016).
- [249] M. Itoh et al., *Phys. Rev. Lett.* **113**, 102501 (2014).
- [250] D. Dell’Aquila et al., *Nucl. Instrum. Meth. Phys. Res. A* **877**, 227 (2018).
- [251] W. Koenig et al., *Il Nuov. Cim.* **39**, 9 (1977).
- [252] J.R. Curry, W.R. Coker, and P.J. Riley, *Phys. Rev.* **185**, 1416 (1969).
- [253] R.J. Barlow, *Statistics* (J. Wiley & Sons, Chichester (UK), 1989).
- [254] G.J. Feldman and R.D. Cousins, *Phys. Rev. D* **57**, 3873 (1998).
- [255] D. Dell’Aquila et al., *Phys. Rev. Lett.* **119**, 132501 (2017).
- [256] R. Smith, Tz. Kokalova, C. Wheldon, J. E. Bishop, M. Freer, N. Curtis, and D. J. Parker, *Phys. Rev. Lett.* **119**, 132502 (2017).
- [257] O. Kirsebom, *Physics* **10**, 103 (2017).
- [258] F. Ajzenberg-Selove, *Nucl. Phys. A* **523**, 1 (1991).
- [259] R.B. Taylor, N.R. Fletcher, and R.H. Davis, *Nucl. Phys.* **65**, 318 (1965).
- [260] J.D. Goss et al., *Phys. Rev. C* **7**, 1837 (1973).
- [261] Z.A. Saleh et al., *Ann. der Phys.* **7**, 76 (1974).
- [262] J. Leavitt et al., *Nucl. Instrum. Meth. Phys. Res. B* **85**, 37 (1994).
- [263] J. Liu, Z. Zheng, and W.K. Chu, *Nucl. Instrum. Meth. Phys. Res. B* **108**, 247 (1996).
- [264] M. Zadro et al., *Nucl. Instrum. Meth. Phys. Res. B* **259**, 836 (2007).
- [265] M. Freer et al., *Phys. Rev. C* **84**, 034317 (2011).

- 
- [266] A.W. Obst, T.B. Grandy, and J.L. Weil, Phys. Rev. C **5**, 738 (1972).
- [267] D.C. De Martini, C.R. Soltész, and T.R. Donoghue, Phys. Rev. C **7**, 1824 (1973).
- [268] D.E. Groce and B.D. Sowerby, Nature **206**, 494 (1965).
- [269] H.D. Knox and R.O. Lane, Nucl. Phys. A **378**, 503 (1982).
- [270] W. Tornow, J. Phys. G: Nucl. Phys. **9**, 1507 (1983).
- [271] H.E. Hall and T.W. Bonner, Nucl. Phys. **14**, 295 (1959/60).
- [272] C. Wheldon et al., Phys. Rev. C **86**, 044328 (2012).
- [273] X. Aslanoglou et al., Phys. Rev. C **40**, 73 (1989).
- [274] T. Kawabata et al., J. Phys. Conf. Ser. **111**, 012013 (2008).
- [275] M. Avila et al., Phys. Rev. C **53**, 2486 (1996).
- [276] L. van der Zwan and K.W. Geiger, Nucl. Phys. A **152**, 481 (1970).
- [277] T. Borello-Lewin, Int. J. Mod. Phys. E **20**, 1081 (2011).
- [278] M.R.D. Rodrigues, AIP Conf. Proc. **1351**, 125 (2011).
- [279] H.G. Bohlen et al., Phys. Rev. C **68**, 054606 (2003).
- [280] D. Dell'Aquila, Il Nuov. Cim. C **39**, 272 (2016).
- [281] G. Verde et al., J. Phys. Conf. Ser. **420**, 0112158 (2013).
- [282] T. Baba and M. Kimura, Phys. Rev. C **95**, 064318 (2017).
- [283] M. Kimura, T. Suhara, and Y. Kanada-En'yo, The European Physical Journal A **52**, 373 (2016).
- [284] T. Baba and M. Kimura, JPS Conf. Proc. **14**, 020619 (2017).
- [285] S. Koyama on behalf the SAMURAI collaboration, talk presented at the *11th International Conference on Clustering Aspects of Nuclear Structure and Dynamics* conference, 2016, Naples (Italy).
- [286] Y. Fujiwara, H. Horiuchi, and R. Tamagaki, Prog. Theor. Phys. **61**, 1629 (1976).
- [287] P. Guazzoni et al., Nuov. Cim. **67**, 407 (1970).
- [288] A. Couture et al., Phys. Rev. C **77**, 015802 (2008).

## Bibliography

---

- [289] K. Spyrou et al., *Eur. Phys. Jour.* **A 7**, 79 (2000).
- [290] S. Lucatello et al., *Astrophys. J.* **729**, 40 (2011).
- [291] K.M. Nollet, M. Busso, and G.J. Wasserburg, *Astrophys. J.* **582**, 1036 (2003).
- [292] M. La Cognata et al., *The Astrophysical Journal Letters* **739**, L54 (2011).
- [293] C. Abia et al., *Astrophys. J. Lett.* **737**, L8 (2011).
- [294] V.V. Smith et al., *Astrophys. J.* **633**, 392 (2005).
- [295] N. Mowlavi, A. Jorissen, and M. Arnould, *Astron. Astrophys.* **311**, 303 (1996).
- [296] M. Wiescher, J. Görres, and H. Schatz, *J. Phys. G: Nucl. Part. Phys.* **25**, R133 (1999).
- [297] R.L. Clarke and E.B. Paul, *Can. J. Phys.* **35**, 155 (1957).
- [298] A. Isoya, H. Ohmura, and T. Momota, *Nucl. Phys.* **7**, 116 (1958).
- [299] G. Breuer, *Zeit. Phys.* **154**, 339 (1959).
- [300] R. Caracciolo et al., *Lett. Nuovo Cim.* **11**, 33 (1974).
- [301] P. Cuzzocrea et al., *Lett. Nuovo Cim.* **28**, 515 (1980).
- [302] H. Lorenz-Wirzba, Ph.D. thesis, Univ. of Münster, 1978.
- [303] A. Couture, Ph.D. thesis, Univ. of Notre Dame, 2005.
- [304] W.B. McLean, A. Ellett, and J.A. Jacobs, *Phys. Rev.* **58**, 500 (1940).
- [305] G. Raimann et al., *Phys. Lett.* **B 249**, 191 (1990).
- [306] C.M. Laymon et al., *Phys. Rev.* **C 45**, 576 (1992).
- [307] S. Cristallo et al., *Astr. Astrophys.* **A 46**, 570 (2014).
- [308] I. Lombardo et al., *Phys. Lett. B* **748**, 178 (2015).
- [309] I. Indelicato et al., *The Astrophysical Journal* **845**, 19 (2017).
- [310] W.P. Liu et al., *EPJ Web Conf.* **109**, 09001 (2016).
- [311] H.A. Bethe, *Rev. Mod. Phys.* **62**, 801 (1990).
- [312] F. Douchin and P. Haensel, *Astron. Astrophys.* **380**, 151 (2001).
- [313] V. Serfling et al., *Phys. Rev. Lett.* **80**, 3928 (1998).

- [314] David J. Morrissey, Walter Benenson, and William A. Friedman, *Ann. Rev. Nucl. Part. Sci.* **44**, 27 (1994).
- [315] G. J. Kunde et al., *Phys. Lett.* **B272**, 202 (1991).
- [316] K. Huang, *Statistical Mechanics*, 1st ed. (Wiley, New York, 1963).
- [317] G. Verde et al., *Phys. Lett.* **B653**, 12 (2007).
- [318] R.Q. Twiss and R. Hanbury Brown., *Nature* **177**, 27 (1956).
- [319] W. Bauer, C. K. Gelbke, and S. Pratt, *Ann. Rev. Nucl. Part. Sci.* **42**, 77 (1992).
- [320] F. M. Marques, G. Martinez, T. Matulewicz, R. W. Ostendorf, and Y. Schutz, *Phys. Rept.* **284**, 91 (1997).
- [321] G. Goldhaber, W.B. Fowler, S. Goldhaber, T.F. Hoang, T.E. Kalogeropoulos, and W.M. Powell, *Phys. Rev. Lett.* **3**, 181 (1959).
- [322] G. Goldhaber, S. Goldhaber, W. Lee, and A. Pais, *Phys. Rev.* **120**, 300 (1960).
- [323] E.V. Shuryak, *Phys. Lett.* **44B**, 387 (1973).
- [324] S. E. Koonin, *Phys. Lett.* **70B**, 43 (1977).
- [325] D.H. Boal, C.-K. Gelbke, and B.K. Jennings, *Rev. Mod. Phys.* **62**, 553 (1990).
- [326] C. B. Chitwood et al., *Phys. Lett.* **B172**, 27 (1986).
- [327] S. Pratt and M.B. Tsang, *Phys. Rev. C* **36**, 2390 (1987).
- [328] G. Verde, A. Chbihi, R. Ghetti, and J. Helgesson, *Eur. Phys. J.* **A30**, 81 (2006).
- [329] M.A. Lisa et al., *Phys. Rev. Lett.* **70**, 3709 (1993).
- [330] G. Verde, D. A. Brown, P. Danielewicz, C. K. Gelbke, W. G. Lynch, and M. B. Tsang, *Phys. Rev. C* **65**, 054609 (2002).
- [331] D.A. Brown and P. Danielewicz, *Phys. Lett.* **B398**, 252 (1997).
- [332] G. Pasquali et al., *Nucl. Instrum. Meth.* **A 570**, 126 (2007).
- [333] M.S. Wallace et al., *Nucl. Instrum. Meth. A* **583**, 302 (2007).
- [334] J. Pouthas et al., *Nucl. Instrum. Meth.* **A357**, 418 (1995).
- [335] G. Lanzaò et al., *Phys. Rev. C* **58**, 281 (1998).

## Bibliography

---

- [336] D.V. Shetty et al., Phys. Rev. C **68**, 054605 (2003).
- [337] B. Davin et al., Nucl. Instrum. Meth. A **473**, 302 (2001).
- [338] C. Cavata, M. Demoulin, J. Gosset, M.-C. Lemaire, D. L'Hôte, J. Poitou, and O. Valette, Phys. Rev. C **42**, 1760 (1990).
- [339] L. Quattrocchi, Ph.D. thesis, Università degli Studi di Messina, 2015.
- [340] M. Bleicher and H. Stoecker, J. Phys. **G30**, S111 (2004).
- [341] O. Schapiro, A. R. DeAngelis, and D. H. E. Gross, Nucl. Phys. **A568**, 333 (1994).
- [342] L. Francalanza, J. Phys. Conf. Ser. **863**, 012061 (2017).
- [343] A. Matta et al., Phys. Rev. C **92**, 041302(R) (2015).
- [344] A.J. Kordyasz et al., Eur. Phys. J. A **51**, 15 (2015).
- [345] GANIL Grand Accélérateur National d'Ions Lourds, Lise++, <http://lise.nsl.msue.edu/lise.html>.
- [346] N. Le Neindre et al., Nucl. Instrum. Meth. A **490**, 251 (2002).
- [347] S.M. Sze (Ed.), *VLSI Technology*, 2nd ed. (Mcgraw-Hill, New York, 1988).
- [348] L. Bardelli et al., Nucl. Instrum. Meth. A **605**, 353 (2009).
- [349] G. Thungström et al., Nucl. Instrum. Meth. A **546**, 312 (2005).

# Ringraziamenti

Il periodo del dottorato di ricerca ha rappresentato per me un percorso di crescita dal punto di vista scientifico ed umano. Desidero ringraziare di cuore il Dr. Ivano Lombardo e il Prof. Mariano Vigilante per aver reso possibile, nel migliore dei modi, lo svolgimento di una fruttuosa attività di ricerca presso l'Università di Napoli Federico II. Ringrazio molto il Dr. Giuseppe Verde, grazie al quale è stato possibile intraprendere una collaborazione scientifica internazionale che ha coinvolto l'Université Paris-Saclay nell'ambito di una co-tutela di tesi.

Dal momento che una lista dei nomi delle persone che in questi tre anni di ricerca hanno contribuito alla realizzazione del presente lavoro sarebbe troppo lunga, voglio almeno ringraziare i gruppi di ricerca con i quali è stata instaurata una proficua collaborazione scientifica e che sono stati determinanti nella produzione del presente lavoro.

Ringrazio in dettaglio i gruppi di Fisica Nucleare delle Università di Napoli Federico II, Orsay e dell'Universidad Nacional Autónoma de México e le collaborazioni internazionali CHIMERA, NUCLEX, INDRA, AsFiN, MAGNEX.

Sono grato agli staff tecnici degli istituti di ricerca INFN-Sezione di Napoli, INFN-Laboratori Nazionali del Sud, INFN-Laboratori Nazionali di Legnaro e del Laboratorio dell'Acceleratore di Napoli per aver prodotto fasci di particelle accelerate di ottima qualità e per il supporto ricevuto nelle fasi di preparazione e realizzazione degli esperimenti.



# Appendix A

## A new device for future clustering and correlation studies: OSCAR

### A.0.4 Detector's layout

OSCAR (hOdoscope of Silicons for Correlations and Analysis of Reactions) [250] is conceived to be a modular hodoscope, based on two segmented silicon detection stages. They are optimized to detect and identify, with high resolution, low energy light particles emitted in nuclear reactions. The main features of this detector are the compactness and the high versatility, given by plug-and-play connections and embedded pre-amplifiers, and the low identification thresholds, thanks to use of a thin silicon detector as a first stage followed by 16 independent silicon pads.

More in detail, the first detection stage is a SSSSD (nominally 20  $\mu\text{m}$  thick) type 2M detector manufactured by *Micron Semiconductor*, operated at a depletion voltage of 2.5 V. On the front side, an aluminium metallization segments the silicon surface into 16 strips, having a pitch of 3.125 mm with an inter-strip of 0.125 mm nominal value. An inspection of the detector at the optical microscope confirms, within a few percent, these nominal values. The rear side is instead constituted by a single surface with a uniform aluminium metallization layer. A detailed investigation of the interface zone between an Al strip and the adjacent inter-strip region has been performed thanks to the use of a non-destructive analysis based on Atomic Force Microscopy (AFM). The height distribution of a  $\approx 46 \times 46 \mu\text{m}^2$  wide area at the interface is shown in Figure A.1 in a colour scale, indicating the relative height distribution in the analysed region. It evidently appears the presence of a deep canal (blue region),  $\approx 10 \mu\text{m}$  wide, that separates the Al metallization of each strip (yellow region) from the  $\text{SiO}_2$  layer of the inter-strip region (light green region). The three dots are due to micro-metric dust grain on the detector surface. The presence of this narrow ( $\approx 10 \mu\text{m}$ ) and deep ( $\approx 200 \text{nm}$  from the inter-strip layer average level) canal is attributed to the manufacturing technique of the detector. If we reasonably assume that the bottom of the narrow canal corresponds to the entrance side of the active detection volume, we can give an estimate of about  $680 \pm 40 \text{ nm}$  for the SSSSD

## Appendix A. A new device for future clustering and correlation studies: OSCAR

---

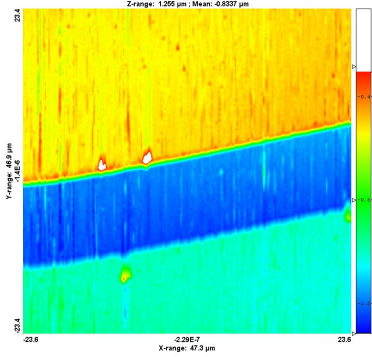


Figure A.1: Atomic Force Microscopy (AFM) profiling of a  $\approx 46 \times 46 \mu\text{m}^2$  area at the interface between an Al strip and the interstrip region. The yellow area corresponds to the Al strip, the green area to the interstrip region. The blue canal is due to the peculiar manufacturing technique of the Si strip detector. The colour scale indicates relative heights between the various parts of the detector.

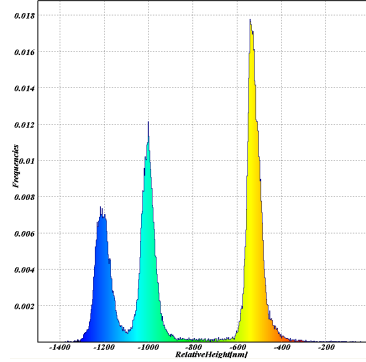


Figure A.2: Frequency histogram of the relative height distribution (in nm) in the region analyzed with the AFM technique. The colour scale visually corresponds to the three regions shown in the bi-dimensional plot.

dead entrance layer, on the basis of the height distribution histogram of Figure A.2.

A connector collects 16 electric lines from the front side of the detector. These lines are displaced in the ceramic frame to minimize cross-talk effects at levels lower than 1%. In the front side they are connected to the active areas of each strip by means of bonds while, in the rear side, only two of them have a bonding connection and the whole surface is maintained to ground. In order to minimize the electronic noise, the strip detector is connected, by means of a short flat cable, with a charge sensitive pre-amplifier model NPA-16FE, manufactured by the *Net Instruments* and installed inside the vacuum chamber. It has a sensitivity of 45 mV/MeV and it was especially designed to work in vacuum, with a low power consumption ( $< 900$  mW) and an aluminium box as heat sink. This compact pre-amplifier works with GND and  $\pm 6$  V service voltages given via a 5+5 pin service connector together with a common bias for the 16 silicon strips. To polarize the silicon we used a bias voltage of 3.0 V, operating in over-depletion regime. In these conditions we observed total leakage currents not exceeding 10 nA with all the strips simultaneously biased. The output signals of the pre-amplifier are then connected, by means of 2 groups of SCI coaxial cables, to 16 repetitions of a NIM front-end electronics with a spectroscopy amplifier.

## Appendix A. A new device for future clustering and correlation studies: OSCAR

---

The second detection stage consists of 16 independent silicon pad detectors manufactured by the Hamamatsu company with an active area of  $1 \text{ cm}^2$  and a ceramic package. The width of the ceramic frame is 1.4 mm except for the bottom side, for which a 3.2 mm frame is required to host the connection pins. The silicon pads are welded, with a tolerance of about 0.1 mm, on a printed circuit board (first layer of Figure A.3), manufactured by the INFN-Sezione di Napoli, containing electronic lines for the Si-pad connections. To minimize the cross-talk level, each detector has an independent ground line parallel to the corresponding signal line. The SSSSD is anchored to the board containing the silicon pads as in Figure A.4, while the board is connected, by means of two SMC Type-Q connectors, to a second board with embedded pre-amplifiers. This type of plug-and-play connection allows, with great versatility, to easily couple the detector stages with the pre-amplifiers board. Two sets of 8 Hamamatsu H4083 charge sensitive pre-amplifiers with 22 mV/MeV sensitivity and a low power consumption (150 mW maximum) are connected to the rear board by means of 9-pin single-line type connectors. A  $\pm 6 \text{ V}$  service voltage is given to the pre-amplifiers with two lemo connections on the rear side of the board, while a further lemo connection is also present to deliver a pulser signal to the electronic channels of the silicon pads. The signals from the second detection stage are collected via SCI connectors and delivered to a 16 channel Mesytec spectroscopic amplifier with integrated logic lines for generating the trigger signals and the corresponding gate for the acquisition system. Each pre-amplifier is dressed with a special material, thermally conductive and electrically insulating, in order to optimize the thermal contact with a copper heat sink, used as passive cooling system. It is clearly visible in the photo of Figure A.4, where the complete version of the OSCAR prototype.

The geometry of OSCAR is determined by the possible crossings between strips and pads. In particular, all the possible reduced overlap of a pad and the corresponding strip identify 64  $\Delta E$ -E pseudo-telescopes. A detailed geometrical scheme is described in Figure A.5, where the active area of each pad is represented by red squares, while blue lines delimit the active areas of each strip.

As visible from the figure, strips and pads are not exactly in geometrical matching. For example, the upper and lower parts of the second detection stage are not completely covered by the first stage. This explains the decreasing in the yield for the first and last rows of pseudo-telescopes observed in Figure A.6, which displays the number of identified particles for each pseudo-telescope obtained during a test experiment of OSCAR with heavy ion reactions (see paragraph A.0.5 for further details). A reduction of the active detection area is also expected for the first and last pseudo-telescopes of each quartet formed by a given pad and 4 consecutive strips, because of the overlap with the ceramic frame of the pads, as seen in Figure A.5. This results in the yield trend shown in Figure A.6, where the population of the first

## Appendix A. A new device for future clustering and correlation studies: OSCAR

---

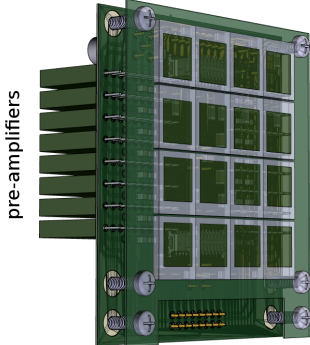


Figure A.3: A schematic view of the second detection stage of OSCAR. The rear board contains two series of 8 compact charge sensitive pre-amplifiers to collect signals from 16 silicon pads welded on the front board.



Figure A.4: A picture of the OSCAR device in the complete configuration. The strip detector and the first detector board are bounded with 4 screws, while the detector stages are connected to the rear board via two SMC Type Q connectors. The passive heat sink is visible in the photo.

and last pseudo-telescope of each quartet is significantly lower than the central ones, reflecting the previously discussed geometrical details. In Figure A.7 we report a lego-plot analogous to Figure A.6 but obtained with a Monte Carlo procedure where a complete simulation of the OSCAR geometry is considered. The two plots are in nice agreement, indicating that the relative efficiency in the detection, observed for the various pseudo-telescopes, can be mainly attributed to pure geometrical effects. Furthermore, the average reduction of the yield for decreasing strip numbers, seen in the experimental spectrum of Figure A.6, can be attributed to the kinematics of nuclear collisions involved, being the polar detection angle increasingly larger while the strip number decreases (see Section A.0.5 for details about the present test experiment). This effect, that requires an accurate modelling of the reaction dynamics, is not included in the simulation for simplicity.

### A.0.5 Detector characterization

A first test, aimed to probe the energy resolution and general capabilities of the silicon pads, has been carried out for the second detection stage standalone by means of a three peaks  $\alpha$ -source.  $\alpha$  particles with energies of the order of 5.5 MeV are indeed stopped in  $300\mu\text{ m}$  of silicon, and a measure of their total energy is possible. A pulse shape inspection with a digital oscilloscope of signals processed by the spectroscopy amplifiers allows to estimate the signal/noise ratio and also the level of the cross-talk between connection lines. In particular, we obtained average

## Appendix A. A new device for future clustering and correlation studies: OSCAR

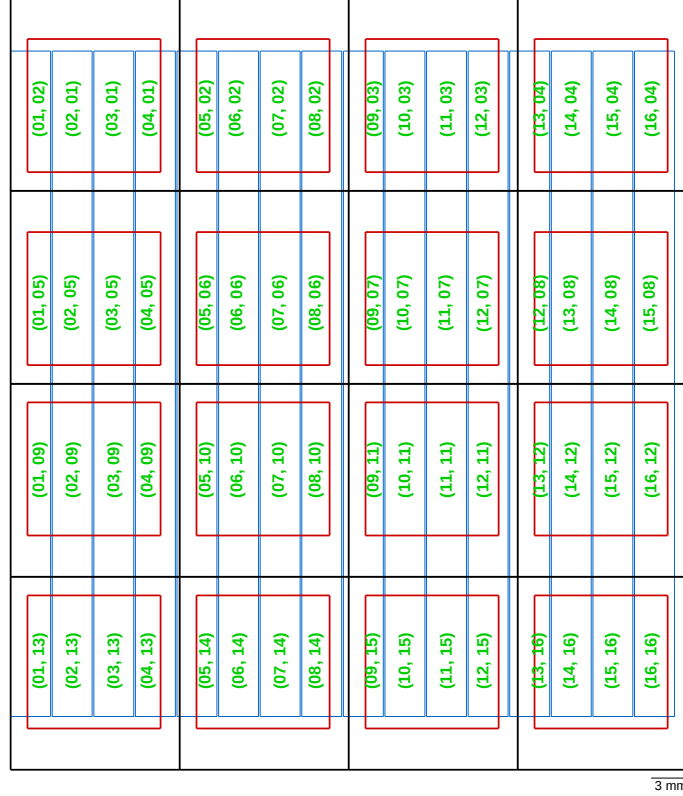


Figure A.5: A schematic view of the OSCAR telescope. The active area of each strip is delimited by a blue line, while each pad of the second detection stage is represented by a red square. Black lines represent the limits of the epoxy frame. Each pseudo-telescope is indicated by a label ( $\#strip, \#pad$ ).

noise levels of the order of 0.3% of signal amplitudes (and not exceeding 0.6% level) when the pads were irradiated by 5.48 MeV  $\alpha$  particles at a rate of  $\approx 300$  Hz on the whole pad layer. These very low noise values indicate that the resolution of pads is not strongly affected by cross-talk, thanks to the above discussed electronic design of the boards.

A test of the cooling systems of pre-amplifiers has been also done by keeping the detector working under vacuum for a few days. The measured temperatures at both the SSSSD and Si-pads pre-amplifiers reached a saturation value of, respectively,  $\approx 30^\circ$  C and  $\approx 40^\circ$  C after 24 hours.

The capabilities of OSCAR in terms of isotopic and energy resolution have been tested in several ways. In a first experiment, OSCAR was used to detect fragments and light charged particles in Ca+Ca collisions at 35 MeV/nucleon.  $^{40}\text{Ca}$  and  $^{48}\text{Ca}$  beams were accelerated by the superconductive cyclotron K-800 of INFN-LNS, impinging on  $^{40}\text{Ca}$  and  $^{48}\text{Ca}$  targets. OSCAR was placed at  $\theta = 55^\circ$  in the laboratory

## Appendix A. A new device for future clustering and correlation studies: OSCAR

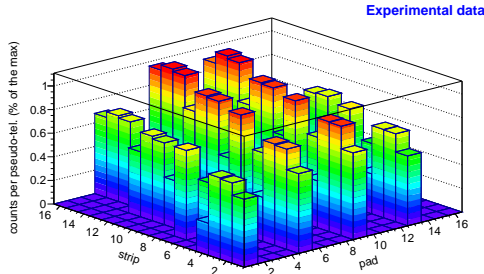


Figure A.6: Identified particle yield distribution on the  $(\#strip, \#pad)$  plane with experimental data taken in the test experiment described in Section A.0.5.

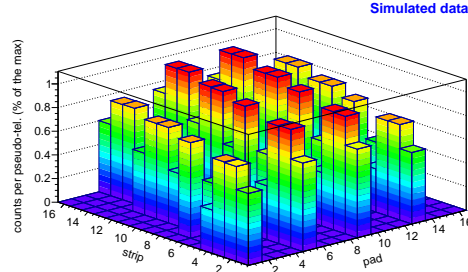


Figure A.7: Simulated detection efficiency represented on the  $(\#strip, \#pad)$  plane. The plot is obtained by filtering flight directions isotropically generated with a Monte-carlo code simulating the geometrical set up and the characteristics of the OSCAR detector.

frame at a distance of 103 cm from the target, while, simultaneously, the 4-block configuration of the FAZIA array was used at forward angles.

A typical  $\Delta E$ - $E$  plot obtained in this experiment is shown in Figure A.8 for a pseudo-telescope of OSCAR. Here  $E_{res}$  is the residual energy measured in the Si-pad while  $\Delta E$  is the corresponding signal in the strip detector. As clearly visible, lines corresponding to light nuclei are highly populated while, essentially due to kinematics, the statistics is lower for heavier ions. Particles with different  $Z$  values are unambiguously identified up to the punch-through points (except for the  $Z = 1$  isotopes, for which the lines overlap the punch-through line of  ${}^4\text{He}$  before their punch-through points), and a nice isotopic separation is also evident.

It is important to specify that with the term *identified particle* we indicate a couple of signals ( $\Delta E$  and  $E_{res}$ ) for which it is possible to reconstruct an unambiguous track inside OSCAR. The construction of tracks is based on a specific geometrical coherence algorithm, and we define *unambiguous* a track when it is the only one that is possible to construct with each used signals, as above discussed.

Energy calibrations for each strip and pad were obtained from punch-through points of various isotopes, assuming a total thickness given by the sum of the thickness of the Si-pad detectors and the measured thickness of the SSSSD (see par. 2.3) in correspondence of the pseudo-telescope analysed. Calibrations have been complemented also by using a 3-peak  $\alpha$ -source, taking also into account the dead layer quoted in the previous paragraph. These particles are close to the punch-through in the SSSSD stage and therefore they release a large part of their energy in the first detection stage, while only weak signals are produced in the second stage; this allows to extend the calibration of the second stage at lower energies.

Appendix A. A new device for future clustering and correlation studies: OSCAR

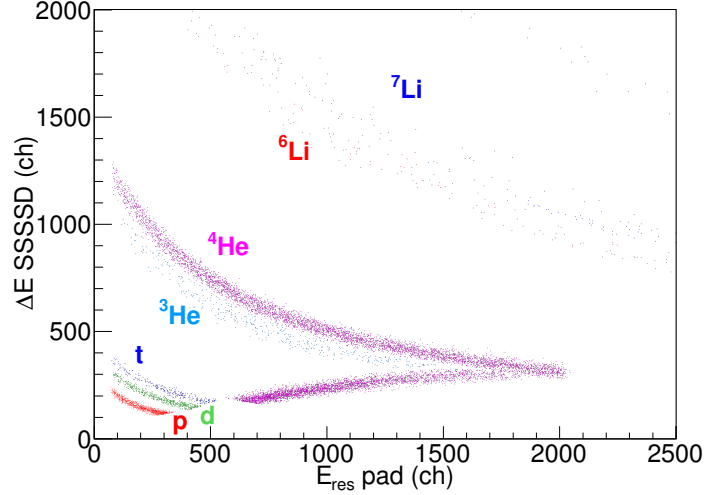


Figure A.8:  $\Delta E$ -E plot for a pseudo-telescope of the OSCAR device. In the y-axis we report the signals released in the SSSSD stage, while in the x-axis we report the residual signals in the pads stage.

In Figure A.9 we report results concerning the detection of  $^4\text{He}$  nuclei. Blue points come from a dedicated run in which OSCAR was irradiated by a 3-peak  $\alpha$ -source containing a mix of  $^{239}\text{Pu}$ ,  $^{241}\text{Am}$  and  $^{244}\text{Cm}$  isotopes ( $E_\alpha = 5.1$  MeV, 5.5 MeV and 5.8 MeV). As visible,  $\alpha$  particles occupy three different regions of the  $^4\text{He}$  line, reflecting the three different energies of the source. Furthermore, the lower energy peak is partly cut. This effect is due to the identification threshold. Indeed,  $\alpha$  particles of  $\approx 5$  MeV are at the limit of identification of OSCAR, and, for this reason, only the most perpendicular flight directions can give signals in the second stage.

In the insert of Figure A.9 we show the spectrum obtained by summing the calibrated energy signals of the two stages for the  $\alpha$ -source data. The red region indicates the part of the spectrum affected by the identification threshold. For the 5.5 MeV peak we can estimate a global energy resolution of  $\approx 70$  keV FWHM, indicating the good performances of the detector.

In Figure A.10 we report the experimental identification thresholds of the OSCAR array for H, He, Li and Be isotopes; they correspond to the punching-through energies in the  $20\ \mu\text{m}$  first silicon stage for each identified nucleus and for each pseudo-telescope. We plot experimental values as a function of the ideal ones, taking only into account the thickness of the first detection stage (as experimentally measured, see next subsection). Error bars in the theoretical values of thresholds are calculated taking into account the detector non-uniformities, and they lie in the interval 3–5% depending on the type of particle and the gradient thickness in the

## Appendix A. A new device for future clustering and correlation studies: OSCAR

---

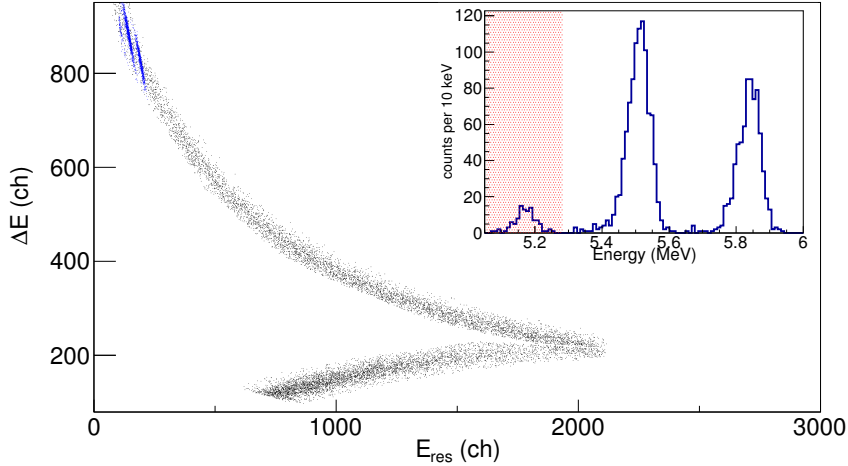


Figure A.9:  $\Delta E$ - $E_{res}$  plot for nuclei identified as  ${}^4\text{He}$ . Blue points represent data taken during a calibration run in which the OSCAR device was irradiated by means of a 3-peaks  $\alpha$ -source. The insert shows an energy spectrum obtained for  ${}^4\text{He}$  detected in the calibration run. The area coloured in red represents the energy region in which we observe a suppression of the yield due to the experimental identification limit at low energies.

SSSSD zone identifying a given pseudo-telescope. Experimental thresholds (y-axis) are determined from the starting points of each reconstructed energy distribution; for these values we assumed a maximum (conservative) indetermination of 3% in agreement with the uncertainties in the energy calibrations and in the assignment of the spectra starting points. The behaviour of the experimental points (in different colours for different isotopes) does not evidence any sizeable systematic divergence from the ideal trend  $E_{thr}^{exp} = E_{thr}^{theor}$  shown by the bisector line (dashed red line), indicating negligible effects due to electronic non-linearities as well as to the entrance dead layer.

### A.0.6 Non-uniformity of the $\Delta E$ stage

When ultra-thin Silicon detectors are used, it is mandatory to fully characterize their thickness uniformity [343, 344]. To this aim we performed a dedicated experiment to obtain a precise characterization of the thickness of the first detection stage of the OSCAR detector. The SSSSD was mounted on a movable support which allowed to set, with a micro-metric accuracy, the spatial position of the SSSSD

## Appendix A. A new device for future clustering and correlation studies: OSCAR

---

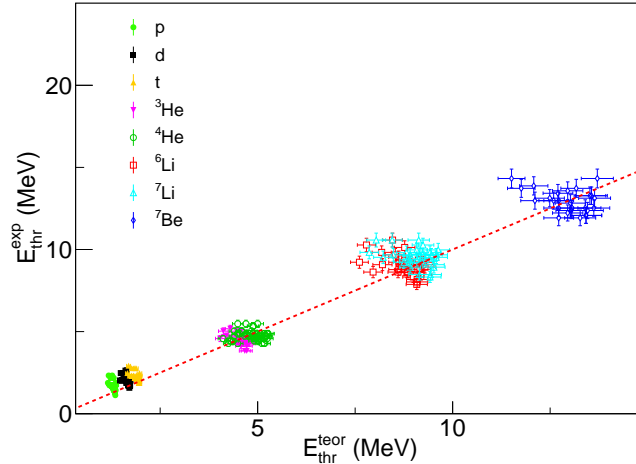


Figure A.10: Correlations between expected theoretical and experimental identification thresholds for different identified isotopes (see the legend) and for each pseudo-telescope. Error bars in the experimental values ( $\approx 3\%$ ) accounts for indeterminacy on the energy calibration, while the calculated theoretical ones (3–5%) are affected by the indeterminacy of the detector thickness. The red dashed line represents the ideal trend for  $E_{thr}^{exp} = E_{thr}^{teor}$ .

respect to a mono-isotopic  $\alpha$ -source. A high resolution Si detector was placed in axial correspondence to the source, with the SSSSD placed between them. The  $\alpha$ -source and the Si detector were both collimated with circular brass diaphragms of 1.0 mm radius. The thickness of the SSSSD was determined in different points of silicon surface, with  $1\mu\text{m}$  maximum uncertainty, by measuring the residual energy of  $\alpha$  particles passing through the silicon layer and using energy loss routines.

Energy calibration of the Si detector was obtained by using  $\alpha$  particles with different energies. A  $^{239}\text{Pu}$ ,  $^{241}\text{Am}$ ,  $^{244}\text{Cm}$   $\alpha$ -mixed source was used to obtain high energy calibration points, while a  $^{241}\text{Am}$   $\alpha$ -source followed by a calibrated  $10.0 \pm 0.5 \mu\text{m}$  Al foil was used to complement the calibration data set with a lower energy point.

With this apparatus, we were able to measure the SSSSD thickness in different points of its surface with 2 mm spatial indeterminacy. We performed 64 measurements at positions corresponding to the centres of each pseudo-telescope. The detector thickness for each point was calculated using the LISE++ software [345] from the measured residual energies. In doing this, we assumed that the whole SSSSD (including the thin Al layers used for electrical contacts) is made by silicon. Results are shown in Figure A.11, where the measured thickness is indicated in  $\mu\text{m}$  by the grey scale, and in the 3-dimensional representation of Figure A.12. Both figures indicate the presence of strong variation of the thickness, that reaches a minimum

## Appendix A. A new device for future clustering and correlation studies: OSCAR

---

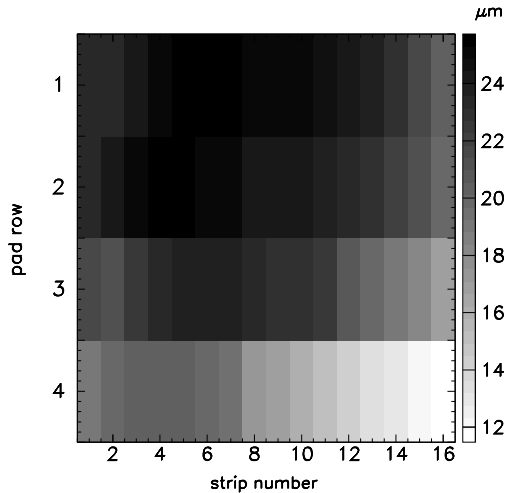


Figure A.11: Bi-dimensional distribution of the SSSSD thickness in the  $(\#strip, \#pad)$  plane. The grey scale indicates the thickness, numbers are expressed in  $\mu\text{m}$ .

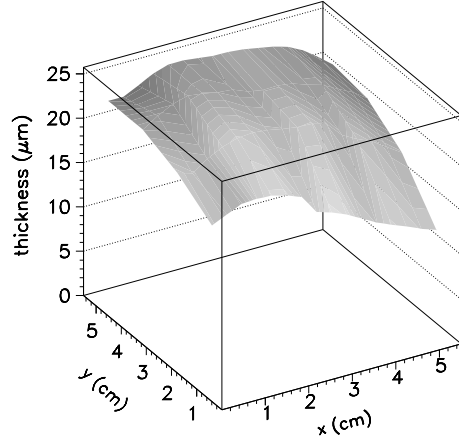


Figure A.12: SSSSD thickness characterization in the cartesian coordinates frame. The y-axis increases for increasing pad number while the x-axis is perpendicular to the strips direction. Thickness levels are expressed in  $\mu\text{m}$  and are represented on the z-axis. The picture puts in evidence the strong thickness gradient observed in correspondence of the right bottom corner of the detector.

in the right-bottom corner of the SSSSD. This effect is attributed to the difficulties of manufacturing very thin (and large) slices of silicon. Thickness varies from  $11.5 \mu\text{m}$  to  $25.6 \mu\text{m}$ , pointing out a non-uniformity level well larger than the nominal one ( $\pm 5 \mu\text{m}$ ).

We estimate also how the isotopic resolution is affected by the SSSSD non-uniformities. In fact, the thickness uniformity of the  $\Delta E$  layer directly affects the  $\Delta E$ -E identification capability of a telescope. A way to quantify this effect is to correlate the isotopic resolution as a function of the thickness gradient.

An estimate of this gradient was obtained by carefully measuring the thickness of SSSSD at 10 positions along a given strip, thus obtaining an accurate thickness profile of a single strip. We selected the strip #14, that is sufficiently far from the border of the SSSSD, and has the maximum thickness excursion. The results were then interpolated with a polynomial function  $f(x, y)$ , being  $y$  the position along the pad row of Figure A.11, i.e. along the strip length, and  $x$  the one along the strip number axis. The thickness gradient along the direction of the strip can be deduced by partial derivative of this function:  $\partial f / \partial y$ . For each pseudo-pixel we

## Appendix A. A new device for future clustering and correlation studies: OSCAR

---

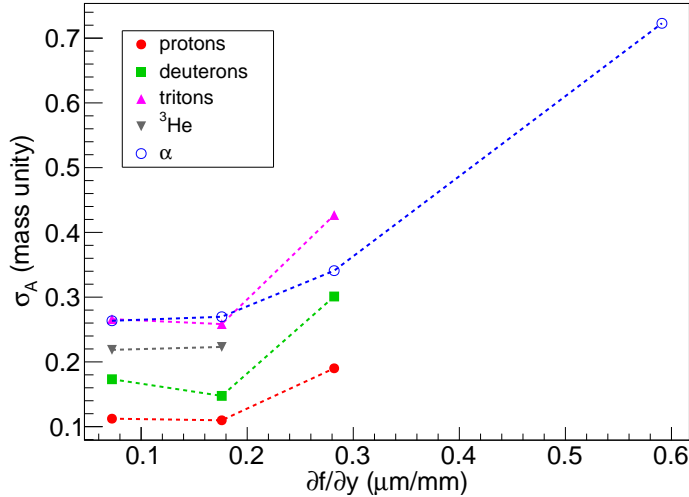


Figure A.13: Mass identification resolution  $\sigma_A$  (in unity of number of masses) as a function of the degree of non-uniformity of the first silicon stage, expressed as the thickness gradient along the strip direction  $\partial f / \partial y$  in  $\mu\text{m}/\text{mm}$ . Each  $\partial f / \partial y$  value is given in correspondence of each pseudo-telescope center identified by the same strip. Different isotopes are reported in different colours as indicated in the legend.

have considered the value that the derivative assumes in the corresponding center.

To quantify the isotopic resolution, we transformed the points of the  $\Delta E$ - $E$  scatter plot into mass spectra. To this aim we used an analytical method [346]. Firstly, we find a set of parameters of a Bethe-Bloch based function that reproduce the shape of each line in the  $\Delta E$ - $E$  plot; secondly, we consider the distance of each experimental point in the  $\Delta E$ - $E$  plane with the corresponding analytical line. For a given isotope, an estimate of the mass resolution is thus obtained as the  $\sigma_A$  of its mass distribution extracted from a gaussian fit. We report in Figure A.13  $\sigma_A$  (in unities of number of masses) as a function of the thickness gradient  $\partial f / \partial x$  (in  $\mu\text{m}/\text{mm}$ ). As expected, the trend indicates an increase of the  $\sigma_A$  values for each isotope as the non-uniformity level increases. More precisely, we observe that a uniformity better than  $0.3 \mu\text{m}/\text{mm}$  is mandatory to obtain a good identification of isotopes up to  ${}^4\text{He}$  when we use a module of OSCAR. Above this value the  $Z = 1$  lines merge together, while we can still estimate  $\sigma_{{}^4\text{He}}$  because of the very low  ${}^3\text{He}$  emission respect to  ${}^4\text{He}$ . Unfortunately, this type of analysis can not be performed on Li and Be isotopes because of the low collected statistics.

### A.0.7 Channeling effects in $\Delta E$ detector

While ions move inside a silicon crystal, atomic planes could line up offering to the ions preferential ways to pass through the crystal with a reduced interaction with

## Appendix A. A new device for future clustering and correlation studies: OSCAR

---

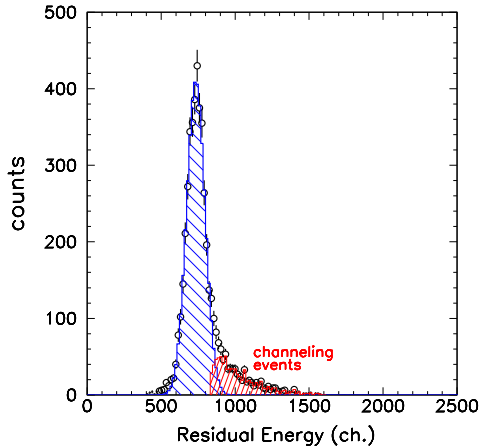


Figure A.14: Channeling effect studied from the residual energy spectrum, for one of the measured points (open circles). The blue line represents the normal (unchanneled) contribution to the spectrum, parametrized with a gaussian curve. Channeling events are associated to the non-gaussian tail of the spectrum (red area).

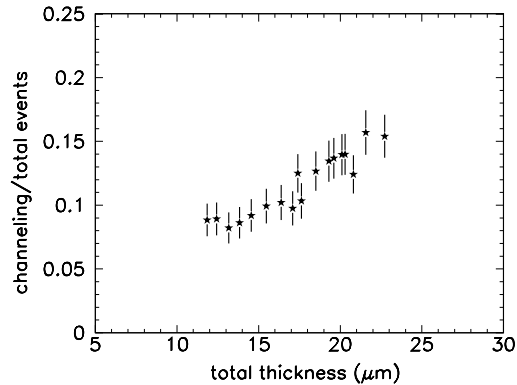


Figure A.15: Evolution of the percentage of channeling events as a function of the detector thickness.

atomic electrons and nuclei. This effect is known as *channeling*, and results in a reduction of the expected energy loss [347]. As shown in Ref. [348], the evaluation of such effects is very important for particle identification and for the design of new silicon detectors. In fact, in the  $\Delta E$ - $E$  technique, channeling effects introduces fluctuations that worsen the isotopic resolution.

The presence of channeling effects can be seen by inspecting the shape of  $\alpha$  particle energy spectra after passing through the  $\Delta E$  stage. To do this we used the same geometrical set-up described in the previous paragraph and an  $^{241}\text{Am}$   $\alpha$  source. A typical energy spectrum is displayed on Figure A.14; it corresponds to a region of the  $\Delta E$  detector having  $21\ \mu\text{m}$  thickness. In absence of channeling, this spectrum should have a gaussian shape due to the statistical nature of the energy loss mechanisms for thick layers; at variance, in presence of channeling, a high energy tail appears. Indeed, this last case is experimentally observed. To estimate the relative yield of the channeling events, we performed a gaussian fit (blue solid line) of the experimental points (open circles); the upper limit of the fit region was set

## Appendix A. A new device for future clustering and correlation studies: OSCAR

---

around the right half-maximum point of the spectrum. The channeling yield was then estimated by subtracting the gaussian component from the experimental data. This contribution is reported on Figure A.14 with the red spectrum.

The percentage of channeling events is, in this case,  $15 \pm 3\%$ ; this value is in reasonable agreement with the ones estimated in [349] for similar silicon thickness and a similar geometrical setup. An overall view of the percentage of channeling events as a function of the silicon thickness is reported in Figure A.15. Even if the error bars are quite large, we see a correlation between the thickness of the silicon detector and the percentage of channeling events, at least in the thickness domain here explored (12-22  $\mu\text{m}$ ). This finding is in agreement with the one of Ref. [349] and seems to indicate that the channeling plays a minor role in the case of ultra-thin detectors ( $< 15 \mu\text{m}$ ).

### A.0.8 Correlations: the case of $\alpha$ - $\alpha$ correlation and the reconstruction of ${}^8\text{Be}$

Particle-particle and multi-particle correlations are topics of great interest in heavy ion collisions [319, 328]. They allow not only to investigate on the structure of resonant states produced in nuclear collisions but also on the space-time properties of the nuclear medium itself. In this paragraph we report on the possibility of taking advantage from the good energy resolution and angular segmentation of the OSCAR hodoscope to investigate the decay of resonances produced in Heavy Ion collisions by means of the invariant mass technique (paragraph 1.5.3). In particular, we discuss the reconstruction of  ${}^8\text{Be}$  via the  $\alpha$ - $\alpha$  correlation. In Figure A.16 we show the  $\alpha$ - $\alpha$  invariant mass spectrum obtained by selecting couples of  $\alpha$  particles; to increase the statistics we summed events from all the colliding systems. For simplicity, we show it in terms of *relative energy*, i.e. the kinetic energy of the particles in the reference of the emitting source, which is defined as  $E_{rel} = w - \sum m_i$ , being  $w$  the invariant mass of the system and  $m_i$  the mass of the  $i$ th particle. As expected, we found a peak centered at about 90 keV, which corresponds to the ground state of  ${}^8\text{Be}$  produced in the collisions. Unfortunately, due to the limited angular coverage of the hodoscope, placed at a distance of 103 cm from the target, we collected low statistics and we are not sensitive to the first excited state of  ${}^8\text{Be}$ , located at around 3 MeV. If a couple of  $\alpha$  particles is emitted from the latter state we are indeed not able to simultaneously detect the two particles, being the corresponding kinematical cone larger than the angular acceptance of our detector.

The distance from the target to the OSCAR hodoscope is therefore a parameter of fundamental importance to be taken into account, for correlation studies, since it regulates not only the efficiency in the reconstruction of resonances but also the relative energy resolution. Being OSCAR a modular device, designed to be installed with high versatility in different configurations, a precise study of the above mentioned aspects as a function of the distance from the target is required to fully

## Appendix A. A new device for future clustering and correlation studies: OSCAR

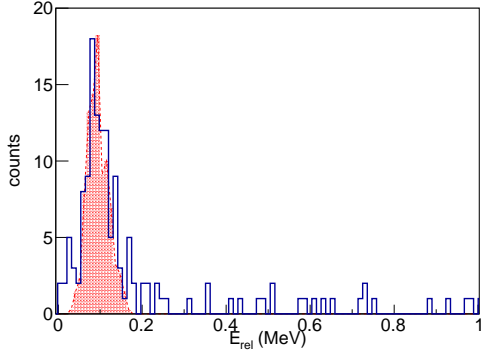


Figure A.16:  $\alpha$ - $\alpha$  invariant mass spectrum (in the form of  $E_{rel}$ ) obtained by summing the statistics from the three nuclear systems here studied. Data exhibit a peak at about 90 keV which corresponds to the ground state of  ${}^8\text{Be}$ . The low statistics is due to the large distance of OSCAR from the target.

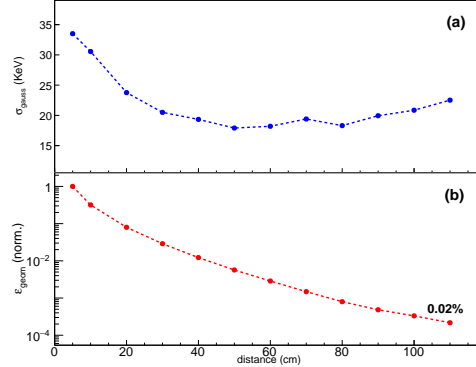


Figure A.17: (a) Resolution in the reconstruction of the  ${}^8\text{Be}$  ground state via  $\alpha$ - $\alpha$  correlations, extracted as the  $\sigma$  of a gaussian fit, as a function of the distance of OSCAR from the target. (b) Same plot for the efficiency, normalized to the point at 5 cm. A value of 0.02% is reached at 110 cm.

characterize the powerful of the device.

To this aim we developed a Monte Carlo simulation of the geometry of OSCAR, used as a filter to process simulated  ${}^8\text{Be}$  decays data. To produce the set of simulated events we have considered a flat angular distribution of the emitting  ${}^8\text{Be}$  nuclei, having values of momentum extracted uniformly from 500 MeV/c to 1200 MeV/c, as suggested by the reconstructed  ${}^8\text{Be}$  momentum spectrum derived from the experimental data of Figure A.16. The results of our simulation are reported in Figure A.17. The upper panel shows the relative energy resolution in the reconstruction of the ground state of  ${}^8\text{Be}$  as a function of the distance from the target. With resolution we indicate the  $\sigma_{gauss}$  of a gaussian fit reproducing the ground state peak seen in the invariant mass spectrum. Varying the distance from 5 cm to 110 cm we observe a decrease of the resolution from about 31 keV to about 9 keV, which represents a very good value. The simulation shows also that the expected resolution saturates for values of distance higher than 80 cm. This effect can be attributed to the reduced number of pseudo-telescopes which contribute to the spectrum; in fact, when the distance is larger the kinematical cone of the emitted particles becomes wider compared to the size of the detector. In the bottom panel we show the efficiency in the reconstruction of such resonance as a function of distance. In this case we have normalized the values to 100% at 5 cm from the target. The plot reveals a strong decrease of the geometrical efficiency with the distance. In correspondence of

## Appendix A. A new device for future clustering and correlation studies: OSCAR

---

110 cm it reaches 0.02% of the value observed at a distance of 5 cm. Such plots are useful to fix the optimal distance for studying the decay of a particular resonance, and the versatility of OSCAR allows to reach a good balance between efficiency and resolution.